

**Preparation, Characterization and Application
of Proton, Lithium and Zinc-ion Conducting
Polymer Electrolytes for Supercapacitors,
Lithium- and Zinc-Metal Batteries**

**Thesis Submitted to AcSIR
For the Award of the Degree of
DOCTOR OF PHILOSOPHY**

In

Chemical Sciences



By

Mr. Vidyanand V

Registration Number: 10CC15J26006

**Under the guidance of
Dr. Sreekumar Kurungot**

**CSIR-National Chemical Laboratory
Pune-411008**

CERTIFICATE

This is to certify that the work incorporated in this Ph.D. thesis entitled **“Preparation, Characterization and Application of Proton, Lithium and Zinc-ion Conducting Polymer Electrolytes for Supercapacitors, Lithium- and Zinc-Metal Batteries”** submitted by **Mr. Vidyanand V** to Academy of Scientific and Innovative Research (AcSIR) in fulfillment of the requirements for the award of the Degree of Doctor of Philosophy, embodies original research work under my guidance. I further certify that this work has not been submitted to any other University or Institution in part or full for the award of any degree or diploma. Research materials obtained from other sources has been duly acknowledged in the thesis. Any text, illustration, table etc., used in the thesis from other sources, have been duly cited and acknowledged.

It is also certified that this work done by the student, under my supervision, is plagiarism free.



Vidyanand V
(Student)



Dr. Sreekumar Kurungot
(Supervisor)

DECLARATION

I, hereby declare that all the experiments in thesis entitled “**Preparation, Characterization and Application of Proton, Lithium and Zinc-ion Conducting Polymer Electrolytes for Supercapacitors, Lithium- and Zinc-Metal Batteries**” submitted for the degree of Doctor of Philosophy in Chemical Sciences to the Academy of Scientific and Innovative Research (AcSIR) have been carried out by me at the Physical and Materials Chemistry Division, CSIR-National Chemical Laboratory, Pune-411008, India, under the supervision of **Dr. Sreekumar Kurungot**. This work is original and has not been submitted to any other University or Institution in part or full for the award of any degree or diploma.



Mr. Vidyanand V

Date: 26-06-2020

Physical and Materials Chemistry Division,

CSIR- National Chemical Laboratory

Pune-411008, India.

Acknowledgment

With immense pleasure, I take this opportunity to thank everyone who has knowingly or unknowingly involved in the completion of this most precious document of my lifetime in the form of a doctoral thesis. It was an enjoyable but challenging journey for the past five and a half years at CSIR-NCL, Pune, revealing me the literal meaning of the quote 'perseverance is the key to success'.

During this fantastic journey, I am very much obliged and thankful to my research supervisor Dr. Sreekumar Kurungot for his outstanding guidance, which enormously helped me to grow as a confident and independent researcher. He has always given me space and freedom to pursue original research ideas, with his timely suggestions holding me on the right track. His positive approach to collaborative research has undoubtedly helped me learn, develop, and contribute to diverse research areas within our research group. Once again, I mark my gratitude to my 'boss' for facilitating an excellent research atmosphere at CSIR-NCL during my Ph.D. tenure.

I devote my sincere greetings to Dr. Manohar V. Badiger for enabling a fruitful interdisciplinary research atmosphere in his lab at the Polymer Science and Engineering Division of CSIR-NCL, Pune. His cheerful demeanor, filled with positivity, has always inspired me while working at his lab. Also, I am indebted to his student Dr. Arun Torris for being a perfect collaborator. Many of my discussions on polymers with Dr. Arun Torris have reflected at several parts of this document shaping it into the form of a Ph.D. thesis. At this point, I am recollecting all the helps he has done for me with a token of wholehearted gratitude. Besides, I thank all other lab members of Dr. Badiger's group for considering me as one of them.

Another unforgettable person who has always supported me during this beautiful journey is Dr. Bihag Anothumakkool, the former doctoral researcher from our group. I would like to thank him for introducing me to the world of electrochemical energy storage research and profoundly acknowledge his scientific and non-scientific contributions in the present thesis. I also thank another senior member from our lab Dr. Sreekuttan M. Unni, for motivating me with all his genuine encouragements.

The opportunity to carry out a part of my research work related to polymer electrolytes for lithium metal batteries at Helmholtz Institute Muenster (HIMS), Germany, was a life-changing experience. I thank my mentors Dr. Jijeesh R. Nair and Prof. Dr. Martin Winter, from HIMS, for making my tenure at Germany an unforgettable scientific experience. I also

thank Dr. Krishnan Kartha and all my other friends in Germany for making my stay at Muenster even happier.

I take this opportunity to thank my DAC members, Dr. Mahesh J. Kulkarni, Dr. Paresh L. Dhepe, and Dr. Santosh Babu Sukumaran, for all their support, suggestions, and constant evaluation of my research work during the half-yearly meetings. Also, I thank Dr. Kumar Vanka, Dr. Pankaj Poddar, Dr. Rajesh Gonande, Dr. Sayan Bagchi, Dr. Suman Chakraborty, and my research supervisor Dr. K. Sreekumar for their excellent lectures as part of the CSIR-NCL coursework. I also thank the current and former directors of CSIR-NCL, AcSIR, UGC, and CSIR for establishing all the scientific infrastructure at CSIR-NCL for conducting high-quality research. The service from the CMC division of CSIR-NCL with the timely characterization of the samples was admirable, and I thank Venkatesh, Harsha, Chetan, Tushar, Pankaj, and Sheethal for their bits of help. The indispensable support from the SAO and AcSIR coordinators from CSIR-NCL is also acknowledged. Besides the scientific and technical personnel, I thank the non-scientific staff at various departments of CSIR-NCL for making the official paper works hassle-free. Among the CSIR-NCL staff, I would like to specially mention the efforts of security-staffs and hygiene workers, keeping our campus safe and clean. Considering that the Ph.D. is the highest degree in the academic hierarchy, I feel this is the right moment to remember all my former teachers with gratitude for building the foundation for my upbringing.

My sincere thanks to all my current and former labmates Dr. Bihag, Dr. Sreekuttan, Dr. Vishal, Dr. Harshita, Dr. Santosh, Dr. Kashyap, Dr. Roby Soni, Dr. Rajith, Dr. Sidhu, Dr. Ayasha, Pranav, Meena, Sachin, Manna, Ajmal, Swati, and Geeta, with all whom I have shared my precious moments in the lab. I am happy for the time I shared in the lab with former researchers Pandiaraj, Sarath Ramadas, Maya, and all other internship students from various universities across India. I convey my special gratitude to Nikhil Chandran and Maria for carrying out their internship research projects with me. Thanks to the current and former post-docs in the lab Dr. Gaurav, Dr. Raji, and Dr. Shilpa.

I always cherish the beautiful moments spent in my room 'G1' with my dear friends Sanoop, Shubin, Rajith, and Pranav. Special thanks to my chunk-friends Vipin, Shebeeb, Rashid, Ranjeesh, Munnavar, Abdul Khayum, Fayiz, and Zinoy for being a part of the unforgettable memories at CSIR-NCL. I also thank Dr. Prajitha, Dr. Leena George, Dr. Sarath Kandambath, Dr. Anumon, and Dr. Unnikrishnan for their warm friendship. I am pleased to meet and befriend many other unique people at CSIR-NCL from various parts of India. Thanks to my football teammates, Ajith, Zlatan, Sandy, Pogba, Singam, Abdul Motaleb, Asif, and

Subhrasish, for making the evenings sporty. I thank my other friends and well-wishers at CSIR-NCL and Pune like Sayanthan, Pinka, Arun Dadwal, Rajan Pandya, Shailaja, Poonam, Pravin, Apurva, Vedi, Kumar, Sudhakar, TT man, Anurag, Prabhanjan, Taha, Vivek, Anupriya, Betsy, Aswathy, Vaishnavi, Moumitha, Dr. Vandana, Dr. Suresha, Manaf Ikka, and many others. I thank all the junior students of the Malayali group at CSIR-NCL for the moments spent together during the excursions and cultural programs. Also, thanks to all my friends from the GJPL cricket fraternity, HoR-4, GJ, and New hostel as well.

I know there is no need for a formal mentioning, but special thanks to you, Meena, for all the emotional support and for being the best part of my Pune life.

Finally, but most importantly, I extend my deep sense of gratitude to my family for their continuous support and love. I am always obliged and find it difficult to express my feelings for my Achan and Amma for raising the three of us children to be independent with their never-settling determination. I am always grateful to my dear Manu Chettan, for his love and affection towards me. It has always strengthened, inspired, and supported me to proceed with my decisions in my life confidently. I thank Paru Chechi for all the care and always cherish the innocence and moments I shared with my dear Pappa and Nanda. I am grateful to my dear Ammukutty for always listening to my thoughts with utmost patience and rejuvenating the happiness within me. Thanks to Sidhhu for being part of us and supporting Ammu. Ultimately, I am dedicating this thesis to my family, and I am happy to make them feel proud.

Vidyanand V

List of Abbreviations

AC	Activated carbon
ACN	Acetonitrile
AIW	Acid-in-Water
AMU	Atomic mass unit
AOETMA	[2-(acryloyloxy)ethyl]trimethylammonium chloride
APS	Ammonium persulfate
ASSEs	All-solid-state electrolytes
BET	Brunauer–Emmett–Teller
CD	Charge-discharge
CEI	Cathode electrolyte interphase
CNF	Carbon nano-fiber
CNT	Carbon nanotube
CT	Computed tomography
CV	Cyclic voltammetry
DCM	Dichloromethane
DFT	Density functional theory
DMA	Dynamic mechanical analyzer
DMC	Dimethyl carbonate
DMF	Dimethylformamide
DOL	Dioxalane
DSC	Differential scanning calorimetry
D-XPE	Dual salt cross-linked polymer electrolyte
EC	Ethylene carbonate
EDL	Electric double layer
EDLCs	Electric Double Layer Capacitors
EEDs	Electrochemical energy storage devices
EIS	Electrochemical impedance spectroscopic
EO	Ethylene oxide
ESR	Equivalent series resistance
FESEM	Field emission scanning electron microscope
FTIR	Fourier transform infrared spectroscopy
GPEs	Gel polymer electrolytes

HEMA	2-hydroxyethyl methacrylate
HER	Hydrogen evolution reaction
HMPP	2-hydroxy-2-methylpropiophenone
HPA	2-hydroxy-3-phenoxypropyl acrylate
HSAL	High surface area lithium
ISEs	Inorganic solid-state electrolytes
LB	Lithium battery
LCO	Lithium cobalt oxide
LED	Light emitting diode
LFP	Lithium iron phosphate
LIBs	Lithium-ion batteries
LiFSI	Lithium bis(fluorosulfonyl) imide
LiTFSI	Lithium bis(trifluoromethanesulfonyl)imide
LMBs	Lithium-metal batteries
LMO	Lithium manganese oxide
LNMO	Lithium nickel manganese oxide
LSV	Linear sweep voltammetry
LTO	Lithium titanium oxide
LVR	Linear visco-elastic region
NCA	Nickel cobalt aluminum oxide
NMC	Nickel manganese cobalt oxide
NMP	N-methyl-2-pyrrolidone
NMR	Nuclear magnetic reference
OCP	Open circuit potential
OER	Hydrogen evolution reaction
PAN	Poly(acrylonitrile)
PANI	Polyaniline
PC	Propylene carbonate
PEG	Poly(ethylene glycol)
PEGDA	Poly(ethylene glycol) diacrylate
PEGDAE	Poly(ethylene glycol) diallyl ether
PEGDME	Poly(ethylene glycol) dimethyl ether
PEGMA	Poly(ethylene glycol) methyl ether methacrylate
PEO	Poly(ethylene oxide)

PGPE	Polyelectrolyte gel polymer electrolyte
pLMB	Primary lithium metal battery
PMMA	Poly(methyl methacrylate)
PVA	Polyvinyl alcohol
PVAc	Polyvinyl acetate
PVCA	poly(vinylene carbonate)
PVdF	Poly(vinylidene fluoride)
PVdF-HFP	Poly(vinylidene difluoride-co-hexafluoropropylene)
QC	Quantum chemical
SAED	Selected area electron diffraction
SCs	Supercapacitors
SEI	Solid electrolyte interphase
SPEs	Solid polymer electrolytes
SSA	Specific surface area
SSEs	Solid-state-electrolytes
StSt	Stainless steel
S-XPE	Single salt cross-linked polymer electrolyte
TEM	Transmission electron microscope
TGA	Thermogravimetric analyser
UV	Ultraviolet
VEC	4-vinyl-1,3-dioxolan-2-one
VTF	Vogel–Tamman–Fulcher
WIA	Water-in-Acid
WiSE	Water in salt electrolyte
XPE	Cross-linked polymer electrolyt
XPS	x-ray photoelectron spectroscopy
XRD	X-ray diffraction
ZIP	Zn ²⁺ -ion conducting polymer electrolyte
ZMBs	Zinc-metal batteries
ZMPBs	Zinc-metal polymer batteries
ZMPs	Zinc-metal hybrid polymer supercapacitors
ZMSC	Zinc-metal hybrid supercapacitors

Table of Contents

Preface		1-3
Chapter 1		
General Insights on Batteries, Supercapacitors, and Polymer electrolytes		4-44
1.1	Introduction	5-9
1.2	Fundamentals of batteries and supercapacitors	9-30
1.2.1	Batteries in general	9-12
1.2.2	Lithium-ion batteries (LIBs)	12-19
1.2.3	Transition from LIB to LMBs	19-22
1.2.4	Lithium batteries to post-lithium battery technologies	22-24
1.2.5	Supercapacitors	24-29
1.2.6	Conclusive remarks on batteries and supercapacitors	29-30
1.3	Solid-State Electrolytes (SSEs)	30-36
1.3.1	Polymer Electrolytes	31-36
1.3.2	Inorganic Solid Electrolytes (ISEs)	36
1.4	Electrode Electrolyte interface and their challenges in EEDs	36-38
1.5	Conclusion, scope, and objectives of this thesis	38-41
1.6	References	41-44
Chapter 2		
<i>Water-in-acid</i> Gel Polymer Electrolyte Realized through a Phosphoric Acid-Enriched Polyelectrolyte Matrix toward Solid-State Supercapacitors		45-76
2.1	Introduction	46-47
2.2	Experimental Section	47-52
2.2.1	Materials	47-48
2.2.2	Preparation of <i>Water-in-Acid</i> PGPE	48
2.2.3	Preparation of PVA-H ₃ PO ₄ Acid-in-Water/Water-in-Acid GPE solutions	48-49
2.2.4	Preparation of PANI	49
2.2.5	Electrode Preparation and SC Device Fabrication	49
2.2.6	Material Characterisation	49-50
2.2.7	Electrochemical characterisation of GPE and SC devices	50-52
2.3	Results and Discussion	52-69

2.4	Conclusion	69-70
2.5	References	70-76

Chapter 3

A High-Voltage Supercapacitor Possessing Nonaqueous Gel Polymer Electrolyte Prepared Using the <i>In Situ</i> Polymerization Process		77-116
3.1	Introduction	78-80
3.2	Experimental Section	80-86
3.2.1	Materials	80
3.2.2	Preparation of the electrode	80
3.2.3	Preparation of GPEs by UV curing	81
3.2.4	Preparation of the PMMA-based GPE solution	81
3.2.5	SC device fabrication	81-82
3.2.6	Material characterization	82-83
3.2.7	Electrochemical characterization of GPE and the devices	83
3.2.8	Equations used for Electrochemical Characterization	83-84
3.2.9	Mechanical characterization of PHPA, H-P-80% and GPEs	84-86
3.3	Results and Discussion	86-110
3.3.1	NMR and ATR-FTIR characterizations of HPA-based GPEs	86-90
3.3.2	Mechanical characterization of HPA-based GPEs	90-95
3.3.3	Ionic conductivity and activation energy of HPA-based GPEs	95-98
3.3.4	Electrochemical characterization of the supercapacitor devices	98-108
3.3.5	Scalability of the <i>in situ</i> process	108-110
3.4	Conclusion	110
3.5	References	110-116

Chapter 4

Dioxolanone Anchored Poly (Allyl Ether)-Based Crosslinked Dual-Salt Polymer Electrolytes for High-Voltage Lithium Metal Batteries		117-160
4.1	Introduction	118-120
4.2	Experimental Section	120-126
4.3	Results and discussion	126-152
4.3.1	Synthesis of XPE membranes	126-128
4.3.2	Characterization of XPEs by ATR-FTIR spectroscopy	128-134
4.3.3	Thermal analysis	134-137
4.3.4	Quantum chemical calculations	137

4.3.5	Ionic conductivity and related characteristics	138-141
4.3.6	Electrochemical stability window (ESW)	141-146
4.3.7	Galvanostatic lithium plating/stripping	146-149
4.3.8	Performance of XPE membranes in LMBs	149-152
4.4	Conclusion	152
4.5	References	152-160

Chapter 5

An <i>In Situ</i> Crosslinked Nonaqueous Polymer Electrolyte for Zinc-Metal Polymer Batteries and Hybrid Supercapacitors		161-193
5.1	Introduction	162-166
5.2	Experimental Section	166-172
5.2.1	Materials	166
5.2.2	Preparation of polymer electrolyte membranes	166-167
5.2.3	Synthesis of vanadyl phosphate cathode (VOPO ₄ · 2H ₂ O)	167
5.2.4	Electrode coating and fabrication of zinc-metal cells	167-169
5.2.5	Characterization methods and techniques	169-172
5.3	Results and discussion	172-188
5.4	Conclusion	188-189
5.5	References	189-193

Chapter 6

Summary & Future Perspectives		194-198
6.1	Summary	194-197
6.2	Future perspectives	197-198
Achievements		199-201
Erratum		202

Preface

In the past two centuries, the technology of electrochemical energy storage devices (EEDs) has seen tremendous advancements with the most notable one being the evolution of rechargeable batteries. Especially, within the last three decades, rechargeable lithium-ion batteries (LIBs) have become an integral part of our daily life. The high energy density of LIBs makes them suitable to be heavily employed in applications ranging from small-scale electric devices to large-scale automotive applications and beyond. Besides, the potential of using LIBs for energy distribution in the form of smart-grids is also being explored. The conceptualization of Gigafactories by Tesla and several other corporate giants as well as the 2019 Nobel Prize in Chemistry has further fuelled the vision of attaining energy sustainability through hard-core research in LIBs and other related battery technologies. The technology of supercapacitors is also very important considering their high power-capability compared to the batteries. Supercapacitors are commercialized but often used in combination with LIBs (or other battery technologies) to improve their power capability. Recently, Maxwell Technologies, one of the biggest producers of supercapacitors, was dissolved into Tesla, emphasizing the importance of supercapacitors along with the LIB technology. The supercapacitor-battery hybrids are envisaged as the next big thing in electric vehicles and the consumer electronics industry since they can enable fast-charging energy storage devices with a high energy density that can enable the long-term operation of mobile phones, electric vehicles, etc. Also, supercapacitors are employed in regenerative braking technology to reduce the work-load of battery in electric vehicles that can enhance the travel-range and shelf-life of the battery systems.

In batteries and supercapacitors, electrolytes are one of the most important components. The widely used liquid electrolytes can be either aqueous or nonaqueous depending on the type of electrochemistry operating in the battery or supercapacitor. Nonaqueous liquid electrolytes are popular in commercial LIBs (aqueous electrolytes are rarely explored), whereas both aqueous and nonaqueous electrolytes are used in supercapacitors. Liquid electrolytes are free-flowing and they require stringent packaging norms to avoid the risk of leakage. Besides, the lack of dimensional stability makes them unfit to be employed in futuristic flexible electronic applications. The inflammable nature of the liquid electrolytes used in the *state-of-the-art* LIBs is another huge concern. The corrosive nature of the commonly used acidic and alkaline liquid electrolytes is also well known. Apart from the aforementioned common intricacies associated with the liquid electrolytes, the safe operation of certain battery technologies cannot be realized with liquid electrolytes. For instance, in commercial LIBs, graphite-based intercalation anodes

(theoretical capacity of 380 mAh/g) are employed, enabling them to deliver an energy density value of ≈ 250 -300 Wh/kg in combination with high-voltage cathodes (oxides of Ni, Co, etc., with a theoretical capacity in the range of 150-250 mAh/g). However, replacing the graphite-based anodes by lithium-metal (theoretical capacity of ≈ 3800 mAh/g) can help in a further improvement of the energy density. Such batteries employing Li-metal as the anode are popularly known as lithium-metal batteries (LMBs) or often considered as a separate category called ‘beyond Li-ion’ technology. However, the conventional nonaqueous liquid electrolytes used in lithium-ion batteries restrict the rechargeability of LMBs. These liquid electrolytes incite/accelerate the growth of the Li-dendrites during the continuous cycling of LMBs leading to cell-failure or even fire-hazards. However, it is proven that the use of lithium-ion conducting solid-state electrolytes (SSEs) can inhibit the dendrite-growth over the Li-metal anode facilitating the rechargeability.

SSEs are broadly classified into inorganic SSEs (ISEs) and polymer electrolytes. Polymer electrolytes are further classified into solid polymer electrolytes (SPEs) and gel polymer electrolytes (GPEs). The ISEs and SPEs are also known as all-solid-state electrolytes (ASSEs) due to the absence of any liquid-phase in them. Due to the same reason, they are hard, often suffer from low ionic conductivity, and cannot ensure effective contact with the electrode surface. However, GPEs are intermediate between the ASSEs and liquid electrolytes owing to the presence of a certain amount of liquid-phase in them. Despite the presence of the liquid phase, with the judicious selection of the polymer hosts, GPEs can exhibit solid-like operability satisfying the requirement of a safe electrolyte. Besides, the presence of liquid phase helps in improved ionic conductivity compared to the all-solid-state counterparts (SPEs and ISEs). Moreover, the proper combination of a liquid electrolyte and polymer host can result in GPEs exhibiting a variety of ion conduction including H^+ , OH^- , Li^+ , Na^+ , Zn^{2+} , Mg^{2+} , etc. This is not always possible with ASSEs, where the ionic conduction is limited to certain alkali metal ions (Li^+ and Na^+) and few multivalent ions such as Mg^{2+} , Zn^{2+} , and Al^{3+} . Therefore, it is reasonable to address the GPEs as universal SSEs that can be adopted for both batteries and supercapacitors. In a nutshell, the current dissertation focuses on the preparation, and characterization of GPEs exhibiting H^+ , Li^+ , and Zn^{2+} ion conductivity for the applications in supercapacitors and rechargeable batteries.

Chapter 1 of this thesis aims at providing a detailed and general overview of EEDs with an emphasis on supercapacitors and rechargeable batteries. Among the rechargeable batteries, the emerging technologies of the zinc-metal batteries (ZMBs) and LMBs are covered. Similar to LMBs, a ZMB is nothing but a rechargeable battery employing zinc-metal as the

anode against a suitable cathode in the presence of a zinc-ion conducting electrolyte. ZMB can be considered as a post-lithium battery technology that operates similarly to an LMB but is free of Li. The requirement of nonaqueous electrolytes over conventional aqueous electrolytes to improve the average operating voltage of ZMBs is discussed. Overall, the importance of the gradual transition from the liquid electrolytes to SSEs for improving the prospects of EEDs and the associated challenges incurred during the transition are thoroughly covered in **Chapter 1**. At the end of **Chapter 1**, the scope and objectives of the thesis are also stated in detail.

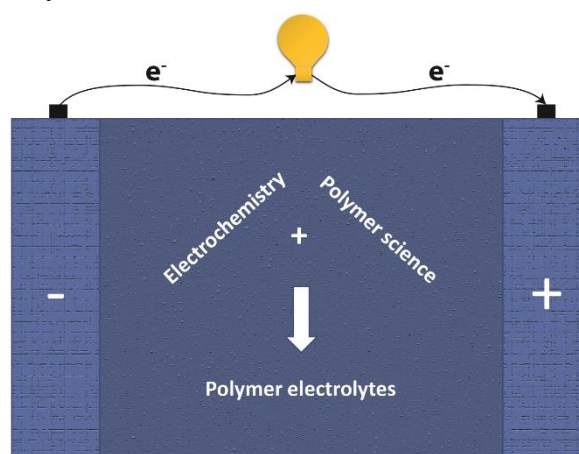
With the background information as introduced in **Chapter 1**, **Chapters 2** and **3** explore the designing of aqueous (H^+ conducting) and nonaqueous (Li^+ -ion conducting) GPEs for polyaniline (PANI)-based pseudocapacitors and activated carbon (AC)-based high-voltage electric double layer capacitors (EDLCs), respectively. For the preparation of the GPEs under investigation, the strategy of ultraviolet (UV)-light assisted free-radical polymerization method is employed. The superiority of the prepared GPEs over the conventional GPE solutions is demonstrated using electrochemical and physicochemical characterizations. The capability of the UV-polymerization method of GPE preparation as a tool for mimicking the electrode|electrolyte interface similar to that of a liquid electrolyte in the case of EDLC is also addressed. Later, the developed UV-light induced polymerization method is extended towards the preparation of Li^+ - and Zn^{2+} -ion conducting GPEs and concomitant fabrication of LMB and ZMBs, respectively. In the case of LMBs (**Chapter 4**), the properties of cross-linked polymer electrolyte (XPE) membranes are tuned in such a way that it can display high oxidation stability window beyond 4.3 V *vs.* $Li|Li^+$. This allows the XPE to be used along with Ni-based cathode for the LMB fabrication, which is often missing in the existing literature. Finally, in **Chapter 5**, the preparation of a Zn^{2+} -ion conducting polymer electrolyte (ZIP) is realized by using the UV-polymerization technique for the first time in literature. The ZIP exhibited oxidation stability of ≈ 2.5 V *vs.* $Zn|Zn^{2+}$, which is higher than the conventional aqueous electrolytes. In this work also, the tuning of electrode|electrolyte interface in the ZMB full-cell using the GPE synthesis by UV-polymerization approach is attempted.

In the concluding **Chapter 6**, the important observations and outcomes evolved from each working chapter of the thesis are summarized. This section emphasizes the fact that why the obtained results are important. It also rationalizes the excellent scope of the interdisciplinary research between electrochemistry and polymer chemistry, which can contribute to efficient EEDs. This chapter also includes a short note on future perspectives as well as the scope of improvements.

Chapter 1

General Insights on Batteries, Supercapacitors, and Polymer electrolytes

The core theme of the present thesis is to design efficient polymer electrolytes that can be used along with electrochemical energy storage devices (EEDs) *viz.*, lithium batteries, post-lithium batteries, and supercapacitors. In line with this, this chapter introduces the core concepts related to EEDs with an emphasis on different types of electrolytes used in them. The chapter starts with the introductory section covering the importance of attaining energy sustainability. Later, the concepts of the state-of-the-art lithium-ion batteries (LIBs) employing nonaqueous liquid electrolytes are introduced, which is followed by a discussion on lithium-metal batteries (LMBs). The inevitability of Li^+ -ion conducting solid-state-electrolytes (SSEs) is explained in terms of inhibiting the Li-dendrite induced cell-failure so that the rechargeable models of LMBs can be designed. The importance of transition towards post-lithium battery technologies is discussed with the example of the emerging technology of rechargeable zinc-metal batteries (ZMBs). The rationale behind the requirement of high-voltage Zn^{2+} -ion conducting nonaqueous polymer electrolytes for ZMBs is addressed. Later, the chapter also explains the types of supercapacitors based on the electrochemical processes occurring across the interface between the electrode and electrolyte. Followed by a discussion on the difference between the aqueous and nonaqueous electrolytes for the supercapacitors, the types of SSEs employed in EEDs are summarized with specific consideration into the polymer electrolytes. The practical intricacies associated with the use of polymer electrolyte-films resulting in the inferior utilization of the active electrode material compared to the liquid electrolytes are illustrated. The concept of the *in situ* polymerization process as a tool to improve the electrode|electrolyte interface is followed by a section dedicated to discussing the scope and objectives of the thesis.



**Electrochemical Energy Storage Devices
(Batteries & Supercapacitors)**

1.1 Introduction

Superseding the fossil fuel-based energy production with renewable alternatives is an indispensable requirement towards attaining energy sustainability. In the current scenario, energy production from non-renewable fossil fuels cannot be considered as a long-term remedy due to their fast depletion and the associated environmental pollution. Despite the enormous funding and investments dedicated to developing energy production from renewable resources, the practical intricacy lies in their intermittent nature. Therefore, apart from energy production, the storage of the produced energy is also equally important. For these reasons, the concomitant development of highly efficient and eco-friendly energy storage devices is also of utmost importance. In this scenario, electrochemistry comes for the rescue with tremendous opportunities to design a variety of electrochemical energy storage devices (EEDs).¹ EEDs can be either used along with conventional power sources (e.g. a hybrid electric vehicle with an internal combustion engine and a battery) or as a stand-alone power source (e.g. a fully electric vehicle). Apart from mobility, EEDs are already being extensively used for micro- and macro-electronic appliances (e.g. mobile phones, biosensors, pacemakers, etc.,) accelerating the prospects of the Internet Of Things (IoT) as well as envisaged to be employed for energy storage and distribution through smart grids.² In other words, electrochemical energy storage devices have already revolutionized all aspects of our lifestyle.

Batteries and supercapacitors are generally accepted to be the most important among the EEDs.¹ Batteries are characterized by their high energy density making them suitable for electric devices required to be operated for a long period. One such application is an electric vehicle, which is expected to cover a long distance per recharge. The requirement is similar for other small electronic devices such as smart-phones and laptop computers. However, the recharging of the battery usually takes more time once they are exhausted due to their low power density. For applications requiring rapid power delivery and recharging, EEDs exhibiting high power density are required. The most suitable choice among high power EEDs is electrochemical capacitors, also known as supercapacitors or ultracapacitors. For example, regenerative braking is one such application that is used to recover power in cars and other heavy electric vehicles that would otherwise lose energy as heat during braking. Supercapacitors are also used for improving the cold start capability of automotive engines. Despite exhibiting high power density, the energy density of the supercapacitors is very low compared to the batteries. It is a challenging task to combine both the features of high energy

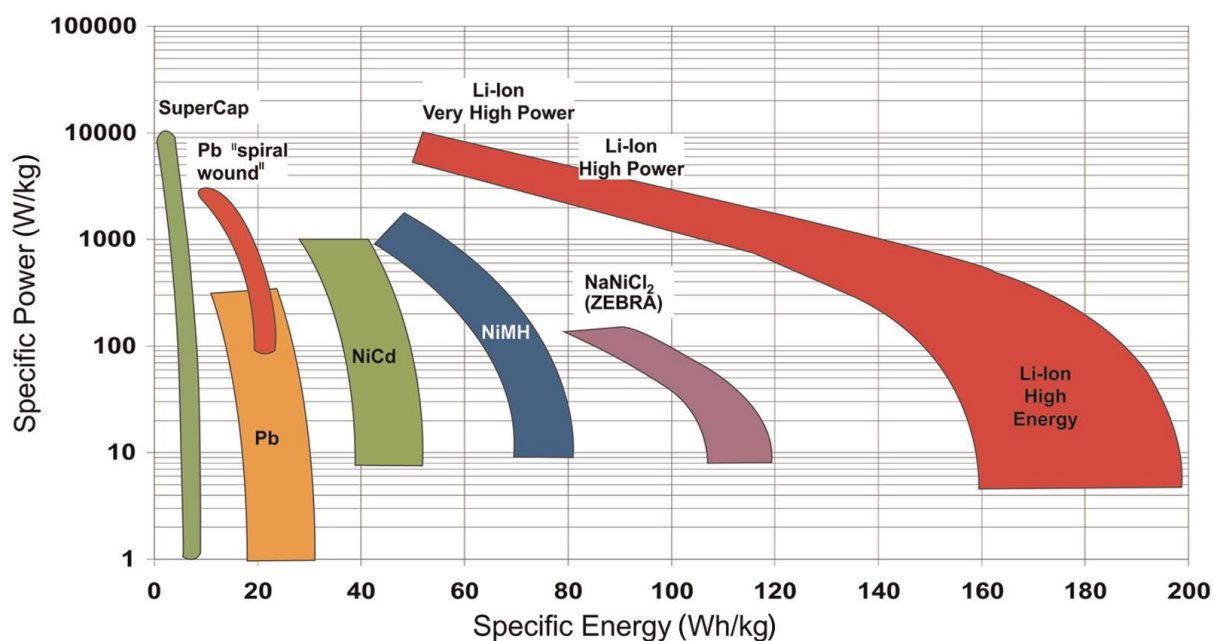


Figure 1.1. The Ragone plot comparing the energy and power density of various EEDs. Only supercapacitors and rechargeable batteries are considered for comparison. SuperCap: supercapacitor; Pb: lead-acid battery; Li-ion: LIB; NiCd: Ni-Cd battery; NiMH: nickel-metal hydride battery; NaNiCl₂: sodium–nickel chloride battery. (Reproduced with permission from reference 3, SAGE Publications, Copyright © 2013, © SAGE Publications).

and power density in the same EED due to the limitations related to the electrochemical processes. However, a hybrid EED invoking the extreme features of batteries and supercapacitors can be envisaged in the future that can be used to cope up with the trade-off between energy and power capabilities. This is one of the reasons why a hand-in-hand research towards improving the state-of-the-art batteries and supercapacitors is of extreme importance in the contemporary world. **Figure 1.1**, shows a Ragone plot comparing the energy and power density values of supercapacitors and various rechargeable battery technologies.³

In any EEDs, whether it be supercapacitors or batteries, electrolytes are one of the most important components. The role of an electrolyte in any EEDs is to balance the flow of electrons across the external circuit during the charge/discharge process by internally allowing the transport of ions between the electrodes.⁴ Conventional electrolytes are generally electrolytic-solution type in the service-temperature range, which consist of mobile ions and a solvent. The solvent often being a liquid, they are known as liquid electrolytes. In a liquid electrolyte, the mobile ions are generated as a result of the dissociation of salts/acids/alkalis (known as electrolyte solutes) in the solvent of interest. Mainly, aqueous (water) and nonaqueous (organic solvents or inorganic solvents) solvents are employed for the preparation of electrolytes, and hence they can be broadly classified into aqueous and nonaqueous liquid

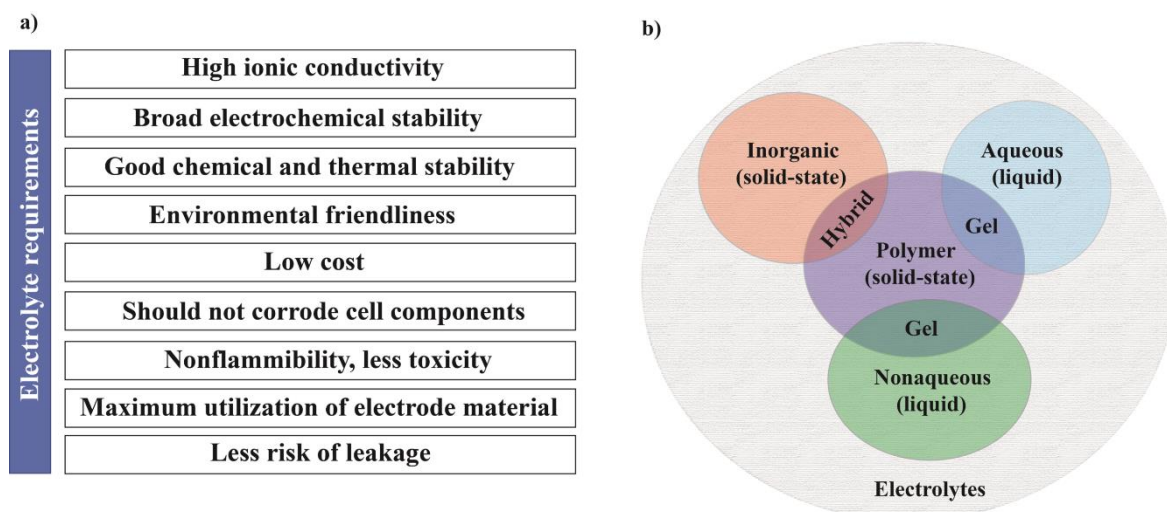


Figure 1.2. (a) Desirable features of an electrolyte used in EEDs; (b) broad classification of the electrolytes.

electrolytes.⁵ All electrolytes are ionic conductors, or in other words, the mobile ions in the electrolyte direct the movement of charges between the electrodes of an EED depending on the potential/voltage.⁴ The desirable features of an electrolyte and the general classification of the electrolytes are summarized in **Figure 1.2**.

Both aqueous and nonaqueous liquid electrolytes are ubiquitously employed in the commercial EEDs. However, the use of these liquid electrolytes in EEDs is associated with several practical limitations and constraints. For example, a good electrolyte is generally expected to be safe, economic, and easily integrable with the electrochemical devices. It should be also able to offer uncompromised performance when employed in commercial devices. The term ‘safety’ in the context of an electrolyte covers more than one aspect as follows. An electrolyte is expected to possess non-flammability, environmental friendliness, and chemical inertness to the other cell components (e.g. separator, electrode substrates, and packaging materials). Other features such as non-toxicity, free from potential leakage, evaporation, and gas evolution during the operation of the electrochemical cell, are also highly desirable.⁵ Despite being heavily employed in the commercial devices, most of the aforementioned features are not satisfied in the case of the state-of-the-art liquid electrolytes. For instance, nonaqueous carbonate solvent-based liquid electrolytes used in the commercial LIBs and supercapacitors are toxic as well as inflammable. The acidic electrolytes employed in the lead-acid batteries are highly corrosive to their components. Therefore, liquid electrolytes incite several environmental and safety concerns.⁶ Moreover, the free-flowing nature of the liquid

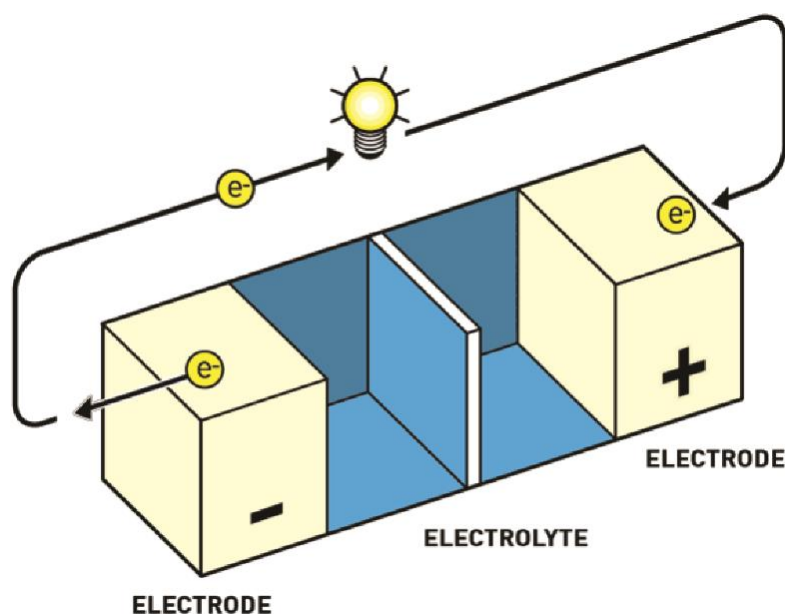


Figure 1.3. Scheme depicting the components of a battery cell. The two electrodes, electrolyte, and the separator are visible. Since the electron flows from the negative (anode) to the positive electrode (cathode), the process depicted is the discharge of the battery cell. The discharge mode of a battery is also known as the galvanic mode. (Reproduced from the press releases on the Nobel Prize in Chemistry 2019: © The Royal Swedish Academy of Sciences, <https://www.nobelprize.org/>).

electrolytes demand sophisticated packaging norms to be adopted for the fabrication of EEDs, which in turn increases the cost of production. Besides, liquid electrolytes are not suitable for flexible architectures and micro-EEDs (e.g. micro-supercapacitors, micro-batteries, etc.), which are highly desired in the industry of smart and flexible electronics.

To overcome the practical intricacies associated with the liquid electrolytes, the paradigm shift in tuning the physicochemical properties of the electrolytes is inevitable. In recent times, solid-state electrolytes (SSEs) are emerging as a suitable alternative to the liquid electrolytes. SSEs can improve the prospects of safe and flexible futuristic EEDs. An SSE is nothing but a material, which can allow the conduction of ions in the solid-state. Polymer electrolytes (solid polymer electrolytes (SPEs) and gel polymer electrolytes (GPEs)) and inorganic solid-state electrolytes (ISEs) are the two major classes of SSEs (explained in **Section 1.3**).^{7, 8} SSEs leverage the safety, mechanical, and thermal properties compared to the liquid-state counterpart. The less inherent reactivity of SSEs compared to the liquid electrolytes helps in mitigating the side reactions with the cell components so that an enhanced shelf-life of the EED can be expected. SSEs can enhance the high-temperature operability of the EEDs, at which conventional liquid electrolytes (aqueous and nonaqueous) undergo decomposition, ignition, and/or evaporation. Also, the easy integrability of SSEs with flexible devices avoids

the obvious constraints imposed by free-flowing liquid electrolytes with the risk of leakage. Among the SSEs, SPEs and ISEs are generally known as all-solid-state electrolytes (ASSEs), since they are completely free from a liquid phase. However, in the case of SPEs, to improve the ionic conductivity as well as ensuring an extended electrode|electrolyte interface, a certain amount of liquid electrolyte is also often added. Such polymer electrolytes that are intermediate between a liquid electrolyte and ASSEs are popularly known as GPEs (**Figure 1.2b**).⁷

The core theme of this thesis is to develop the polymer electrolyte-based SSEs suitable for EEDs. Among the polymer electrolytes, the category of dimensional stable aqueous and nonaqueous GPEs are extensively explored for various types of ion conduction such as proton H^+ , Li^+ , and Zn^{2+} . In all the works discussed in this thesis, the preparation of GPEs is achieved by simple and scalable ultraviolet (UV)-light induced polymerization process. In this method, the constituent monomers are mixed with a suitable liquid electrolyte in the presence of a photo-initiator to form a reactive mixture. This reactive mixture in the liquid state is either cast on a flat surface or directly spread over the electrode surface to be converted into GPE followed by UV-curing. The latter approach of polymer electrolyte generation directly over the electrode surface in line with the device fabrication is known as the *in situ* process. The *in situ* process as a tool to improve the electrode|electrolyte interface in polymer electrolyte-based EED is also emphasized in this thesis.

1.2 Fundamentals of batteries and supercapacitors

This section is intended to provide insights into the mechanism of operation of batteries and supercapacitors. In the case of batteries, LIBs are taken as an example considering their wide-spread application. Two types of supercapacitors *viz.*, 1) Electric Double Layer Capacitors (EDLCs) and 2) Pseudocapacitors are also explained with emphasis on the reactions occurring at the interface between the electrode and electrolyte leading to their different charge-storage behavior.⁹ As already mentioned, the key difference between a battery and supercapacitor is the high energy density and low power density in the former, and vice versa in the latter.¹

1.2.1 Batteries in general

The basic configuration of the battery cell (discharge process is depicted) is displayed in **Figure 1.3** and its working principle is relatively straightforward.⁴ The battery cell consists of two electrodes that can be connected to an electric circuit. These two electrodes are separated by an electrolyte, which accommodates the charged species known as ions. Usually, a physical barrier (known as separator) is used to avoid the physical contact between the electrodes. The role of a separator is to avoid the short-circuit that may arise if the two electrodes come in

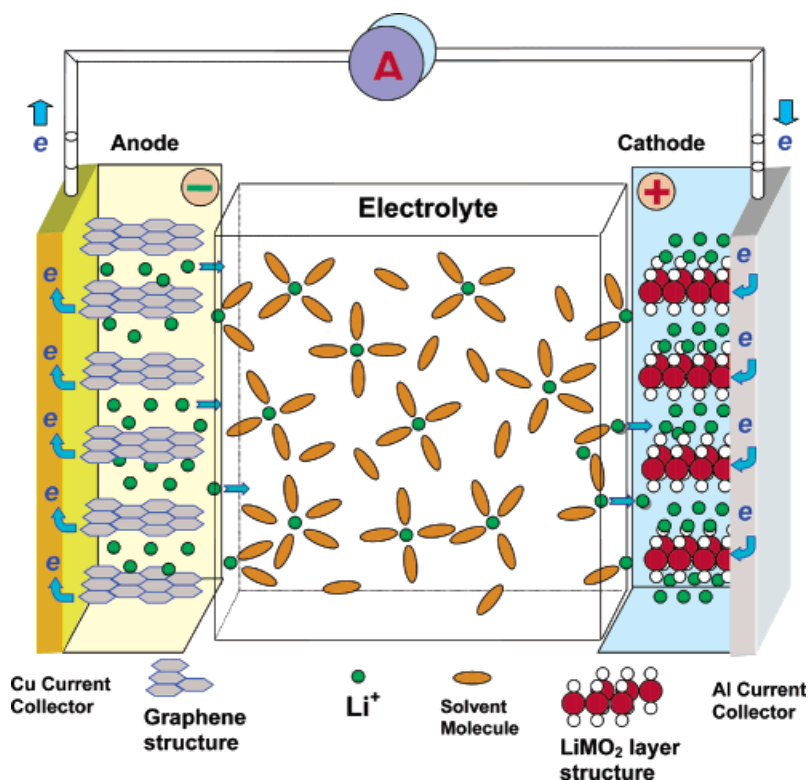


Figure 1.4. Scheme depicting the components and operation of a commercial LIB. The anode (graphitic carbon) and the cathode (transition metal oxide) are layered materials, which can reversibly intercalate Li^+ -ion (from the nonaqueous liquid electrolyte) during the charge/discharge process. Here also, the spontaneous discharge process is depicted. For simplicity, the porous barrier (separator) separating the two electrodes is not shown. In the context of this chapter, a state-of-the-art LIB configuration is considered as the 2nd generation LB. (Reprinted with permission from reference 4. Copyright (2004) American Chemical Society).

contact with one another. At the same time, the separator should facilitate the permeation of ions between the respective half-cells.⁴

In the case of batteries, redox processes, also known as Faradaic processes (due to the transfer of electrons across the interface between the electrode and electrolyte) lead to the storage or release of electric charge. During the discharge mode of a battery (similar to a galvanic cell as shown in **Figure 1.3**), an oxidation process occurs at the anode (negative electrode), which is balanced by a complementary reduction process occurring at the cathode (positive electrode).¹⁰ These processes are accompanied by the flow of electrons from the negative to the positive electrode through the external circuit, manifested as an electric current. The voltage of the battery cell largely depends on the potential difference between the electrodes. Depending on the reversibility of the redox processes occurring at the anode and cathode, batteries are broadly classified into primary and secondary. A secondary battery is a

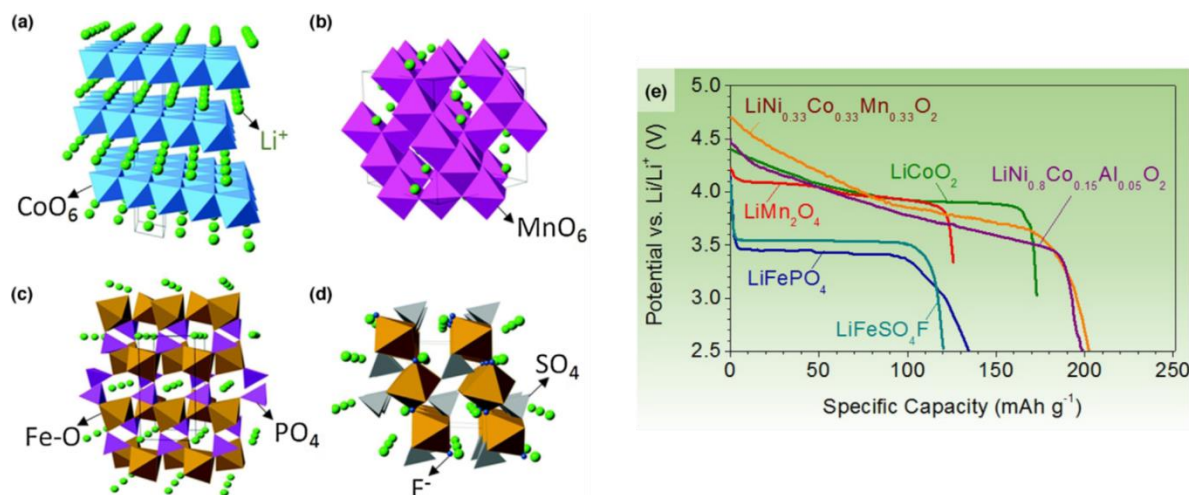


Figure 1.5. Crystal structure of the typical intercalation cathode materials used in LIBs: (a) layered LiCoO_2 , (b) spinel LiMn_2O_4 , (c) olivine type LiFePO_4 , and (d) tavorite type LiFeSO_4F ; (e) typical discharge profiles of the intercalation cathode materials used in LIBs. ((a) to (d) are reproduced with permission from: [reference 14] - Published by The Royal Society of Chemistry; (e) Reproduced with permission from reference 13, Copyright © 2014 The Authors. Published by Elsevier Ltd).

rechargeable, which can facilitate the spontaneous conversion of stored chemical energy to electrical energy (discharge), and the non-spontaneous conversion of an externally supplied electrical energy to be stored as chemical energy (similar to the electrolytic cell, recharging). Unlike secondary batteries, a primary battery is non-rechargeable, which is designed to be used only once and discarded after it is completely discharged. In simple words, it can be concluded that primary batteries are a type of galvanic cell whereas, the secondary batteries are both galvanic as well as electrolytic cells.

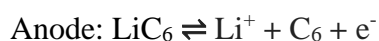
The surge in interest in rechargeable batteries (secondary batteries) technology started with the first demonstration of the Lead-Acid battery in 1859 by French physicist Gaston Plante. Before the invention of rechargeable batteries, stalwarts like Alessandro Volta, Luigi Galvani, and John Frederic Daniell had already contributed enormously towards the earlier day developments of electrochemical energy storage technology, especially, primary batteries. Although the term ‘rechargeability’ is the golden standard in the contemporary world towards attaining sustainability, the technology of primary batteries is historically important, which paved the path towards modern-day energy storage technologies.¹¹ The examples for primary batteries include dry cells (Zn-metal anode and carbon cathode in a gel-based electrolyte made of NH_4Cl and ZnCl_2), alkaline cells (Zn anode and MnO_2 cathode in gel-based alkaline electrolyte, also known as Zn-Mn cells), Li-Mn cell (Li-metal as the anode and MnO_2 as the

cathode in the nonaqueous liquid electrolyte), etc. However, the market share of primary batteries is generally in the decline with their use limited to low-voltage applications such as house-hold items (clocks, flashlights, remote controllers, toys, etc.,) and certain niche applications (military combats, rescue missions, animal tracking, etc.,), wherever the rechargeability is impractical or impossible. In the context of this chapter and thesis, the discussion is confined to secondary batteries (especially lithium-ion batteries (LIBs), lithium-metal batteries (LMBs), and zinc-based post-lithium batteries).

1.2.2 Lithium-ion batteries (LIBs)

To understand the rechargeable batteries in detail, the most important modern-day example of commercial (state-of-the-art technology) LIBs is considered here. LIBs are a wonderful choice as EEDs owing to their rechargeability, with state-of-the-art LIB technology capable of delivering high energy density of $\approx 260 \text{ Whkg}^{-1}$. Besides, the energy density of LIB can expand above 500 Whkg^{-1} with judicious engineering and selection of high-voltage cathode materials with high theoretical capacity. Ever since the commercialization of LIBs in 1991 (SONY), they are extensively used in portable electric devices and electric vehicles.¹² The schematic of a typical LIB cell is presented in **Figure 1.4**.⁴

The graphite-anode and transition metal-based cathode materials in a LIB are compounds often containing lithium atoms (lithiated materials). During the discharge process, the oxidation reaction occurring at the anode releases Li^+ -ions and electrons to the electrolyte and external circuit, respectively, and are transported towards the cathode side followed by recombination.¹² This recombination is concerted with a reduction reaction occurring at the cathode material. On the other hand, during the charging process, the electric energy provided by the external circuit facilitates the redox processes, ion transport, and flow of electrons occur in the opposite direction. Hence, the supplied electric energy is stored in the form of chemical energy in the LIB cell. The electrochemical processes occurring at the anode and cathode of a LIB based on $\text{LiCoO}_2||\text{LiC}_6$ is presented below (LiC_6 represents lithiated graphite as the anode). Here, LiCoO_2 (LCO) is the layered cathode material.



The electrode materials such as LiCoO_2 and graphite used in state-of-the-art LIBs are generally called as intercalation compounds (more specifically intercalation anodes and cathodes). They are layered materials, which can reversibly intercalate the Li^+ -ions in between their interlayer spacing depending on the cell potential. The intercalation electrodes

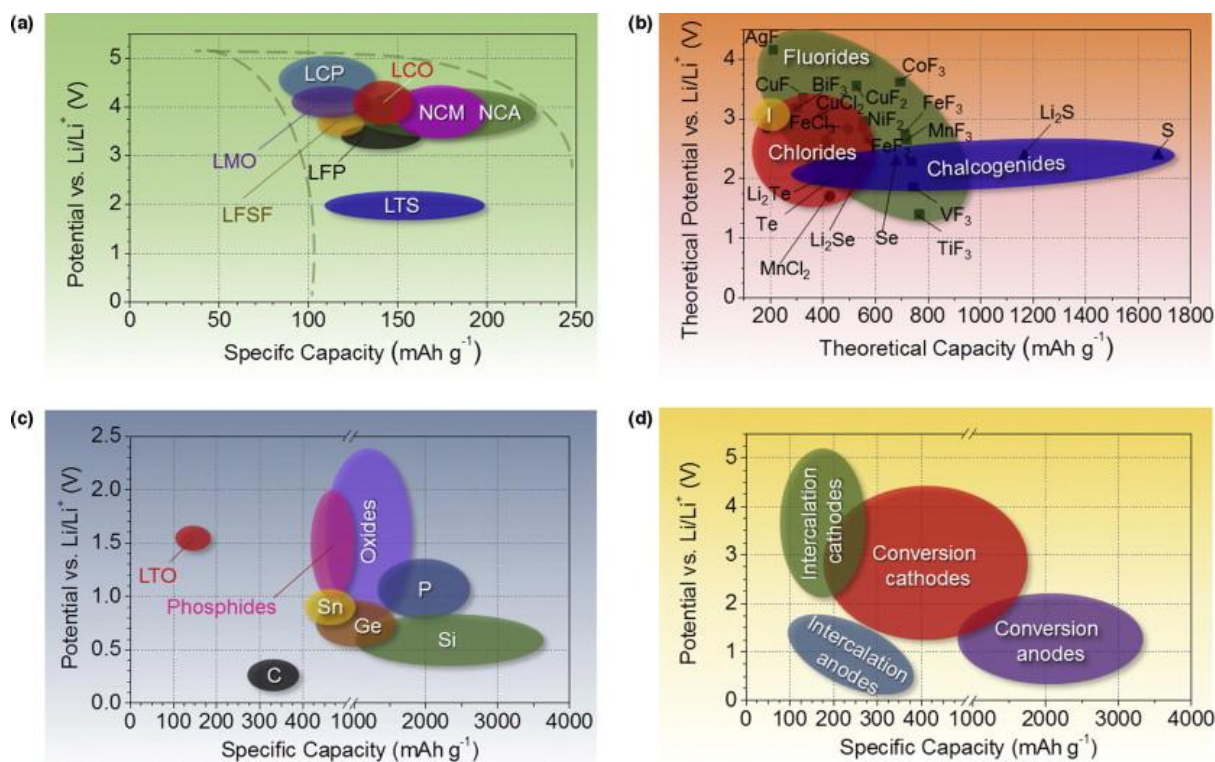


Figure 1.6. Illustration of the average discharge potential vs. specific capacity of (a) intercalation cathodes (experimental) and (b) conversion-type cathodes (experimental) in LIBs; (c) comparison of the average discharge potential vs. specific capacity of the popular intercalation, alloying, and conversion-type anode materials in LIBs; (d) a summary of the average discharge potential vs. specific capacity of all types of the electrode materials used in LIBs. (Reproduced with permission from reference 13, Copyright © 2014 The Authors. Published by Elsevier Ltd).

can be considered as a host network for the Li^+ -ions. The process of release of Li^+ -ions from a host material is known as extraction or deintercalation. The complementary process of holding Li^+ -ions in the host lattice is called insertion or intercalation. Due to the shuttling of Li^+ -ions between the anode and cathode host materials, LIBs are also known as rocking-chair batteries or swing batteries. In certain cases, lithium titanium oxide (LTO), which is a transition metal-based layered material, is also used as the anode instead of LiC_6 for improving the power capability. However, shifting to LTO compromises the energy density compared to LiC_6 . Apart from LCO, there is a pool of other transition-metal-based intercalation materials, which can be employed as cathodes. Depending on the application, all these materials are employed in one or another kind of commercial LIBs. These include, layered transition metal oxides [e.g. $\text{LiNi}_x\text{Mn}_y\text{Co}_z\text{O}_2$ (NMC), $\text{LiNi}_x\text{Co}_y\text{Al}_z\text{O}_2$ (NCA)] in several compositions, olivine-type metal phosphates [e.g. LiFePO_4 (LFP), LiMnPO_4], spinel oxides (e.g. LiMn_2O_4 (LMO), $\text{LiMn}_x\text{Ni}_y\text{O}_4$

(LNMO)) etc., are popular amongst the available cathodes.¹³ The crystal structure and typical discharge curves of the popular cathode materials are presented in **Figure 1.5a-e**.^{13, 14}

In the case of LIBs, the energy density is generally represented as the product of specific capacity per unit weight (mAh/kg), volume (mAh/cm³) or area (mAh/cm²) by the voltage (V). According to several calculations, as reported earlier, it is understood that the total energy density of a LIB can be improved either by increasing the capacity of the cathode or anode. For instance, a double-fold increment in the capacity of the cathode electrode in the LIB can increase the energy density value by $\approx 57\%$. Similarly, a 10-fold increment in the capacity of the anode can increase the energy density by 47%.^{15, 16} **Figure 1.6a** compares the theoretical capacity value and approximate average operating potential of the commonly used transition-metal based layered cathodes (theoretical capacity ranges from 150-200 mAh/g).¹³ Apart from the transition metal-based layered cathodes, another type of cathode known as ‘conversion type’ is also being explored for LIBs in recent times, which can exhibit high capacity (200-1600 mAh/g) than state-of-the-art layered cathodes. Unlike the intercalation reactions in the layered cathode materials, the conversion type cathode materials are operated by solid-state redox reactions inducing breaking and making of chemical bonds and changing the crystal structure. However, the conversion type cathode materials are not as popular as the layered type cathodes due to their low average operating potential and inferior stability. The commonly used conversion type cathode materials are transition metal halides and chalcogenide elements (S, Se, etc., are used for Li-S and Li-Se). The electrochemical properties of the conversion cathodes are compared in **Figure 1.6b**.¹³

Similar to the conversion type cathode materials, conversion type anode materials with high theoretical capacity than LiC₆ are also available. In the case of LiC₆, the theoretical capacity value is ≈ 380 mAh/g. The usually employed conversion-type anode materials are nanoscale metal oxides of transition metals such as SnO₂, Fe₂O₃, TiO₂, so forth and so on. Similar to conversion type cathodes, conversion type anodes are also prone to low stability during cycling due to changes in the crystal structure. Compared to LiC₆, they operate at high lithiation potentials, limiting the voltage and are yet to be used in commercial LIBs. Another promising type of anodes for LIBs are neither conversion nor intercalation type, but alloying in nature. They are commonly known as alloying anodes (Si, Sn, etc.,). Compared to LiC₆, they have very high theoretical capacity values (400-3500 mAh/g) and can be operated lower potential than the conversion anodes. The most popular alloying anode is Si, and it is envisaged that the Si-based LIBs can replace LiC₆ in future LIBs. For instance, in the case of Si, during the charging process Li-Si (Li_xSi) alloy formation takes place, which is reversed

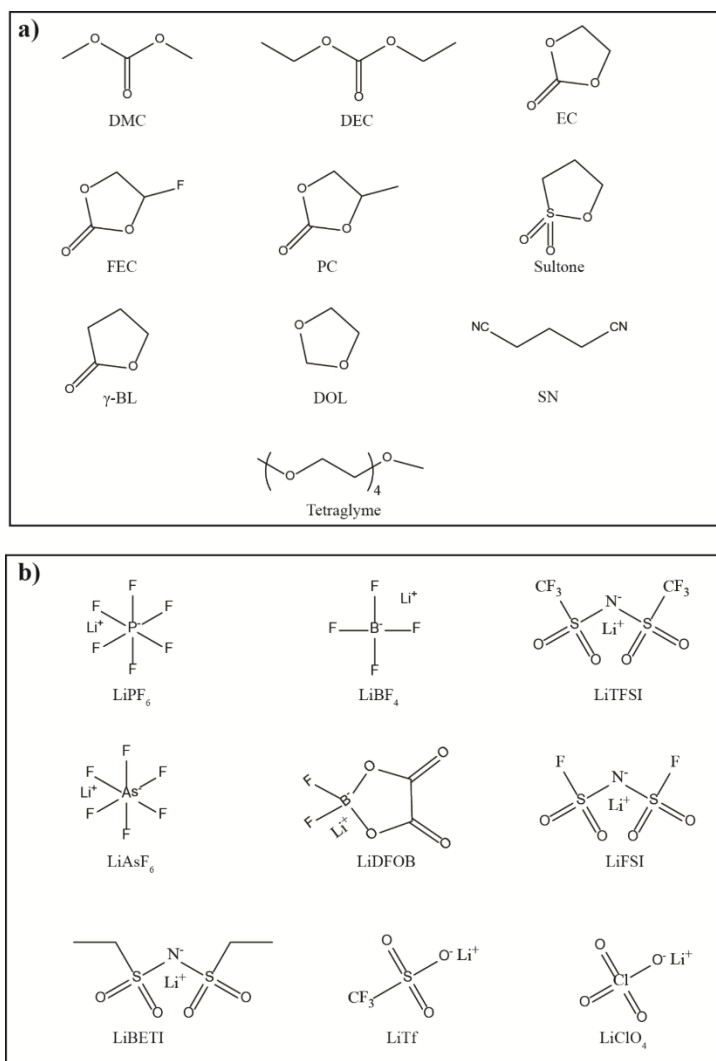


Figure 1.7. Commonly used (a) nonaqueous solvents and (b) salts used in LIB electrolytes. Many of the mentioned organic carbonate solvents and the lithium salts are used in the preparation of nonaqueous electrolytes for supercapacitors also. All these solvents can be employed as a plasticizer in the preparation of GPEs as well. DMC: dimethyl carbonate, DEC: diethyl carbonate, EC: ethylene carbonate, FEC: fluoroethylene carbonate, PC: propylene carbonate, sultone: 1,3-propane sultone, γ -BL: γ -butyrolactone, DOL: dioxalane, SN: succinonitrile, LiPF_6 : lithium hexafluoro phosphate, LiBF_4 : lithium tetrafluoro borate, LiTFSI : lithium bis(trifluoromethanesulfonyl)imide, LiAsF_6 : lithium hexafluoro arsenate, LiDFOB : lithium difluoro(oxalato)borate, LiFSI : lithium bis(fluorosulfonyl)imide, LiBETI : lithium bis(pentafluoroethanesulfonyl)imide, LiTf : lithium triflate, LiClO_4 : lithium perchlorate.

during the discharge. The theoretical capacity and average working potential of several anode materials in LIBs are summarized in **Figure 1.6c**.¹³ Also, in **Figure 1.6d** the average discharge potentials and specific capacities values of several types of the above-discussed electrode materials (both anode and cathodes) are summarized.¹³

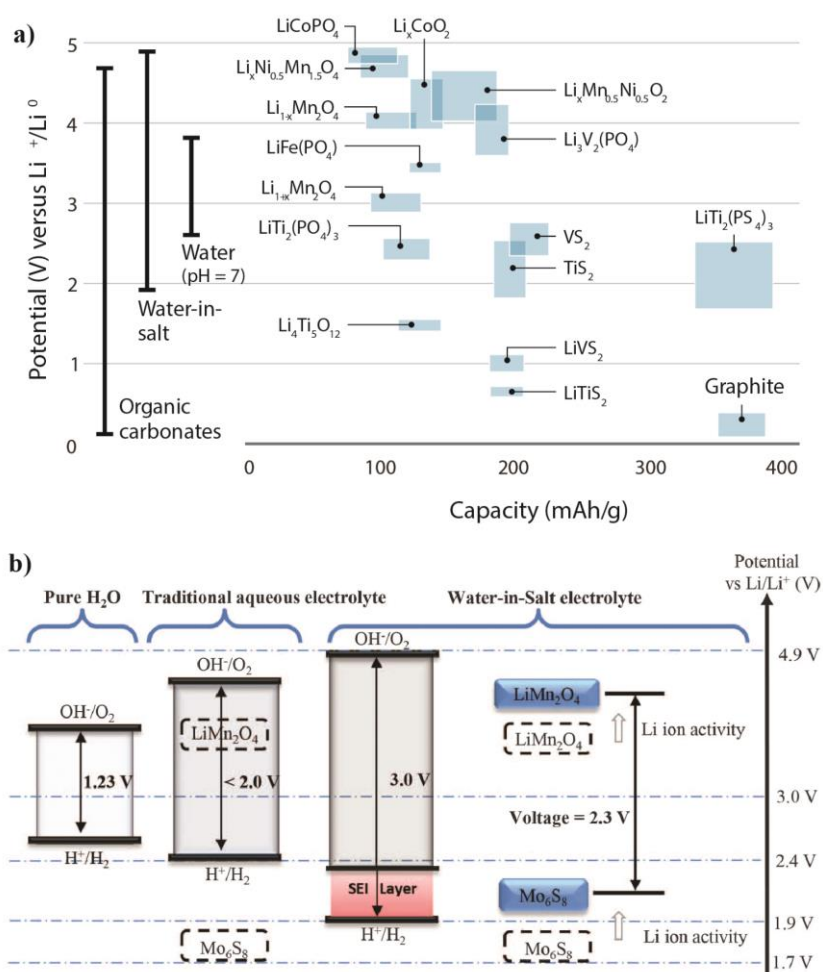


Figure 1.8. (a) The voltage stability limits of the neutral water, WiSE, and nonaqueous electrolytes are compared. The average operating voltage and capacity of various intercalation materials are also illustrated, which can help in choosing the right electrode-electrolyte combination; (b) expanded voltage window of WiSE compared to the aqueous electrolytes with low-salt concentration allowing 3V $\text{LiMn}_2\text{O}_4//\text{Mo}_6\text{S}_8$ aqueous LIB. ((a) is reproduced from reference 20. Reprinted with permission from AAAS; also (a) include the content adapted with permission from reference [J. B. Goodenough, Y. Kim, *Chem. Mater.* 2010, 22, 3, 587–603]. Copyright (2010) American Chemical Society; (b) is reproduced from reference 19. Reprinted with permission from AAAS).

Apart from the electrode materials, the electrolyte is also an inevitable component in LIBs. In LIBs, nonaqueous Li^+ -ion conducting electrolytes are preferred that can withstand the extreme potential conditions at which a LIB normally operates. In commercial LIBs, nonaqueous liquid electrolytes are used. They are based on organic solvents such as linear (e.g. dimethyl carbonate, DMC) and cyclic (e.g. ethylene carbonate, EC) carbonates.⁴ The commonly used solvents and salts used in LIB electrolytes are summarized in **Figure 1.7a** and **b**. These solvents in combination with lithium salts, lithium fluoroborate (e.g. LiBF_4),

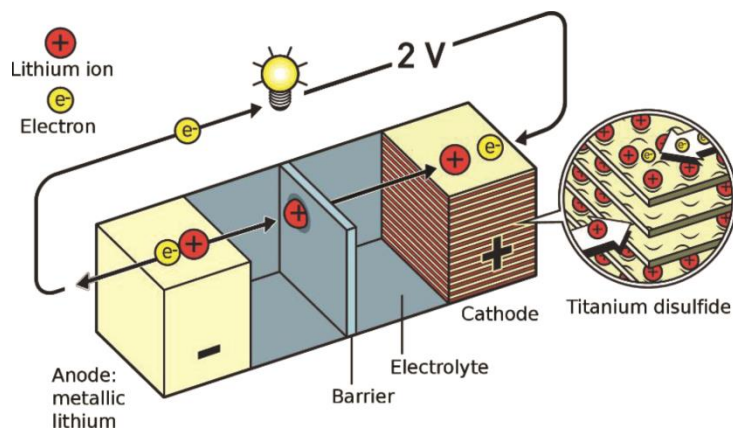


Figure 1.9. A nonaqueous liquid electrolyte-based pLMB that was invented by Whittingham *et al.*, demonstrating the intercalation chemistry for the first time using layered TiS_2 cathode in the 1970s. In the context of this chapter, pLMBs employing liquid electrolytes are considered as the 1st generation LB. (Reproduced from the press releases on the Nobel Prize in Chemistry 2019: © The Royal Swedish Academy of Sciences, <https://www.nobelprize.org/>).

fluorophosphate (e.g. LiPF_6), sulfonylimide (e.g. LiFSI , LiTFSI), etc., can form suitable electrolytes for LIBs. The nonaqueous liquid electrolyte in a LIB has the role of ensuring the formation of solid electrolyte interphase (SEI) and cathode electrolyte interphase (CEI) at the anode and cathode electrode surfaces, respectively.¹⁷ Usually, the anodes and electrolytes that are operated at a decently negative potential range in LIBs are thermodynamically unstable against each other. Therefore, to protect the anode from the direct attack of the electrolyte, a passivation film is inevitable. The SEI is a passivation film formed over the anode surface of a LIB during the initial charging cycles. The composition of SEI is electrolyte decomposition products. However, once a stable SEI formed over the anode surface during the initial charging cycles, further decomposition of the electrolyte is prevented, which facilitates the reversible cycling of a LIB. Thanks to the electrically insulating but ionically conducting property of SEI. Similar to SEI, CEI is also a passivation layer that is formed at the cathode surface. Compared to SEI, CEI is less explored, but it is generally agreed upon the fact that the CEI is effective in improving the anodic stability of the electrolyte.

Recently, there are efforts to develop LIBs using aqueous liquid electrolytes that are more environmentally friendly as well as nonflammable compared to the nonaqueous counterparts.¹⁸ However, when aqueous electrolytes are used, the decomposition products are mainly hydrogen (reduction products) and oxygen (oxidation product) gases along with soluble hydroxides, which cannot get deposited on the respective electrode surfaces to form SEI or CEI layers. Since, the hydrogen evolution reaction (HER) and oxygen evolution reaction (OER) happen within a voltage window of 1.23 V, using conventional aqueous electrolytes, high-

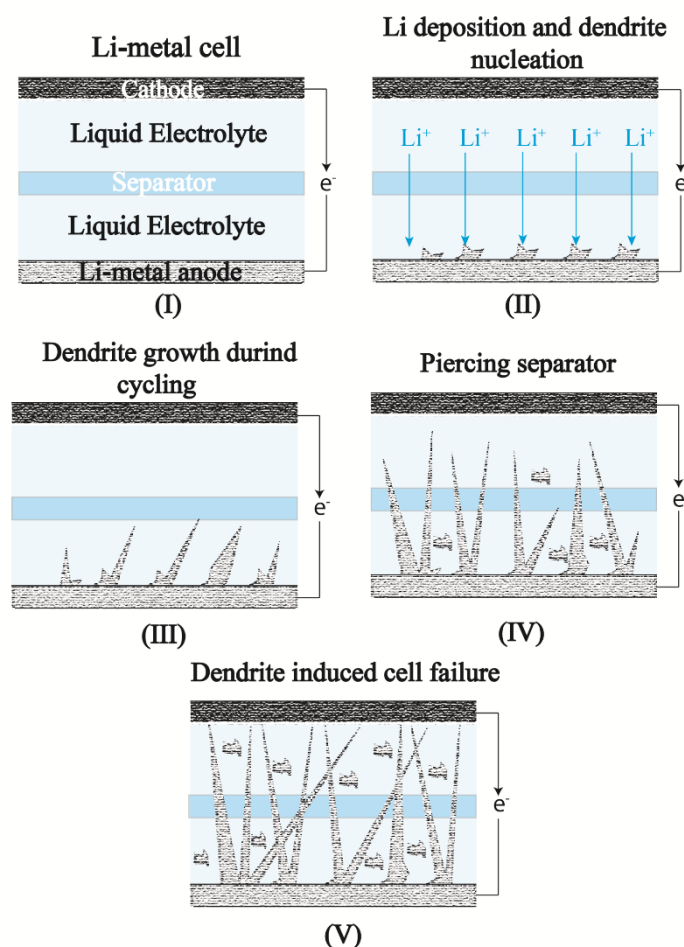


Figure 1.10. HSAL induced failure of a liquid electrolyte-based pLMB during repeated charge/discharge cycles.

voltage LIBs cannot be realized. To overcome this low voltage window offered by aqueous electrolytes, highly concentrated *water-in-salt* (WiSE) electrolytes are used in aqueous LIB fabrication.¹⁹ The *WiSE* electrolytes can induce overpotential for the HER and OER so that aqueous LIBs that can be operated at a voltage of 3 V has been realized. Due to the requirement of a high concentration of expensive LiTFSI salts, *WiSE* electrolytes, and aqueous LIB are not cost-effective and the technology is still in their infant state. The voltage window of aqueous and nonaqueous electrolytes in the context of Li^+ -ion conducting electrolytes are summarized in **Figure 1.8a** and **b**.^{19, 20} It should be noted that the same limiting factors apply to all electrolytes irrespective of the EED under consideration. Apart from liquid electrolytes, SSEs are also proposed for LIBs but are more important in another technology called LMBs, which is discussed in the later sections (**Section 1.2.3**).

As already mentioned before, separators are also often used in all types of batteries to avoid short-circuit. In LIBs polyolefin sheets (e.g. Celgard) or glass fiber mats are used as the separator. When SSEs are used for the fabrication of LIBs, an additional separator

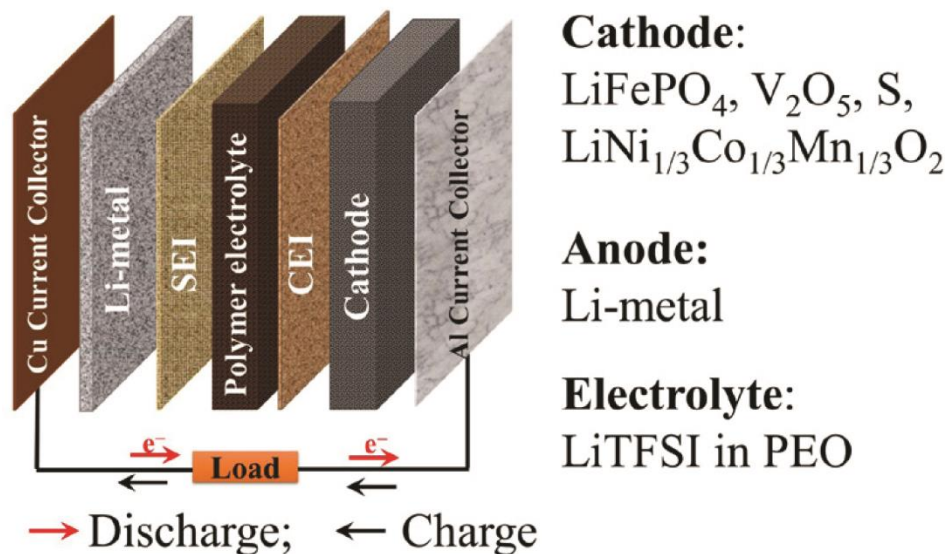


Figure 1.11. Schematic representation of a typical LMB cell using SSE. The only difference compared to LIB is the liquid electrolyte and the intercalation anode are replaced by SSE and Li-metal, respectively. In the context of this chapter, an LMB using SSE is considered as the 3rd generation LB. (Republished with permission of IOP Publishing, Ltd, from reference 22; permission conveyed through Copyright Clearance Center, Inc).

is not necessary for the battery device that can reduce the overall cost. Other than the aforementioned components *viz.*, electrodes, electrolytes and separators, binders, and conductive additives are important in LIB electrodes. The role of the conductive additive is to improve the overall conductivity of the coated electrodes. Binders are introduced in electrodes to hold the electrode particles (active electrode material and the conductive additive) together, and to improve the adhesion over the respective current collectors (Cu for the anode and Al for the cathode). Poly(vinylidene fluoride) (PVdF) or the copolymer PVdF-HFP (poly(vinylidene difluoride-co-hexafluoropropylene)) are widely used as the binders. Carbon black (e.g. Super P® and Super C®) is one of the most common conductive additives used.

1.2.3 Transition from LIB to LMBs

The previous section briefly explained the basic features of LIBs. As discussed in **Section 1.2.2**, in the commercial LIBs, graphite-based intercalation anodes with a theoretical capacity of ≈ 380 mAh/g are used. To improve energy density, anode, and cathode materials with high theoretical capacity values can be used. In this scenario, the use of Li-metal itself as an anode in LIBs can be considered. This is reasonable since the fact that Li-metal has a theoretical capacity value of 3842 mAh/g, which is 10 times higher than that of the graphite-based anode.^{15, 21} LIB configurations that are using Li-metal foil directly as the anode are called as LMBs. However, designing a rechargeable form of LMB is not as straight forward as

conventional LIBs. The main intricacy preventing the rechargeability in LMBs arises from the electrolyte end.²² Most of the conventional nonaqueous liquid electrolytes currently pursued in LIBs are noncompatible with Li-metal and are not able to retain a stable SEI. The electrochemical processes occurring at the anode half-cell in the case of LMB are the plating (during the charge) and stripping (during discharge) of metallic Li as shown below.



This process is way different from the intercalation pathway followed in the case of the layered graphite-anode as in the case of the conventional LIBs. When the conventional nonaqueous liquid electrolytes are employed for LMB fabrication, during the repeated charge/discharge cycles, high surface area lithium (HSAL, also known as dendrites) growth is accelerated at the anode surface.²³ The HSAL grows from the anode side and may pierce the separator to come in contact with the cathode thereby resulting in cell short-circuit.²² Ultimately, the increase in temperature during the cell short-circuit (called thermal runaway) can result in fire hazards in the presence of the inflammable liquid electrolytes present in the cell. Hence, the liquid electrolytes are the main reason contributing to the non-rechargeable behavior of LMBs and are called as primary LMBs (pLMBs). The schematic of a pLMB ($\text{Li}_x\text{TiS}_2\|\text{Li}$) conceived by Whittingham *et al.*, in the 1970s is displayed in **Figure 1.9**. The process of HSAL growth and cell-failure in the presence of liquid electrolyte during continuous cycling is also illustrated in **Figure 1.10**.

To bring the transition from a pLMBs to rechargeable LMBs, the HSAL induced cell failure should be controlled/inhibited, which demands alternative electrolytes that are compatible with Li-metal. This has intensified research in SSEs. It is reported that the Li^+ -ion conducting SSEs possessing a high shear modulus ($G' > 3.4$ GPa) than that of Li-metal are capable of hindering the HSAL growth during continuous charge/discharge cycles.²⁴ Therefore, the combination of SSEs and Li-metal is inevitable in fuelling the imminent transition from pLMBs to the rechargeable form of LMB. In the context of this thesis and chapter, the term LMB always refers to a rechargeable battery employing SSE, unless specified. The schematic representation of LMB using polymer-based SSEs is depicted in **Figure 1.11**.²²

Evolution of lithium battery technology

With the preliminary ideas about pLMB, LIB, and LMB (can be combinedly called lithium batteries (LBs)) as discussed above, the history, evolution, and current status of LB technology can be summarized as follows.¹² The evolution of LB technology can be divided

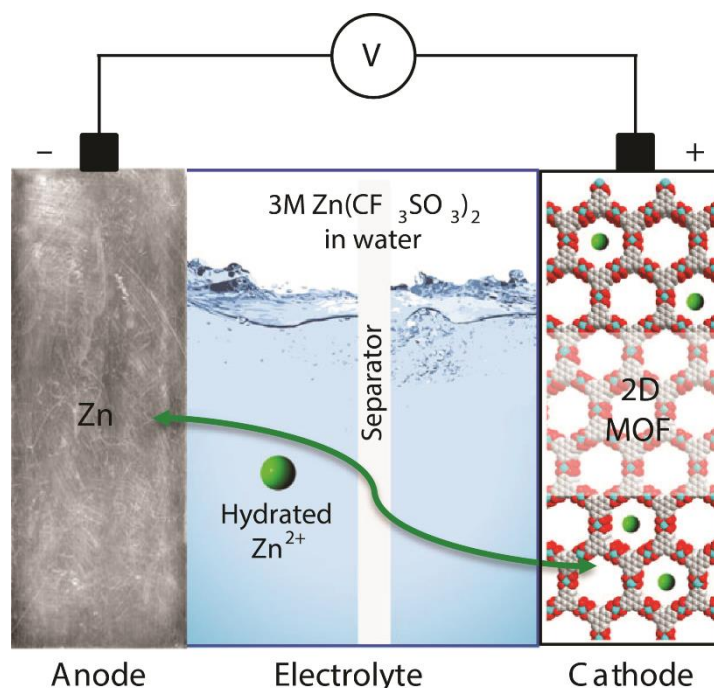


Figure 1.12. A typical representation of a rechargeable aqueous ZMB employing Zn-metal as the anode and a suitable cathode (here, the metal organic framework is used as the cathode) in the presence of Zn^{2+} -ion conducting aqueous electrolyte. (Reproduced with permission from reference 27, Copyright © 2019, Springer Nature).

into three generations. As it is portrayed in **Figure 1.9**, the 1st generation of LBs were liquid electrolyte-based pLMBs in which Li-metal was directly employed as the anode. The pLMBs were popular during the 1960s and 1970s. Later, there were several attempts during the 1970s-1990s to transform the pLMB design to LMBs. During this period, it was generally believed that the tuning of already available liquid electrolytes and cathode materials can gradually lead to LMB configuration. However, the concerns related to HSAL and cell-failure were not resolved and several companies recalled the few already commercialized liquid electrolyte-based LMB models from the market.⁴ Still, the various studies that occurred during the same period led to several ground-breaking discoveries such as the intercalation cathodes by Goodenough *et al.*, and Whittingham *et al* (during the mid-1970s).

Followed by the discovery of intercalation cathodes, attempts to realize the intercalation anodes were initiated by Besenhard *et al.*, Basu *et al.*, and Yazami *et al.*, and several other researchers during the late-1970s. The primary aim of the research with the intercalation anodes was to find a replacement for the Li-metal anode. These attempts culminated in the inception of carbonaceous materials such as graphite and coke as efficient Li-intercalating materials. Later, in 1985, Yoshino *et al.*, from the Asahi Kasei Corporation designed the first practical prototype of LIB using intercalation anodes as we see today (2nd generation LB). This LIB

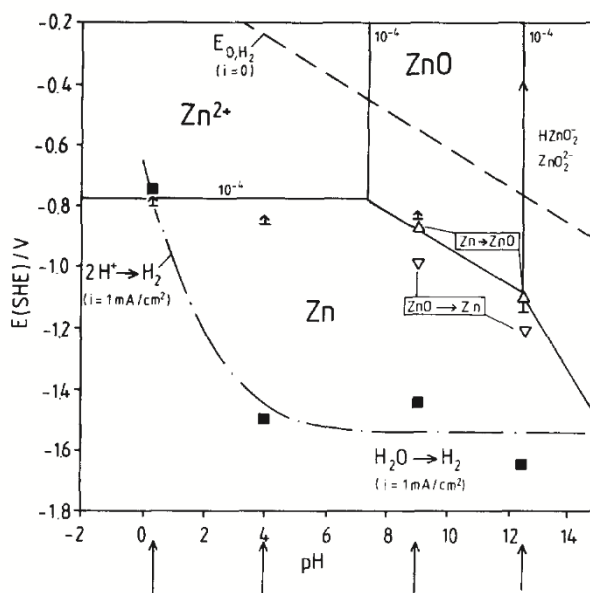


Figure 1.13. Pourbix diagram representing the relationship between the potential and pH of a Zn/H₂O system. (Reproduced with permission from reference 30, Copyright © 1990 Published by Elsevier Ltd.).

model was later commercialized in 1991 by Sony, which remains as the state-of-the-art technology. Ever since the commercialization of LIBs, the basic configuration remains the same as already depicted in **Figure 1.4** in which the two electrodes are separated by a porous separator soaked in a liquid-electrolyte.¹² With the advancements in SSEs, the constraints incited by liquid electrolytes against realizing rechargeable form of LMBs have been compensated to an extent. Such LMBs (**Figure 1.11**) invoking SSEs are considered as 3rd generation LBs.²²

1.2.4 Lithium batteries to post-lithium battery technologies

Aqueous ZMBs

The previous section covered the concept of various types of LBs in detail. The technology of LIBs, since its inception in the 1980s, has revolutionized our daily life. If the current scenario is considered, LIBs are the most widely used EED along with the other potential candidates such as LMBs. Although the LB technology is expected to be capable of satisfying most of the energy demands for at least the next 2-3 decades, it is generally considered that a single battery technology alone cannot be a solution for all the types of applications. For instance, the distribution of major lithium sources is centralized in certain regions of the globe as well as the low-natural abundancy of the electrode components such as Ni, Co, etc., which can impact the cost-efficiency of LBs in the imminent future. Therefore, the know-how regarding the LB technology should be reciprocated towards generating new rechargeable battery technologies. In this respect, post-lithium batteries are important.²⁵ Post-

lithium batteries are lithium-free rechargeable batteries, but employing the chemistry similar to LBs. In line with this, other monovalent and multivalent metals such as Na, K, Mg, Ca, Al, and Zn are also recently being explored for developing post-lithium batteries. Among them, multivalent metal anode-based batteries coupled with a cation intercalating cathode are attractive owing to the multielectron redox processes involved.

Among the post-lithium batteries, recently, zinc-metal batteries (ZMB) are receiving popular attention among researchers. As the name implies, similar to LMBs, ZMBs are rechargeable EEDs that use zinc-metal directly as the anode in combination with suitable cathode materials.²⁶ The basic structure of a typical rechargeable aqueous ZMB is displayed in **Figure 1.12**.²⁷ The theoretical capacity of Zn is 820 mAh/g, which is higher than that of LiC₆ anodes used in LIBs. Provided that high-voltage cathodes with high theoretical capacity can be coupled in ZMBs, the energy density may be surpassed over LIBs. Moreover, the relatively low-cost and high abundance of Zn is also an added advantage. If the current reports on ZMBs are considered, Zn²⁺-ion conducting aqueous electrolytes are widely used (aqueous solution of ZnSO₄, Zn(OTf)₂ etc.). Mainly, transition metal oxides (V₂O₅, MnO₂), conducting polymers (polyaniline (PANI), Prussian blue analogues, etc.), are used as the cathode materials. Recently, metal organic frameworks (MOFs), covalent organic frameworks (COFs), etc., are also employed as the cathode.²⁸ In the case of the aqueous electrolytes, since the voltage window is restricted, in most of the cases, aqueous ZMBs operate at a potential less than 2 V. Therefore, to further leverage the prospects of ZMBs, high-voltage electrolytes are indispensable. In the case of ZMBs, the electrochemical reaction occurring at the anode is plating and stripping of Zn during the charge and discharge steps, respectively.

The operability of the aqueous ZMBs largely depends upon the pH of the electrolyte solution. Normally, electrolytes with pH between 4-6 are desirable for ZMBs.^{29, 30} This is evident from the Pourbix diagram of the Zn/H₂O system (**Figure 1.13**).³⁰ As it is presented in **Figure 1.13**, the electrochemistry of Zn differs in different pH conditions. In a ZMB, the process taking place at the anode is the oxidation (stripping) of Zn to form Zn²⁺-ions similar to the case of Li to Li⁺-ions in LMBs. Provided that the pH condition is alkaline, the formed Zn²⁺-ions can further undergo complexation reaction leading to the formation of zincate ions (Zn(OH)₄²⁻). These zincate ions can dissolve in the electrolyte and undergo precipitation to ZnO once the solubility limit is reached. However, this process during the discharge ultimately results in the loss of active Zn from the anode due to the irreversibility of ZnO to Zn during charging. The same process also results in dendrite growth and/or passivation of the Zn metal surface. Therefore, alkaline electrolytes are not suitable for rechargeable zinc-metal anode

batteries (ZMABs). Still, for certain commercially available primary batteries such as Zn-MnO₂, Zn-air, and Ni-Zn batteries (they also employ Zn-metal as the anode), highly concentrated alkaline electrolytes ($\approx 6\text{M}$) with high pH are used.

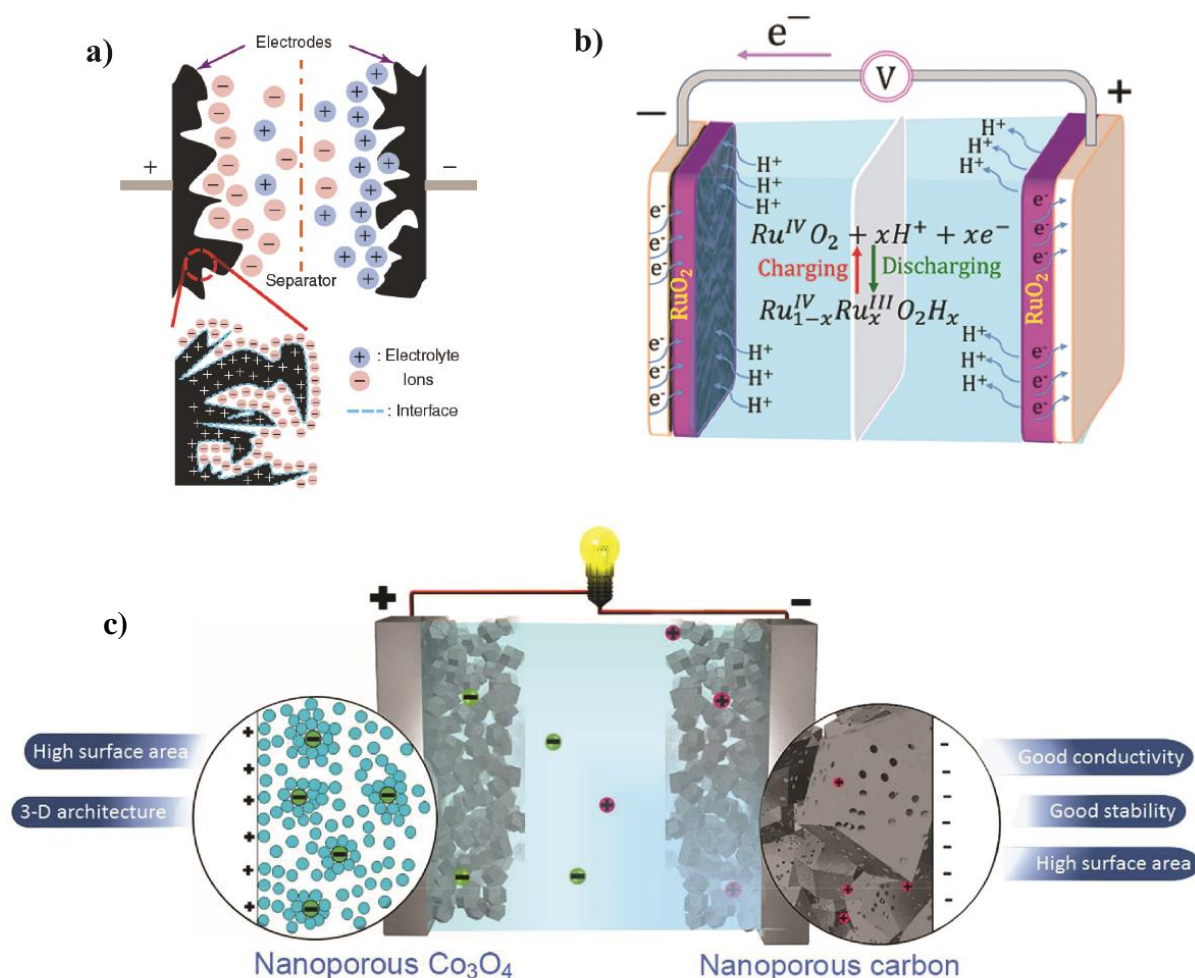
Further looking at the Pourbix diagram of Zn/H₂O couple (**Figure 1.13**), it is seen that the aforementioned parasitic reactions (formation of zincate ion and ZnO) can be suppressed by maintaining the electrolyte pH in between 4-6. At this electrolyte environment, the Zn²⁺-ions can freely exist in the electrolyte without further conversion into complex species. Moreover, the reduction of Zn²⁺-ion to Zn is also favored during the charging process. This indicates that the facile plating/stripping of Zn is facilitated with a Zn²⁺-ion conducting aqueous electrolytes in mildly acidic media improving the prospects of rechargeability. Even though the standard reduction potential of Zn (-0.76 V vs. SHE) is higher than that of hydrogen evolution reaction (HER, -0.236 V vs. SHE at pH of 4), the kinetic limitation favors the deposition of Zn before H₂ gas evolution. Or it is right to say that Zn induces high kinetic overpotential for HER evolution, which is the fundamental reason that the realization of an aqueous rechargeable ZMAB is possible.²⁹

Nonaqueous ZMBs

The main practical intricacy associated with the aqueous ZMBs is their limited average operating voltage due to the use of the water-based electrolytes.³¹ As already mentioned, normally, the water-based electrolytes are characterized by their limited operating voltage window of 1.23 V without decomposition. However, the higher overpotential for HER can favor the aqueous ZMB full-cell to be operated close to a voltage of 2 V. Still, compared to the commercial LIBs that are normally operated between 3-4 V, the operating voltage of ZMB is very low. Since these practical constraints are mainly evolved from the aqueous electrolytes, the research in high-voltage electrolytes for ZMBs must be progressed hand-in-hand with the aqueous counterpart. As high-voltage electrolytes, inspired by the LIB literature, nonaqueous electrolytes can be of suitable choice. However, the nonaqueous Zn electrochemistry is rarely explored. Besides, suitable electrode materials with the capability to intercalate/insert Zn²⁺-ions at high-voltage conditions are also rare. To further advance in the field of nonaqueous ZMBs, one chapter of this thesis (**Chapter 5**) is dedicated to the development of nonaqueous Zn²⁺-ion conducting polymer electrolytes (ZIPs) for ZMBs.

1.2.5 Supercapacitors

With the extensive discussion on batteries as already provided in the previous sections, familiarizing the concept of supercapacitors is rather easy. The configuration of a supercapacitor is similar to that of a battery, which consists of two electrodes, electrolyte, and



Asymmetric supercapacitor

Figure 1.14. Different types of supercapacitors are represented. (a) a symmetric EDLC; (b) a symmetric pseudocapacitor; (c) an asymmetric supercapacitor. ((a) Reproduced with permission from reference 32, Copyright © 2015 John Wiley & Sons, Ltd. All rights reserved; (b) Republished with permission of Royal Society of Chemistry, from reference 35, permission conveyed through Copyright Clearance Center, Inc; (c) Reprinted with permission from reference 36. Copyright (2015) American Chemical Society).

a separator (**Figure 1.14a-c**).^{1, 32, 33} Unlike batteries in which the charge-storage/release occurs as a result of slow and bulk Faradaic processes, a supercapacitor can be simply defined as an EED storing/releasing energy using the fast Faradaic or non-Faradaic processes that are exclusively confined on the electrode surfaces.³⁴ A non-Faradaic process is nothing but an electrochemical process that does not involve any electron transfer across the interface between electrode and electrolyte (can also be referred to as the one in which there is no redox reactions take place). An example of a non-faradaic process leading to charge-storage as in the case of a supercapacitor is the formation of an electric double layer (EDL) at the electrode-electrolyte

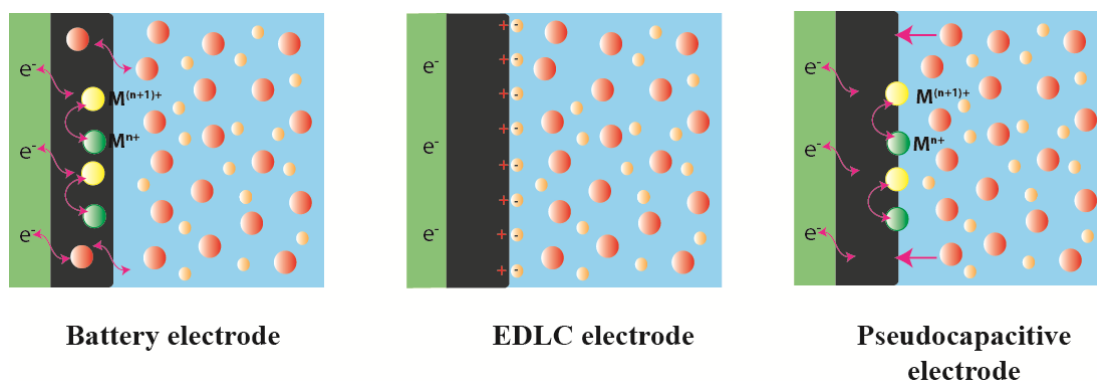


Figure 1.15. The fundamental differences between the electrochemical processes occurring at the interface between the electrode and electrolyte in a battery, EDLC, and pseudocapacitive electrode material. In the case of a battery, the bulk Faradaic reactions are involved, which are diffusion-controlled and slow. In the case of an EDLC, non-Faradaic reversible adsorption of ions on the electrode surface leads to charge-storage. In the case of a pseudocapacitive material, the fast-Faradaic reactions occurring at the electrode surface helps in charge-storage.

interface. The EDL formed in the case of a supercapacitor using activated carbon (AC) as the electrode material is also displayed in **Figure 1.14a**.³² Depending on the polarity of the electrodes, the ions of opposite charge in the electrolyte can be reversibly adsorbed on the electrode surface. Hence, the charge is electrostatically stored in the EDL similar to that of a conventional dielectric capacitor. A supercapacitor, which stores charge utilizing purely non-Faradaic processes (by the formation of EDL) are known as EDLCs, whereas, the one involving fast-surface Faradaic processes are known as pseudocapacitors (**Figure 1.14b**).³⁵ The electrochemical processes involved in a battery, EDLC, and pseudocapacitors are schematically represented in **Figure 1.15**.³⁴ A supercapacitor can be either symmetric or asymmetric.³³ The symmetric supercapacitor is one that uses the same electrode materials at each electrode with the same mass-loading (**Figure 1.14a** and **b**).³⁵ An asymmetric supercapacitor is the one which uses a different type of electrode materials at each electrode. For example, an asymmetric supercapacitor, which uses an EDLC material as the negative and pseudocapacitive material as the positive electrode is represented in **Figure 1.14c**.^{33, 36}

The amount of electrical energy stored in a capacitor or supercapacitor is called capacitance (C) and it is generally represented in the unit of Farad (F). The capacitance per unit mass, area, and volume are represented as F/g, F/cm², and F/cm³, respectively. The special relationship between the quantities *viz.*, the extent of charge acceptance (ΔQ), and the change of potential (ΔV) account for the capacitance (C). Therefore, the capacitance (C) is defined as the ratio of $\Delta Q/\Delta V$.³⁴ This value should be almost constant within a fixed voltage or potential

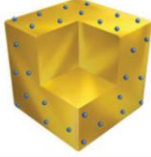
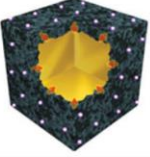
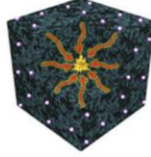
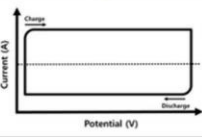
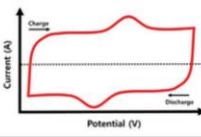
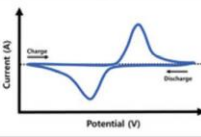
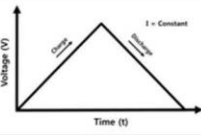
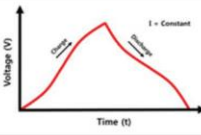
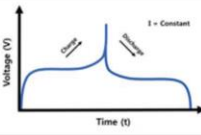
Types of energy storage device	Non-faradaic	Faradaic		
	Electrical double layer capacitor (EDLC)	Pseudocapacitor		Battery (based on intercalation)
		Surface redox	Intercalation	
Mechanism	Reversible ion adsorption/desorption without phase transition	Continuous change in oxidation state without phase transition	Intercalation and change in oxidation state without phase transition	Intercalation and change in oxidation state with phase transition
Kinetics		$i \sim v$ (surface confined)		$i \sim v^{0.5}$ (diffusion controlled)
Capacity	0.17 ~ 0.2 e ⁻ per atom of accessible surface	ca. 2.5 e ⁻ per atom of accessible surface, depending on oxidation state		1-3 e ⁻ per atom of bulk phase, depending on oxidation state
Examples of 2D materials	Graphene, Carbon nanosheets	Heteroatom-doped or functionalized graphene, 2D heteronanosheet,	TMO, TMDC, MXene	Bulk layered materials
Electrochemical features				
				
				

Figure 1.16. Characteristic features of Faradaic and non-Faradaic energy storage. The characteristic features, types of materials, and electrochemical signatures (cyclic voltammetry and galvanostatic charge-discharge profiles) of EDLC, pseudocapacitor, and battery are compared. (Reproduced with permission from reference 37, Copyright © 2015 John Wiley & Sons, Ltd. All rights reserved).

range for the electrochemical device to be called a capacitor. Provided that the value deviates, the electrochemical process is governed by diffusion and can be called a battery. For instance, in the case of a LIB, the redox reactions enabled by the insertion of Li⁺-ions mainly occur into the bulk of the electrode material and is diffusion controlled. These bulk Faradaic reactions contribute to the high energy density of LIBs. The charge-storage process proceeds through the electrostatic adsorption of electrolyte ions onto the surface of electrode materials in an EDLC is presented in **Figure 1.15**.⁹ The absence of any redox reactions allows a rapid response to the changes in potential without diffusion limitation. This is the underlying reason behind the high-power density displayed by EDLCs. However, in EDLCs, the charge is confined to the surface unlike the bulk in the case of a battery, which makes them less energy-dense than the batteries.

In a commercial EDLC, AC is used as the electrode material with high-voltage nonaqueous liquid electrolytes exhibiting an energy density between 5-10 Wh/kg. Compared to the low power density value between 2000-3000 W/kg exhibited by commercial LIBs, the EDLC counterpart is characterized by a power density value ≈ 10000 W/kg. Based on the

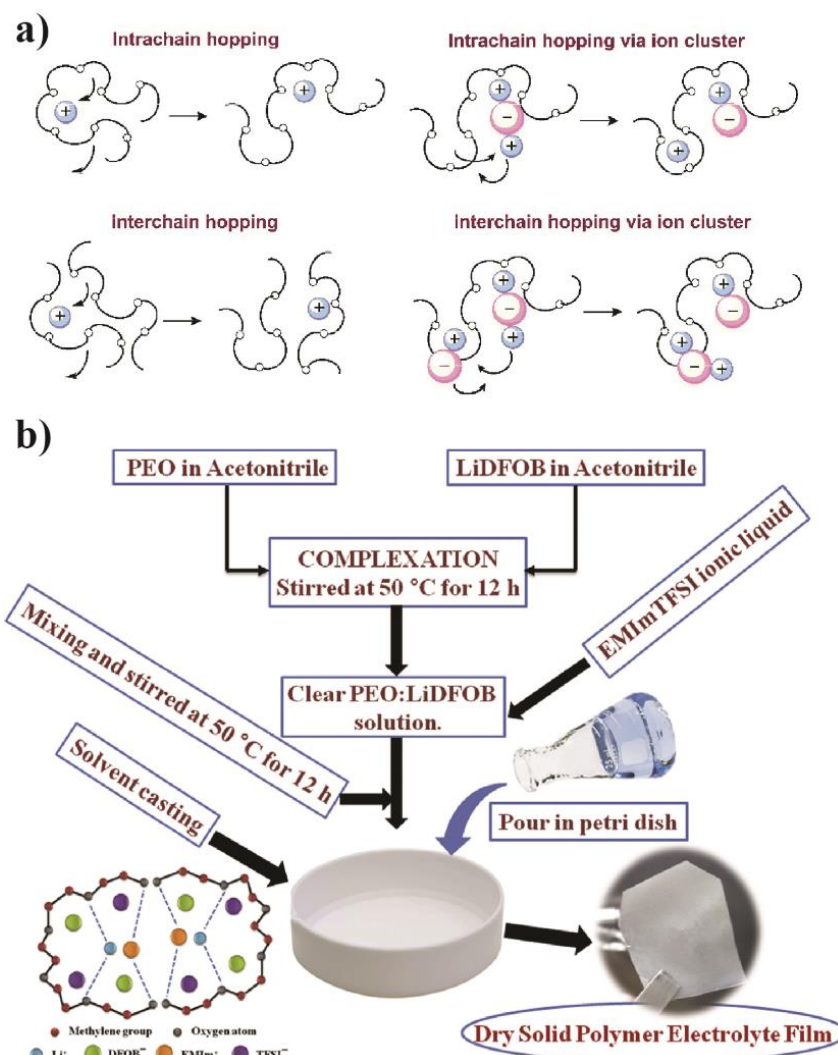


Figure 1.17. (a) Li^+ -ion conduction mechanism in a PEO-based SPE (Republished with permission of Royal Society of Chemistry, from reference 9, permission conveyed through Copyright Clearance Center, Inc); (b) preparation of an SPE film by solution casting method for LMB fabrication (the *ex situ* process) (Reprinted from Publication in reference 40, Copyright 2017, with permission from Elsevier).

electrochemical signals obtained from potentiostatic and galvanostatic experiments, an EDLC and the battery can be distinguished. In the case of an EDLC, the cyclic voltammetry (CV) profiles are characterized by a classic rectangular shaped voltammogram (**Figure 1.16**).^{9, 37} Besides, at a constant-current (galvanostatic) mode, a linear time-dependent change in potential can be observed (**Figure 1.16**).³⁷ In the case of a battery, the CV features are extremely different, which are characterized by peaks corresponding to bulk-Faradaic redox reactions (**Figure 1.16**).^{9, 37} These peaks are associated with phase transitions in the electrodes and are often separated by large voltage differences between 0.1 and 0.2V. In the galvanostatic experiments, the phase changes appear as voltage plateaus (**Figure 1.16**).^{9, 37} In the case of

EDLC, electrode materials with high surface areas are always preferred. As already mentioned, the commercial EDLCs use AC with a high surface area beyond 2000 m²/g as the electrode material. Other carbon morphologies such as graphene, carbon nanotube (CNT), carbon nano-fiber (CNF), and carbon nano-particles are also explored in EDLCs.

In the 1970s, the phenomenon of pseudocapacitance was observed by Conway et al., as the reversible redox reactions occurring at the surface of certain materials leading to EDLC-like electrochemical features (**Figure 1.15**).⁹ Since the redox reactions are Faradaic in origin, these pseudocapacitive materials can display enhanced charge-storage compared to the traditional EDLCs. However, it should be noted that the energy density of pseudocapacitors cannot match with that of batteries, but can be considered as a bridge between batteries and EDLCs. In the case of pseudocapacitive electrodes, due to the presence of Faradaic redox processes, it could be right to say that they behave more-or-less similar to battery type materials. However, the electrochemical signatures do not resemble that of the battery-type materials with sharp redox peaks in the CV but a (quasi)-rectangular CVs resembling more to that of an EDLC-type (**Figure 1.16**).³⁷ Besides, at galvanostatic conditions, the voltage vs. time profile in the case of a pseudocapacitor is also more or less similar to EDLC (**Figure 1.16**).^{9, 37} Metal oxides and conducting polymers are the most popular pseudocapacitive materials used for the fabrication of pseudocapacitors. The examples of pseudocapacitive materials include RuO₂, MnO₂, polyaniline (PANI), Poly(3,4-ethylenedioxythiophene) (PEDOT), etc. Certain metal oxides such as V₂O₅ and LiCoO₂, which exhibit battery-like features in bulk-scale, when reduced in size to less than 10 nm, also act similar to pseudocapacitive materials.⁹ This is because, at nanoscale dimensions, a large fraction of sites for the storage of cation by Faradaic reaction is on the surface.

1.2.6 Conclusive remarks on batteries and supercapacitors

The discussion on batteries, EDLCs, and pseudocapacitors can be concluded with a general discussion on the commonly used electrolytes.^{4, 6} Generally, all the commercial EEDs employ liquid electrolytes despite the recent trend of undergoing a transition from liquid electrolytes to SSEs. In the case of the commercial LIBs, Li-ion conducting nonaqueous liquid electrolytes are used. As already mentioned, the state-of-the-art liquid electrolytes used in LIBs are not useful in the fabrication of LMBs due to HSAL induced cell-failure. Due to the spontaneous reaction of Li-metal and water, aqueous electrolytes are also unsuitable for LMBs. For realizing efficient LMBs, a different category of electrolytes called SSEs is indeed important. **Section 1.3** is dedicated to explaining the types of SSEs and especially emphasizing the polymer electrolytes in the context of this chapter and thesis. In terms of the new technology

of the nonaqueous LMBs, the thesis addresses the gradual transition from aqueous to nonaqueous liquid electrolytes and then to nonaqueous polymer electrolytes. The importance of this transition is already explained in **Section 1.2.4**.

When it comes to supercapacitors, depending on the electrode materials, a variety of electrolytes such as aqueous electrolytes (acidic, alkaline, neutral), organic solvent-based nonaqueous electrolytes exhibiting various types of ion conduction (Li^+ , Na^+ , etc.), or even ionic liquids can be used.⁴ Many of the nonaqueous carbonate solvent-based liquid electrolytes used in LIBs are employed in supercapacitors as well. The advantage of using the aqueous electrolytes is associated with their high ionic conductivity (0.5 to 1 S cm^{-1} at 25°C), environmental benignity, and easy handling, which simplify the device assembling processes. However, the aqueous electrolytes are not employed in commercial supercapacitor devices due to their low electrochemical stability window (**Figure 1.10**). In any supercapacitor device, the energy density value is accounted by **Equation 1** as follows,³⁸

$$E = \left(\frac{1}{2}\right) CV^2 \quad (\text{Equation 1})$$

Here, ‘C’ is the specific capacitance and ‘V’ refers to the operating voltage window of the supercapacitor device. Therefore, it is clear that if the voltage of the supercapacitor with capacitance C is doubled, a four-fold increment in energy density can be achieved. Compared to the aqueous electrolytes, nonaqueous electrolytes are electrochemically stable and can be operated beyond a voltage window of 2.5 V .³⁸ Therefore, high-voltage supercapacitors can be realized with the help of nonaqueous electrolytes. This is the reason behind the commercial EDLCs based on AC use nonaqueous electrolytes. However, nonaqueous electrolytes are moisture sensitive and the ionic conductivity is less compared to the aqueous counterparts. Also, they demand complex purification procedures as well as a controlled environment for handling. This may add to the cost of the nonaqueous supercapacitors. Therefore, the aqueous electrolytes can be used for bringing down the cost of the supercapacitor devices. In this aspect, the aqueous electrolytes can be more suitable for the pseudocapacitive materials. The high capacitance of the pseudocapacitors compared to EDLCs offset the low-voltage window imposed by the aqueous electrolytes. It should be noted that such pseudocapacitors are yet to be commercialized.

1.3 Solid-State Electrolytes (SSEs)

In the past sections, a detailed overview of the EEDs is provided with a brief discussion on the commonly employed liquid electrolytes. The difference between aqueous electrolytes and nonaqueous electrolytes is explained in line with the various EEDs. The importance of the

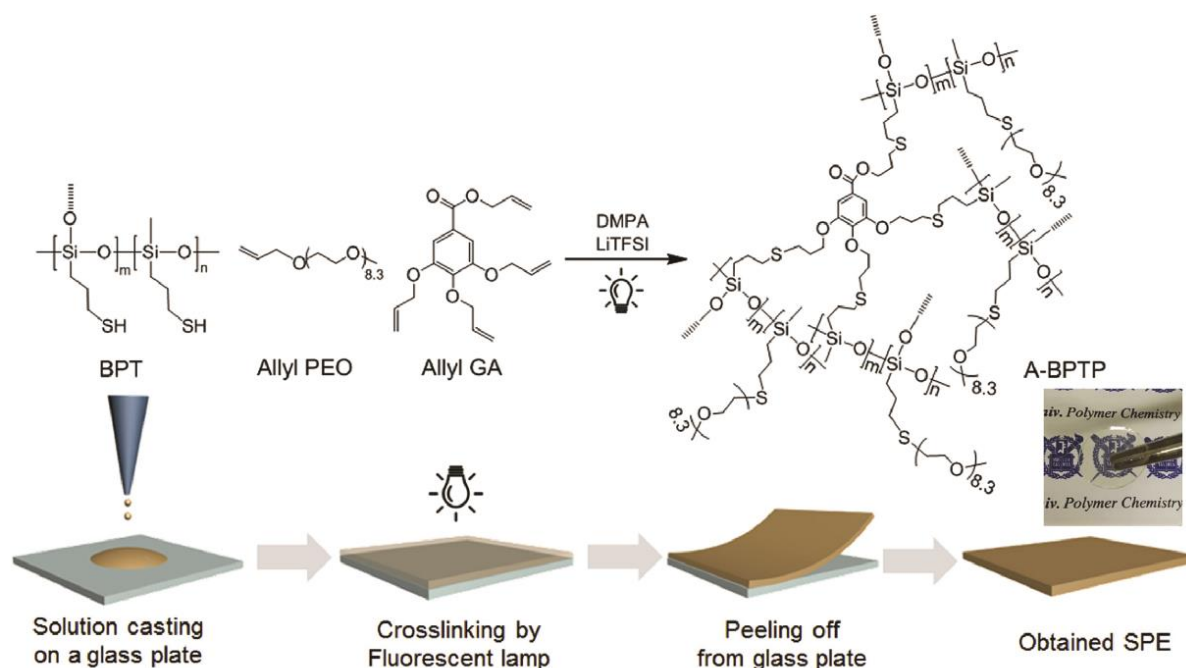


Figure 1.18. Preparation of an SPE film by UV-light induced free-radical polymerization for the LMB fabrication (the *ex situ* process) (Reprinted from Publication in reference 41, Copyright 2017, with permission from Elsevier).

transition from liquid electrolytes to SSEs is also covered. This section on SSEs is intended to provide a brief overview of their types and importance in the context of the batteries and supercapacitors.

1.3.1 Polymer Electrolytes

Solid polymer electrolytes

An SPE exhibits the property of the conduction of ions within a solid polymeric matrix. Here, the polymer matrix acts as a solid-solvent, which can dissociate the salt into ions similar to the role of a liquid-solvent in the liquid electrolytes. The dissociation of the salt occurs by the Lewis base functional moieties present in the polymer framework. In SPEs, the ionic conduction is generally accepted to follow the hopping mechanism. The hopping of ions can be coupled or decoupled with the segmental motion of the polymer chains (also called polymer chain dynamics), in particular, above the glass transition temperature (T_g) of the polymer. The mechanism of Li^+ -ion conduction in polyethylene oxide (PEO)- Li^+ SPE is depicted in **Figure 1.17a**.⁷ The first-ever reported SPE was semi-crystalline PEO-based Li^+ -ion conducting, proposed by P.V. Wright *et al.* in the 1970s.³⁹ In PEO, the oxygen atoms act as the Lewis base sites facilitating the salt dissociation. However, the generally used PEO and several other polymer matrices (polymethyl methacrylate (PMMA), PVDF-HFP, polyvinyl acetate (PVAc), polyacrylonitrile (PAN), etc.) are highly crystalline, or in other words, the T_g values of the

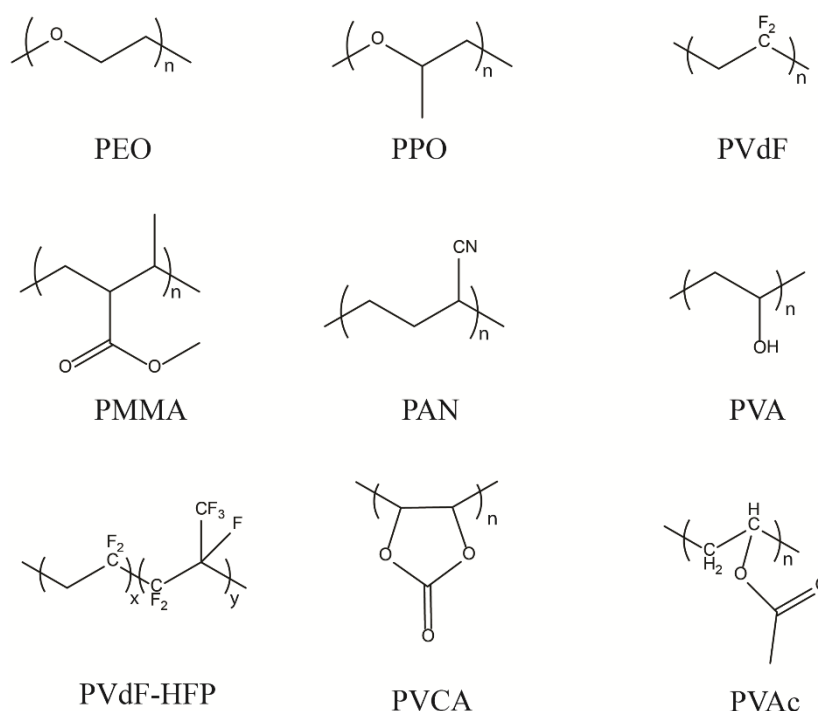


Figure 1.19. Generally used polymer hosts for the preparation of SPEs and GPEs by the *ex situ* method. The mentioned polymer hosts can be dissolved in a volatile solvent followed by casting over a flat surface. Once the solvent is evaporated off, the polymer film can be peeled off. The polymer film can be swollen in a suitable liquid electrolyte to prepare GPE. The preparation of SPEs using similar polymer hosts is already depicted in **Figure 1.17b**.

SPEs are very high. This results in restricted chain dynamics and leading to very low ionic conductivity. The ionic conductivity of the PEO-based SPEs displays lies in the order of 10^{-8} to 10^{-4} S cm^{-1} at room temperature (RT). This value is very low compared to the conventional Li^+ -ion conducting nonaqueous liquid electrolytes (10^{-2} to 10^{-3} S cm^{-1} at RT). There have been continuous efforts dedicated to developing novel polymer hosts with low T_g value, which can be used for the preparation of SPEs exhibiting ionic conductivity in par with liquid electrolytes. Despite these attempts have been resulted in a pool of new polymer hosts that can surpass the classical PEO and several other polymer hosts, elevating the ionic conductivity of SPEs matching with that of liquid electrolytes is yet to be achieved.

In **Figure 1.17b**, the conventional method used for the preparation of the PEO-based Li^+ -ion conducting SPEs by the solvent casting method is presented.⁴⁰ In this method, the polymer host and the electrolyte are first dissolved in a volatile solvent such as acetonitrile (ACN) to form a viscous solution. Later, the viscous solution is cast on a flat surface followed by the evaporation of the solvent to deliver an SPE film. This process involves multiple steps and also it is time-consuming. Recently, another simple method of SPE preparation in a single-step by free-radical polymerization is also receiving popular attention. In this method, instead

of using a polymer host directly, the electrolyte salt is dissolved in the constituent monomer(s) that are polymerizable in the presence of a free-radical initiator to form a reactive mixture. The reactive mixture can be later cast on a flat surface followed by triggering the polymerization by light or heat to give the SPE films. This process is illustrated in **Figure 1.18**, where the cross-linked SPE is prepared by the photopolymerization of a reaction mixture made of allyl ether monomer and lithium salt(s).⁴¹ Apart from the allyl ether monomers, the acrylate-based monomers are also heavily employed for this purpose. The two processes explained in **Figure 1.17b** and **Figure 1.18** involve the preparation of an SPE film in a separate step followed by the EED fabrication (in this case an LMB is fabricated). The aforementioned strategy of polymer electrolyte preparation is referred by the term *ex situ* polymer electrolyte preparation or *ex situ* method. The fabrication of EEDs by using the polymer electrolytes prepared by the *ex situ* method is called as the *ex situ* process.

As already mentioned, the primary role of an electrolyte in any EEDs is to mediate the transfer of charge in the form of ions. How fast the energy can be released or stored (this is known as power capability or rate capability or more specifically power density) depends on the rate of mobility of ions between a pair of electrodes. As per the current status, the low ionic conductivity of SPEs restricts their utility in EEDs, which are ought to display high power capability. For the same reason, the applicability of SPEs in supercapacitors is very limited. In the case of LIBs also, the low rate capability incited by SPEs is commonly observed. However, for micro-EEDs such as micro-batteries and micro-supercapacitors, the potential application of SPEs can be envisaged, although not much explored. In the case of micro-EEDs, the sleek nature of SPEs used can help in providing a short diffusion path for ion transport, which can offset the limitation associated with low ionic conductivity. Most of the SPEs are nonaqueous electrolytes and are designed for LMB applications. SPEs, which can conduct other ions such as Na^+ , Mg^{2+} , and Zn^{2+} are also known, but rare. As already explained, SPEs can inhibit HSAL growth in LMBs. However, it is very challenging but important that the physical and electrochemical properties of SPEs can be further tuned so that it can completely replace liquid electrolytes as a universal choice for all types of EEDs.

Gel polymer electrolytes

The concept of gel polymer electrolytes (GPEs) is suitable to overcome the several limitations imposed by SPEs. GPEs can be considered as a special case of SPEs in which the polymer matrix encompasses a liquid phase (plasticizer) along with the conducting species. Both the aqueous and nonaqueous solvents can be used as the plasticizer for the gelation of the polymer matrix. The use of water as the solvent

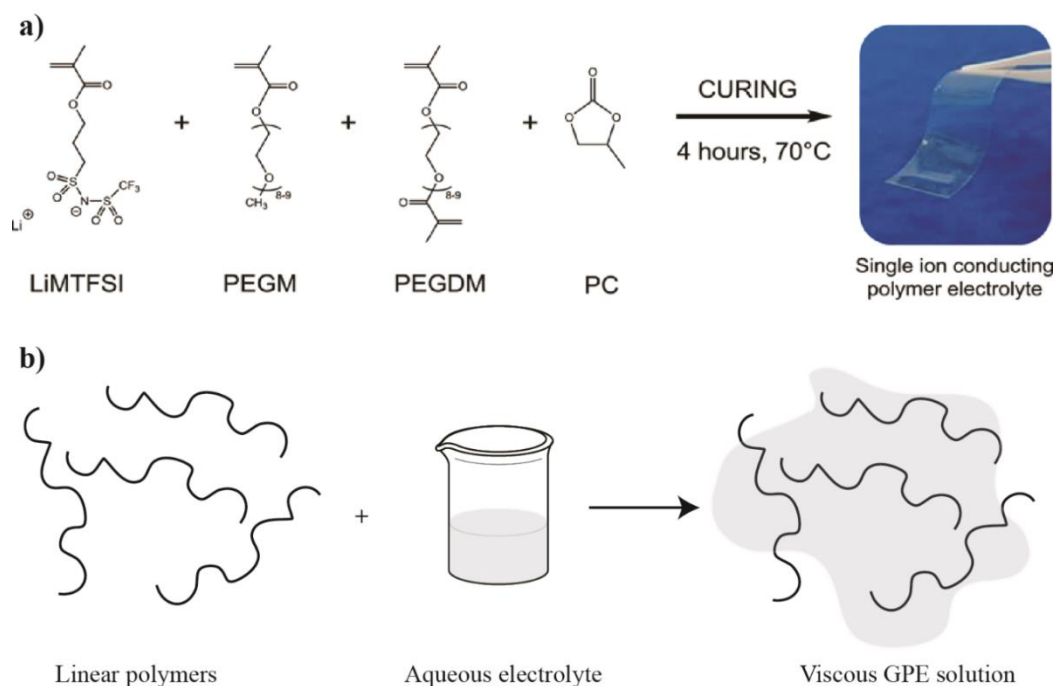


Figure 1.20. (a) Preparation of a GPE film by UV-light induced free-radical polymerization for LMB fabrication (the *ex situ* process) (Reprinted with permission from reference 42. Copyright (2016) American Chemical Society); (b) preparation of aqueous GPE solutions (e.g. aq. PVA/H₂SO₄, aq. PVA/LiCl, etc.,) by dissolving a linear polymer host in an aqueous electrolyte solution. By changing the aqueous electrolyte to a nonaqueous electrolyte solution, a nonaqueous GPE solution can be also prepared (e.g. PMMA/PC-LiClO₄).

provides the opportunity to realize proton (H⁺) and alkaline (OH⁻) ion conducting GPEs, which is often not possible with SPEs. Therefore, the application of GPEs is rather broad compared to SPEs.

In the case of nonaqueous GPEs, owing to the presence of the liquid phase, the T_g value of the macromolecular system is decreased, or in other words, the amorphous character is increased. As already explained, the reduced crystallinity facilitates the segmental motion/dynamics of the polymer chains compared to that in a classical SPE. Any polymer hosts, which have been employed in SPEs, in combination with suitable liquid phase can be used for the preparation of GPEs as well. The commonly employed polymer hosts for the polymer electrolyte (both SPE and GPE preparation) preparation are presented in **Figure 1.19**. Among them, polyvinyl alcohol (PVA) is the most sought after for aqueous GPEs and widely employed in supercapacitors. Other polymer matrices are generally used for nonaqueous SPE and GPEs that can be used EEDs. Especially, when the polymer hosts with low T_g values are used, nonaqueous GPEs with

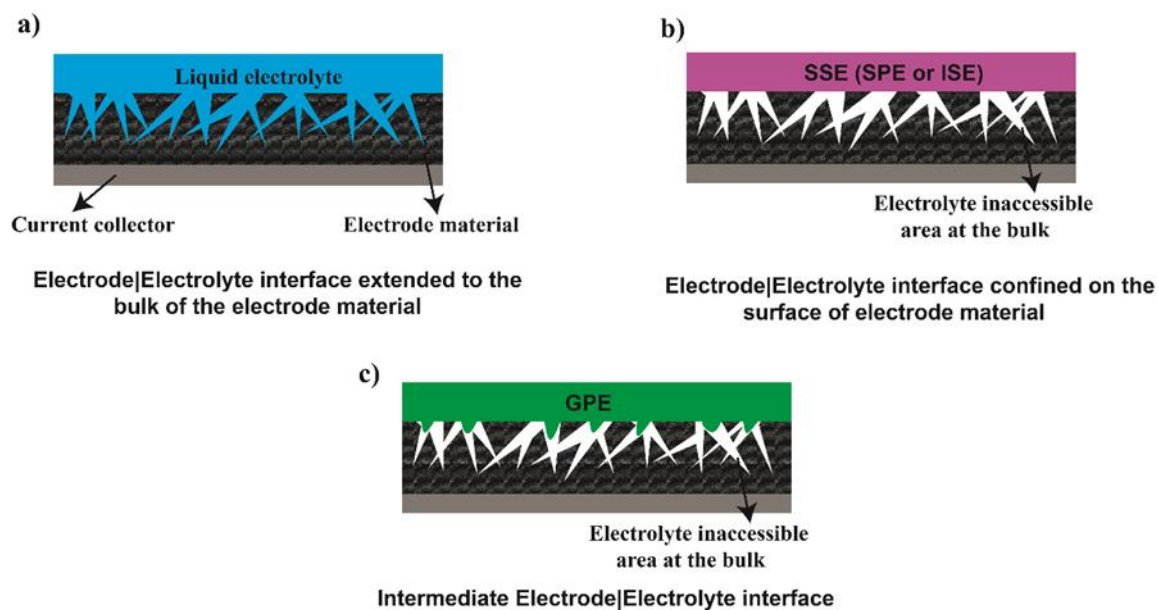


Figure 1.21. Illustration of electrode/electrolyte interface achieved with different types of electrolytes in EEDs. (a) in the case of a liquid electrolyte maximum utilization of the active material can be achieved or in other words, the best electrode/electrolyte interface; (b) in the case of the SPE films or ISE pellets, the electrolyte is not capable enough to infiltrate into the bulk and small-pores within the electrode material. Hence, the poorest electrode/electrolyte interface is exhibited by the SPE-films or ISE-pellets; (c) the GPE films can exhibit an intermediate electrode/electrolyte interface. Due to the presence of a liquid phase and a certain degree of softness compared to ASSEs, limited infiltration into the bulk and pores within the electrode material is possible.

ionic conductivity values close to that of liquid electrolytes can be achieved. Compared to SPEs, the potential of GPEs in facilitating different types of ion conduction make them suitable for the fabrication of all types of EEDs (supercapacitors, LIBs, LMBs, post-lithium batteries, etc.), and even several electrochemical energy conversion devices (fuel cells, DSSC, etc.).

The *ex situ* method of polymer electrolyte preparation as explained in the context of SPE films applies to GPEs as well. The preparation of a Li^+ -ion conducting free-standing GPE film by UV-light induced free-radical polymerization is shown in **Figure 1.20a**.⁴² Here, the only difference compared to the SPE film preparation explained in **Figure 1.18** is that the reaction mixture contains a plasticizer (PC is used as the plasticizer) along with the monomers, lithium salt, and the initiator. During the polymerization, the PC is trapped inside the polymer matrix without compromising mechanical stability. Compared to the SPE counterpart, such a GPE film can exhibit high ionic conductivity due to the presence of the liquid phase. UV-light induced polymerization for the preparation of aqueous GPEs is rarely attempted in the

literature. The most commonly used strategy for the preparation of a dimensionally unstable aqueous GPE solution is depicted in **Figure 1.20b**. In this method, a high-molecular-weight linear polymer such as PVA is dissolved in an aqueous electrolyte solution (aq. H_2SO_4 , aq. KOH, an aqueous solution of LiCl, etc.). This highly viscous GPE solution can be applied over the electrode surface and can be used for the EED fabrication in the presence or absence of a separator. By changing from water to organic solvents, nonaqueous GPE solutions can be also prepared (e.g. PMMA/PC- LiClO_4). However, the GPE solutions compromise the ultimate aim of achieving high performing mechanically stable polymer electrolytes. Therefore, the GPE solutions do not attract the research community beyond the lab scale. The difference between such GPE solutions and the advantage of mechanically stable GPEs are addressed in **Chapter 2 and 3**.

1.3.2 Inorganic Solid Electrolytes (ISEs)

Inorganic solid-state electrolytes (ISEs) are inorganic materials such as inorganic crystalline, polycrystalline and amorphous solids, ceramics, glasses, and glass-ceramics, which possess mobile ions.⁸ The movement of mobile-ions in crystalline ISEs is proven to take place *via* the hopping mechanism between the rigid crystal lattices. The mechanism of ion conduction in the amorphous ISEs are yet to be well established. Unlike SPEs, several ISEs are possessing room temperature ionic conductivity in par with that of liquid electrolytes. For instance, the room temperature (RT) ionic conductivity of several sulfide glasses, thio-LISICON, and glass-ceramics are in the order of $10^{-2} \sim 10^{-3} \text{ S cm}^{-1}$.²² However, compared to the SPEs, ISEs demands tedious synthesis and processing steps, which make them expensive for EEDs. Most of the ISEs are also used in the form of pellets separating the respective electrodes. This approach allows only the utilization of the active materials on the surface of the electrode coating, but not the bulk. Therefore, the electrode|electrolyte interface (electrode|electrolyte interface refers to the extent of contact between electrolyte and electrode materials) is comparatively poor in the case of ISEs. The poor electrode|electrolyte interface result in low-active material utilization and high charge-transfer resistance.⁴³ Besides, most of the ISEs are Li^+ or Na^+ -ion conductors, which restrict their practical utility in EEDs other than the related batteries. The application of ISEs for supercapacitors is rarely reported in the literature (few reports are available for micro-supercapacitors). The lack of flexibility associated with ISEs compared to SPEs remains a grave concern for its wide-spread applicability in flexible EEDs.

1.4 Electrode|Electrolyte interface and their challenges in EEDs

The discussion regarding the EEDs and electrolytes underlines the importance of the polymer electrolytes over the liquid electrolytes in the futuristic EEDs. Among the polymer

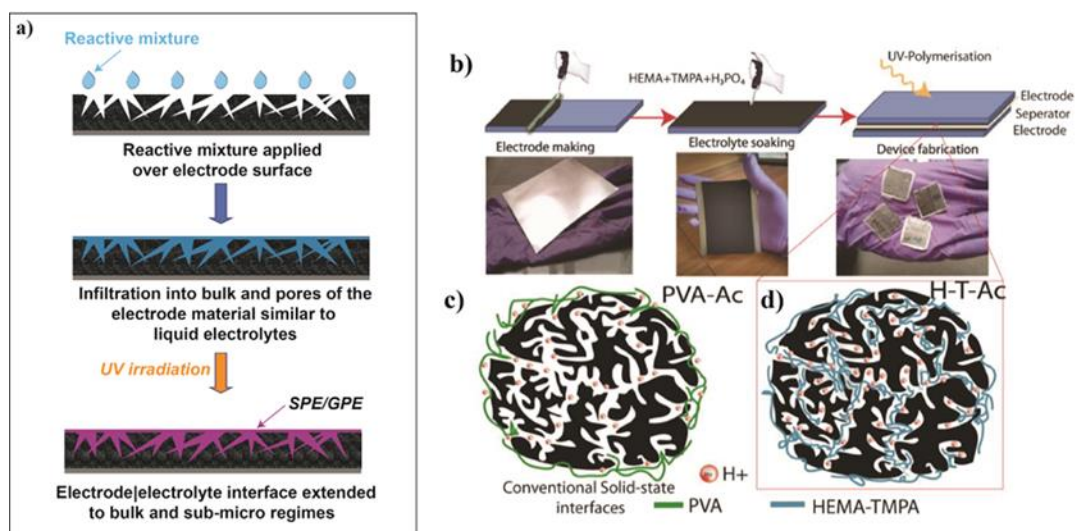


Figure 1.22. (a) The schematic representation of the improved electrode|electrolyte interface that can be obtained with the *in situ* process; (b) the fabrication of EDLC by adopting the *in situ* process. Here, the reactive mixture is composed of acrylate monomers, UV-initiator, and aq. H₃PO₄ as the electrolyte. AC is used as the electrode material; (c) the electrode|electrolyte interface obtained with the PVA-based GPE solution (the *ex situ* process) is compared with that of (d) the *in situ* processed counterpart ((Reprinted with permission from reference 44. Copyright (2016) American Chemical Society).

electrolytes, in particular the GPEs are of prime importance due to their wide applicability. In any EEDs, one of the main parameters defining the electrochemical performance is the nature of the electrode|electrolyte interface. As already mentioned in the context of ISEs, electrode|electrolyte interface is a measure of how much electrode material has been accessed by the electrolyte. Hence, a good electrode|electrolyte interface indicates a better infiltration of the electrolyte into the electrode material. Owing to the inherent free-flowing nature and low viscosity of the liquid electrolytes (aqueous and nonaqueous), their impregnation deep into the bulk and sub-micro regimes of the electrode material is rather easy (**Figure 1.21a**). Therefore, undoubtedly, the best electrode|electrolyte interface and the maximum active material utilization are observed with the liquid electrolytes. In the case of SPEs (or ISEs), as it is depicted in **Figure 1.21b**, the electrode|electrolyte interface is confined only on the surface of the electrode material since it used as a film prepared by the *ex situ* method.⁴⁴ Due to the presence of a certain amount of liquid phase, compared to the SPE-films, the electrode|electrolyte interface in GPE-films is superior but inferior to the liquid electrolytes. The limitations about electrode|electrolyte interface in SSEs become more severe when the electrode material possesses high micro-porosity or coated over the current collector with high areal mass-loading (thick electrodes). The best electrode|electrolyte interface achievable with

the liquid electrolytes is one of the main reasons for the superior performance displayed by the liquid electrolyte-based EEDs over the SSE-based ones.

If the complete replacement of the liquid electrolytes by SSEs has to be progressed, the aforementioned intricacy of the poor electrode|electrolyte interface offered by SSEs should be addressed. The tuning of the electrode|electrolyte interface in the polymer electrolytes can be achieved by moving away from the conventional *ex situ* process of device fabrication to a new and effective strategy of *in situ* process. In this method, instead of casting the polymer electrolyte as a film as in the case of the *ex situ* process, the possibility of direct generation of GPE or SPE over the electrode surface in line with the device fabrication can be attempted. The schematic representation of the *in situ* process is presented in **Figure 1.22a**. For this purpose, similar to the *ex situ* process, a reactive mixture containing polymerizable monomers, a polymerization initiator (photo, thermal, or even ionic initiators can be used), and the electrolyte salt (and plasticizer if any) is prepared. Depending on the presence or absence of the electrolyte solvent, GPEs or SPEs can be prepared. The reactive mixture being in a liquid-state can easily infiltrate into the bulk regions and pores of the electrode materials. Once the polymerization is triggered by light or heat, the reactive mixture undergoes polymerization within the electrode material ensuring an extended electrode|electrolyte interface. Since the electrode|electrolyte interface formation and polymer electrolyte generation occur in a single step, this technique is known as the *in situ* process. Adopting the *in situ* process for the EED fabrication can help in achieving electrochemical performance comparable to the liquid electrolytes with the additional advantage of improved safety associated with the use of the polymer electrolytes. For instance, the electrode|electrolyte interface in a high-surface-area porous carbon with a polymer electrolyte prepared by the *ex situ* method and *in situ* method is compared in **Figure 1.22b-d**.⁴⁴ In the *ex situ* process using PVA/H₃PO₄ GPE solution, the infiltration of the polymer electrolyte into the micro-pores of the AC electrode is hindered. However, in the *in situ* counterpart, maximum utilization of the electrode material is achieved with an extended electrode|electrolyte interface. The advantage of the *in situ* process for improving the performance of supercapacitors and ZMBs is addressed in **Chapters 2 and 5**, respectively.

1.5 Conclusion, scope, and objectives of this thesis

In conclusion, this introductory chapter provided a detailed overview of the two most important electrochemical energy storage technologies *viz.*, batteries, and supercapacitors. The chapter explains the fundamental differences leading to the difference in the electrochemical signatures of batteries and supercapacitors emphasizing the difference in the electrochemical

process occurring at the interface between the electrode and electrolyte. The diffusion-controlled slow-Faradaic reactions lead to the high energy density, but low power density of the batteries. Whereas, the high-power density associated with the supercapacitors is the result of ultrafast Faradaic and non-Faradaic processes occurring at the electrode surface rather than the bulk. The chapter also discusses the importance of the transition from the liquid electrolytes to the solid-state counterparts such as polymer electrolytes, which is the core theme of the thesis. Apart from the safety perspective, high-energy EEDs such as rechargeable LMBs can be realized only with the help of SSEs, where the polymer electrolytes are the frontrunners. The importance of the post-lithium batteries over LBs is addressed by taking the example of rechargeable ZMBs. Finally, the important concept of electrode|electrolyte interface is established, which is decisive in the performance of any EEDs. The inherent limitation associated with ensuring a proper electrode|electrolyte interface with the *ex situ* processed SSE-based EEDs prevents the maximum utilization of the active electrode materials. To mimic the electrode|electrolyte interface close to that of a liquid electrolyte, EEDs can be fabricated using the *in situ* process. With the aforementioned background information in hand, this thesis is designed to fuel the prospects of the polymer electrolytes for EEDs.

If the current literature reports are considered, proton-conducting GPE solutions based on PVA are extensively used for the supercapacitors. However, the GPE solutions do not interest the research community beyond the lab scale due to their lack of dimensional stability. To improve the prospects of safe and flexible supercapacitors, mechanically stable proton conducting GPEs that can be easily prepared and integrated into the supercapacitor devices are indeed important.

- *The second chapter of this thesis deals with the preparation of a proton-conducting GPE film by UV-light induced free-radical polymerization to be used in PANI-based pseudocapacitors (the ex situ process). The phosphoric acid-enriched H⁺-ion conducting GPE film exhibiting polyelectrolyte characteristics is termed as water-in-acid GPE. The superiority of the developed water-in-acid GPE films over the conventional dimensionally unstable PVA-based GPEs was proven through physicochemical as well as electrochemical characterizations.*

Similarly, in the context of the high-voltage nonaqueous supercapacitors, nonaqueous GPEs are indeed important to ensure safety and flexibility. Unlike the case with a liquid electrolyte, when commercial-grade electrode materials such as AC with high surface area ($\approx 2000 \text{ m}^2/\text{g}$) and micro-porosity are used in nonaqueous EDLCs, the conventional GPE-films or GPE solutions (PMMA-PC/LiClO₄) cannot ensure maximum utilization of the electrode

material. Therefore, a new strategy to design the polymer electrolyte-based EDLCs should be developed, which can mimic the electrode|electrolyte interface as in the case of a liquid electrolyte.

- *In the third chapter of this thesis, the preparation of a novel nonaqueous GPE is attempted by using UV-light induced free-radical polymerization. The Li⁺-ion conducting nonaqueous GPE is later used for the fabrication of EDLC devices with high electrode mass-loading by the in situ process. The device could be operated at a voltage window of 2.5 V. The capability of the in situ process to improve the electrode|electrolyte interface in the nonaqueous GPE-based EDLC is proven by comparing the electrochemical performance with the ex situ counterpart (GPE film and PMMA-PC/LiClO₄ GPE solution).*

Nonaqueous electrolytes are also inevitable in the case of LIBs as well. To improve the low energy density of LIBs, the graphite-based intercalation anode can be replaced by Li-metal so that LMBs can be designed. However, the conventional liquid electrolytes are not suitable for the rechargeable LMBs as they incite dendrite-growth over the Li-metal anode and consequent failure of the cell. To realize safe rechargeable LMBs, the polymer electrolytes can be used. To be used along with high-voltage cathodes based on Ni, Co, etc., the polymer electrolytes should possess high oxidation stability, preferably above 4V vs. Li|Li⁺.

- *In the fourth chapter, high-voltage Li⁺-ion conducting nonaqueous GPEs are developed for LMBs, again using UV-light induced free-radical polymerization. The series of cross-linked polymer electrolytes prepared display high oxidation stability beyond 4.2 V vs. Li|Li⁺ depending on the concentration of the lithium-salt present in it. The compatibility of the polymer electrolytes in LMB full-cells is evidenced by using high-voltage (NCA) as well as low-voltage (LFP) cathodes. The NCA||Li cell with the optimized GPE could be operated beyond 1000 cycles with more than 55% specific capacity retention at 20°C.*

Along with the LB technology, concomitant development of post-lithium battery technologies must be progressed. The aqueous electrolyte-based rechargeable ZMBs have attracted prominent interest among the electrochemists within the past few years. To improve the operating voltage window of ZMBs, nonaqueous electrolytes can be employed. However, the Zn²⁺-ion conducting nonaqueous liquid electrolytes and polymer electrolytes are rarely reported.

- *In the final working chapter of this thesis, the applicability of UV-crosslinked Zn²⁺-ion conducting nonaqueous polymer electrolytes in high-voltage ZMBs is demonstrated. The polymer electrolyte with high room temperature ionic conductivity in the order of 10⁻³ S/cm possessed high oxidation stability beyond 2.5 V vs. Zn|Zn²⁺. This chapter further emphasizes the advantage of the in situ process as a tool to leverage the electrode|electrolyte interface in ZMBs.*

In a nutshell, the present thesis underlines the importance of interdisciplinary research, especially in the field of electrochemistry and polymer science. The synergy between electrochemistry and polymer science can help in developing efficient and reliable EEDs, which can accelerate the race towards energy sustainability.

1.6 References

- [1] Winter, M.; Brodd, R. J., What Are Batteries, Fuel Cells, and Supercapacitors? *Chemical Reviews* 2004, 104 (10), 4245-4270.
- [2] Gür, T. M., Review of electrical energy storage technologies, materials and systems: challenges and prospects for large-scale grid storage. *Energy & Environmental Science* 2018, 11 (10), 2696-2767.
- [3] Budde-Meiwes, H.; Drillkens, J.; Lunz, B.; Muennix, J.; Rothgang, S.; Kowal, J.; Sauer, D. U., A review of current automotive battery technology and future prospects. *Proceedings of the Institution of Mechanical Engineers, Part D: Journal of Automobile Engineering* 2013, 227 (5), 761-776.
- [4] Xu, K., Nonaqueous Liquid Electrolytes for Lithium-Based Rechargeable Batteries. *Chemical Reviews* 2004, 104 (10), 4303-4418.
- [5] Xia, L.; Yu, L.; Hu, D.; Chen, G. Z., Electrolytes for electrochemical energy storage. *Materials Chemistry Frontiers* 2017, 1 (4), 584-618.
- [6] Pal, B.; Yang, S.; Ramesh, S.; Thangadurai, V.; Jose, R., Electrolyte selection for supercapacitive devices: a critical review. *Nanoscale Advances* 2019, 1 (10), 3807-3835.
- [7] Long, L.; Wang, S.; Xiao, M.; Meng, Y., Polymer electrolytes for lithium polymer batteries. *Journal of Materials Chemistry A* 2016, 4 (26), 10038-10069.
- [8] Famprakis, T.; Canepa, P.; Dawson, J. A.; Islam, M. S.; Masquelier, C., Fundamentals of inorganic solid-state electrolytes for batteries. *Nature Materials* 2019, 18 (12), 1278-1291.
- [9] Simon, P.; Gogotsi, Y.; Dunn, B., Where Do Batteries End and Supercapacitors Begin? *Science* 2014, 343 (6176), 1210.

- [10] Schmidt-Rohr, K., How Batteries Store and Release Energy: Explaining Basic Electrochemistry. *Journal of Chemical Education* 2018, 95 (10), 1801-1810.
- [11] Whittingham, M. S., History, evolution, and future status of energy storage. *Proceedings of the IEEE* 2012, 100 (Special Centennial Issue), 1518-1534.
- [12] Winter, M.; Barnett, B.; Xu, K., Before Li Ion Batteries. *Chemical Reviews* 2018, 118 (23), 11433-11456.
- [13] Nitta, N.; Wu, F.; Lee, J. T.; Yushin, G., Li-ion battery materials: present and future. *Materials Today* 2015, 18 (5), 252-264.
- [14] Islam, M. S.; Fisher, C. A. J., Lithium and sodium battery cathode materials: computational insights into voltage, diffusion and nanostructural properties. *Chemical Society Reviews* 2014, 43 (1), 185-204.
- [15] Tarascon, J.-M., Key challenges in future Li-battery research. *Philosophical Transactions of the Royal Society A: Mathematical, Physical and Engineering Sciences* 2010, 368 (1923), 3227-3241.
- [16] Tarascon, J.-M.; Armand, M., Issues and challenges facing rechargeable lithium batteries. In *Materials for sustainable energy: a collection of peer-reviewed research and review articles from Nature Publishing Group*, World Scientific: 2011; pp 171-179.
- [17] Winter, M., The solid electrolyte interphase—the most important and the least understood solid electrolyte in rechargeable Li batteries. *Zeitschrift für physikalische Chemie* 2009, 223 (10-11), 1395-1406.
- [18] Bin, D.; Wen, Y.; Wang, Y.; Xia, Y., The development in aqueous lithium-ion batteries. *Journal of Energy Chemistry* 2018, 27 (6), 1521-1535.
- [19] Suo, L.; Borodin, O.; Gao, T.; Olguin, M.; Ho, J.; Fan, X.; Luo, C.; Wang, C.; Xu, K., “Water-in-salt” electrolyte enables high-voltage aqueous lithium-ion chemistries. *Science* 2015, 350 (6263), 938-943.
- [20] Smith, L.; Dunn, B., Opening the window for aqueous electrolytes. *Science* 2015, 350 (6263), 918-918.
- [21] Shi, P.; Zhang, X.-Q.; Shen, X.; Zhang, R.; Liu, H.; Zhang, Q., A Review of Composite Lithium Metal Anode for Practical Applications. *Advanced Materials Technologies* 2020, 5 (1), 1900806.
- [22] Nair, J. R.; Imholt, L.; Brunklaus, G.; Winter, M., Lithium Metal Polymer Electrolyte Batteries: Opportunities and Challenges. *The Electrochemical Society Interface* 2019, 28 (2), 55-61.

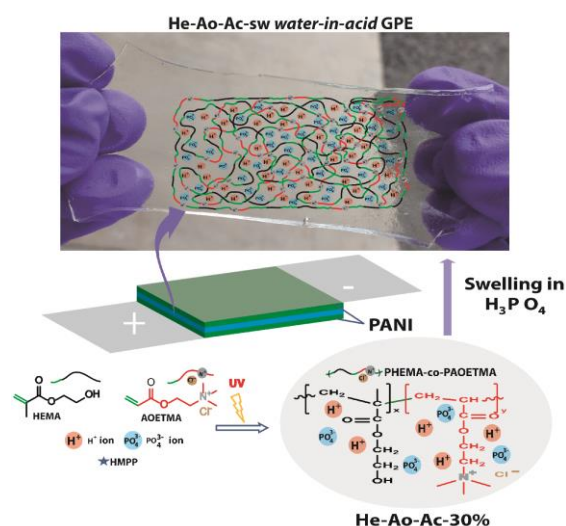
- [23] Li, L.; Basu, S.; Wang, Y.; Chen, Z.; Hundekar, P.; Wang, B.; Shi, J.; Shi, Y.; Narayanan, S.; Koratkar, N., Self-heating-induced healing of lithium dendrites. *Science* 2018, 359 (6383), 1513.
- [24] Barai, P.; Higa, K.; Srinivasan, V., Lithium dendrite growth mechanisms in polymer electrolytes and prevention strategies. *Physical Chemistry Chemical Physics* 2017, 19 (31), 20493-20505.
- [25] Placke, T.; Kloepsch, R.; Dühnen, S.; Winter, M., Lithium ion, lithium metal, and alternative rechargeable battery technologies: the odyssey for high energy density. *Journal of Solid State Electrochemistry* 2017, 21 (7), 1939-1964.
- [26] Xu, W.; Wang, Y., Recent Progress on Zinc-Ion Rechargeable Batteries. *Nano-Micro Letters* 2019, 11 (1), 90.
- [27] Nam, K. W.; Park, S. S.; Dos Reis, R.; Dravid, V. P.; Kim, H.; Mirkin, C. A.; Stoddart, J. F., Conductive 2D metal-organic framework for high-performance cathodes in aqueous rechargeable zinc batteries. *Nature communications* 2019, 10 (1), 1-10.
- [28] Selvakumaran, D.; Pan, A.; Liang, S.; Cao, G., A review on recent developments and challenges of cathode materials for rechargeable aqueous Zn-ion batteries. *Journal of Materials Chemistry A* 2019, 7 (31), 18209-18236.
- [29] Shin, J.; Lee, J.; Park, Y.; Choi, J. W., Aqueous zinc ion batteries: focus on zinc metal anodes. *Chemical Science* 2020, 11 (8), 2028-2044.
- [30] Wippermann, K.; Schultze, J.; Kessel, R.; Penninger, J., The inhibition of zinc corrosion by bisaminotriazole and other triazole derivatives. *Corrosion Science* 1991, 32 (2), 205-230.
- [31] Wan, F.; Zhang, Y.; Zhang, L.; Liu, D.; Wang, C.; Song, L.; Niu, Z.; Chen, J., Reversible Oxygen Redox Chemistry in Aqueous Zinc-Ion Batteries. *Angewandte Chemie International Edition* 2019, 58 (21), 7062-7067.
- [32] Kim, B. K.; Sy, S.; Yu, A.; Zhang, J., Electrochemical supercapacitors for energy storage and conversion. *Handbook of Clean Energy Systems* 2015, 1-25.
- [33] El-Kady, M. F.; Ihns, M.; Li, M.; Hwang, J. Y.; Mousavi, M. F.; Chaney, L.; Lech, A. T.; Kaner, R. B., Engineering three-dimensional hybrid supercapacitors and microsupercapacitors for high-performance integrated energy storage. *Proceedings of the National Academy of Sciences* 2015, 112 (14), 4233-4238.
- [34] Jiang, Y.; Liu, J., Definitions of Pseudocapacitive Materials: A Brief Review. *ENERGY & ENVIRONMENTAL MATERIALS* 2019, 2 (1), 30-37.

- [35] Noori, A.; El-Kady, M. F.; Rahmanifar, M. S.; Kaner, R. B.; Mousavi, M. F., Towards establishing standard performance metrics for batteries, supercapacitors and beyond. *Chemical Society Reviews* 2019, 48 (5), 1272-1341.
- [36] Salunkhe, R. R.; Tang, J.; Kamachi, Y.; Nakato, T.; Kim, J. H.; Yamauchi, Y., Asymmetric Supercapacitors Using 3D Nanoporous Carbon and Cobalt Oxide Electrodes Synthesized from a Single Metal–Organic Framework. *ACS Nano* 2015, 9 (6), 6288-6296.
- [37] Yu, X.; Yun, S.; Yeon, J. S.; Bhattacharya, P.; Wang, L.; Lee, S. W.; Hu, X.; Park, H. S., Emergent Pseudocapacitance of 2D Nanomaterials. *Advanced Energy Materials* 2018, 8 (13), 1702930.
- [38] Béguin, F.; Presser, V.; Balducci, A.; Frackowiak, E., Carbons and Electrolytes for Advanced Supercapacitors. *Advanced Materials* 2014, 26 (14), 2219-2251.
- [39] Wright, P. V., Electrical conductivity in ionic complexes of poly (ethylene oxide). *British polymer journal* 1975, 7 (5), 319-327.
- [40] Polu, A. R.; Rhee, H.-W., Ionic liquid doped PEO-based solid polymer electrolytes for lithium-ion polymer batteries. *international journal of hydrogen energy* 2017, 42 (10), 7212-7219.
- [41] Shim, J.; Kim, L.; Kim, H. J.; Jeong, D.; Lee, J. H.; Lee, J.-C., All-solid-state lithium metal battery with solid polymer electrolytes based on polysiloxane crosslinked by modified natural gallic acid. *Polymer* 2017, 122, 222-231.
- [42] Porcarelli, L.; Shaplov, A. S.; Bella, F.; Nair, J. R.; Mecerreyes, D.; Gerbaldi, C., Single-Ion Conducting Polymer Electrolytes for Lithium Metal Polymer Batteries that Operate at Ambient Temperature. *ACS Energy Letters* 2016, 1 (4), 678-682.
- [43] Nie, K.; Hong, Y.; Qiu, J.; Li, Q.; Yu, X.; Li, H.; Chen, L., Interfaces between cathode and electrolyte in solid state lithium batteries: challenges and perspectives. *Frontiers in chemistry* 2018, 6, 616.
- [44] Anothumakkool, B.; Torris A. T, A.; Veeliyath, S.; Vijayakumar, V.; Badiger, M. V.; Kurungot, S., High-Performance Flexible Solid-State Supercapacitor with an Extended Nanoregime Interface through in Situ Polymer Electrolyte Generation. *ACS Applied Materials & Interfaces* 2016, 8 (2), 1233-1241.

Chapter 2

***Water-in-acid* Gel Polymer Electrolyte Realized through a Phosphoric Acid-Enriched Polyelectrolyte Matrix toward Solid-State Supercapacitors**

The simple and scalable ultraviolet (UV)-light-assisted synthesis methodology for producing a water-in-acid gel polymer electrolytes (GPEs) for solid-state supercapacitor application is introduced in this chapter. The synthesis of the copolymer matrix possessing polyelectrolyte behavior, followed by swelling in minimally diluted bottle-grade commercial H_3PO_4 (15.1 M/88 wt.% aqueous solution), lead to the formation of a high proton-conducting, self-standing, and mechanically stable polyelectrolyte GPE (PGPE). Retention of high mechanical stability despite the presence of a large amount of liquid species makes it a promising candidate for replacing conventional GPEs. The high proton conductivity ($9.8 \times 10^{-2} \text{ S cm}^{-1}$) of the PGPE at an ambient temperature of 303 K is attributed to the high concentration of the conducting species present in the polymer matrix. The PGPE-based polyaniline (PANI) supercapacitor device (PANI-1) with a mass-loading of 1.0 mg cm^{-2} exhibits a high specific gravimetric capacitance of 385 F g^{-1} at a current density of 0.25 mA cm^{-2} . At the same current density, the PANI-5 device retains high gravimetric and areal capacitance values of 258 F g^{-1} and 1288 mF cm^{-2} , respectively. The low equivalent series resistance value of $0.78 \text{ } \Omega$ (for the PANI-5 device) further proves the excellent electrode/electrolyte interface formed by the *water-in-acid* GPE. A 100% capacitance retention even after 9000 continuous charge-discharge cycles strongly indicates the feasibility of adopting *water-in-acid* GPEs in future supercapacitors.



Contents in this chapter are published in the article: DOI: 10.1021/acssuschemeng.8b01175. Reprinted (adapted) with permission from (ACS Sustainable Chem. Eng. 2018, 6, 10, 12630-12640). Copyright (2018) American Chemical Society.

2.1 Introduction

Polymer electrolytes are recently being widely adopted instead of liquid electrolytes in supercapacitors (SCs) to improve their safety and flexibility.^{1,2} In the case of conventional proton-conducting gel polymer electrolytes (GPEs) based on inorganic acids such as H_3PO_4 and H_2SO_4 , a considerable amount of water is used for dilution, and it is appropriate to call them *acid-in-water* GPEs. They are unsuitable for long-term use since the gradual evaporation of water from the polymer matrix deteriorates the ionic conductivity, shelf life, and cycling stability in the SC devices.^{3,4} However, the high-water content in the GPE has a significant role in facilitating the ionic conductivity through hydrogen bonding and proper dissociation of the acid molecules. There have been efforts where the water in the GPE is replaced with organic electrolytes to resolve the water evaporation problem in proton-conducting GPEs.⁵ However, this hampers the ionic conductivity because of the decrease in the degree of hydrogen bonding present in the final system.

The highly viscous nature of the benchmark polyvinyl alcohol (PVA)-based GPEs is due to the lack of covalent crosslinks present in it. Besides, PVA chains fail to induce non-covalent interactions with the conducting species/solvent due to the absence of functional moieties other than the -OH group.³ Hence, the mechanical stability and solvent retention capability of the PVA matrix are compromised. The efforts to crosslink PVA with glutaraldehyde, in turn, deteriorate the degree of non-covalent interactions due to the lack of hydrophilic pendant groups in the long carbon chain. These attempts negatively affect the water retention capability compared to the already inferior PVA-based *acid-in-water* GPEs.⁶ Despite the drawbacks of PVA, it is ubiquitously used for the preparation of mechanically unstable GPE solutions but do not incite interest rather than of mere academic purpose. Judicious selection of the polymer matrix as well as the conducting species are the key factors to overcome the above mentioned practical intricacies. The polymer matrix can be highly crosslinked such that it can possess a self-standing nature along with enough number of various functional group moieties. The functional groups can induce non-covalent interactions within the polymer chains as well as between the polymer chain and the species incorporated inside (ion-conducting species and solvents).⁷ These non-covalent interactions can help in improving the mechanical stability and facilitating the ionic conductivity. They can ultimately effect in a mechanically stable GPE even with a high content of the liquid phase.

Several published studies are available regarding the use of H_2SO_4 for the preparation of GPEs for SC applications.^{3,8-11} However, the use of the H_2SO_4 -based electrolytes cannot be extended beyond the lab from a commercial perspective due to their highly corrosive nature. Moreover, the high dilution required before the use of H_2SO_4 as an electrolyte is also not desirable owing to the gradual evaporation of water from the polymer matrix. Therefore, the peculiar property of neat H_3PO_4 , unlike the other concentrated inorganic acids, becomes relevant, where it can exhibit extremely high ionic conductivity as a consequence of a network of frustrated, strong, and highly polarizable hydrogen bonds¹²⁻¹⁵ Even the minimally diluted bottle-grade commercial H_3PO_4 is reported to show high ionic conductivity which provides the opportunity to employ it as an electrolyte directly.¹⁵⁻¹⁷ Such bottle-grade conc. H_3PO_4 doped proton conducting membranes are already used for fuel cell applications.^{18,19} However, the concept has never been adopted to effect a GPE for SC applications.

In this work, for the first time, a mechanically self-standing polyelectrolyte GPE (PGPE) film with a high content of bottle-grade conc. H_3PO_4 (commercially available 15.1 M/88 wt.% aqueous solution of H_3PO_4 is used throughout this work) encapsulated in a polyelectrolyte matrix is demonstrated. Here, a new term “*water-in-acid* GPE” is introduced for such a highly concentrated bottle-grade H_3PO_4 -based electrolyte with relatively less amount of water present in it. The polymer matrix used here possesses a polyelectrolyte nature, which is synthesized by the ultraviolet (UV)-light assisted^{3,7,20} copolymerization of acrylate monomers, viz., 2-hydroxyethyl methacrylate (HEMA) and [2-(acryloyloxy)ethyl]trimethylammonium chloride (AOETMA).^{21,22} This copolymer swells on exposure to bottle-grade H_3PO_4 , giving the highly conducting PGPE. The real-life application of this *water-in-acid* PGPE film is then demonstrated as an electrolyte in the solid-state SC, where polyaniline (PANI) is used as the active electrode material. Despite being used as a film, the PGPE can deliver an excellent electrode|electrolyte interface even at high-mass-loaded PANI electrodes with improved cycling stability compared to that of the highly viscous and mechanically unstable PVA-based *acid-in-water* GPE solution. It is envisaged that the reported *water-in-acid* PGPE will be suitable for use along with other acid-stable electrode materials (carbon/metal oxides/conducting polymers) and can potentially replace the conventional GPEs in SCs.

2.2 Experimental section

2.2.1 Materials

Aniline (used after distillation), ammonium persulfate (APS), N-methyl-2-pyrrolidone (NMP), 2-hydroxy-2-methylpropiophenone (HMPP), phytic acid, and [2-(acryloyloxy)ethyl]trimethylammonium chloride (AOETMA) were purchased from Aldrich Chemicals. 2-Hydroxyethyl methacrylate (HEMA) was purchased from Fluka, and polyvinyl alcohol (PVA) (MW 115000) was procured from Loba Chemie Pvt. Ltd. Bottle-grade H_3PO_4 (88 wt.%/15.1 M aqueous solution) was purchased from Merck Life Science Pvt. Ltd., and a polypropylene membrane purchased from Celgard was used as the separator. Grafoil[®], used as the current collector, was procured from the GrafTech. Kynar[®] PVDF (polyvinylidene fluoride) used as the binder was procured from Global Nanotech. The UV chamber used contained four fluorescent lamps (Model: OSRAM L BL UVA 15 W/78).

2.2.2 Preparation of *Water-in-Acid* PGPE

The *water-in-acid* PGPE was prepared by immersing a pre-swollen film in concentrated bottle-grade H_3PO_4 (15.1 M / 88 wt.% aqueous solution of H_3PO_4) until equilibrium swelling. To prepare the pre-swollen film, a solution containing fixed volumes of the monomers HEMA and AOETMA (volume ratio of the monomers is HEMA: AOETMA = 2:1) along with 30% v/v of H_3PO_4 , in the presence of a UV-initiator HMPP was subjected to UV-curing for 15 min. In a typical procedure, 560 μl of HEMA and 280 μl of AOETMA monomers were mixed with 360 μl of bottle-grade H_3PO_4 . About 2 μl of UV initiator was also added. The precursor solution was then transferred into a flat plastic mould with a dimension of 7 cm (length) \times 2 cm (width) \times 0.5 cm (height). On UV irradiation, the pre-swollen film, represented as He-Ao-Ac-30%, was formed and could be easily peeled out from the mould. ‘He’ and ‘Ao’ correspond to the monomers HEMA and AOETMA, respectively, whereas ‘Ac’ and ‘30%’ correspond to the term ‘acid’ and the volume of bottle-grade H_3PO_4 present in the specimen, respectively. The pre-swollen film was then again immersed in 500 ml of bottle-grade H_3PO_4 for about 24 h. to get the final *water-in-acid* PGPE (He-Ao-Ac-sw), where ‘sw’ indicates that it is ‘swollen’. A pre-swollen film was also prepared without H_3PO_4 and represented as He-Ao-Ac-0%. Here, ‘0%’ indicates the absence of H_3PO_4 in the matrix. The term ‘P(HEMA-co-AOETMA)’ used throughout the paper represents the copolymer matrix present in the PGPE.

2.2.3 Preparation of PVA- H_3PO_4 *Acid-in-Water/Water-in-Acid* GPE solutions

To prepare the conventional *acid-in-water* PVA- H_3PO_4 (PVA-AIW) GPE solution, 1.0 g of PVA was weighed and added into an RB flask containing 10 ml of de-

ionized (DI) water and heated at 80 °C with constant stirring until a clear solution was obtained. The solution was then cooled to room temperature, followed by the addition of 1.0 g of concentrated bottle-grade H_3PO_4 and further stirred for 30 min. The obtained GPE solution was used for SC fabrication. For the preparation of the PVA-based *water-in-acid* GPE solution (PVA-WIA), 5.0 g of PVA is dissolved in a solution of 50 ml of bottle-grade H_3PO_4 and 10 ml water. The resultant *water-in-acid* GPE solution was 12.8 M/78.8 wt % aqueous solution of H_3PO_4 in PVA.

2.2.4 Preparation of PANI

In a typical procedure, 400 μl of distilled aniline and 960 μl of phytic acid were added to 10 ml of DI water in a beaker of 20 ml capacity. The beaker was then kept in an ice bath with stirring followed by the addition of 286 mg of APS to trigger the polymerization. The stirring was continued for about 10 h to obtain the highly conducting emeraldine form of PANI. The obtained PANI was filtered and washed with DI water several times followed by drying in a vacuum oven at 60°C for 2 h. The physical characterizations were carried out by X-ray diffraction (XRD), Raman spectroscopy, Brunauer–Emmett–Teller (BET), and field emission scanning electron microscope (FESEM) analyses.

2.2.5 Electrode Preparation and SC Device Fabrication

To prepare the electrodes, a slurry containing 95 and 5 wt % of the PANI and PVDF binder, respectively, in NMP was prepared and coated over 1 cm^2 area of a grafoil current collector. The volume of the slurry coated over the current collector was varied to get electrodes with mass-loading ranging from 1 to 5 mg cm^{-2} . Two such electrodes were used to sandwich the 1.5 mm-thick *water-in-acid* GPE to affect the final SC device generally designated as PANI-x, where ‘x’ corresponds to the loading of PANI in the electrode ($x = 1$ to 5 mg cm^{-2}).

Similarly, for comparison purposes, PVA- H_3PO_4 GPE solution-based SC devices (with $x = 5 \text{ mg cm}^{-2}$) was also prepared for the studies. The *water-in-acid* and *acid-in-water* GPE solution-based devices were represented as PANI-5-PVA-WIA and PANI-5-PVA-AIW, respectively. To fabricate the devices, the GPE solution was applied on the PANI coated area of two electrodes (with PANI loading of 5 mg cm^{-2}), which was then sandwiched together with a polycarbonate separator between them. All devices were sealed with adhesive tapes before testing. The area left uncoated with PANI on each electrode was used to provide the connection.

2.2.6 Material Characterisation

Structure and morphology of PANI were analyzed with the help of a FESEM (Nova Nano SEM 450.). The specific surface area (SSA) of the PANI was determined by the BET adsorption method (Quantochrome Autosorb automated gas sorption analyzer). Powder X-ray diffraction (PXRD) data of PANI were collected using a Rigaku, MicroMax-007HF with high-intensity Microfocus rotating anode X-ray generator in the 2θ range between $2-80^\circ$ (Cu $K\alpha$ ($\lambda = 1.54 \text{ \AA}$)). Raman analysis for PANI was performed with the help of a LabRam spectrometer (HJY) equipped with a laser wavelength of 632 nm. Infrared spectra of the He-Ao-Ac-0%, He-Ao-Ac-30%, and He-Ao-Ac-sw were recorded using a Bruker FTIR spectrophotometer in attenuated total reflection (ATR) mode for the range of $4000-600 \text{ cm}^{-1}$. The thermal stability of the specimens was analyzed using a PerkinElmer STA-6000 thermogravimetric analyzer (TGA) under nitrogen atmosphere. Dynamic mechanical analyzer (DMA) (RSA III, TA Instruments USA.) equipped with TA Orchestrator software (Version 7.2.0.4) was used for the uniaxial tensile measurements (static mode). For the uniaxial tensile measurements, He-Ao-Ac-30% and He-Ao-Ac-sw GPE specimens with a rectangular geometry of 5 mm width, 1.5 mm thickness, and 15 mm length were prepared. The specimens were clamped onto tensile grips with a constant torque of 20 cN.m, and the loads were applied at a speed of 1 mm min^{-1} up to failure.

2.2.7 Electrochemical characterization of GPE and SC devices

A BioLogic SP-300 Potentio-Galvanostat was used for electrochemical evaluations. Cyclic voltammetry (CV) measurements were taken at different scan rates from 10 to 500 mV s^{-1} . The potential window was fixed in the range of 0 to 0.80 V. Charge-discharge (CD) measurement was carried out at different current densities from 0.25 to 20 mA cm^{-2} . Cycling stability was monitored by using charge-discharge experiments at a current density of 10 mA cm^{-2} for many thousand cycles. Electrochemical impedance spectroscopic (EIS) investigation for the SC device was performed from 10^6 to 0.1 Hz frequency against the open circuit potential with a sinus amplitude of 10 mV ($V_{\text{rms}} = 7.07 \text{ mV}$).

Conductivity values of the pre-swollen film (He-Ao-Ac-30%) and water-in-acid GPE (He-Ao-Ac-sw) are obtained from the EIS investigation. Disc-shaped films were used for this purpose. GPE disc with a thickness of 0.1 cm and a radius of 0.75 cm was used for the measurement of ionic conductivity at ambient temperature (303 K). To determine the temperature-dependent ionic conductivity values, the thickness and radius of the discs used were 0.15 cm and 0.5 cm, respectively (thick films were used to avoid

the wear and tear of the GPE at high temperatures). The discs were kept in between two stainless steel plates, and the terminals were connected to the potentiostat through crocodile clips. The whole-cell assembly was then held in an Espec environmental test chamber to control the temperature. The EIS studies were carried out in a frequency range of 10^6 Hz to 1 Hz for room-temperature ionic conductivity measurements. For temperature-dependent ionic conductivity measurements, a frequency range of 10^6 Hz to 0.1 Hz was used. All the experiments were done against the open circuit potential with a sinus amplitude of 10 mV ($V_{\text{rms}} = 7.07$ mV). The x-intercept of the Nyquist plot is taken as the bulk resistance of the membrane, and the conductivity can be measured using **Equation 2.5** and **2.6**. The Arrhenius relationship is given in **Equation 2.7**.

The swelling ratio (Q) of the PGPE is calculated from **Equation 2.1**

$$Q = \frac{W_s - W_d}{W_d} \times 100 \quad (\text{Equation 2.1})$$

W_s = Mass of swollen specimen

W_d = Mass of pre-swollen specimen

Equation 2.2 is used for the calculation of specific gravimetric (F g^{-1})/areal capacitance (mF cm^{-2}) from the charge-discharge method.

$$C = \frac{2 \times (I \times \Delta t)}{\Delta V * M \text{ or } A} \quad (\text{Equation 2.2})$$

where,

Δt = Discharge time

ΔV = Potential window

I = Constant current used for charging and discharging

M = Weight of active material in one of the electrodes

A = Active material coated area in the electrode.

To get the single electrode capacitance, the obtained device capacitance was multiplied by a factor of 2, which is included in **Equation 2.2**.

The gravimetric energy density (E_d) and power density (P_d) were calculated from the capacitance value obtained from the charge-discharge method.

$$\text{Energy density } (E_d) \text{ ((Wh kg}^{-1}\text{))} = \frac{C_s}{8 \times 3.6} V^2 \quad (\text{Equation 2.3})$$

where,

‘ C_s ’ is the specific capacitance calculated by the charge-discharge (F g^{-1}) method, and ‘ V ’ is the voltage window.

$$\text{Power density (P}_d\text{)} ((\text{W kg}^{-1})) = \frac{E_d}{t} \quad (\text{Equation 2.4})$$

where, 'E_d' is the energy density from **Equation 2.3**, and 't' is the discharge time in hour calculated from the discharge curve.

The ionic conductivity of the GPEs was calculated from **Equation 2.5** and **2.6**.

$$\rho (\Omega \text{ cm}) = \frac{RA}{l} \quad (\text{Equation 2.5})$$

$$\sigma (S \text{ cm}^{-1}) = \frac{1}{\rho} \quad (\text{Equation 2.6})$$

σ = Conductivity of the membrane

ρ = Resistivity of the membrane

R = bulk resistance of the membrane

A = Area of the membrane

l = Thickness of the membrane

The Arrhenius relationship is given in **Equation 2.7**,

$$\sigma = \sigma^0 \exp(-E_a/RT) \quad (\text{Equation 2.7})$$

In **Equation 2.7**, σ, σ⁰, E_a, R, and T are the ionic conductivity, the pre-exponential factor, the activation energy for ion transport, the gas constant, and the absolute temperature, respectively.

The activation energy calculated for He-Ao-Ac-sw is obtained from the linear fitting of the ln σ vs. 1/T plot.

2.3 Results and discussion

Figure 2.1a schematically represents the general scheme adopted for the preparation of the *water-in-acid* PGPE (described as He-Ao-Ac-sw) from the precursor film He-Ao-Ac-30% (see **Experimental Section 2.2.2** for the detailed synthetic procedure; 30% corresponds to the volume percentage of bottle-grade H₃PO₄ already present in the precursor solution used for the preparation of the He-Ao-Ac-30% film). The He-Ao-Ac-30% film prepared through the UV assisted polymerization of the precursor solution is immersed in 500 ml of bottle-grade H₃PO₄ till equilibrium swelling to prepare the H₃PO₄ rich *water-in-acid* PGPE. The digital images of the PGPE in its normal and stretched states are also presented in **Figure 2.1a**, qualitatively indicating its stretchability, self-standing character, and mechanical stability. Moreover, the *water-in-acid* PGPE obtained is transparent and self-standing. The large swelling ratio (see **Equation 2.1**)²³ of about 2100% indicates the high H₃PO₄ content in the PGPE. These PGPEs are free of the electrolyte starvation that arises as a result of gradual electrolyte

evaporation from the polymer matrix, which is a severe drawback associated with the low-boiling solvents contained in conventional GPEs.³

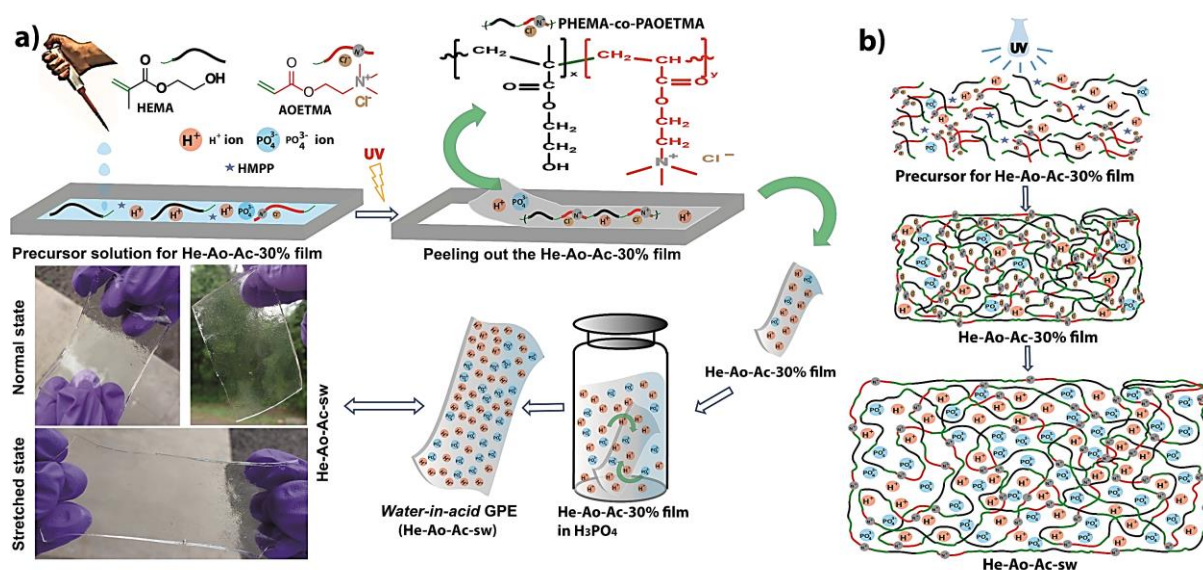


Figure 2.1. (a) Scheme illustrating the synthesis of water-in-acid PGPE (He-Ao-Ac-sw); (b) a schematic representation of the arrangement of the monomer molecules in the precursor solution for the He-Ao-Ac-30% film, polymer molecules in the pre-swollen film (He-Ao-Ac-30% film) and the water-in-acid PGPE (He-Ao-Ac-sw). For simplicity, only PO_4^{3-} and H^+ ions are depicted. In addition to them, di-hydrogen phosphate (H_2PO_4^-) and mono-hydrogen phosphate (HPO_4^{2-}) ions will be also present in the polymer matrix. (Reprinted (adapted) with permission from (ACS Sustainable Chem. Eng. 2018, 6, 10, 12630-12640). Copyright (2018) American Chemical Society).

It is observed that the intrinsically flexible and elastic PAOETMA (polymerized form of [2-(acryloyloxy)ethyl]trimethylammonium chloride (AOETMA)) film swells uncontrollably, forming a viscous gel that is mechanically unstable (**Figure 2.2a**). The swelling of PAOETMA is attributed to its polyelectrolyte nature where the electrostatic repulsion between the N^+ moieties present in the polymer chains facilitates the high H_3PO_4 intake.^{24,25} Partial dissolution of the PAOETMA in H_3PO_4 is also observed as a result of the lack of efficient covalent crosslinks in it. However, the tough and brittle PHEMA (the polymerized form of 2-hydroxyethyl methacrylate (HEMA)) exhibits insignificant swelling in H_3PO_4 (**Figure 2.2b**) since it does not possess any polyelectrolyte nature. Interestingly, the copolymer He-Ao-Ac-0% (He-Ao-Ac-0% is the copolymer formed by the UV polymerization of HEMA and AOETMA monomers in a volume ratio of HEMA: AOETMA = 2:1 without H_3PO_4 ; “0%” indicates the absence of H_3PO_4 in the obtained film) is found to exhibit significant swelling in H_3PO_4 ,

leading to a self-standing *water-in-acid* PGPE film with the desired mechanical properties (He-Ao-Ac-30%, before and after swelling, **Figure 2.2c** and **d**, respectively).

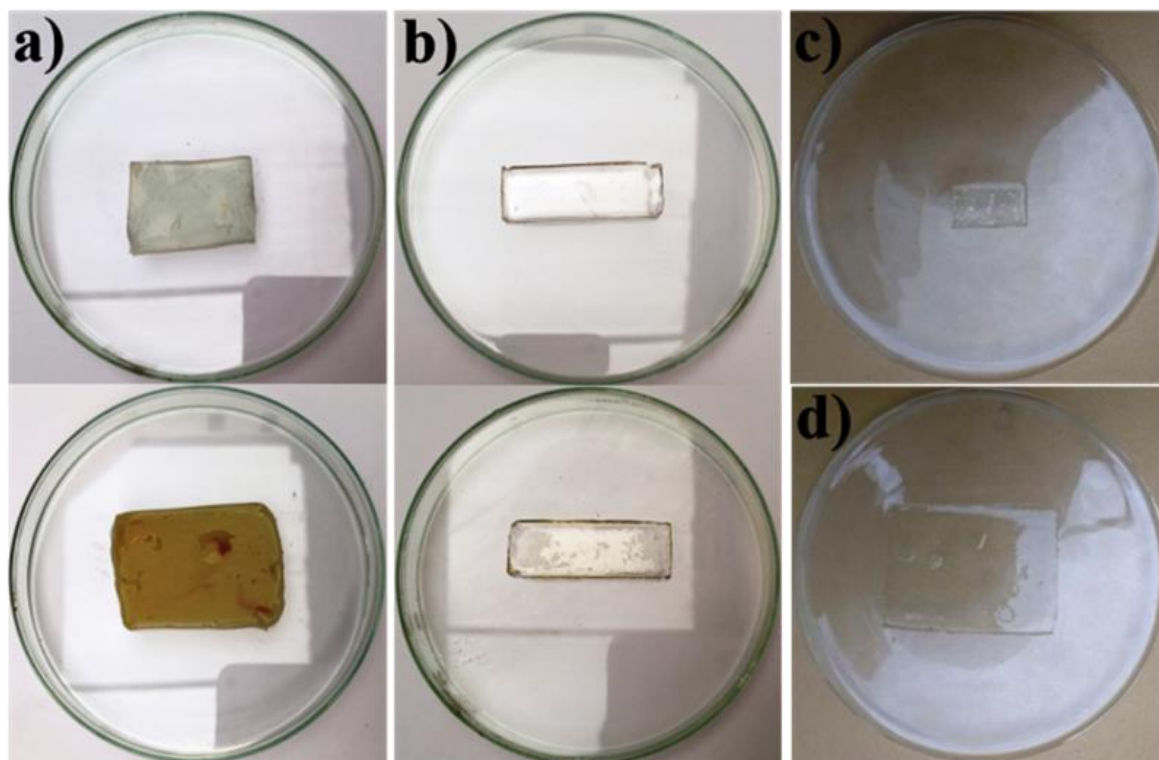


Figure 2.2. The digital images of (a) PAOETMA gel, and (b) PHEMA gel before and after swelling in H_3PO_4 ; (c) pre-swollen He-Ao-Ac-30% film and (d) swollen He-Ao-Ac-sw PGPE. (Reprinted (adapted) with permission from (ACS Sustainable Chem. Eng. 2018, 6, 10, 12630-12640). Copyright (2018) American Chemical Society).

In the case of He-Ao-Ac-0%/He-Ao-Ac-30% pre-swollen films, the PAOETMA matrix favors the swelling while the tough PHEMA takes care of mechanical stability. Even in the absence of any external crosslinker, the covalent links that exist between the PHEMA and PAOETMA prevent the dissolution of PAOETMA, unlike when it is used alone. It is reasonable to say that the copolymer matrix (represented as P(HEMA-co-AOETMA)) acts as a superabsorbent to H_3PO_4 . The term *water-in-acid* PGPE is meaningful here since the amount of water present in the liquid phase entrapped in the PGPE is about 7 times less than the total amount of H_3PO_4 present in it. A similar concept of the *water-in-salt* electrolyte has been explored by Suo *et al.*, where very high concentrations of a conducting salt dissolved in the water had to be used as electrolytes in aqueous lithium-ion batteries.^{26,27}

The swelling of the pre-swollen film (He-Ao-Ac-30%) on exposure to H_3PO_4 is due to the influx of the solvent into the free-volume available in the polymer matrix. The reason for using He-Ao-Ac-30% instead of He-Ao-Ac-0% for the preparation of

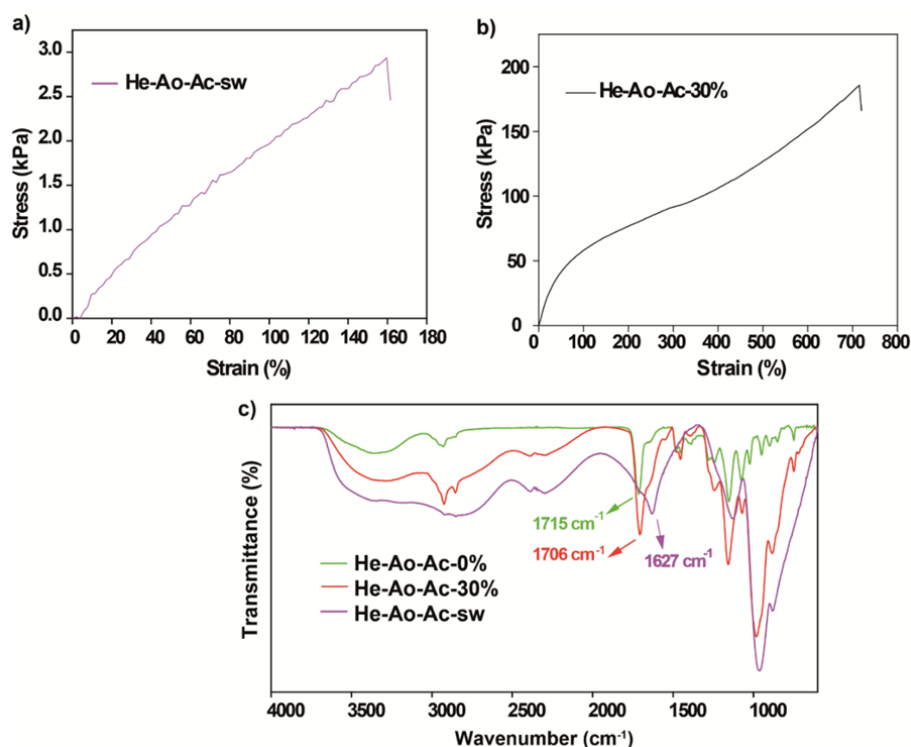


Figure 2.3. Tensile property of the (a) He-Ao-Ac-sw PGPE and (b) He-Ao-Ac-30% films; (c) ATR-FTIR spectra of the He-Ao-Ac-0%, He-Ao-Ac-30% pre-swollen films and the water-in-acid PGPE (He-Ao-Ac-sw). (Reprinted (adapted) with permission from (ACS Sustainable Chem. Eng. 2018, 6, 10, 12630-12640). Copyright (2018) American Chemical Society).

the water-in-acid PGPE is that the free-volume in the polymer matrix is expected to increase owing to the plasticizing effect of the pre-incorporated bottle-grade H_3PO_4 (liquid-phase) in He-Ao-Ac-30%.²⁸ As a result, the time required for equilibrium swelling of the He-Ao-Ac-30% pre-swollen film is lower compared to that needed for He-Ao-Ac-0%, which in turn, leverages the processability advantages. A schematic representation of the arrangement of the monomer molecules/polymer chains in the He-Ao-Ac-30% and the swollen He-Ao-Ac-sw film is given in **Figure 2.1b**. It is seen that the presence of H_3PO_4 opens up more free-volume in the P(HEMA-co-AOETMA) copolymer matrix and in turn facilitates the rapid swelling of the He-Ao-Ac-30% on further exposure to H_3PO_4 to form the He-Ao-Ac-sw water-in-acid PGPE.

The quantitative determination of the tensile strength of the He-Ao-Ac-30% and the He-Ao-Ac-sw films was carried out by dynamical mechanical analysis (DMA). The plots representing the tensile stress vs. strain for the He-Ao-Ac-sw PGPE specimen are given in **Figure 2.3a**. A similar plot corresponding to the pre-swollen film (He-Ao-Ac-30%) and He-Ao-Ac-sw is given in **Figure 2.3b**. The He-Ao-Ac-30% film possesses a

tensile strength value of 1900 kPa and is stretchable to up to 700 % of its original length without any failure. However, the mechanical properties of the He-Ao-Ac-sw are found to vary significantly due to the presence of a large amount of H_3PO_4 . The soft nature of the He-Ao-Ac-sw (tensile strength value of 3 kPa and stretchable up to 150 % of original length) compared to the tough He-Ao-Ac-30% film is due to the plasticizing effect induced by the extra H_3PO_4 introduced into it. Still, these values corresponding to the He-Ao-Ac-sw are promising enough to be used as a solid-state electrolyte in SCs.

In addition to the influence of the polyelectrolyte nature of the polymer matrix, other non-covalent physical interactions such as the hydrogen bonding between the carbonyl group of the polymer matrix and H_3PO_4 ,²⁹ interaction of the N^+ moiety with dihydrogen phosphate (H_2PO_4^-), mono-hydrogen phosphate (HPO_4^{2-}) or normal phosphate (PO_4^{3-}) ions from H_3PO_4 ^{30,31} also play a key role in deciding the behavior of the PGPE film. These interactions favor the swelling as well as the retention of the desired mechanical stability of PGPE. Further proof for these interactions is given by the ATR-FTIR spectra (**Figure 2.3c**) captured for the pre-swollen films and the GPEs. The carbonyl peak at 1715 cm^{-1} corresponding to the He-Ao-Ac-0% film is found to be red-shifted to 1705 cm^{-1} in the case of He-Ao-Ac-30%. All the while, the very large amount of H_3PO_4 (He-Ao-Ac-sw) causes the disappearance of the sharp carbonyl peak and a new peak at 1627 cm^{-1} is observed. This can be due to the combined effect of protonation of the carbonyl group by the extremely high concentration of H_3PO_4 along with the hydrogen bonding induced by the interaction of H_3PO_4 with the carbonyl group. The partial protonation of the carbonyl oxygen gives more $-\text{OH}$ characteristics to the carbonyl group and leads to the broad signal in the range of $2000\text{--}3500\text{ cm}^{-1}$. The broad nature of the spectra in the region between 2000 and 3500 cm^{-1} further underlines the enhanced hydrogen bonding in the presence of H_3PO_4 .³²⁻³⁵

The superiority of the P(HEMA-co-AOETMA) copolymer matrix over the conventional PVA polymer matrix in realizing the mechanically stable *water-in-acid* GPE is also studied. To prepare the PVA-based *water-in-acid* GPE, 5.0 g of PVA is tried to be dissolved in 50 ml of bottle-grade H_3PO_4 . However, it is observed that PVA is insoluble in the aforementioned concentration of H_3PO_4 and further dilution is indeed required. **Figure 2.4a** shows the digital image of the PVA-based GPE solution obtained by dissolving 5.0 g PVA in 50 ml of 15.1 M H_3PO_4 further diluted with 10 ml water (the resultant PVA-based *water-in-acid* GPE solution contains 12.8 M aqueous solution of H_3PO_4 in it). The viscous nature and the brownish color (because of prolonged heating

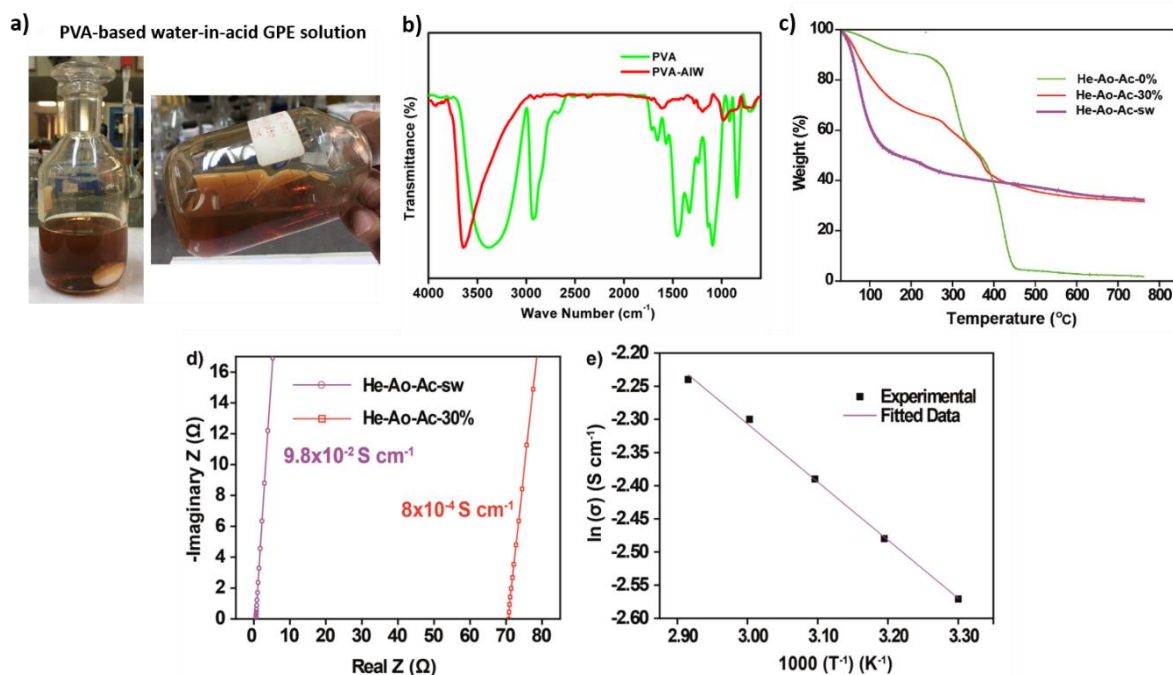


Figure 2.4. (a) Highly viscous nature of the PVA-based water-in-acid GPE solution; (b) FTIR spectra of the pristine PVA powder and the PVA-AIW GPE solution; (c) the thermogravimetric analysis (TGA) profiles of the pre-swollen films (He-Ao-Ac-0% and 30%), and the water-in-acid PGPE (He-Ao-Ac-sw); (d) Nyquist plots corresponding to the He-Ao-Ac-30% pre-swollen film and, the He-Ao-Ac-sw PGPE (only the high-frequency region of the Nyquist plot is shown); (e) $\ln \sigma$ vs. $1/T$ plot for He-Ao-Ac-sw. (Reprinted (adapted) with permission from (ACS Sustainable Chem. Eng. 2018, 6, 10, 12630-12640). Copyright (2018) American Chemical Society).

PVA-H₃PO₄-water mixture for the complete dissolution of PVA) of the PVA-based GPE are also not desirable. This observation further demonstrates that the P(HEMA-co-AOETMA) copolymer matrix is the best fit for realizing the *water-in-acid* GPE. To prove the limited hydrogen bonding interactions associated with the PVA matrix, we have compared the FTIR spectra of pristine PVA powder and the conventional PVA-based *acid-in-water* GPE solution (PVA-AIW). The corresponding plots are given in **Figure 2.4b**. From the figure, it is observed that the broad peak in the region of 3000-3700 cm⁻¹ corresponding to the hydrogen-bonded -OH group in the case of the pristine PVA powder is narrowed with the addition of the acid species. This trend is extremely different from the He-Ao-Ac-sw *water-in-acid* PGPE where the addition of the acid species is found to further improve the hydrogen bonding/other non-covalent interactions. Lack of the abovementioned interactions leads to the inferior mechanical/electrochemical properties of the PVA-based GPE solutions.

The results of the thermogravimetric analysis (TGA) of the pre-swollen films (He-Ao-Ac-0% and 30%) and the *water-in-acid* PGPE (He-Ao-Ac-sw) are summarized **Table 2.1**. The ionic conductivity of the proton conducting GPEs already reported in the literature and the acid-in-water GPE reported in this work are compared and summarised. (Reprinted (adapted) with permission from (ACS Sustainable Chem. Eng. 2018, 6, 10, 12630-12640). Copyright (2018) American Chemical Society).

Composition of the polymer electrolyte	Physical nature of the polymer electrolyte	Ionic Conductivity (Scm ⁻¹)	Temperature	Reference
PHEMA-PTMPA-H ₃ PO ₄	<i>in-situ</i> prepared GPE film	2.80×10^{-2}	At 303 K	3
Carboxymethyl Cellulose doped with oleic acid and plasticized with glycerol (CMC-OA-Gly SBE)	free-standing film	1.64×10^{-4}	At 303 K	37
Gellan gum + Borax + H ₃ PO ₄ /H ₂ SO ₄ /HCl	free-standing film	5 to 3.7×10^{-4}	At 303 K	38
PVA-H ₃ PO ₄	free-standing film	4.1×10^{-3}	At 303 K	39
PVA-H ₃ PO ₄	free-standing film	2.56×10^{-3}	Room temperature	40
PVA-H ₃ PO ₄	free-standing film	3.4×10^{-3}	At 303 K	41
PVP-NH ₄ Br	free-standing film	1.06×10^{-3}	At 303 K	42
PEO + 8 wt % HCF ₃ SO ₃ + 50 wt % DMA + 3 wt % SiO ₂	free-standing film	7.38×10^{-3}	At 303 K	43
PVdF-HFP + EMITf + NH ₄ Tf	GPE solution	2.3×10^{-2}	Room temperature	44
P(MMA-co-HEMA) (60 wt % of HEMA) + (PC+DMF) (30 wt % of DMF) + 40 wt % Diphenyl phosphate	GPE solution	5.7×10^{-4}	At 283 K	5
PVA-Glutaraldehyde-HClO ₄	free-standing film	<i>ca.</i> 1×10^{-3}	At 298 K	6
P(HEMA-co-AOETMA) + H ₃ PO ₄	free-standing film	9.8×10^{-2}	At 303 K	This work

in **Figure 2.4c**. In the plot corresponding to He-Ao-Ac-0%, weight losses are observed at 300 and 420°C. However, the addition of H₃PO₄ (as in the case of He-Ao-Ac-30%) changes the nature of thermal degradation in such a way that the rate of thermal degradation is decreased. This can be attributed to the stabilization facilitated by the

interaction between the H_3PO_4 and the polymer matrix.³⁶ The effect is even more prominent in the case of He-Ao-Ac-sw, where the sharp degradation peaks are absent owing to the high H_3PO_4 content present in it. However, in the case of both He-Ao-Ac-0% and He-Ao-Ac-30%, weight loss occurred below 200°C and can be attributed to the loss of the water molecules as well as free H_3PO_4 present in the polymer matrix.

EIS analysis is used to study the ionic conductivity behaviour of the specimens. The ionic conductivity of the freshly prepared He-Ao-Ac-sw and the He-Ao-Ac-30% film is calculated from the equivalent series resistance (ESR) values (0.50 and 71 Ω for He-Ao-Ac-sw and He-Ao-Ac-30%, respectively) obtained from the corresponding Nyquist plots as given in **Figure 2.4d** (only the high-frequency region of the Nyquist plot is shown). It is worth mentioning that the *water-in-acid* PGPEs reported in this work exhibit far higher ionic conductivity ($9.8 \times 10^{-2} \text{ S cm}^{-1}$) value than the conventional GPE solution and many other free-standing solid-state GPEs reported in the literature (summarized in **Table 2.1**).^{3,5,6,37-44} Compared to the other GPEs mentioned in **Table 2.1**, the presence of a high degree of functional group moieties which can favour hydrogen bonding along with a high concentration of the encapsulated proton-conducting species in P(HEMA-co-AOETMA) facilitates high ionic conductivity of He-Ao-Ac-sw GPE. This is in accordance with the hydrogen bonding interactions proved from the FTIR spectra provided in **Figure 2.3c** and **2.4b**. The low ionic conductivity ($8 \times 10^{-4} \text{ S cm}^{-1}$) of He-Ao-Ac-30% is obviously due to the low H_3PO_4 content present in it.

To predict the underlying mechanism for proton conduction in the GPE, the temperature (T) dependent ionic conductivity (σ) is measured. The plot of $\ln \sigma$ vs. $1/T$ (**Figure 2.4e**) follows the simple Arrhenius relationship (**Equation 2.7**) and the linear fit of the straight line gives an activation energy (E_a) value of 0.55 eV. The activation energy value obtained here is close to that obtained for liquid conc. H_3PO_4 .¹³ This underlines that the incorporation of conc. H_3PO_4 into the polymer matrix has not suppressed its ion transport properties. Considering the strong hydrogen bonding interactions that exist in the system and low activation energy required for proton conduction, it can be said that proton conduction takes place through the Grotthuss-type mechanism operating in the PGPE.^{18,45}

The *water-in-acid* PGPE films (He-Ao-Ac-x%-sw) realized in this work manage to satisfy the most-desired features of a solid-state electrolyte, viz., high mechanical

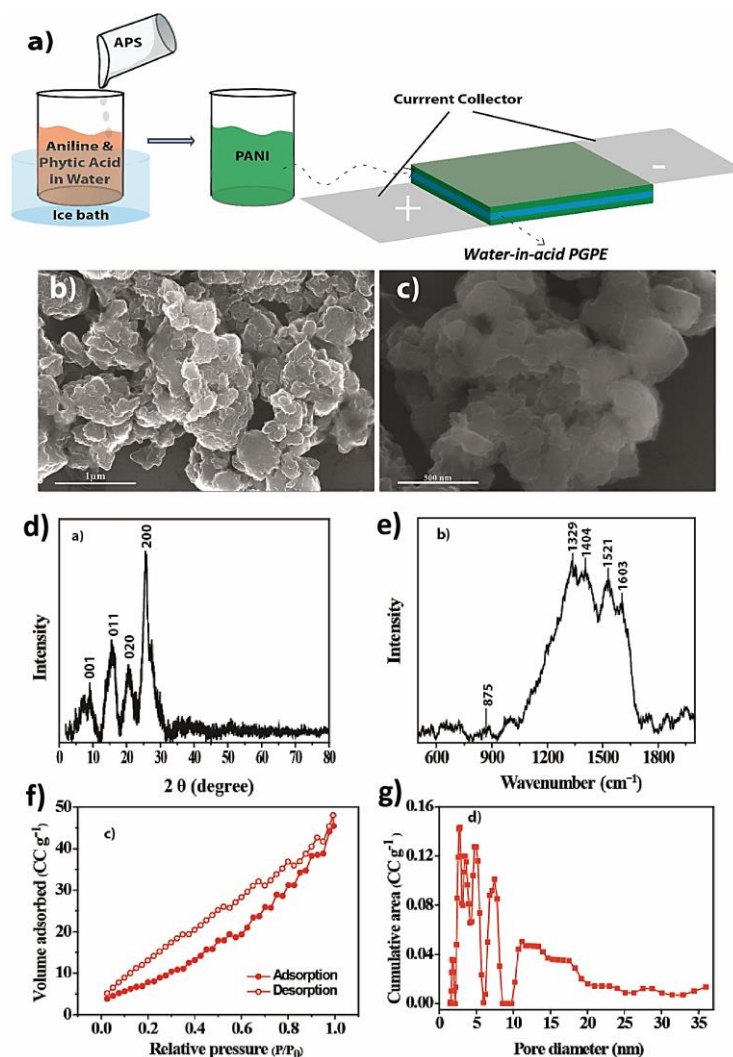


Figure 2.5. (a) Pictorial representation for the PANI synthesis and device fabrication and (b) and (c) represent the FESEM images of the synthesised PANI sample; physical characterisation of the PANI sample: (d) XRD profile, (e) Raman spectrum, (f) BET adsorption-desorption isotherms, and (g) pore-size distribution profile of the PANI sample. (Reprinted (adapted) with permission from (ACS Sustainable Chem. Eng. 2018, 6, 10, 12630-12640). Copyright (2018) American Chemical Society).

stability accompanied by high ionic conductivity. These features open up opportunities for this *water-in-acid* PGPE film to be used for the fabrication of flexible SC devices. The PGPE reported here is envisaged to be used along with many acid-stable electrode materials already reported in the literature. Here, the potential use of the PGPE as an efficient solid-state electrolyte in the PANI-based flexible SC is thoroughly studied. It is worth mentioning that the dearth of published studies on the PANI SCs based on H₃PO₄ electrolytes makes this work relevant.

The procedure adopted for the synthesis of PANI (see the **Experimental Section 2.2.4** for the detailed synthetic procedure) and the SC device fabrication strategy is

schematically represented in **Figure 2.5a**. The phytic acid-assisted synthesis of the crosslinked PANI has already been reported by several researchers.⁴⁶⁻⁴⁸ The as-synthesised PANI was washed with DI water followed by vacuum drying at 60°C for 1 h. The FESEM images of the PANI at different magnifications are presented in **Figure 2.5b** and **c**, respectively. The XRD and Raman spectra of the PANI are given in **Figure 2.5d** and **e**, respectively. The position of the peaks, which are labelled, confirms the formation of the highly conducting emeraldine form of the PANI.⁴⁹⁻⁵¹ From the BET analysis, surface area and pore size distribution are also determined. PANI has a surface area of about 48 m² g⁻¹ with the majority of the pore-size distribution arising from meso-pores. A small fraction of micro-pores is also present. The presence of meso-pores eases the electrolyte infiltration. It provides a buffer matrix to minimize the adverse effect of volume expansion during the redox process, which is expected to improve the cyclic stability of the final SC device. The plots of the adsorption-desorption isotherm and pore-size distribution are provided in **Figure 2.5f** and **g**, respectively.⁵² For fabricating the device, PANI was coated over 1 cm² area of the Grafoil[®] substrate followed by sandwiching the *water-in-acid* PGPE film (1.5 mm) between both the electrodes to make the SC device. **Figure 2.6a** and **b** show the digital images of the components and the final device, respectively. In the device, the PGPE plays the role of a separator as well.

Symmetrical SC devices with mass-loading of the active electrode material varying from 1 to 5 mg cm⁻² were fabricated by using the He-Ao-Ac-sw *water-in-acid* PGPE film as the solid-state electrolyte. The CV profiles and the constant CD profiles for freshly prepared devices at a scan rate of 10 mVs⁻¹ and current density of 0.25 mA cm⁻² are presented in **Figure 2.6c** and **d**, respectively. All the CV and CD profiles show the typical features of the PANI-based symmetrical SCs. From **Figure 2.6c**, it is observed that, as the PANI loading in the electrode increases, a corresponding increase in the total area traced by the CV plot follows. All the while, the discharge time (from CD, **Figure 2.6d**) is also enhanced with increase in the active-material loading. No significant voltage drop is observed in the CD profile of the SC device (**Figure 2.6d**) even with a high mass-loading of 5.0 mg cm⁻² on the electrode. These primary observations themselves indicate the high potential of the *water-in-acid* PGPE as an efficient mechanically stable GPE in solid-state SCs, with high as well as low mass-loading of the active electrode material.

The origin of the excellent charge storage characteristics as mentioned above can be identified through EIS studies. From the Nyquist plot presented in **Figure 2.6e**, the

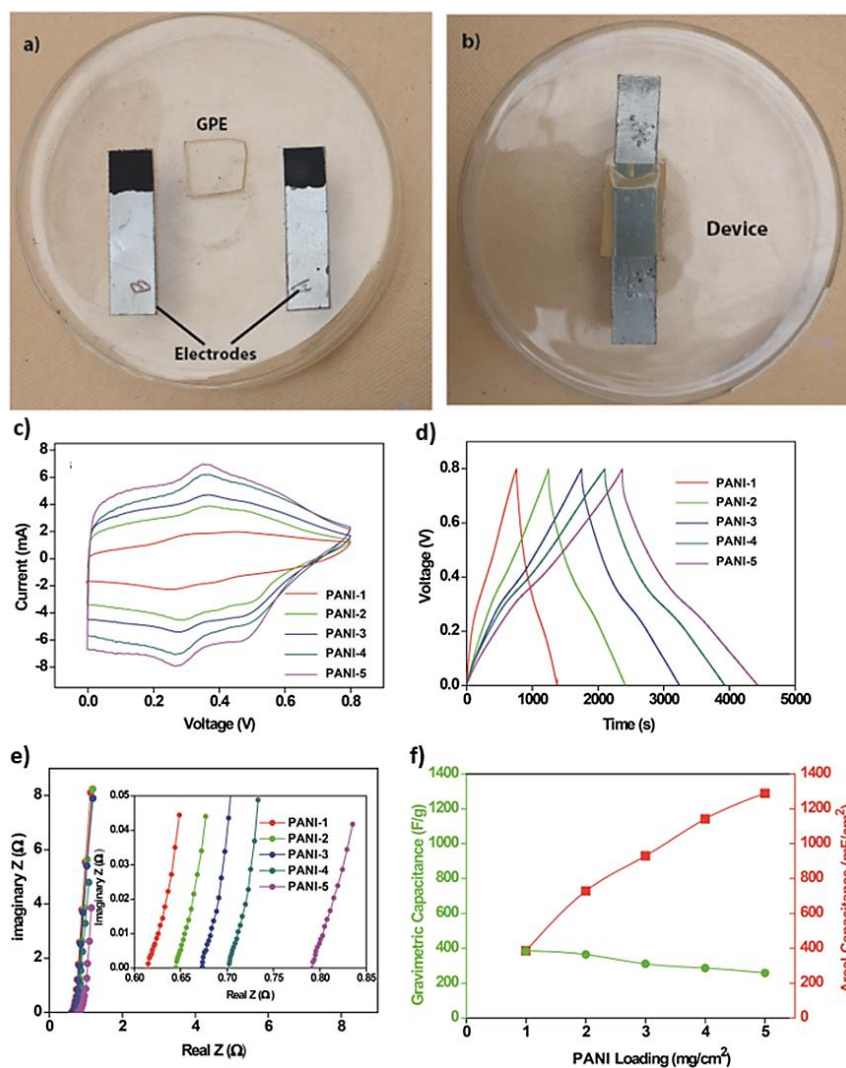


Figure 2.6. (a) The digital images of the various components viz., electrodes and the water-in-acid PGPE used for the SC device fabrication and (b) digital image of the final device; comparison of the electrochemical performance of the PANI-*x* devices: (c) the CV profiles recorded at a scan rate of 0.25 mA cm^{-2} , (d) the CD profiles recorded at a current density of 0.25 mA cm^{-2} , (e) the Nyquist plots, and (f) the plot summarizing the specific gravimetric and areal capacitance at a current density of 0.25 mA cm^{-2} for the PANI-1 to PANI-5 devices. (Reprinted (adapted) with permission from (ACS Sustainable Chem. Eng. 2018, 6, 10, 12630-12640). Copyright (2018) American Chemical Society).

ESR value for the PANI-1 device is as low as 0.61Ω . Even the PANI-5 device can retain a very low ESR value of 0.78Ω . These low ESR values are commendable as they directly indicate the ability of the solid-state GPE to establish an efficient electrode|electrolyte interface even with high mass-loading of the active electrode material. The very high ionic conductivity associated with the PGPE also favors the lowering of the ESR value, which in turn contributes to the high-power capability of the

SC devices. To get more insights into the electrochemical performance of the *water-in-acid* PGPE-based devices, the specific capacitance values, normalized for the single electrode, for each device is calculated from the CD profiles obtained at different current densities. The plot representing the variation of the specific gravimetric and areal capacitance at a current density of 0.25 mA cm^{-2} with respect to change in electrode mass-loading is represented in **Figure 2.6f**. From the plot (**Figure 2.6f**), the PANI-1 device is found to possess a high specific gravimetric capacitance value of 385 F g^{-1} . All the while, even at a high mass-loading of 5 mg cm^{-2} (PANI-5), a high capacitance value of about 258 F g^{-1} is retained (67% retention). The high capacitance retention even at high mass-loading of the active material makes the *water-in-acid* PGPE the main contender as a possible alternative to the GPE solutions.

The plots representing the change in gravimetric and areal capacitance values corresponding to the SC devices with mass-loading ranging from 1 to 5 mg cm^{-2} at various current densities are presented in **Figure 2.7a** and **b**, respectively. The PANI-1 device exhibits a capacitance retention of 45% (corresponding to 175 F g^{-1}) at a current density of 20 mA cm^{-2} compared to the value of 385 F g^{-1} obtained at 0.25 mA cm^{-2} . As the electrode mass-loading is increased, the capacitance retention at higher current densities is also found to be improved. Thus, the capacitance retentions corresponding to the PANI-2, 3, 4, and 5 devices at 20 mA cm^{-2} current density compared to that at 0.25 mA cm^{-2} are 54, 61, 62, and 64%, respectively. The high gravimetric capacitance retention at high loading and high current densities further consolidates the role of *water-in-acid* GPEs in the development of efficient and reliable SCs. The specific areal capacitance normalized for the single electrode for the PANI-1 device is found to be 385 mF cm^{-2} at a current density of 0.25 mA cm^{-2} . As the PANI mass-loading is increased, an obvious increment in the specific areal capacitance is observed. The PANI-5 SC device exhibits very high areal capacitance of about 1288 mF cm^{-2} and 771 mF cm^{-2} at lower and higher current densities of 0.25 and 20 mA cm^{-2} , respectively. Besides, the full CV and CD profiles for the devices (PANI-1 to 5) obtained at different scan rates and current densities are shown in **Figure 2.8a-j**.

Cycling stability and shelf-life are the two desirable features required by SCs from a commercial perspective. The PANI-5 device with *water-in-acid* PGPE is found to retain 100% of its initial capacitance even after 9000 continuous CD cycles recorded at a current density of 10 mA cm^{-2} (**Figure 2.9a**). To demonstrate the excellent shelf-life of the *water-in-acid* GPE-based device, the CD profile (at 0.25 mA cm^{-2}) for the

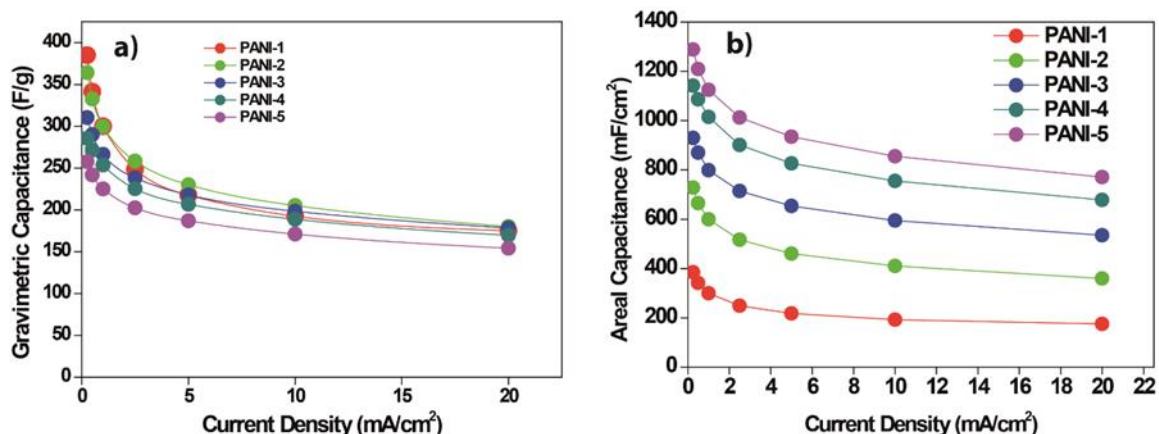


Figure 2.7. (a) The plots representing the specific gravimetric capacitance corresponding to the PANI-*x* SC devices at various scan rates; (b) the plot representing the specific areal capacitance corresponding to the PANI-*x* SC devices at various current densities. (Reprinted (adapted) with permission from *ACS Sustainable Chem. Eng.* 2018, 6, 10, 12630-12640). Copyright (2018) American Chemical Society).

freshly prepared PANI-5 device and the same device after aging for 25 days (represented as PANI-5-aged) are compared. The comparative plots are given in **Figure 2.9b**. It is observed that the specific capacitance value of the aged device (272 F g^{-1}) is almost equal to that of the fresh device (258 F g^{-1}). The slight increment in the capacitance value for the PANI-5-aged device is expected to be due to the improved contact between the electrode material and the PGPE. This is also reflected in the ESR value which is found to be slightly improved from 0.78 to 0.67Ω for the PANI-5 and PANI-5-aged, respectively (**Figure 2.9c**). The high shelf-life offered by the *water-in-acid* PGPE SC is thus validated from the above results.

Finally, the electrochemical performance of the PANI-5 device is compared with the *acid-in-water* and *water-in-acid* PVA- H_3PO_4 GPE solution-based devices represented as PANI-5-PVA-AIW and PANI-5-PVA-WIA, respectively. The CV of the devices recorded at a scan rate of 20 mV s^{-1} is given in **Figure 2.10a**. It is observed that the He-Ao-Ac-sw *water-in-acid* PGPE-based SC devices show superior current-voltage characteristics compared to the PVA-based (both *acid-in-water* and *water-in-acid*) devices. The superior current-voltage characteristic of the PANI-5 over the other two devices is attributed to the high H_3PO_4 content present in the He-Ao-Ac-sw *water-in-acid* GPE. The CD profile of the devices taken at a current density of 0.50 mA cm^{-2} is also shown in **Figure 2.10b**. The specific capacitances calculated from the CD profile are 242 F g^{-1} and 188 F g^{-1} for the PANI-5 and PANI-5-PVA-AIW devices, respectively.

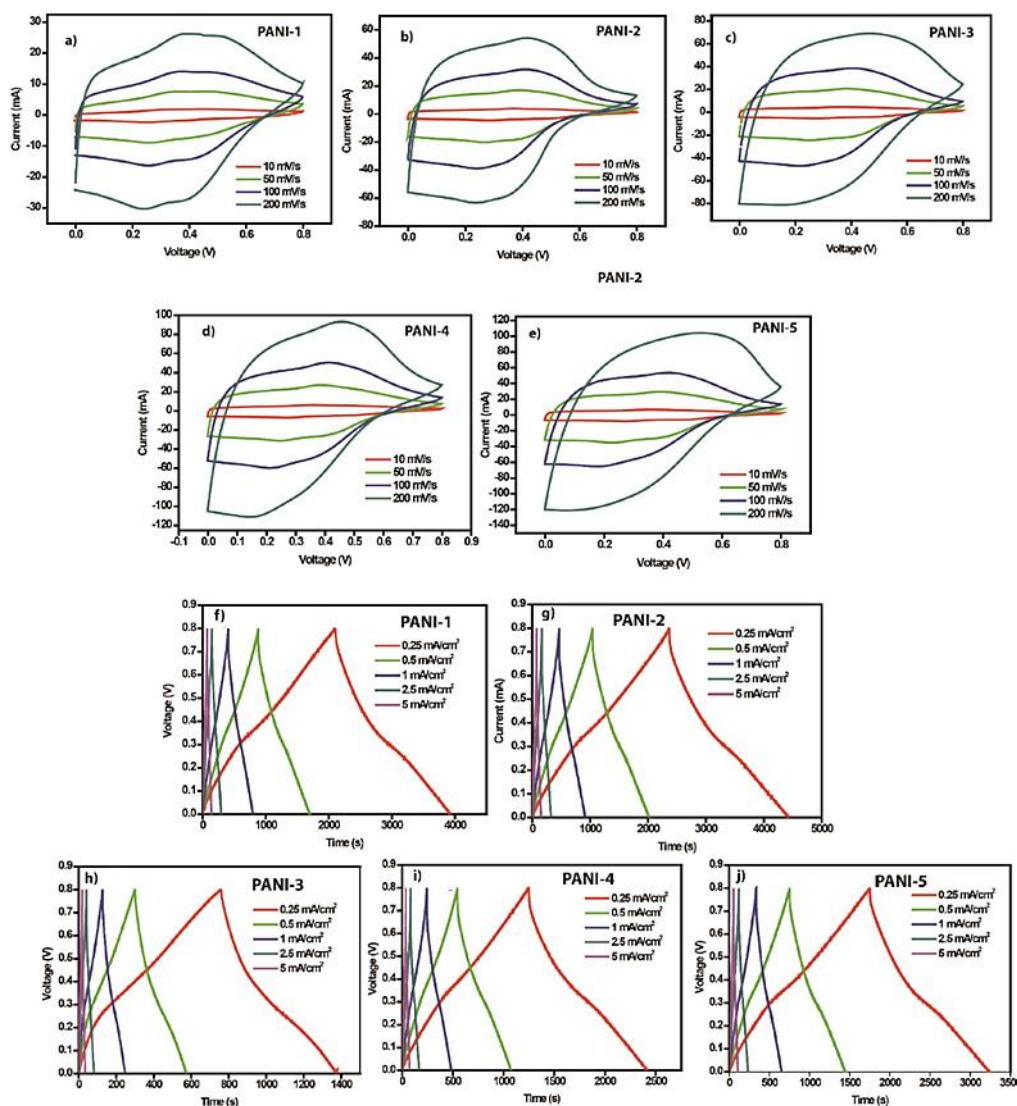


Figure 2.8 (a) to (e) The full CV profiles for the devices (PANI-1 to 5) recorded at various scan rates from 10 mVs^{-1} to 200 mVs^{-1} ; (f) to (j) the CD profiles for the devices (PANI-1 to 5) recorded at various current densities from 0.25 to 5 mA cm^{-2} . (Reprinted (adapted) with permission from (ACS Sustainable Chem. Eng. 2018, 6, 10, 12630-12640). Copyright (2018) American Chemical Society).

In the case of PANI-5-PVA-WIA device, the value is further reduced to 165 Fg^{-1} . Moreover, the voltage-drop associated with the PANI-5 device is found to be as low as 80 mV compared to the high voltage-drop of 170 mV and 200 mV associated with the PANI-5-PVA-AIW and PANI-5-PVA-WIA devices, respectively. This high voltage-drop is a direct indication of the low ionic conductivity as well as the inferior electrode|electrolyte interface formed in the case of the PVA electrolyte-based devices.³ The above experiments underline the inferior nature of the conventional PVA-based *acid-in-water* GPEs and the inability of the PVA matrix to result in efficient *water-*

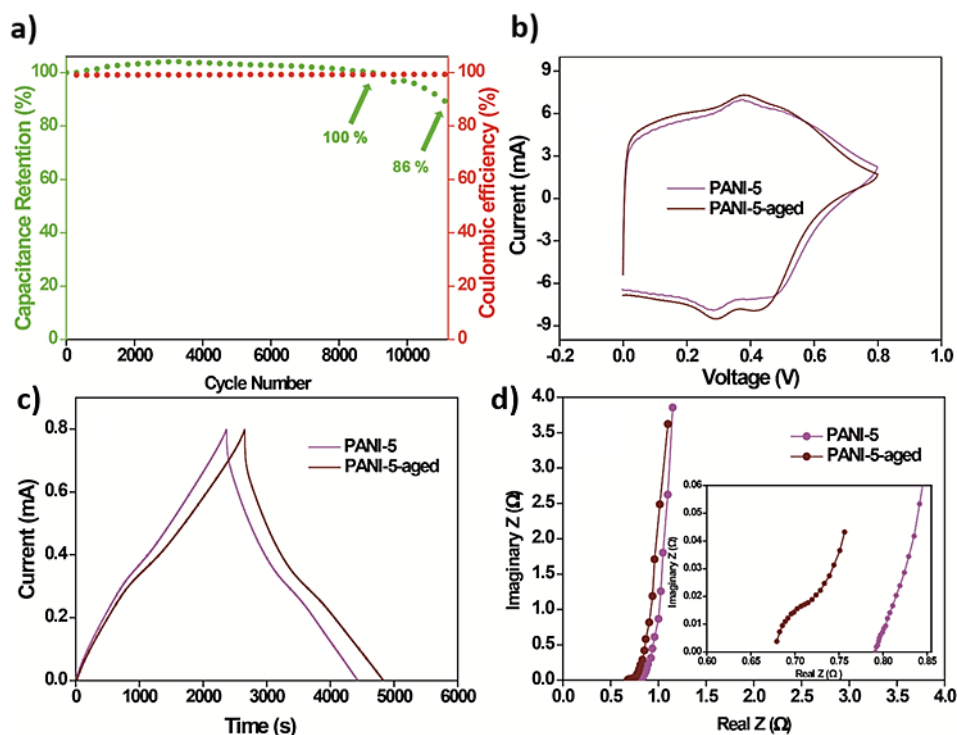


Figure 2.9. (a) Cycling stability of the PANI-5 device recorded at a current density of 10 mA cm^{-2} ; (b) the CV profile recorded at a scan rate of 10 mV s^{-1} ; (c) the CD profile recorded at a current density of 0.25 mA cm^{-2} ; (d) the Nyquist plots corresponding to the freshly prepared PANI-5 device and the same device aged for 25-days (PANI-5-aged); the inset of Figure 6d shows the zoomed high-frequency region of the Nyquist plots. (Reprinted (adapted) with permission from (ACS Sustainable Chem. Eng. 2018, 6, 10, 12630-12640). Copyright (2018) American Chemical Society).

in-acid GPE. The cyclic stability of the PANI-5-PVA-AIW device recorded at a current density of 10 mA cm^{-2} is shown in **Figure 2.10c** and is found to be far inferior to that of PANI-5 device (**Figure 2.10a**). While the PANI-5 device retains 100% of its initial capacitance for up to 9000 continuous CD cycles, the specific capacitance of PANI-5-PVA-AIW device drops to 60% even before reaching 9000 cycles. In **Figure 2.10d**, the cycling stability of the PANI-5-PVA-WIA is also displayed.

Among all the three devices under the study, *viz.*, PANI-5, PANI-5-PVA-WIA, and PANI-5-PVA-AIW, the conventional *acid-in-water* GPE-based SC device (PANI-5-PVA-AIW) exhibit the lowest cycling stability. Apart from the volume changes occurring in PANI during the redox reactions, the hydrolytic degradation of PANI by solvent (water) molecules is also known to derail the cycling stability of the PANI-based SC devices.⁵³⁻⁵⁶ Here, in both the *acid-in-water* and *water-in-acid* GPE-based SC devices, the volume change during the redox process will be low owing to the

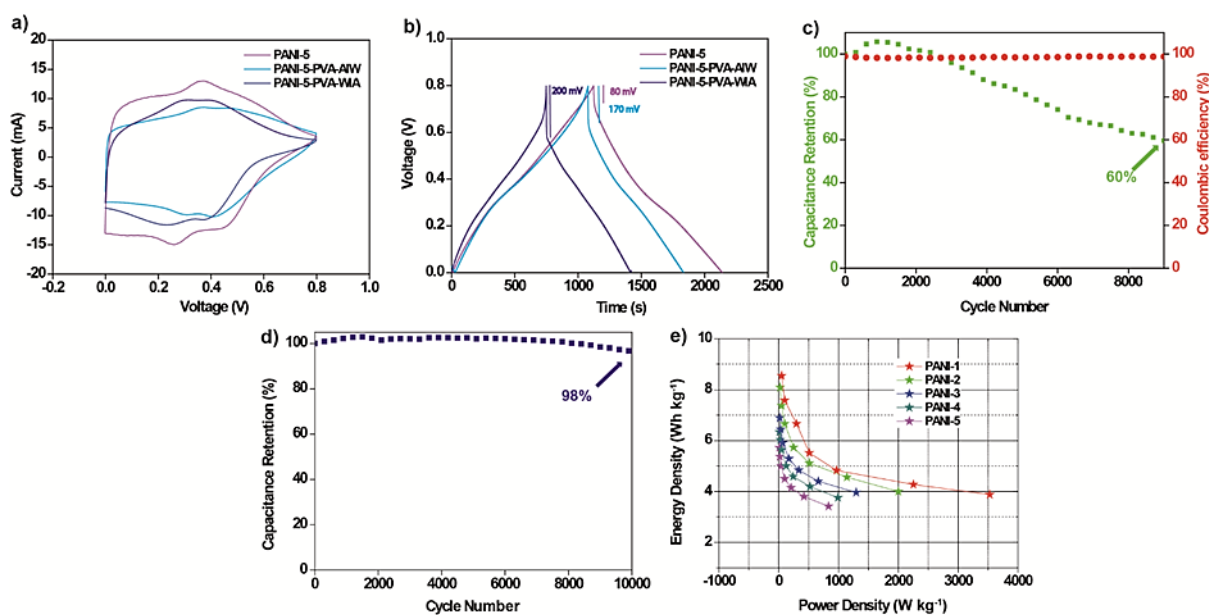


Figure 2.10. Comparative CV (a) and CD (b) are the plots recorded at a scan rate of 20 mV s^{-1} and a current density of 0.5 mA cm^{-2} for the PANI-5, PANI-5-PVA-AIW, and PANI-5-PVA-WIA devices, respectively; (c) cycling stability of the PANI-5-PVA-AIW device recorded at a current density of 10 mA cm^{-2} ; (d) cycling stability of the PANI-5-PVA-WIA device recorded at a current density of 10 mA cm^{-2} ; (e) Ragone plots representing the gravimetric energy and power density of all the PANI-*x* devices under study. (Reprinted (adapted) with permission from (ACS Sustainable Chem. Eng. 2018, 6, 10, 12630-12640). Copyright (2018) American Chemical Society).

mesoporous structure of PANI (**Figure 2.5g**). The high stability of the *water-in-acid* GPE-based device compared to its *acid-in-water* counterpart may be attributed to the very low amount of water content present in such electrolytes. Owing to this, the hydrolytic degradation of PANI by the water molecules will be minimum in the case of the PANI-5 device which leads to its outstanding cycling stability. In the case of PANI-5-PVA-WIA, despite its low capacitance value compared to the PANI-5-PVA-AIW, the low water content still facilitates high stability (**Figure 2.10d**).

A Ragone plot representing the gravimetric energy and power densities of all the PANI-*x* devices is shown in **Figure 2.10e**. The PANI-1 device exhibits the highest energy density of 8.55 Wh kg^{-1} with a power density of 50 W kg^{-1} . The highest power density exhibited by the same device is 3527 W kg^{-1} at an energy density of 3.9 Wh kg^{-1} . In the case of the PANI-5 device, the highest energy density (5.72 Wh kg^{-1}) is obtained at a power density of 10.54 W kg^{-1} whereas the highest power density of 834 W kg^{-1} is exhibited at an energy density of 3.42 Wh kg^{-1} . A table summarising the electrochemical

performance of the previously reported H_3PO_4 electrolyte-based PANI SCs is also given in **Table 2.2**.⁵⁷⁻⁶¹

Table 2.2. A table summarising the electrochemical performance of the previously reported H_3PO_4 electrolyte-based PANI SCs (some other electrode/electrolyte based SCs are also mentioned) compared to the water-in-acid GPE-based SC reported in this work. (Reprinted (adapted) with permission from (ACS Sustainable Chem. Eng. 2018, 6, 10, 12630-12640). Copyright (2018) American Chemical Society).

Electrolyte used	Details of Device Fabrication	ESR	Specific Capacitance	Cyclic stability	Ref.
PVA- H_3PO_4	Polypyrrole as electrode material and GPE solution	9.9 to 16.5 Ω	84 to 93 $F g^{-1}$ at 0.5 $A g^{-1}$	74 to 84 % capacitance retention after 2000 cycles at 0.5 $A g^{-1}$	41
PVA- H_3PO_4	Neat PANI as electrode material and GPE solution	> 1.5 Ω	293 $F g^{-1}$ at 0.5 $A g^{-1}$	60 % retention after 1000 cycles at 1 Ag^{-1}	57
PVA- H_3PO_4	Screen-printed MnO_2 electrode and GPE solution	-	-	80% capacitance retention after 1000 cycles at 50 $\mu A cm^{-2}$	58
PVA- H_3PO_4	PANI-MWCNT thin film and GPE solution		7.8 $mF cm^{-2}$ at 0.5 mA current.	91 % retention of specific capacitance after 1000 cycles	59
PVA- H_3PO_4	MnO_2 /PANI coaxial nanowires, GPE solution electrode mass loading of 8.5 $mg cm^{-2}$ loading	2.9 Ω	346 $mF cm^{-2}$ at 5 $mV s^{-1}$	Almost 100% retention after 1000 cycles at 1.5 $mA cm^{-2}$ current density	60
PVA- H_2SO_4	cellulose nanofibers-PANI electrode, GPE solution	ca. 1.9 Ω	406.8 $F g^{-1}$ at 1 $A g^{-1}$	80% capacitance retention after 1000 cycles	61
P(HEMA-co-AOETMA)+ H_3PO_4	PANI electrodes sandwiched in between the water-in-acid PGPE. PANI mass loading from 1 to 5 $mg cm^{-2}$	0.61 to 0.78 Ω	385 and 285 Fg^{-1} for PANI-1 and PANI-5, respectively at 0.25 Ag^{-1}	100% capacitance retention after 9000 continuous charge discharge cycles at 10 $mA cm^{-2}$	This work

Finally, to demonstrate the potential of the water-in-acid He-Ao-Ac-sw PGPE in flexible SC devices, the PANI-2 device dimension is scaled up (electrode dimension: 5 cm (length) \times 1 cm (width)) and the electrochemical performance at linear (PANI-2-Linear) and bent (PANI-2-Bent) conditions are compared (**Figure 2.11a-c**). The specific areal capacitance values corresponding to the linear and bent devices calculated from

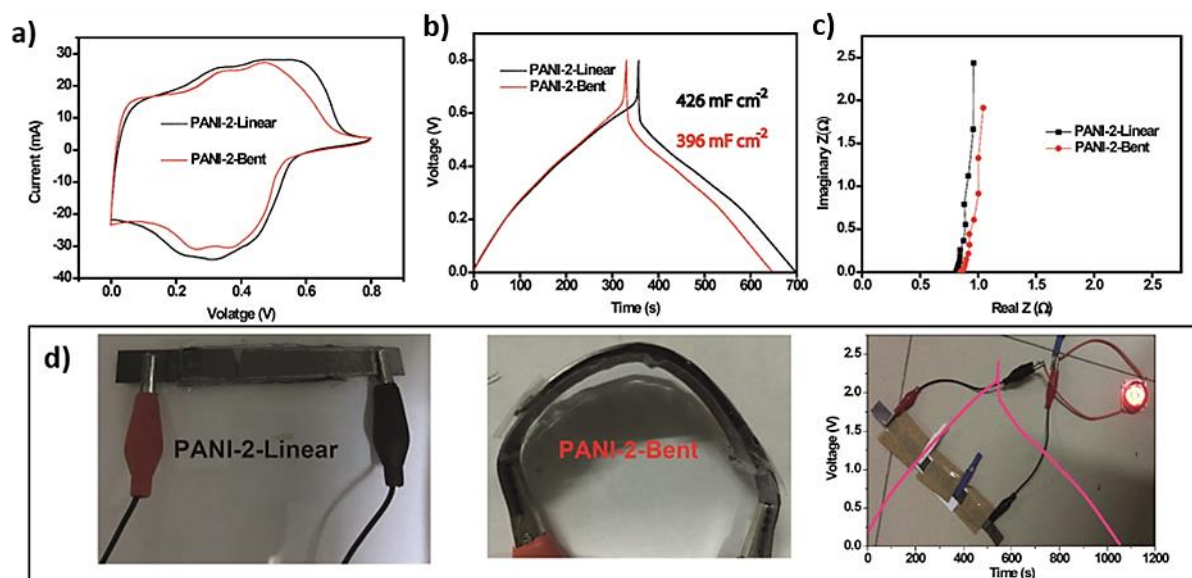


Figure 2.11. Comparative CV (a) and CD (b) plots recorded at a scan rate of 20 mV s^{-1} and a current density of 0.50 mA cm^{-2} for the SC device at Linear and Bent states, respectively; (c) the Nyquist plots corresponding to the PANI-2-Linear and PANI-2-Bent devices; (d) digital images of the PANI-2-Linear and PANI-2-Bent devices along with the real-life demonstration of lighting LED by a 2.4 V power-source (three 0.8 V SC devices connected in series.). (Reprinted (adapted) with permission from (ACS Sustainable Chem. Eng. 2018, 6, 10, 12630-12640). Copyright (2018) American Chemical Society).

the CD-profiles obtained at a current density of 0.50 mA cm^{-2} are 426 and 396 mF cm^{-2} , respectively (**Figure 2.11b**). The obtained very low ESR value of around 0.8Ω with both the bent and linear devices further confirm the retention of good electrode|electrolyte interface even under flexible conditions. The real-life demonstration of the SC device is demonstrated by lighting a LED by a 2.4 V power source (three 0.8 V SC devices connected in series). The digital images of the demonstration along with the PANI-2-Linear and PANI-2-Bent devices are given in **Figure 2.11d**. All the above results point towards the feasibility of replacing the conventional *acid-in-water* GPEs by the *water-in-acid* self-standing PGPEs to realize better-performing flexible SC devices with high cycling stability as well as improved shelf-life.

2.4 Conclusion

In summary, the concept of *water-in-acid* PGPE has been successfully demonstrated to be used in SCs. The simple and scalable synthesis of the novel-polymer matrix which can be used for the PANI-based SCs is being reported for the first time.

The polyelectrolyte nature of the copolymer matrix P(HEMA-co-AOETMA) along with the non-covalent interactions induced by the functional groups account for the high H₃PO₄ intake capability of the *water-in-acid* PGPE (He-Ao-Ac-sw). These interactions augment the overall mechanical as well as the thermal stability of the specimens as evidenced by the results of the ATR-FTIR and TGA studies. It is concluded that hydrogen bonding plays a major role in the retention of H₃PO₄ in the polymer matrix without compromising its self-standing structure. The excellent proton conductivity and the self-standing nature of the GPE make it a suitable candidate for being the solid-state electrolyte in SCs. When used in the PANI-based SCs, the *water-in-acid* PGPE is found to outperform the conventional PVA-H₃PO₄ GPE solutions. The PANI-1 (device with 1 mg cm⁻² active material mass-loading) device exhibits a high gravimetric specific capacitance value of 385 F g⁻¹ at a current density of 0.25 mA cm⁻². At the same current density, the high mass-loaded device (PANI-5, mass-loading of 5 mg cm⁻²) exhibits gravimetric and areal capacitance values of 257 F g⁻¹ and 1288 mF cm⁻², respectively. The high cycling stability (100 % capacitance retention even after 9000 continuous CD cycles) and shelf-life (stable performance even after aging for 25 days) of the *water-in-acid* GPE-based device (PANI-5) is commendable whereas the PVA-H₃PO₄-based device (PANI-5-PVA-AIW) shows inferior cycling stability (60% capacitance retention after 8000 CD cycles). Based on the above-mentioned results, it is envisaged that the concept of *water-in-acid* PGPEs is extended to other acid-stable electrode materials and used as an alternative to conventional GPE solutions.

2.5 References

- [1] Béguin, F.; Presser, V.; Balducci, A.; Frackowiak, E., Carbons and Electrolytes for Advanced Supercapacitors. *Advanced Materials* **2014**, *26* (14), 2219-2251.
- [2] Zhong, C.; Deng, Y.; Hu, W.; Qiao, J.; Zhang, L.; Zhang, J., A review of electrolyte materials and compositions for electrochemical supercapacitors. *Chemical Society Reviews* **2015**, *44* (21).
- [3] Anothumakkool, B.; Torris A. T, A.; Veeliyath, S.; Vijayakumar, V.; Badiger, M. V.; Kurungot, S., High-Performance Flexible Solid-State Supercapacitor with an Extended Nanoregime Interface through in Situ Polymer Electrolyte Generation. *ACS Applied Materials & Interfaces* **2016**, *8* (2), 1233-1241.
- [4] Peng, X.; Liu, H.; Yin, Q.; Wu, J.; Chen, P.; Zhang, G.; Liu, G.; Wu, C.; Xie, Y., A zwitterionic gel electrolyte for efficient solid-state supercapacitors. *Nature communications* **2016**, *7*, 11782-11789.

- [5] Łatoszyńska, A. A.; Żukowska, G. Z.; Rutkowska, I. A.; Taberna, P.-L.; Simon, P.; Kulesza, P. J.; Wieczorek, W., Non-aqueous gel polymer electrolyte with phosphoric acid ester and its application for quasi solid-state supercapacitors. *Journal of Power Sources* **2015**, *274*, 1147-1154.
- [6] Sampath, S.; Choudhury, N.; Shukla, A., Hydrogel membrane electrolyte for electrochemical capacitors. *Journal of Chemical Sciences* **2009**, *121* (5).
- [7] Vijayakumar, V.; Anothumakkool, B.; Torris A. T, A.; Nair, S. B.; Badiger, M. V.; Kurungot, S., An all-solid-state-supercapacitor possessing a non-aqueous gel polymer electrolyte prepared using a UV-assisted in situ polymerization strategy. *Journal of Materials Chemistry A* **2017**.
- [8] Gao, H.; Lian, K., Proton-conducting polymer electrolytes and their applications in solid supercapacitors: a review. *RSC Advances* **2014**, *4* (62).
- [9] Wada, H.; Yoshikawa, K.; Nohara, S.; Furukawa, N.; Inoue, H.; Sugoh, N.; Iwasaki, H.; Iwakura, C., Electrochemical characteristics of new electric double layer capacitor with acidic polymer hydrogel electrolyte. *Journal of Power Sources* **2006**, *159* (2), 1464-1467.
- [10] Kalupson, J.; Ma, D.; Randall, C. A.; Rajagopalan, R.; Adu, K., Ultrahigh-Power Flexible Electrochemical Capacitors Using Binder-Free Single-Walled Carbon Nanotube Electrodes and Hydrogel Membranes. *The Journal of Physical Chemistry C* **2014**, *118* (6).
- [11] Yamazaki, S.; Takegawa, A.; Kaneko, Y.; Kadokawa, J.-i.; Yamagata, M.; Ishikawa, M., An acidic cellulose–chitin hybrid gel as novel electrolyte for an electric double layer capacitor. *Electrochemistry Communications* **2009**, *11* (1), 68-70.
- [12] Vilčiauskas, L.; Tuckerman, M. E.; Bester, G.; Paddison, S. J.; Kreuer, K.-D., The mechanism of proton conduction in phosphoric acid. *Nat Chem* **2012**, *4* (6), 461-466.
- [13] Wang, Y.; Lane, N. A.; Sun, C.-N.; Fan, F.; Zawodzinski, T. A.; Sokolov, A. P., Ionic Conductivity and Glass Transition of Phosphoric Acids. *The Journal of Physical Chemistry B* **2013**, *117* (26), 8003-8009.
- [14] Krueger, R. A.; Vilčiauskas, L.; Melchior, J.-P.; Bester, G.; Kreuer, K.-D., Mechanism of Efficient Proton Conduction in Diphosphoric Acid Elucidated via First-Principles Simulation and NMR. *The Journal of Physical Chemistry B* **2015**, *119* (52), 15866-15875.

- [15] Melchior, J.-P.; Kreuer, K.-D.; Maier, J., Proton conduction mechanisms in the phosphoric acid-water system ($\text{H}_4\text{P}_2\text{O}_7\text{-H}_3\text{PO}_4\cdot 2\text{H}_2\text{O}$): a ^1H , ^{31}P and ^{17}O PFG-NMR and conductivity study. *Physical Chemistry Chemical Physics* **2017**, *19* (1), 587-600.
- [16] Chin, D.-T.; Chang, H. H., On the conductivity of phosphoric acid electrolyte. *Journal of Applied Electrochemistry* **1989**, *19* (1), 95-99.
- [17] Chung, S. H.; Bajue, S.; Greenbaum, S. G., Mass transport of phosphoric acid in water: A ^1H and ^{31}P pulsed gradient spin-echo nuclear magnetic resonance study. *The Journal of Chemical Physics* **2000**, *112* (19), 8515-8521.
- [18] Aili, D.; Cleemann, L. N.; Li, Q.; Jensen, J. O.; Christensen, E.; Bjerrum, N. J., Thermal curing of PBI membranes for high temperature PEM fuel cells. *Journal of Materials Chemistry* **2012**, *22* (12), 5444-5453.
- [19] Kongstein, O. E.; Berning, T.; Børresen, B.; Seland, F.; Tunold, R., Polymer electrolyte fuel cells based on phosphoric acid doped polybenzimidazole (PBI) membranes. *Energy* **2007**, *32* (4), 418-422.
- [20] Nair, J. R.; Gerbaldi, C.; Meligrana, G.; Bongiovanni, R.; Bodoardo, S.; Penazzi, N.; P.Reale; Gentili, V., UV-cured methacrylic membranes as novel gel-polymer electrolyte for Li-ion batteries. *Journal of Power Sources* **2008**, *178* (2), 751-757.
- [21] La Gatta, A.; Schiraldi, C.; Esposito, A.; D'Agostino, A.; De Rosa, A. Novel Poly(HEMA-Co-METAC)/Alginate Semi-Interpenetrating Hydrogels For Biomedical Applications: Synthesis And Characterization. *Journal of Biomedical Materials Research Part A* **2009**, *90A*, 292-302.
- [22] Goel, N.; Kumar, V.; Bhardwaj, Y.; Chaudhari, C.; Dubey, K.; Sabharwal, S. Swelling Response Of Radiation Synthesized 2-Hydroxyethylmethacrylate-Co-[2-(Methacryloyloxy)Ethyl] Trimethylammonium Chloride Hydrogels Under Various In Vitro Conditions. *Journal of Biomaterials Science, Polymer Edition* **2009**, *20*, 785-805.
- [23] Divakaran, A. V.; Azad, L. B.; Surwase, S. S.; Torris A. T, A.; Badiger, M. V., Mechanically Tunable Curcumin Incorporated Polyurethane Hydrogels as Potential Biomaterials. *Chemistry of Materials* **2016**, *28* (7), 2120-2130.
- [24] Rumyantsev, A. M.; Pan, A.; Ghosh Roy, S.; De, P.; Kramarenko, E. Y., Polyelectrolyte Gel Swelling and Conductivity vs. Counterion Type, Cross-Linking Density, and Solvent Polarity. *Macromolecules* **2016**, *49* (17), 6630-6643.
- [25] Shukla, N. B.; Rattan, S.; Madras, G., Swelling and Dye-Adsorption Characteristics of an Amphoteric Superabsorbent Polymer. *Industrial & Engineering Chemistry Research* **2012**, *51* (46), 14941-14948.

- [26] Suo, L.; Hu, Y.-S.; Li, H.; Armand, M.; Chen, L., A new class of solvent-in-salt electrolyte for high-energy rechargeable metallic lithium batteries. *Nature communications* **2013**, *4*, 1481-1489.
- [27] Suo, L.; Borodin, O.; Sun, W.; Fan, X.; Yang, C.; Wang, F.; Gao, T.; Ma, Z.; Schroeder, M.; von Cresce, A.; Russell, S. M.; Armand, M.; Angell, A.; Xu, K.; Wang, C., Advanced High-Voltage Aqueous Lithium-Ion Battery Enabled by “Water-in-Bisalt” Electrolyte. *Angewandte Chemie International Edition* **2016**, *55* (25), 7136-7141.
- [28] Kufian, M. Z.; Majid, S. R.; Arof, A. K., Dielectric and conduction mechanism studies of PVA-orthophosphoric acid polymer electrolyte. *Ionics* **2007**, *13* (4), 231-234.
- [29] Vieira, M. G. A.; da Silva, M. A.; dos Santos, L. O.; Beppu, M. M., Natural-based plasticizers and biopolymer films: A review. *European Polymer Journal* **2011**, *47* (3), 254-263.
- [30] Lee, K.-S.; Spendelow, J. S.; Choe, Y.-K.; Fujimoto, C.; Kim, Y. S., An operationally flexible fuel cell based on quaternary ammonium-biphosphate ion pairs. *Nature Energy* **2016**, *1*, 16120-16126.
- [31] Woods, A. S.; Moyer, S. C.; Jackson, S. N., Amazing Stability of Phosphate-Quaternary Amine Interactions. *Journal of proteome research* **2008**, *7* (8), 3423-3427.
- [32] Tang, Q.; Qian, G.; Huang, K. Hydrophobic Hydrogel Caged H₃PO₄ As A New Class Of High-Temperature Proton Exchange Membranes With Enhanced Acid Retention. *RSC Advances* **2013**, *3*, 3520-3525.
- [33] Bouchoux, G. Gas-Phase Basicities Of Polyfunctional Molecules. Part 4: Carbonyl Groups As Basic Sites. *Mass Spectrometry Reviews* **2014**, *34*, 493-534.
- [34] Sinirlioglu, D.; Çelik, S.; Muftuoglu, A.; Bozkurt, A. Novel Composite Polymer Electrolyte Membranes Based On Poly(Vinyl Phosphonic Acid) And Poly (5-(Methacrylamido)Tetrazole). *Polymer Engineering & Science* **2014**, *55*, 260-269.
- [35] Tang, Q.; Yuan, S.; Cai, H. High-temperature proton exchange membranes from microporous polyacrylamide caged phosphoric acid. *J. Mater. Chem. A* **2013**, *1*, 630-636.
- [36] Rathod, D.; Vijay, M.; Islam, N.; Kannan, R.; Kharul, U.; Kurungot, S.; Pillai, V., Design of an “all solid-state” supercapacitor based on phosphoric acid doped polybenzimidazole (PBI) electrolyte. *Journal of Applied Electrochemistry* **2009**, *39* (7), 1097-1103.

- [37] Chai, M. N.; Isa, M. I. N., Novel Proton Conducting Solid Bio-polymer Electrolytes Based on Carboxymethyl Cellulose Doped with Oleic Acid and Plasticized with Glycerol. *Scientific Reports* **2016**, *6*, 27328-27334.
- [38] Sudhakar, Y.N.; Selvakumar, M.; Bhat, D. K., Effect of acid dopants in biodegradable gel polymer electrolyte and the performance in an electrochemical double layer capacitor. *Physica Scripta* **2015**, *90* (9), 095702-095712.
- [39] Sudhakar, Y. N.; Selvakumar, M.; Bhat, D. K., Preparation and characterization of phosphoric acid-doped hydroxyethyl cellulose electrolyte for use in supercapacitor. *Materials for Renewable and Sustainable Energy* **2015**, *4* (3), 10-18.
- [40] Sa'adu, L.; Hashim, M.; Baharuddin, M. B., Conductivity Studies and Characterizations of PVA-Orthophosphoric Electrolytes. *Journal of Materials Science Research* **2014**, *3* (3), 48-58.
- [41] Zhao, C.; Wang, C.; Yue, Z.; Shu, K.; Wallace, G. G., Intrinsically Stretchable Supercapacitors Composed of Polypyrrole Electrodes and Highly Stretchable Gel Electrolyte. *ACS Applied Materials & Interfaces* **2013**, *5* (18), 9008-9014.
- [42] Vijaya, N.; Selvasekarapandian, S.; Karthikeyan, S.; Prabu, M.; Rajeswari, N.; Sanjeeviraja, C., Synthesis and Characterization of Proton Conducting Polymer Electrolyte Based on Poly(N-vinyl pyrrolidone). *Journal of Applied Polymer Science* **2012**, *127*, 1538-1543.
- [43] Kumar, R.; Sharma, S.; Pathak, D.; Dhiman, N.; Arora, N., Ionic conductivity, FTIR and thermal studies of nano-composite plasticized proton conducting polymer electrolytes. *Solid State Ionics* **2017**, *305*, 57-62.
- [44] Sellam; Hashmi, S. A., Quasi-solid-state pseudocapacitors using proton-conducting gel polymer electrolyte and poly(3-methyl thiophene)-ruthenium oxide composite electrodes. *Journal of Solid State Electrochemistry* **2014**, *18* (2), 465-475.
- [45] Kreuer, K.-D., Proton Conductivity: Materials and Applications. *Chemistry of Materials* **1996**, *8* (3), 610-641.
- [46] Pan, L.; Yu, G.; Zhai, D.; Lee, H. R.; Zhao, W.; Liu, N.; Wang, H.; Tee, B. C.-K.; Shi, Y.; Cui, Y., Hierarchical nanostructured conducting polymer hydrogel with high electrochemical activity. *Proceedings of the National Academy of Sciences* **2012**, *109* (24), 9287-9292.
- [47] Sekar, P.; Anothumakkool, B.; Vijayakumar, V.; Lohgaonkar, A.; Kurungot, S., Unravelling the Mechanism of Electrochemical Degradation of PANI in

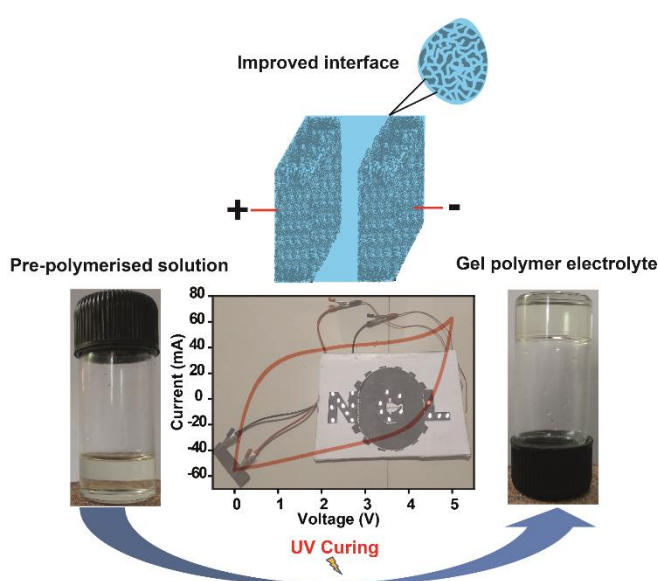
- Supercapacitors: Achieving a Feasible Solution. *ChemElectroChem* **2016**, 3 (6), 933-942.
- [48] Xu, G.; Ding, B.; Pan, J.; Han, J.; Nie, P.; Zhu, Y.; Sheng, Q.; Dou, H., Porous nitrogen and phosphorus co-doped carbon nanofiber networks for high performance electrical double layer capacitors. *Journal of Materials Chemistry A* **2015**, 3 (46), 23268-23273.
- [49] Lin, W.; Xu, K.; Xin, M.; Peng, J.; Xing, Y.; Chen, M., Hierarchical porous polyaniline-silsesquioxane conjugated hybrids with enhanced electrochemical capacitance. *RSC Advances* **2014**, 4 (74), 39508-39518.
- [50] Rajagopalan, B.; Hur, S. H.; Chung, J. S., Surfactant-treated graphene covered polyaniline nanowires for supercapacitor electrode. *Nanoscale Research Letters* **2015**, 10, 183-191.
- [51] Shakoor, A.; Rizvi, T. Z.; Nawaz, A., Raman spectroscopy and AC conductivity of polyaniline montmorillonite (PANI–MMT) nanocomposites. *Journal of Materials Science: Materials in Electronics* **2011**, 22 (8), 1076-1080.
- [52] Thommes, M.; Kaneko, K.; Neimark, A. V.; Olivier, J. P.; Rodriguez-Reinoso, F.; Rouquerol, J.; Sing, K. S., Physisorption Of Gases, With Special Reference To The Evaluation Of Surface Area And Pore Size Distribution. *Pure Appl. Chem* **2015**, 87(9-10), 1051–1069.
- [53] Xing, J.; Liao, M.; Zhang, C.; Yin, M.; Li, D.; Song, Y. The Effect Of Anions On The Electrochemical Properties Of Polyaniline For Supercapacitors. *Physical Chemistry Chemical Physics* **2017**, 19, 14030-14041.
- [54] Deng, J.; Wang, T.; Guo, J.; Liu, P. Electrochemical Capacity Fading Of Polyaniline Electrode In Supercapacitor: An XPS Analysis. *Progress in Natural Science: Materials International* **2017**, 27, 257-260.
- [55] Chen, W.; Wen, T.; Gopalan, A. Negative Capacitance For Polyaniline: An Analysis Via Electrochemical Impedance Spectroscopy. *Synthetic Metals* **2002**, 128, 179-189.
- [56] Snook, G.; Kao, P.; Best, A. Conducting-Polymer-Based Supercapacitor Devices And Electrodes. *Journal of Power Sources* **2011**, 196, 1-12.
- [57] Liu, M.; Miao, Y.-E.; Zhang, C.; Tjiu, W. W.; Yang, Z.; Peng, H.; Liu, T., Hierarchical composites of polyaniline–graphene nanoribbons–carbon nanotubes as electrode materials in all-solid-state supercapacitors. *Nanoscale* **2013**, 5 (16), 7312-7320.
- [58] Wang, Y.; Shi, Y.; Zhao, C. X.; Wong, J. I.; Sun, X. W.; Yang, H. Y., Printed all-solid flexible microsupercapacitors: towards the general route for high energy storage devices. *Nanotechnology* **2014**, 25 (9), 094010-094017.

-
- [59] Khalid, M.; Tumelero, M. A.; Pasa, A. A., Asymmetric and symmetric solid-state supercapacitors based on 3D interconnected polyaniline–carbon nanotube framework. *RSC Advances* **2015**, *5* (76), 62033-62039.
- [60] Zhou, J.; Yu, L.; Liu, W.; Zhang, X.; Mu, W.; Du, X.; Zhang, Z.; Deng, Y., High performance all-solid supercapacitors based on the network of ultralong manganese dioxide/polyaniline coaxial nanowires. *Scientific reports* **2015**, *5*, 17858-17866.
- [61] Zheng, W.; Lv, R.; Na, B.; Liu, H.; Jin, T.-X.; Yuan, D., Nanocellulose-mediated hybrid polyaniline electrodes for high performance flexible supercapacitors. *Journal of Materials Chemistry A* **2017**, *5*(25), 12969-1297

Chapter 3

A High-Voltage Supercapacitor Possessing Nonaqueous Gel Polymer Electrolyte Prepared Using the *In Situ* Polymerization Process

In this work, a mechanically stable nonaqueous gel polymer electrolyte (GPE) is prepared by using ultraviolet (UV)-light induced photopolymerization. The GPE composed of the liquid electrolyte (LiClO_4 /propylene carbonate), which is entrapped in a poly(2-hydroxy-3-phenoxypropyl acrylate) matrix, is used for the fabrication of high-voltage supercapacitors by the *in situ* polymerization process. The *in situ* process ensures an electrode|electrolyte interface extended to the inner and outer surface area of the electrode material. The SC devices are operable in the voltage window of 2.0 V with a high active material (activated carbon (AC), YP-80F, a high surface area porous carbon) mass-loading of 3.8 mg cm^{-2} . The SC device shows an equivalent series resistance (ESR) as low as 2.2Ω , which is close to that of the device fabricated from the corresponding liquid electrolyte and is far better than that of the conventional polymer electrolyte (PE) films. The scalability of the process is demonstrated by fabricating a large area (area of 16 cm^2 and loading of 4.0 mg cm^{-2}) solid-state-flexible-supercapacitor (H-P-L-3M-S-4.0) device that can be operated at a potential window of 2.5 V. The device was found to show a mass-specific capacitance of 111 F g^{-1} at a current density of 1 mA cm^{-2} (0.25 A g^{-1}), with cycling stability over 10000 cycles. The potential of the *in situ* process to mimic the liquid-like electrode|electrolyte interface, augmented with the ability to tune further, opens up new horizons for energy storage devices.



Contents in this chapter are published in the article: doi.org/10.1039/C7TA01514C.

[*J. Mater. Chem. A*, 2017, 5, 8461-8476] - Reproduced by permission of The Royal Society of Chemistry.

3.1 Introduction

Aqueous and nonaqueous electrolytes are being extensively used in electrochemical energy storage devices. The larger potential window offered by the nonaqueous electrolytes makes them the preferred candidates for high energy density commercial supercapacitors (SCs)¹⁻⁵ and batteries.^{2, 6, 7} Once the advantages of the solid-state electrolytes are conceived, in a realistic perspective, radical changes in the design aspects of the future flexible electronic gadgets in the application domain can be expected. Consequently, there has been a significant thrust in the research interest in developing appropriate nonaqueous solid-state electrolytes which hold the potential to replace the conventional liquid electrolytes in SCs and Li-ion batteries.⁷⁻¹³ Along with the anticipated performance enhancements from these solid-state electrolytes, safety and mechanical stability offered by them, in general, can also help to strengthen their demand potential.¹⁴⁻¹⁶ Despite a large number of reports, a solid-state electrolyte which retains the essential characteristics to mimic the advantages of the liquid electrolytes is still missing. In a solid-state form, it is a big challenge to develop a system that can simultaneously ensure high ionic conductivity,¹⁷ good electrode|electrolyte interface formation ability^{18, 19}, etc., and yet retaining its excellent mechanical stability.⁸ Thus, the development of such solid-state electrolytes that hold the conductivity and processability advantages like their liquid-state counterparts is giving both challenges as well as opportunities.

The process by which the solid electrolytes are synthesized has an important role in deciding the mechanical properties and ionic conductivity of the systems. At the same time, the process used to fabricate the device determines the electrode|electrolyte interface formed. Initial reports on the nonaqueous polymer electrolytes came up with mechanically stable dry polymer electrolytes in which a conducting salt is dissolved in a polymer matrix such as PEO (poly(ethyleneoxide)), PAN (poly(acrylonitrile)) etc.^{8, 9} To overcome the hurdle of low interface formation and poor ionic conductivity of the dry polymer electrolytes, gel polymer electrolyte (GPEs) have come into the limelight. GPEs are a physical blend of a high molecular weight polymer (PMMA, PVDF-HFP, PVA, etc.)^{7-9, 20} with a conducting salt dissolved in an aqueous/nonaqueous solvent. Although they perform better than the dry polymer electrolytes in terms of ionic conductivity, mechanical stability is generally found to be compromised. Therefore, considerable efforts have been made to improve the mechanical stability of GPE with a particular interest in mimicking the liquid-like electrode|electrolyte interface. In this

direction, ionic-liquid incorporated tri-block co-polymer GPEs,²¹ organic electrolyte swollen GPE^{22,23}, etc. have been used for SCs. However, the low mass-loading, high ESR, and very low capacitance as well as capacitance retention at high current densities dent their credibility and limit the scalability of the process. The other approach is the porous architecting of the electrode to enhance the interface with the GPE.^{18, 24,25} Even though, this improves the interface, difficulties to prepare such electrodes and controlling the thickness obstacle the commercialization potential. Thus, conventional nonaqueous GPEs fail to provide the liquid-like electrode|electrolyte interface mainly due to the lack of proper device fabrication strategies. These practical intricacies necessitate the development of an efficient nonaqueous GPE and a proper device fabrication process which can essentially assure a liquid-like electrode|electrolyte interface formation at high active mass-loading states of the electrode material. Such a process will contribute towards minimizing the equivalent series resistance (ESR), which is a highly critical parameter as the power rate of the device is determined by the relation $P_{\max} = V^2/4R$, where, 'V' and 'R' represent the operating potential and ESR, respectively.

In this work, a new nonaqueous GPE has been realized by integrating the qualities of liquid, dry polymer electrolytes in the same system. The high ionic conductivity, mechanical stability as well as the ability to mimic the liquid electrolyte-like electrode|electrolyte interface is achieved by an *in situ* process.¹⁹ The process involves the UV curing of a precursor solution containing an acrylate monomer, liquid electrolyte, and a photo-initiator to affect the generation of the GPE. The monomer 2-hydroxy-3-phenoxypropyl acrylate (HPA), owing to the presence of the functional groups (-OH and phenyl group), is found to be the best candidate for the preparation nonaqueous GPEs. The GPE is found to encapsulate about 80 (v/v) % of the liquid electrolyte (3M LiClO₄/propylene carbonate (PC)) in it. The functional groups present in the polymer, *viz.* poly(2-hydroxy-3-phenoxypropyl acrylate) (PHPA) and the solvent (PC) is found to interact with each other through the Li⁺ ions from the conducting salt LiClO₄. Such non-covalent interactions operating in the GPE along with the polymer matrix provide high solvent holding ability while retaining excellent mechanical stability without hampering the intrinsic ionic conductivity. These kinds of non-covalent interactions facilitated through inorganic ions are well-known for various mechanically stable polymer hydrogels,^{26,27} but are explored the first time in a nonaqueous GPE.

The SC device fabrication by the *in situ* process over the high surface area porous carbon electrode with micro-porosity to mimic the liquid-like electrode|electrolyte interface has been previously reported from our group.¹⁹ However, the proton conducting GPE detailed in the above-mentioned work imposes a limitation on the operable potential window beyond 1.2 V as higher potentials can trigger electrolyte decomposition.^{11,28} This leaves an undesirable restriction in devising high energy density SCs. In the present work, a high energy density, nonaqueous SC which could be operated at a potential window of 2.0 V or beyond is devised using the *in situ* process. The system is found to have the potential to replace the conventional liquid and dry polymer electrolytes, with the capability to display electrochemical performance close to that of the systems based on the liquid electrolytes. The process is envisioned to be used in the fabrication of other electrochemical systems such as lithium-ion batteries, metal-air batteries, etc.

3.2 Experimental Section

3.2.1 Materials

Activated carbon (AC, YP-80F) used in this study was purchased from Kuraray Chemical Co., Japan. Conducting carbon filler was procured from Alfa Aesar. Kynar®PVDF (polyvinylidene fluoride) was used as a binder and this was procured from Global Nanotech. N-methyl-2-pyrrolidone (NMP), 2-hydroxy-2-methylpropiophenone (HMPP), and propylene carbonate (PC) were purchased from Aldrich Chemicals. The monomer, 2-hydroxy-3-phenoxypropyl acrylate (HPA) (MW: 222.24 g) was also purchased from Aldrich Chemicals. Polypropylene membrane purchased from Celgard was used as the separator. Grafoil®, used as the current collector, was procured from the GrafTech. The UV chamber used contained four fluorescent lamps (Model: OSRAM Blue UVA / Colour 78).

3.2.2 Preparation of the electrode

A slurry of the activated carbon, conducting carbon, and Kynar® PVDF binder was made by mixing them in a weight ratio of 80:15:5 in NMP, followed by stirring the slurry for about 6 h. It was then probe sonicated for half an hour and a bar coater was used for coating the slurry over the grafoil sheet. The grafoil sheet coated with the electrode material was dried for about 12 h at a temperature of 80 °C in an oven followed by hot pressing at the same temperature for 30 min. It was subsequently dried overnight at about 180 °C in an oven.

3.2.3 Preparation of GPEs by UV curing

A series of PHPA based GPEs were prepared and are designated with the general representation as H-P-L-xM-y%, where 'x' stands for the molarity of LiClO₄ and 'y' denotes the volume percentage of the liquid electrolyte in the GPE. In a typical synthesis, 80% (v/v) of 3 M LiClO₄ in PC was uniformly mixed with HPA and the desired amount of UV initiator (HMPP) is added. Disc-shaped GPE films and cylindrical shaped GPEs were prepared by UV curing (21 minutes of exposure) for performing ionic conductivity measurements and mechanical characterizations, respectively. To study the role of LiClO₄, the gel polymer was also prepared without incorporating the LiClO₄ salt and the corresponding samples are represented as H-P-y%.

3.2.4 Preparation of the PMMA-based GPE solution

For an effective comparison of the present system, a conventional GPE solution composed of LiClO₄, PMMA, and PC was also prepared. In a typical procedure, 1.6 g PMMA is added to 5 mL electrolyte solution of 3.0 M LiClO₄/PC. Followed by vigorous stirring at 115°C, PMMA gets dissolved in the electrolyte. Subsequently, the mixture was allowed to cool slowly to room temperature to obtain a highly viscous GPE solution (shown in **Figure 3.4c** and **d**).

3.2.5 SC device fabrication

The SC devices fabricated employing the *in situ* process using the H-P-L-xM-80% GPE is hereafter termed as H-P-L-xM-S-z, where, 'S' stands for the solid device and 'z' stands for the electrode mass-loading. In a typical device fabrication process, about 125-150 µl of the respective pre-polymerized solution (electrolyte-monomer-initiator mixture before polymerization) was applied uniformly on the surface of a 4 cm² electrode and the specimen was kept in a desiccator under vacuum for 2 h and subsequently cured under UV light for 46 min. Two such electrodes were sandwiched each other followed by perfect sealing with adhesive tape and the requirement of a separator in the system was also eliminated. The system was then kept for 2 days in a desiccator for the effective joining of the electrodes by the *in situ* polymerized GPE layer. All the experiments were done in sealed conditions to avoid any undesirable effects. Hence formed devices with an electrode mass-loading of 3 mg cm⁻² and 3.8 mg cm⁻² are represented as H-P-L-xM-S-3.0 and H-P-L-xM-S-3.8, respectively. The digits '3.0' and '3.8' represent the respective electrode mass-loading of the devices.

For the comparison purpose, SC device was fabricated using the conventional device fabrication process (the *ex situ* process) by using the PMMA-PC-LiClO₄ GPE solution. In a typical procedure, the two electrodes (mass-loading of 3.8 mg cm⁻² and active area of 4 cm²) were directly soaked in the highly viscous PMMA-PC-LiClO₄ gel electrolyte solution and the excess solvent was slowly evaporated at 100 °C for 4 h in a vacuum oven to get a polymer electrolyte film on the electrodes. These electrodes were then sandwiched by keeping a separator in between and sealed using an adhesive tape to make the final device. Henceforth, the device thus formed is termed as PMMA-PC-L-S-3.8, where, ‘S’ stands for the solid device and ‘3.8’ stands for the electrode mass-loading of the device.

Also, the precursor solution-based liquid-state devices (polypropylene separator is soaked with the precursor solution and placed in between the electrodes) were also fabricated and are represented as H-P-L-1M-L-3.0, H-P-L-2M-L-3.0, and H-P-L-3M-L-3.0. Here ‘L’ stands for liquid-state and ‘3.0’ for the electrode mass-loading in the unit of mg cm⁻². Similarly, H-P-L-3M-L-3.8 device was also fabricated and tested. To demonstrate the scalability of the *in situ* process, larger area devices (16 cm²) with two different electrode mass-loadings of 2.5 and 4.0 mg cm⁻² were also prepared. The H-P-L-3M-80% GPE was employed for this purpose as it was found to exhibit desired mechanical stability as well as electrochemical performance when used in the device. The amount of pre-polymerized solution used was about 500-600 µl. The devices with a mass-loading of 2.5 and 4.0 mg cm⁻² are represented as H-P-L-3M-S-2.5 and H-P-L-3M-S-4.0, respectively, where the digits ‘2.5’ and ‘4.0’ represent the respective mass-loading of the scaled-up devices. The SC device was fabricated using an *ex-situ* process where the H-P-L-3M-80% GPE film (thickness = 0.25 mm) was prepared first in a Teflon mold and then sandwiched in between two electrodes as in the case of device fabrication using the conventional dry polymer electrolytes. The hence prepared device is hereafter termed as H-P-L-3M-S-*ex-situ*, where, ‘S’ stands for the solid-state device. The electrode mass-loading was 3.0 mg cm⁻².

3.2.6 Material characterization

The structure and morphology of YP-80F were analyzed with the help of a Hitachi S-4200 field emission scanning electron microscope (FE-SEM). Zeiss Ultra Plus scanning electron microscope coupled with energy dispersive X-ray (EDX) spectrometry (OXFORD Instruments, X-Max) was used for cross-sectional FE-SEM imaging and EDX mapping of the device. The specific surface area (SSA) of the

material was determined by Brunauer-Emmett-Teller (BET) method at 77 K using a Quantachrome Quadraorb automatic volumetric instrument. Before the N₂ gas adsorption-desorption measurements, activation of the sample was done at 100 °C (for 36 h) under ultrahigh vacuum (10⁻⁸ mbar). Infrared spectra were recorded using a Bruker FT-IR (ATR mode) spectrophotometer in the range of 4000-600 cm⁻¹. ¹³C-NMR spectra were recorded on a Bruker-AVANCE 200 MHz spectrometer.

3.2.7 Electrochemical characterization of GPE and the devices

Electrochemical evaluations were carried out using a BioLogic SP-300 Potentiostat-Galvanostat. In the device, the uncoated space of the grafoil sheet was used for providing electrical connections. Cyclic voltammetry (CV) measurements were taken at different scan rates from 50 to 500 mV s⁻¹ by fixing a potential window in the range of 0 to 2.0 V. Charge-discharge measurement was carried out at different current densities from 2 to 20 mA cm⁻². Cycling stability was monitored by using charge-discharge experiments at a current density of 10 mA cm⁻² for many thousand cycles. Further details on the electrochemical measurements are given in **Section 3.1.8** including the equations used for calculating various performance assessment parameters. Electrochemical impedance spectroscopic (EIS) investigation was performed from 10⁶ to 0.01 Hz frequency against the open circuit potential with a sinus amplitude of 10 mV ($V_{\text{rms}} = 7.07$ mV). The conductivity of the GPE films was measured by keeping them between two stainless steel discs and connecting the terminals through crocodile clips. The whole cell assembly was kept in an Espec environmental test chamber to control the temperature. The x-intercept of the Nyquist plot is taken as the bulk resistance of the membrane and the conductivity can be measured using **Equation 3.4** and **Equation 3.5** as given in **Section 3.2.8**.

3.2.8 Equations used for Electrochemical Characterization

Equation 3.1 is used for the calculation of Gravimetric capacitance (F g⁻¹) from the charge-discharge method.¹⁹

$$C = \frac{2 \times (I \times \Delta t)}{\Delta V \times M} \quad (\text{Equation 3.1})$$

where,

Δt = Discharge time

ΔV = Potential window

I = Constant current used for charging and discharging

M = Weight of active carbon material in one of the electrodes

The obtained device capacitance was multiplied by a factor of 2 to get the single electrode capacitance which is included in **Equation 3.1**.

The gravimetric energy density (E_d) and power density (P_d) were calculated from the capacitance value obtained from the charge-discharge method.

$$\text{Energy density } (E_d) \text{ (Wh kg}^{-1}\text{)} = \frac{Cs}{8 \times 3.6} V^2 \quad (\text{Equation 3.2})$$

where,

‘Cs’ is the specific capacitance calculated by the charge-discharge ($F \text{ g}^{-1}$) method and ‘V’ is the voltage window.

$$\text{Power density } (P_d) \text{ (W kg}^{-1}\text{)} = \frac{Ed}{t} \quad (\text{Equation 3.3})$$

where ‘ E_d ’ is the energy density from **Equation 3.3** and ‘ t ’ is the discharge time in hour calculated from the discharge curve.

The ionic conductivity of the GPEs films was calculated from equation (5).

$$\rho \text{ } (\Omega \text{ cm}) = \frac{RA}{l} \quad (\text{Equation 3.4})$$

$$\sigma \text{ } (S \text{ cm}^{-1}) = \frac{1}{\rho} \quad (\text{Equation 3.5})$$

σ = Conductivity of the membrane

ρ = Resistivity of the membrane

R = bulk resistance of the membrane

A = Area of the membrane

l = Thickness of the membrane

3.2.9 Mechanical characterization of PHPA, H-P-80%, and GPEs

Dynamic mechanical analyzer (DMA) (RSA III, TA Instruments USA) equipped with the TA Orchestrator software (Version 7.2.0.4) was used for uni-axial tensile measurements (static mode) and dynamic compression measurements (dynamic mode) of the H-P-L-xM-y% GPEs. The uni-axial un-confined compression and cyclic compression measurements were performed with cylindrical H-P-L-3M-80% and H-P-80% gels of 15 mm diameter and 15 mm height using a single column tabletop electromechanical material testing station of 1 kN load cell capacity (Model: Instron

5943, Instron Ltd., MA, USA), equipped with cylindrical compression platens of 50 mm diameter and Bluehill 3 software with TestProfiler module for recording as well as analyzing the data. For the uni-axial tensile measurements, H-P-L-3M-80% GPE specimens with a rectangular geometry of 5 mm width, 0.8 mm thickness, and 15 mm length were prepared. The specimens were clamped onto tensile grips with a constant torque of 20 cN.m and applied the load at a speed of 1 mm min⁻¹ up to failure. Dynamic mechanical measurements were performed on cylindrical specimens (8 mm dia. x 8 mm height) of neat PHPA, H-P-80% and H-P-L-xM-80% (x = 1,2 and 3) GPEs. Initially, the linear visco-elastic region (LVR) of the gels was identified by performing linear strain sweep measurements followed by frequency sweep analysis to measure the modulus of the specimens in the range 0.1 to 10 Hz at ambient temperature.

For the uni-axial tensile measurements of the electrodes, two sets of electrodes were prepared. One set of electrodes coated with carbon and another set with carbon as well as a photo-polymerized gel electrolyte. Electrode dimensions were 20 mm width, 0.5 mm thickness, and 40 mm height. Electrodes were loaded onto the tensile grips of universal testing machine (Model: Instron 5943, Instron Ltd., MA, USA) with the aid of elastomeric strips on both side of the electrodes to avoid slippage during measurements. A pre-load to 0.01 N is applied to rectify the alignment and the tensile test is performed up to rupture at the cross-head speed of 3 mm/min.

Uni-axial un-confined compression and cyclic compression measurements were performed with cylindrical H-P-L-3M-80% and H-P-80% gels of 15 mm diameter and 15 mm height using single column tabletop electromechanical material testing station of 1kN load cell capacity (Model: Instron 5943, Instron Ltd., MA, USA), equipped with cylindrical compression platens of 50 mm diameter and Bluehill 3 software with TestProfiler module for recording as well as analysis of data sets. To prevent slippage and displacement of gels during the measurements, both the compression plate surfaces were glued with sand-coated paper of grade 100 (Multicut Paper, Vinal Abrasives, India). A pre-load of 0.01 N is applied before compression measurements to attain uniform contact between the surface of gels and compression platens. A cross-head speed of 10 mm min⁻¹ is used for all compression measurements with $\pm 0.1\%$ speed and position accuracy. A minimum of 3 samples was measured and representative histograms were plotted.

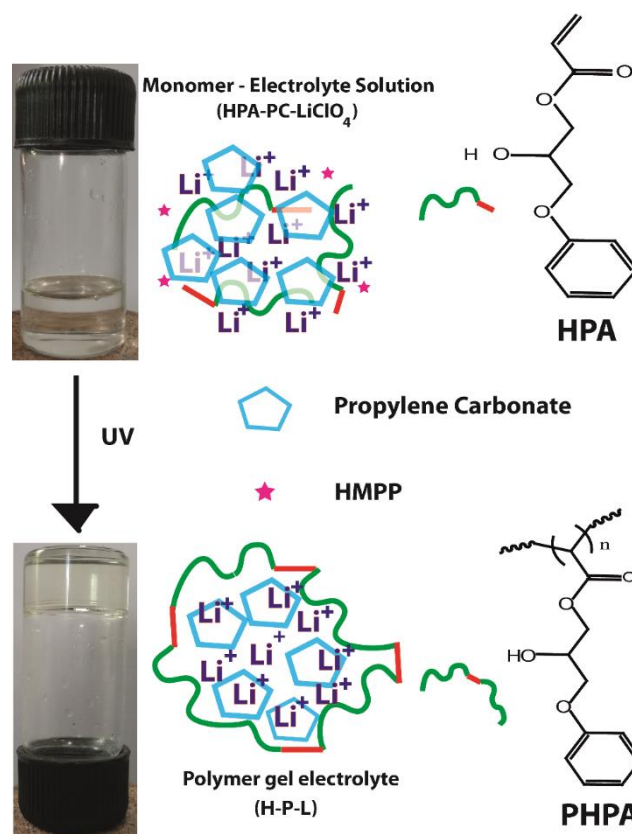


Figure 3.1. Scheme illustrating the synthesis of the GPE by UV-curing. ([*J. Mater. Chem. A*, 2017, 5, 8461-8476] - Reproduced by permission of The Royal Society of Chemistry).

Uni-axial compression was performed on H-P-L-3M-80% and H-P-80% gels up to 98% compression or till specimen failure, whichever is earlier. Two sets of the uni-axial cyclic compression measurements were performed on cylindrical H-P-L-3M-80% and H-P-80% gels with the first set of measurements comprising of a sequence of 8 or 9 cyclic measurements with varying compressive strain starting from 10 to 80 or 90 %. The second set of cyclic measurement involves continuous 200 cycles of compression at constant 70 or 90% compressive strain without interval. The samples used were having a dimension of hysteresis energy is calculated from the histogram of compressive stress versus compressive strain following **Equation 3.6**²⁹ given below:

$$U_{90\%} = \frac{\int_0^{0.9\text{loading}} F ds - \int_0^{0.9\text{unloading}} F ds}{\pi r^2} \quad (\text{Equation 3.6})$$

where ‘ $U_{90\%}$ ’ represents the dissipated energy for 90% compressive strain, ‘ F ’ is the loading, ‘ s ’ is the displacement to the corresponding strain and ‘ r ’ is the radius of the gel.

3.3 Results and Discussion

3.3.1 NMR and ATR-FTIR characterizations of HPA-based GPEs.

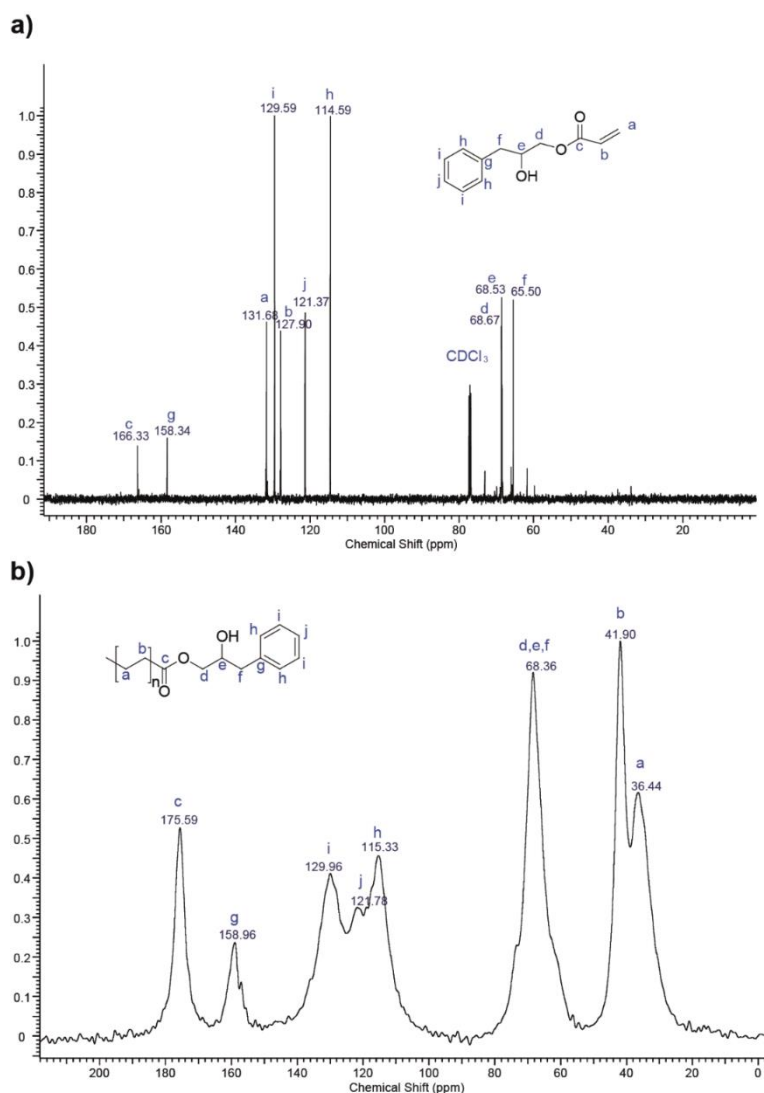


Figure 3.2. The ^{13}C -NMR spectra of the (a) HPA monomer and (b) PHPA polymer. ([*J. Mater. Chem. A*, 2017, 5, 8461-8476] - Reproduced by permission of The Royal Society of Chemistry).

Photo-assisted free radical polymerization of the monomer (HPA) and PC with LiClO_4 salt dissolved in the presence of a UV initiator, HMPP, is used to prepare the GPEs. The scheme illustrating the synthesis of HPA-based GPE is given in **Figure 3.1**. Besides, ^{13}C -NMR spectra of the HPA monomer and the PHPA polymer with their characteristic peaks assigned are given in **Figure 3.2a** and **3.2b**, respectively. The chemical shift values corresponding to the olefin carbons in the monomer, $C_a = 131.68$ ppm and $C_b = 127.90$ ppm, are found to be moved to $C_a = 36.44$ ppm and $C_b = 41.90$ ppm, respectively, in the case of the PHPA polymer. This stands out as valid evidence on the complete polymerization achieved upon the UV irradiation. To study the interactions existing between the different moieties present in the GPE such as the polymer matrix, solvent, and electrolyte ions, ATR-FTIR spectra of the monomer HPA,

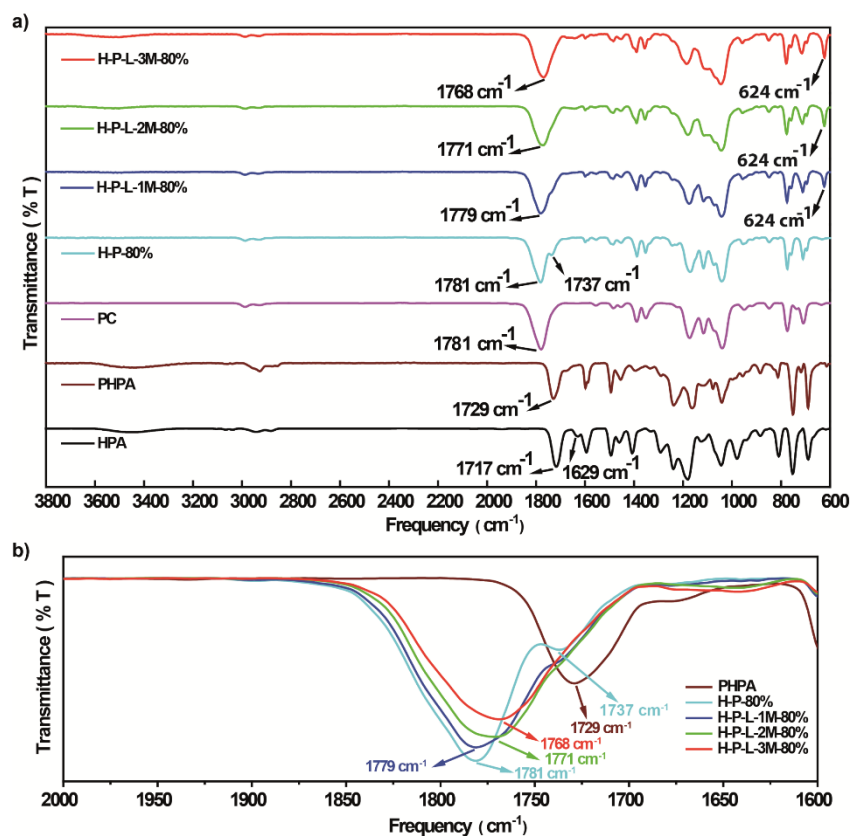


Figure 3.3. (a) ATR-FTIR spectra of HPA, PHPA, PC, and the other GPEs investigated in this study; (b) the zoomed region between 1600-2000 cm^{-1} from Figure 3.3a. ([*J. Mater. Chem. A*, 2017, 5, 8461-8476] - Reproduced by permission of The Royal Society of Chemistry).

neat-polymer PHPA, solvent PC, and GPEs containing 80% of the liquid electrolytes were recorded and the corresponding spectra are presented in **Figure 3.3a** and **b**. On comparing the FTIR spectra of the monomer and neat PHPA, the peak corresponding to the C=C stretching at 1629 cm^{-1} is present in the monomer, whereas, it is absent in the case of the polymer PHPA. The C=O stretching band of the monomer is observed at 1717 cm^{-1} , whereas, in the polymer, it is shifted to a frequency of 1729 cm^{-1} . This is due to the difference between the α,β -unsaturated conjugated carbonyl in acrylate double bonds and the α,β -saturated conjugated carbonyl in the polymer.³⁰ This further confirms that the polymerization is complete which is already been proved from NMR. In the spectrum of H-P-80%, the peak corresponding to the carbonyl group of the polymer matrix of PHPA shows a shift from 1729 cm^{-1} to 1737 cm^{-1} . This blue shift can be attributed to the hindrance to the hydrogen bonding present in the polymer matrix, once the plasticizer solvent (PC) is introduced into the system. In the case of pure PC, the FTIR data shows a peak at 1781 cm^{-1} , which is corresponding to the stretching mode of

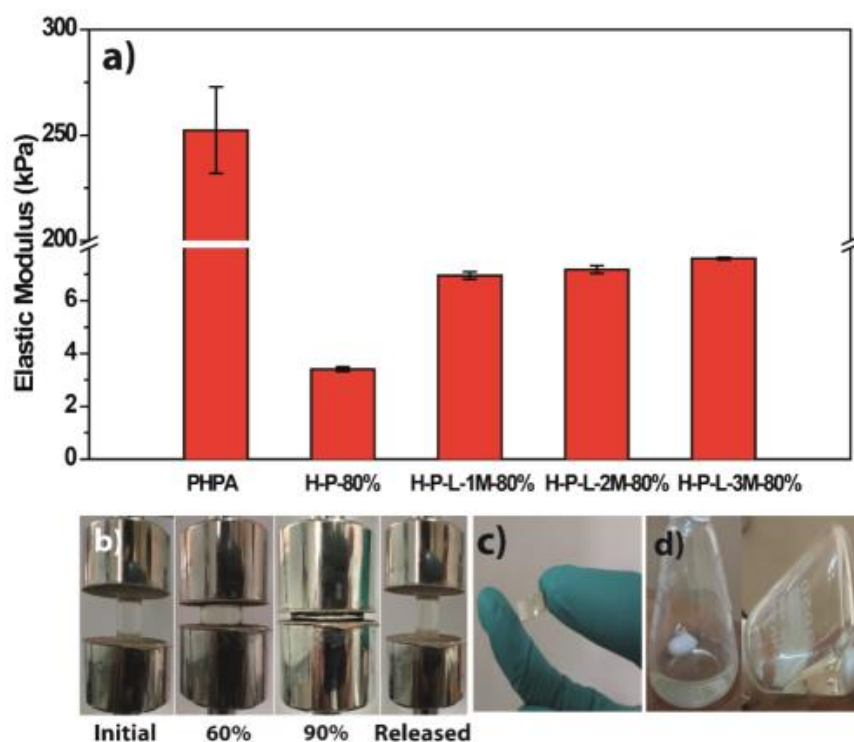


Figure 3.4. (a) DMA studies of PHPA and the other polymer gel electrolytes; (b) mechanical stability and reversibility of the H-P-L-3M-80% GPE; (c) and (d) comparison of the nature of the H-P-L-3M-80% and PMMA-PC-L-S-3M-80% GPE solution. ([*J. Mater. Chem. A*, 2017, 5, 8461-8476] - Reproduced by permission of The Royal Society of Chemistry).

the C=O group of PC.³¹ In the GPEs, this peak (1781 cm^{-1}) shows a gradual redshift as the concentration of the LiClO_4 is increased. This is attributed to the interaction between the carbonyl group of PC and the Li^+ cation. At the same time, it is observed that the peak at 1737 cm^{-1} also shows a shift towards lower frequency when the LiClO_4 is introduced and on successive increment in the concentration of LiClO_4 , the peak is disappeared. The disappearance of the peak is due to the broadening of the peak corresponding to the carbonyl group of PC, where, it is merged with the carbonyl peak of the polymer matrix. Moreover, the amount of the solvent is excess in the system compared to the polymer, which also contributes to the disappearance of the carbonyl band of the polymer matrix. The increase in the intensity of the peak at 624 cm^{-1} as the concentration of LiClO_4 increases in the gel polymer electrolyte is attributed to the increase in the amount of the free ClO_4^- ions. This confirms the improved dissociation of the conducting salt in the H-P-L-3M-80% gel polymer electrolyte compared to the others.

In the GPEs, as the concentration of LiClO_4 is increased, the carbonyl stretching frequency of both PC and the polymer matrix shows a gradual redshift. Thus, this gives strong evidence that the Li^+ ion is interacting with the carbonyl group of the solvent (PC) and the polymer matrix (PHPA). Since Li^+ is known to coordinate with more than one electron-donating groups at a time,³²⁻³⁵ it is expected that quite a large number of the Li^+ ions in GPE are coordinated to the carbonyl groups of both the polymer (PHPA) and the solvent (PC) at the same instant (solvent- Li^+ -polymer interaction). Thus, Li^+ acts as a non-covalent crosslinker between the polymer matrix and the solvent. Similarly, the solvent-solvent³⁶⁻³⁸ interaction established through the Li^+ ion is also envisaged. It is also reasonable to assume that the polymer chains in GPE are also interacting each other owing to the numerous types of possible non-covalent interactions (hydrogen bonding,³⁰ π - π stacking, etc.,³⁹) in the polymer matrix, induced by the functional groups (-OH and phenyl groups) present in it. The Li^+ assisted interaction helps the GPE to hold a large amount of the solvent, all the while, along with other non-covalent interactions, contributing to their mechanical stability and flexibility.

3.3.2 Mechanical characterization of HPA-based GPEs

The primary effect of PC in PHPA was determined using dynamic mechanical analysis (DMA) and the corresponding plots are given in **Figure 3.4a**. The hardness of pristine PHPA is evident from its elastic modulus (250 kPa), which is reduced to 3.4 kPa in H-P-80% owing to the plasticizing effect of PC. The ability of HPA to form mechanically stable H-P-80% gel further proves the inherent ability of the polymer and PC to induce non-covalent interactions inside the polymer matrix, as explained through the ATR-FTIR analysis. As the concentration of LiClO_4 is increased in H-P-80%, the elastic modulus value shows gradual improvement. The values of H-P-L-1M-80%, H-P-L-2M-80%, and H-P-L-3M-80% are 6.9, 7.2, and 7.6 kPa, respectively. This is attributed to the secondary effect of Li^+ in determining the elastic modulus of the formed gels. The improved elastic modulus is assumed to be due to the non-covalent crosslinking interactions induced by the Li^+ ion in GPE, which is already evident from the ATR-FTIR spectra.^{33, 40} The degree of these interactions increases along with an increase in the LiClO_4 concentration, exhibiting an improvement in the elastic modulus of GPEs. This Li^+ assisted non-covalent crosslinking and other non-covalent interactions along with the covalently bonded interpenetrated network of PHPA

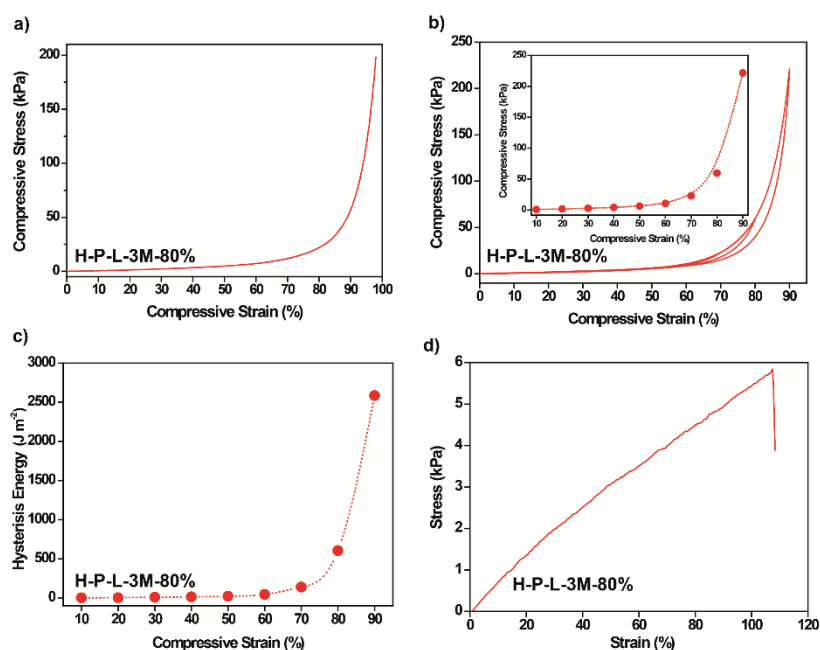


Figure 3.5. (a) Uni-axial compression of H-P-L-3M-80%; (b) sequential uni-axial compression cycles of H-P-L-3M-80% from 10 to 90% strain where the inset shows the maximum stress per cycle; (c) hysteresis energy of the sequential uni-axial compression cycles from 10 to 90% compressive strain for H-P-L-3M-80%; (d) tensile properties of H-P-L-3M-80%. ([J. Mater. Chem. A, 2017, 5, 8461-8476] - Reproduced by permission of The Royal Society of Chemistry).

prevents the exudation of the solvent from the solid electrolyte and improves its mechanical properties compared to the specimens without LiClO₄.

The excellent mechanical stability as well as the reversibility of the gel electrolyte (H-P-L-3M-80%) is depicted in **Fig. 3.4b**, where it is shown that GPE attains its original dimensions even after mechanically compressing it up to 90% strain. The high withstanding ability of GPE to strain can be attributed to the self-recovery of the non-covalent bonds present in it. The non-covalent bonds act as sacrificial bonds that break and recover themselves when subjected to strain thereby protecting the covalent bonds in GPE.^{27, 41-42} A GPE is tried to be prepared using the conventional process²²⁻²³ in which a PHPA block is kept soaked in PC for two days. It is observed that the PHPA is not able to absorb the PC to its interior network. This underlines the advantage of the single-step GPE synthetic process by UV curing in realizing robust GPEs with desirable mechanical properties. For comparison, the digital images of the H-P-L-3M-80% GPE and a PMMA-PC-L GPE solution are shown in **Figure 3.4c** and **3.4d**, respectively. Being a mere physical mixture of the polymer with a liquid electrolyte and due to the

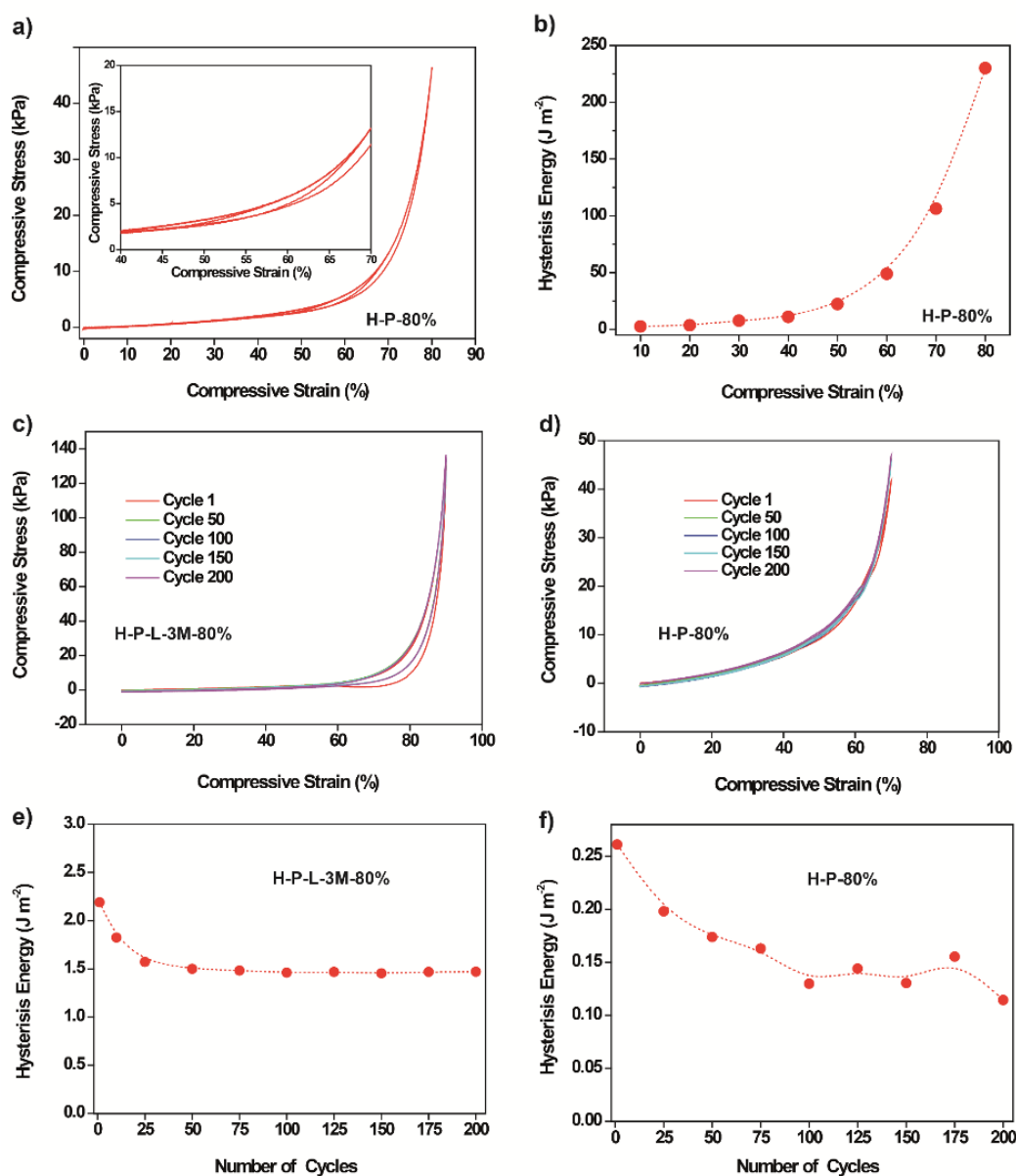


Figure 3.6. (a) Sequential uni-axial compression cycles of H-P-80% from 10 to 80% strain where the inset shows the maximum stress per cycle versus the corresponding strain from 40% to 70% compression strain; (b) hysteresis energy of the sequential uni-axial compression cycles from 10 to 80% compressive strain for H-P-80%; (c) compressive stress vs. compressive strain plot recorded for 200 repeated cycles of uni-axial compression for the H-P-L-3M-80% GPE at an interval of 50 cycles; (d) compressive stress vs. compressive strain plot recorded for 200 repeated cycles of uni-axial compression for H-P-80% gel at an interval of each 50 cycles; hysteresis energy of 200 repeated uniaxial compressive strain cycles, (e) at 90% compression for the H-P-L-3M-80% GPE and (f) at 70% compression for the H-P-80% gel. ([J. Mater. Chem. A, 2017, 5, 8461-8476] - Reproduced by permission of The Royal Society of Chemistry).

absence of any functional groups in the polymer matrix, the interactions between the different moieties in PMMA-PC-L are too weak.⁴³ Therefore, the PMMA fails to hold large amounts of the solvent, and, by doing so, the mechanical property deteriorates (**Figure 3.4d**).

The histogram of the uni-axial compression measurement performed on H-P-L-3M-80% at a cross-head speed of 10 mm min^{-1} is given in **Figure 3.5a**. The maximum compressive stress attained by the GPE is 198.32 kPa without failure at 98% compressive strain. The GPE is not compressed beyond 98% due to the limitations of the testing station. Critical strain at which the stress shows the abrupt increase is found to be 92.24%, after which it exhibits a significant degree of strain hardening. In the viewpoint of the flexibility required during the end-use application of the all-solid-state SCs, compressibility (98%) of the GPE is an added advantage. **Figure 3.5b** shows the sequential cyclic compression measurements comprising of continuous 9 cycles of the compression with varying compressive strain sequentially, ranging from 10 to 90%. The maximum stress at 90% strain is 221.80 kPa, whereas at 10% strain it is 0.96 kPa. The inset shows the increase in the maximum stress at each cycle, from 10 to 90% strain, wherein the critical strain is found to be 77.32%. The critical strain is the direct indication of the degree of flexibility the gel electrolyte can withstand during the bending and folding of the solid-state SC.

Figure 3.5c shows the results of the hysteresis energy calculated from each sequential compression cycles as a function of the compressive strain. It is calculated after measuring the area between each loading and unloading cycle at respective compressive strain and applying **Equation 3.6**. Dotted lines are kept in between each value as a guide to the eye. It is evident from the histogram that the energy loss is virtually nil from 10 to 60% compressive strain and follows a plateau after which it shows an abrupt increase. As compared to the energy loss at 60% compression, the loss at 70, 80, and 90% compressive strain shows approximately 3, 13, and 53 fold increase. **Figure 3.5d** shows the tensile stress vs. strain graph of the gel which exhibits stretchability up to 107% strain and possesses tensile stress of 5.8 kPa. Cyclic compression experiments were performed using the H-P-80% gels as well. **Figure 3.6a** shows the sequential cyclic compression experiments comprising of 8 cycles with varying strain from 10 to 80%. Since the specimen breaks before 90% strain, the experiments could not be continued to this level. In comparison with H-P-L-3M-80%, the H-P-80% is unable to withstand 90% strain, which is a piece of direct evidence for the role played by the lithium salt in dissipating the energy effectively throughout the gel network during the stress. The hysteresis energy of the sequential uni-axial compression cycles from 10 to 80% compressive

strain for H-P-80% is presented in **Figure 3.6b**. The critical strain in the case of H-P-80% calculated from **Figure 3.6a** and **b** is found to be less than 60%, which is inferior to that of the H-P-L-3M-80% specimen obtained from **Figure 3.5 b** and **c** (77.32 %).

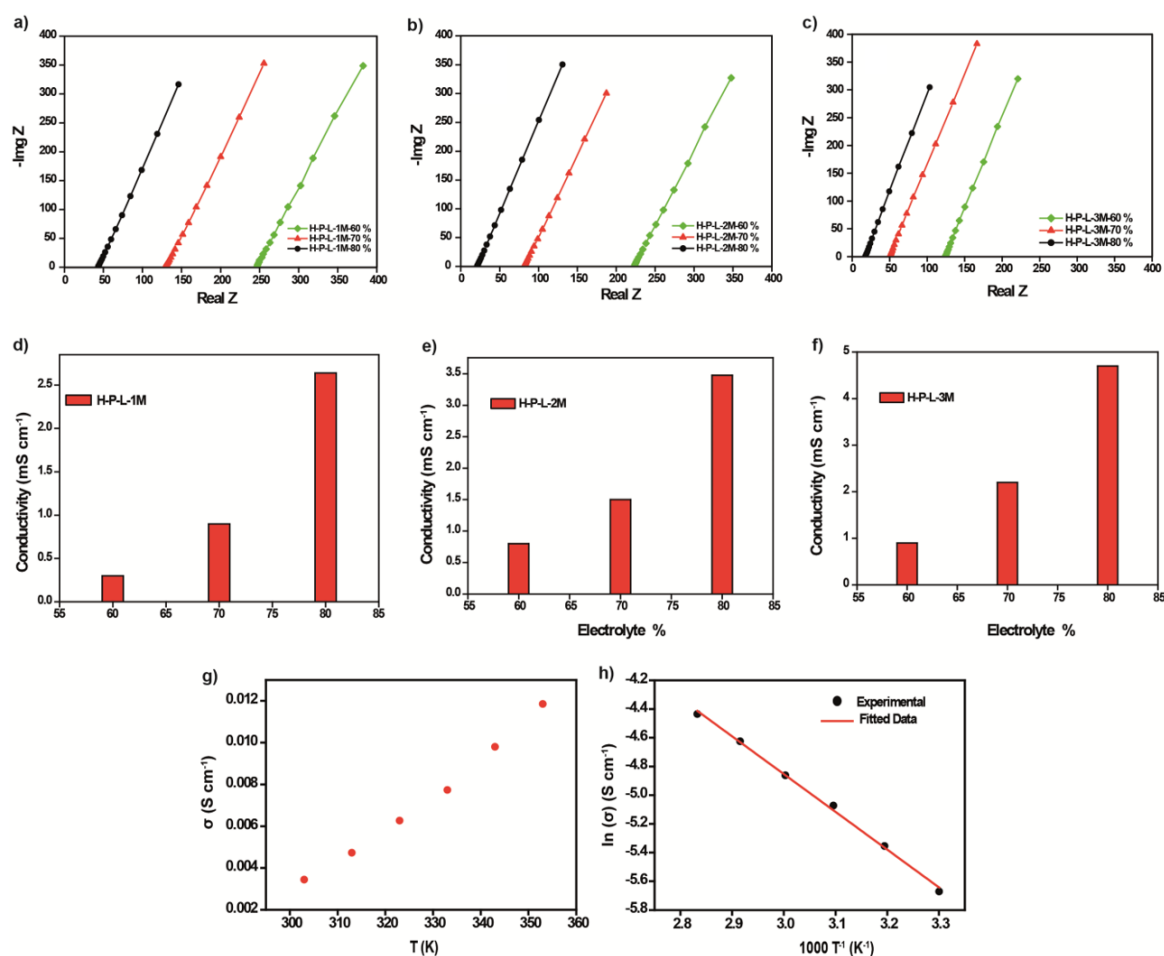


Figure 3.7. (a) to (c) The Nyquist plots of the polymer gel electrolytes blended with different weight percentages of the liquid electrolyte at different molar concentrations of the conducting salt; (d) to (f) plots of conductivity vs. volume percentage of the electrolyte present; (g) change in the ionic conductivity vs. temperature for the H-P-L-3M-80% polymer gel electrolyte; (h) $\ln \sigma$ vs. $1/T$ plot for H-P-L-3M-80%. [*J. Mater. Chem. A*, 2017, 5, 8461-8476] - Reproduced by permission of The Royal Society of Chemistry).

The fatigue resistance associated with the UV cured GPE is an added advantage that is not exhibited by the GPEs prepared using the conventional strategies. The fatigue resistance is an important quality required for a GPE which decides the mechanical flexibility of the device when it is subjected to various degrees of physical strains. To study the role of the Li^+ ion-assisted non-covalent crosslinking interactions in the fatigue resistance and energy dissipation efficacy of H-P-80% and H-P-L-3M-80%, we have performed consecutive 200 cycles of compression measurements at a compressive strain of 90% for H-P-L-3M-80% and 70% for

H-P-80%. The compression cycles recorded for H-P-L-3M-80% GPE and H-P-80% gel at an interval of 50 cycles are given in **Figure 3.6c** and **Figure 3.6d**, respectively. Corresponding hysteresis energy from Cycle 1 to 200 for H-P-L-3M-80% and H-P-80% at an interval of 25 cycles is presented in **Figure 3.6e** and **f**, respectively, as a function of the number of the cycles. In both cases, it is evident that the hysteresis energy corresponding to the first compression cycle stands out among others because it is related to the irreversible fracture of the covalent bonds present within the gel network. In the case of the H-P-L-3M-80% GPE (**Figure 3.6e**), the energy loss in the successive cycles shows an equilibrium regime after 50 cycles followed by a slight increment in the hysteresis energy towards the end. This in turn throws light on the subsequent elastic behavior of the polymer network and the self-recovering nature of the system which is facilitated through the reversible non-covalent bonds involving the Li^+ ion, the polymer matrix, and PC. The same non-covalent interactions help the system to withstand a compressive strain as high as 98 % (**Figure 3.5a**) by an effective dissipation of the applied energy throughout the gel network. Since the Li^+ assisted non-covalent interactions are absent in the case of the H-P-80% polymer gel, even a compressive strain lower than 90% (**Figure 3.6a**) causes the covalent bonds to be broken permanently and the lack of self-recovery is reflected in the gradual hysteresis energy loss as shown in **Figure 3.6f**. Therefore, it is confirmed that the reversible interactions present in H-P-L-3M-80% GPE underline the degree of flexibility the gel electrolyte can impart to the SC device.

3.3.3 Ionic conductivity and activation energy of HPA-based GPEs

Conductivity measurements of the GPEs were carried out using EIS investigation at room temperature. The Nyquist plots of the GPEs with different volume percentages of the liquid electrolyte at different molar concentrations of the conducting salt are given in **Figure 3.7a** to **c**. It is observed that, as the liquid electrolyte amount is increased from 60% (v/v) to 80% (v/v), the internal resistance (x-intercept of the Nyquist plot) gradually decreases for all the GPEs under study. The trend is common in the case of the GPEs where the conductivity increases with an increase in the amount of liquid electrolyte. In other words, more plasticized GPE gives more conductivity.^{44,45} The conductivity values are calculated for the GPEs from the ESR values obtained from the Nyquist plots (**Figure 3.7a** to **c**) and the plots of the conductivity vs. volume percentage of the liquid electrolyte present in the GPE are given in **Figure 3.7d** to **f**. It is observed that in all the cases, the conductivity value is highest for the GPEs with 80% (v/v) of the liquid electrolyte in it. As the concentration of the salt is increased in the system, the

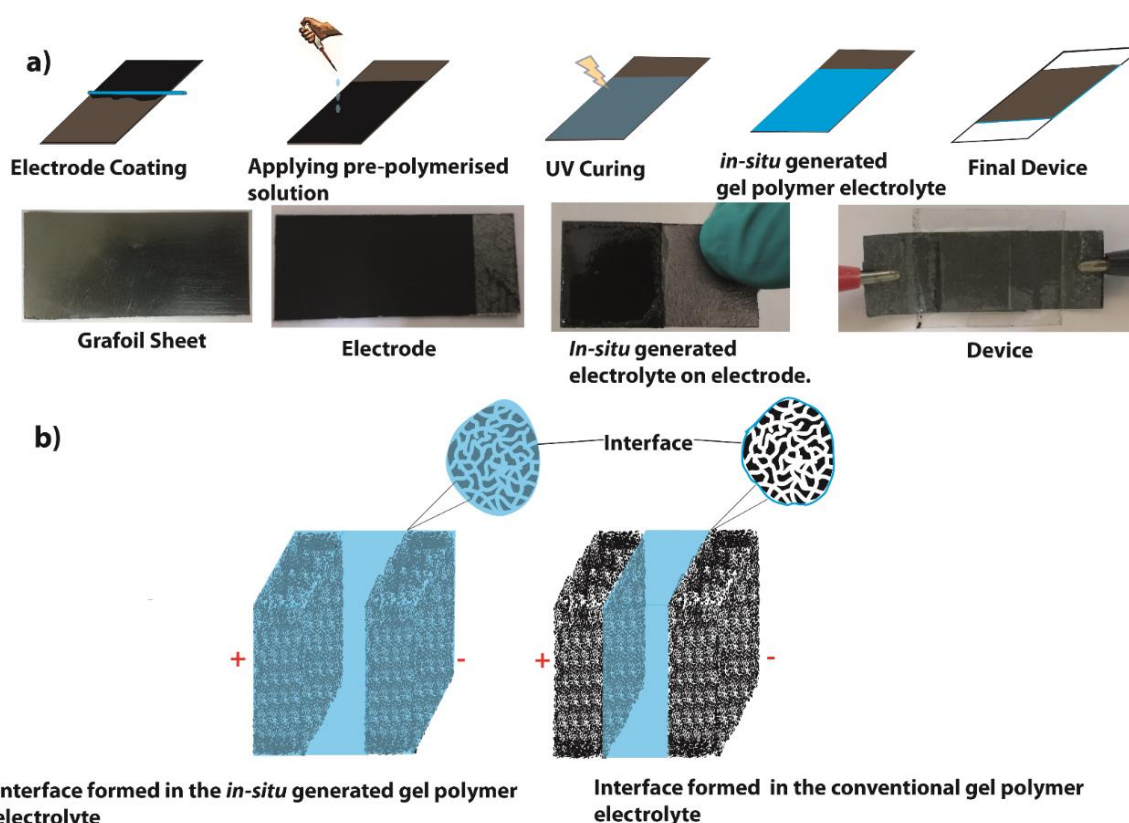


Figure 3.8. (a) Schematic representation and digital images of the solid-state SC device fabricated using the in situ process, and (b) pictorial representations on the difference between the nature of the electrode/electrolyte interface in the case of the in situ process and conventional ex situ systems. ([*J. Mater. Chem. A*, 2017, 5, 8461-8476] - Reproduced by permission of The Royal Society of Chemistry).

conductivity also increases which is due to the improved LiClO_4 dissociation due to the interactions existing in the GPE as explained with the help of the ATR-FTIR spectral investigation (**Figure 3.3**). H-P-L-3M-80% shows the maximum conductivity value of $4.7 \times 10^{-3} \text{ S cm}^{-1}$, which is comparable to the conductivity of the various conventional liquid electrolytes used in batteries and SCs.^{6, 46-49} This value is superior to the conductivity of many of the dry polymer electrolytes, and GPEs previously reported.^{22, 50-53}

It is observed that the increase in the amount of PC in the GPE leads to more plasticized GPE, which in turn reduces the crystallinity of the polymer and provides more free volume around the polymer chains. Due to the amorphous nature of the plasticized GPE, the segmental motion of the polymer chains also increases. These effects facilitate the improvement in the ionic conductivity when more amount of PC is introduced in the GPE.⁵⁴⁻⁵⁵ Moreover, as the amount of PC is increased in the system, the dissociation of LiClO_4 is enhanced because of the high dielectric constant of the

solvent as well as the interaction of the Li^+ ion with the carbonyl group of the solvent. The coordinate bonds formed by the Li^+ ion with the carbonyl group of the polymer matrix also helps to improve the dissociation of LiClO_4 , thereby reducing the ion-pairing effect.^{40, 56-58} These combined effects result in the improved conductivity of H-P-L-3M-80% compared to its 1 M and 2 M counterparts. The origin of these interactions has already been discussed using ATR-FTIR spectral investigations (**Figure 3.3**).

The activation energy of GPE towards the ion conductivity for H-P-L-3M-80% was also calculated from the conductivity values of the GPEs taken at different temperatures from 30 to 80 °C. The plot representing the change in the conductivity with respect to the change in temperature for H-P-L-3M-80% is given in **Figure 3.7g**. At higher temperatures, the carrier ions attain higher mobility and the vibration and expansion of the polymer chain are also promoted. Therefore, the ions can move much easily compared to the conditions at lower temperatures which is reflected in the increased conductivity at higher temperatures. Besides these factors, the dissociation of the LiClO_4 salt is also favored at higher temperatures which also contributes to the conductivity enhancement.⁴⁰ From the linear behavior of the $\ln \sigma$ vs. $1/T$ plot for H-P-L-3M-80% given in **Figure 3.7h**, it is clear that the relationship between the logarithm of the ionic conductivity and temperature follows the simple Arrhenius relationship^{11, 40, 59, 60} as given in **Equation 3.7** below:

$$\sigma = \sigma^0 \exp(-E_a/RT) \quad (\text{Equation 3.7})$$

In the above equation, σ , σ^0 , E_a , R , and T are the ionic conductivity, the pre-exponential factor, the activation energy for ion transport, the gas constant, and the absolute temperature, respectively. The linear nature of the plot underlines that the mechanism of the ionic conduction could be from the hopping of the Li^+ ions associated with the improved segmental motion of the polymer chains. The segmental motion of the polymer chains enhances the hopping of the Li^+ ions from one site to the other and the increased free volume in the polymer matrix helps in facilitating a much better pathway for the free movement of the Li^+ ion.^{42, 59, 60} The activation energy calculated for H-P-L-3M-80% is 0.23 eV, which is obtained from the linear fitting of the $\ln \sigma$ vs. $1/T$ plot. The value obtained is comparable to several other lithium conducting GPEs and liquid electrolytes that have been reported in the literature.^{55-57, 61}

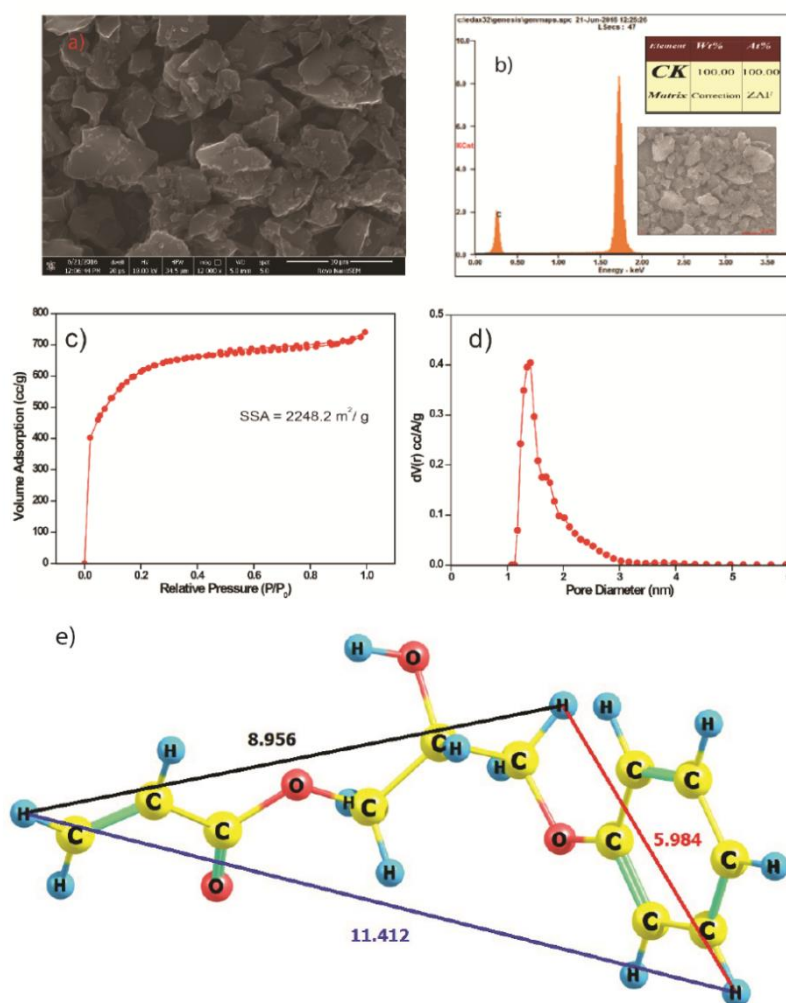


Figure 3.9. (a) FESEM image of YP-80F; (b) EDAX of YP-80F; (c) N_2 -adsorption isotherm of the carbon (YP-80F) used for preparing the electrode for the SC; (d) pore-size-distribution profile of the carbon powder used for making the device; (e) optimized conformation of the monomer (HPA) at PBE/TZVP level of theory (distances between the hydrogen atoms are given in Angstrom (\AA) unit). ([*J. Mater. Chem. A*, 2017, 5, 8461-8476] - Reproduced by permission of The Royal Society of Chemistry).

3.3.4 Electrochemical characterization of the supercapacitor devices

Comparison between H-P-L-xM-S-3.0 and H-P-L-xM-L-3.0 devices ('x'= 1, 2 and 3)

The process of the *in situ* GPE generation in the inner and outer surface of the pores of the carbon (YP-80F) electrode is adopted for the SC device fabrication. The scheme illustrating the fabrication of the devices, generally represented as H-P-L-

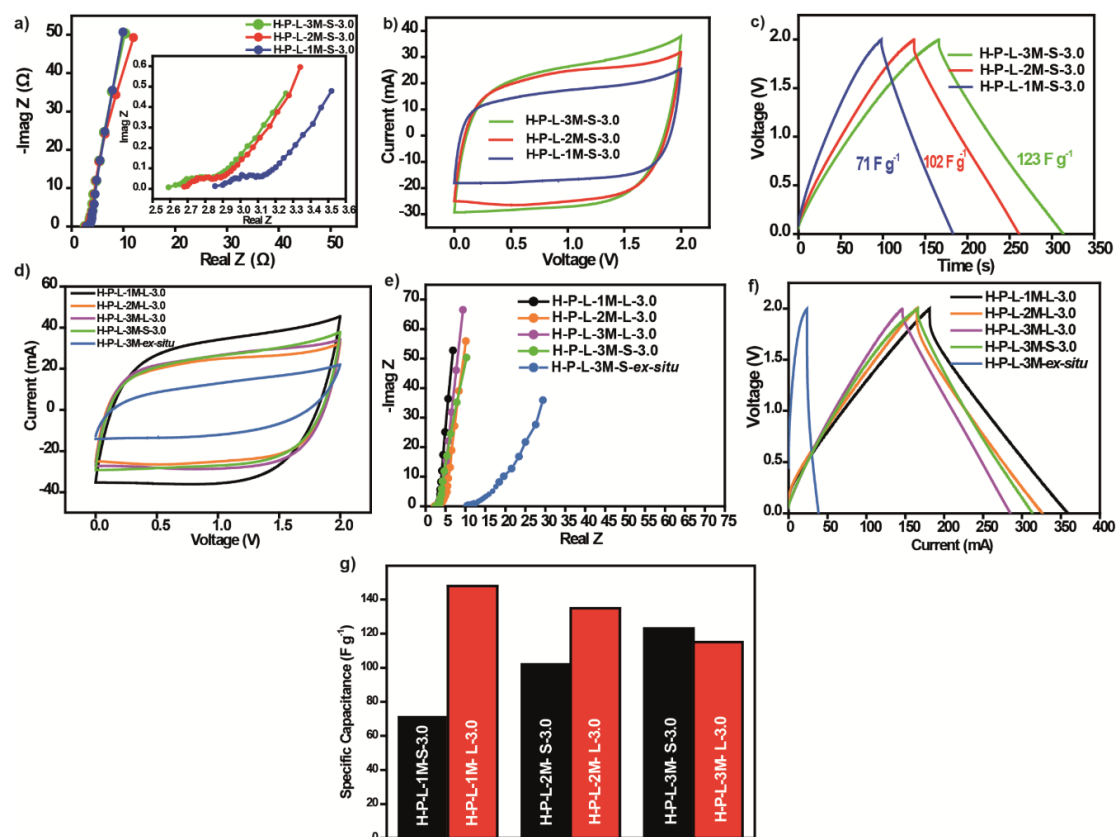


Figure 3.10. (a) to (c) Combined Nyquist plots (a), CV profiles recorded at a scan rate of 50 mV s^{-1} (b), and CD profiles recorded at a current density of 2 mA cm^{-2} (c) for the supercapacitor devices: H-P-L-xM-S-3.0, where 'x' = 1, 2 and 3; d) to f) the combined CV profiles recorded at a scan rate of 50 mV s^{-1} (d), Nyquist plots (e), and the CD profiles recorded at a current density of 2 mA cm^{-2} (f) taken for the various liquid-state and solid-state devices under the study; (g) comparison of the specific capacitance values obtained for the various devices at a current density of 2 mA cm^{-2} . ([J. Mater. Chem. A, 2017, 5, 8461-8476] - Reproduced by permission of The Royal Society of Chemistry).

xM-S (where, 'x' = 1, 2, and 3), is shown in **Figure 3.8a**. The schematic representation of the electrode|electrolyte interface formed in the *in situ* process and conventional GPE film-based SC device is also presented in **Figure 3.8b**. The FE-SEM image and the energy-dispersive X-ray spectroscopy (EDX) data of YP-80F, presented in **Figure 3.9a** and **b**, quantify the morphology and elements present in the material, respectively. The hard carbon powder with a grain boundary between 2-5 μm contains about 99.9% carbon indicating the absence of any heteroatoms such as nitrogen, phosphorus, or oxygen. This confirms the absence of any pseudo-capacitive contribution from the active material and whatever the capacity obtained is from the pure double layer capacitance

of the active material. The BET adsorption-desorption isotherm of YP-80F and the corresponding pore size distribution profile are presented in **Figure 3.9c** and **d**, respectively. The SSA of the material is found to be about $2250 \text{ m}^2 \text{ g}^{-1}$. The average pore-size distribution of YP-80F lies between 1-3 nm and the major contribution comes from the pores which have a size between 1-1.5 nm (**Figure 3.9d**). Full quantum mechanical calculations were done with density functional theory (DFT) at the PBE/TZVP⁶²⁻⁶³ level of theory using Turbomole 7.0 program⁶⁴ to gain further insight into the dimension and geometry of the HPA monomer. The optimized geometry is shown in **Figure 3.9e**. The length of the monomer (HPA) used in this work is about 1.14 nm (11.4 Å) as shown in **Figure 3.9e** (the XYZ coordinates of the PBE/TZVP optimized geometry are not shown in this chapter, and can be accessed at supplementary information of the following article, *J. Mater. Chem. A*, 2017, 5, 8461-8476). The maximum distance between the two terminal atoms (H (1) and H (3)) is 11.412 Å, which is very much less than that of the carbon pore size (10-15 Å). Therefore, the monomer is expected to go easily into the pores which are comparable in size to it.¹⁹

To show the excellent potential of the H-P-L-3M-80% GPE as a solid-state electrolyte in an SC device, the electrochemical performances of the devices, H-P-L-1M-S-3.0, H-P-L-2M-S-3.0 are compared with that of H-P-L-3M-S-3.0. The combined Nyquist plots of the devices are presented in **Figure 3.10a**. The inset shows the high-frequency region of the Nyquist plots, where it is observed that the ESR values of the H-P-L-3M-S-3.0, H-P-L-2M-S-3.0, and H-P-L-1M-S-3.0 devices are too close to each other (2.60, 2.70 and 2.90 Ω, respectively). This underlines the fact that the nature of the electrode|electrolyte interface formed in all three devices is comparable. The low ESR value associated with the H-P-L-3M-S-3.0 is following the high ionic conductivity value ($4.7 \times 10^{-3} \text{ S cm}^{-1}$) obtained for the H-P-L-3M-80% GPE as already explained in **Figure 3.7**. The combined CV profiles of the three devices recorded at a scan rate of 50 mV s^{-1} are presented in **Figure 3.10b**. The superior current-voltage characteristics of the H-P-L-3M-S-3.0 device compared to the other devices is attributed to the lower ESR associated with the device as well as the improved electric double layer formation due to the higher concentration of the conducting salt (3M LiClO₄) incorporated in the H-P-L-3M-80% GPE used for the device fabrication. The combined CD profiles recorded at a current density of 2 mA cm^{-2} for the three devices along with their gravimetric specific capacitance are presented in **Figure 3.10c**. The maximum capacitance of 123 F g^{-1}

obtained for the H-P-L-3M-S-3.0 device further underlines the superiority of the H-P-L-3M-80% GPE as the desired candidate as a solid-state electrolyte in a solid-state SC.

The electrochemical performance of the H-P-L-3M-S-3.0 device is then compared with the liquid-state devices, *viz.*, H-P-L-1M-L-3.0, H-P-L-2M-L-3.0, H-P-L-3M-L-3.0, and the *ex-situ* prepared device, H-P-L-3M-*ex-situ*. The combined CV profiles recorded at a scan rate of 50 mV s^{-1} , Nyquist plots, and the charge-discharge profiles recorded at a current density of 2 mA cm^{-2} for the devices are summarised in **Figure 3.10d-f**. The ESR value (**Figure 3.10a**) of the H-P-L-3M-S-3.0 device and all the other liquid-state devices lies approximately in the close-range between $2.3\text{-}2.8 \Omega$. This shows the liquid-like electrode|electrolyte interface achieved in the H-P-L-3M-S-3.0 solid-state device. However, the electrochemical performance of the H-P-L-3M-*ex-situ* device is far inferior to the other devices. The very high ESR of 10Ω obtained for the device underlines the inability of the *ex-situ* prepared GPE film to achieve an efficient liquid-like electrode|electrolyte interface. This shows the advantage of the *in situ* process in achieving high performing solid-state SC devices. The gravimetric specific capacitance values obtained for each device at a current density of 2 mA cm^{-2} are summarised in **Figure 3.10g**. The specific capacitance (123 F g^{-1}) obtained for the H-P-L-3M-S-3.0 device is in close agreement with the specific capacitance (115 F g^{-1}) obtained for its liquid-state counterpart (H-P-L-3M-L-3.0). At the same time the value obtained is higher compared to the other two solid-state devices, *viz.*, H-P-L-2M-S-3.0 (102 F g^{-1}), and H-P-L-1M-S-3.0 (71 F g^{-1}). In the following sections, the superior edge of the *in situ* process in the supercapacitor device fabrication is thoroughly explored by using the H-P-L-3M-80% GPE and compared it with the conventional supercapacitor devices made out of the PMMA based GPE solution.

Comparison between the *in situ* and conventional device fabrication strategies

The *in situ* polymerization of H-P-L-3M-80% is carried out on the electrode surface (active material loading = 3.8 mg cm^{-2}) to form an inter-penetrated network of the polymer and the conducting medium favored by the interactions between donor atoms of PC and the monomer (HPA) through the Li^+ ions as proved from the ATR-FTIR studies. Combined CV profiles of the H-P-L-3M-S-3.8, H-P-L-3M-L-3.8, and PMMA-PC-L-S-3.8 recorded at a scan rate of 50 mV s^{-1} are given in **Figure 3.11a**. It is observed that the current-voltage characteristics of H-P-L-3M-S-3.8 give a perfect square behavior which matches with that of H-P-L-3M-L-3.8. However, the CV profile

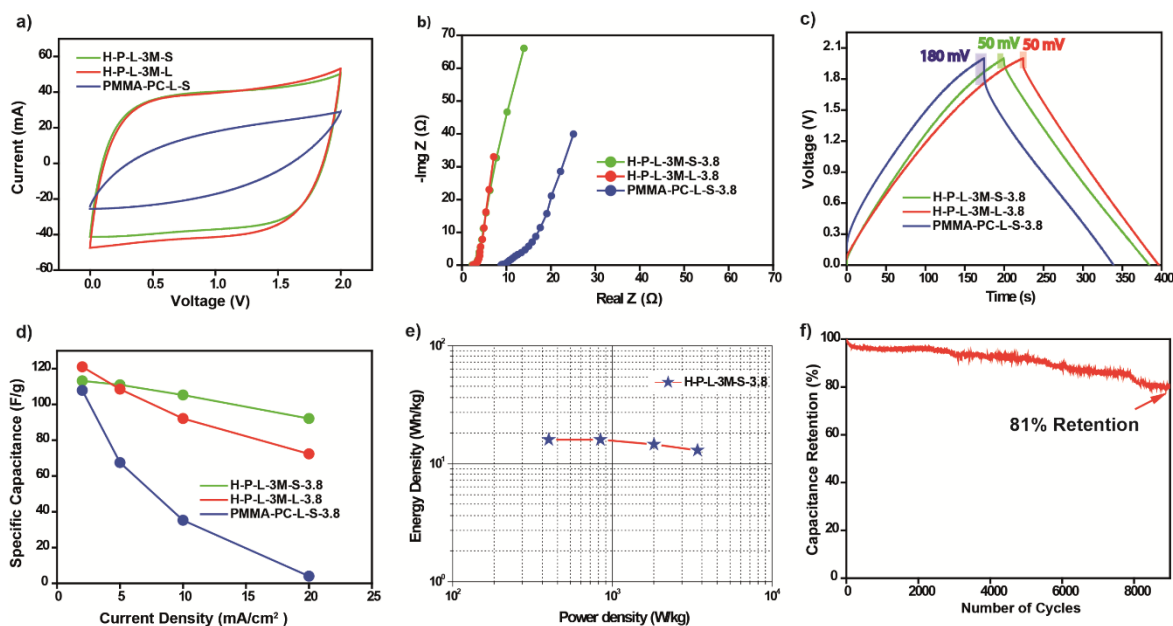


Figure 3.11. Comparison of the electrochemical performance of H-P-L-3M-S-3.8, H-P-L-3M-L-3.8, and PMMA-PC-L-S-3.8: (a) CV profiles recorded at a scan rate of 50 mV s^{-1} ; (b) Nyquist plots generated from the EIS studies; (c) CD profiles recorded at a current density of 2 mA cm^{-2} ; (d) plots representing the mass-specific capacitance vs. the current density; (e) Ragone plot comparing the energy and power densities of H-P-L-3M-S-3.8; (f) cycling stability of H-P-L-3M-S-3.8 at a current density of 10 mA cm^{-2} . ([J. Mater. Chem. A, 2017, 5, 8461-8476] - Reproduced by permission of The Royal Society of Chemistry).

of PMMA-PC-L-S-3.8 deviates from the perfect square behavior and shows inferior current-voltage characteristics compared to the corresponding liquid and the *in situ* processed devices. In the conventional way of device fabrication using the GPE solution, the efficient utilization of the surface area of the active carbon electrode material is not possible unlike in the liquid electrolytes. The incomparable dimension of the micro-pores of the carbon and the higher molecular weight of the polymer in GPE solutions (in this case, PMMA-PC-LiClO₄) prevent the effective infiltration of the electrolyte into the pores of the carbon. Therefore, the electrode|electrolyte interface formed in the case of PMMA-PC-L-S-3.8 will be inferior as represented schematically in **Figure 3.8b**, since, the outer surface of the electrode material is only accessible to the electrolyte.

In the case of the *in situ* polymerization process, both the inner and outer surfaces as well as micro-, meso- and macro-pores of the electrode material will be available to the electrolyte. When the pre-polymerized solution is applied on the electrode surface,

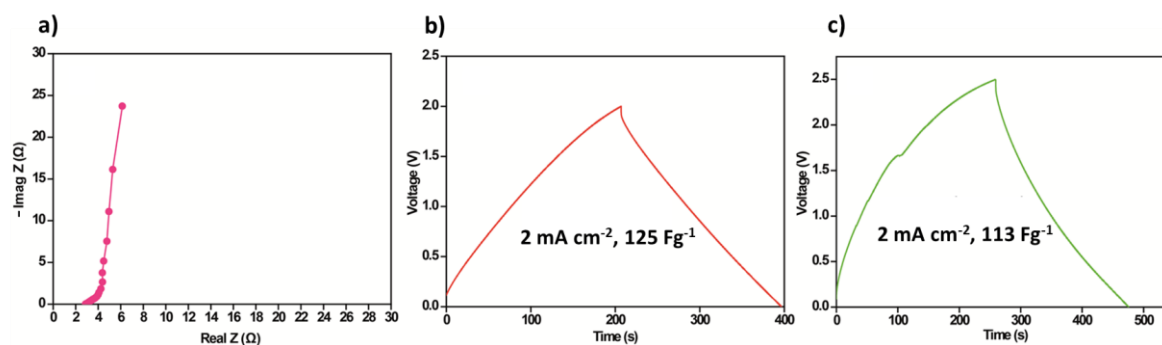


Figure 3.12. (a) The Nyquist plot associated with the YP-80F carbon-based SC device using standard nonaqueous electrolyte (3 M LiClO₄/PC) representing its ESR value; (b) charge-discharge profile recorded for the YP-80F carbon-based SC device at a current density of 2 mA cm⁻² in the standard nonaqueous electrolyte (3 M LiClO₄/PC) at (b) 2.0 V window, and (c) at 2.5 V window. ([*J. Mater. Chem. A*, 2017, 5, 8461-8476] - Reproduced by permission of The Royal Society of Chemistry).

these available pores are filled by the different species present in the solution. Occupancy of the PC molecules in the carbon micro-pores (1.0 to 2.0 nm) due to the interaction between the inner wall of the pores and solvent molecule is already explained in the literature.⁶⁵⁻⁶⁷ All the while, the non-covalent interactions operating between the PC and HPA monomer through the Li⁺ ions also facilitate the micro-pores which are already filled by the PC molecule to be occupied by HPA and Li⁺ ions as well. Therefore, in all the pores (including those pores having size > 2.0 nm), it is expected that all the moieties present in the pre-polymerized solution can exist simultaneously. Once all the pores are occupied, the remaining solution stays on the outer surface of the active material. Thus, during the UV curing process, the polymerization will take place inside the pores as well as on the outer surface of the pores and, hence, the interface formed is enhanced. Hence, the electrode|electrolyte interface formed will be similar to that formed by a liquid electrolyte. Therefore, the H-P-L-3M-S-3.8 shows a current-voltage characteristic similar to that of the H-P-L-3M-L-3.8 whereas superior to that of the PMMA-PC-L-S-3.8.

Further confirmation on the liquid-like electrode|electrolyte interface in the case of H-P-L-3M-S-3.8 is obtained from the EIS studies. The Nyquist plots obtained for H-P-L-3M-S-3.8, H-P-L-3M-L-3.8, and PMMA-PC-L-S-3.8 are superimposed and are given in **Figure 3.11b**. It is confirmed that the device with an area of 4 cm², made using H-P-L-3M-S-3.8, provides an ESR of approximately 2.20 Ω which is comparable to that of the system based on H-P-L-3M-L-3.8 (2.40 Ω). The true capacitive behavior of the

supercapacitor device prepared from the *in situ* process (H-P-L-3M-S-3.8) is apparent from the vertical nature of the Nyquist plot where there is a sharp increase in the imaginary part of the impedance, which is similar to that of the device made using the pre-polymerized liquid electrolyte. The device made using the standard nonaqueous electrolyte *viz.*, 3M LiClO₄/PC was also found to be showing an ESR of 2.8 Ω (**Figure 3.12a**) which is also comparable to that of H-P-L-3M-S-3.8. On the other hand, in the case of PMMA-PC-L-S-3.8, the ESR is found to be 8.50 Ω, and the plot shows a larger deviation from its true capacitive behavior as evident from the nature of the Nyquist plot at lower frequencies. The obtained ESR in the case of the supercapacitor device prepared using the *in situ* polymerization process is better compared to many reports available in the literature where dry polymer electrolytes, GPE solutions, and liquid electrolytes are used for the supercapacitor device fabrication.^{21-23,68} The absence of any semi-circle in the high-frequency region of the Nyquist plot indicates the very low charge transfer resistance offered by the solid-state device (H-P-L-3M-S-3.8) realized using the *in situ* processed H-P-L-3M-80% GPE.

The charge-discharge profile for H-P-L-3M-S-3.8 taken at a current density of 2 mA cm⁻² is compared to that of the H-P-L-3M-L-3.8 and PMMA-PC-L-S-3.8 counterparts. The superimposed plots are presented in **Figure 3.11c**. At a low current density of 2 mA cm⁻², H-P-L-3M-S-3.8 shows a mass-specific capacitance of 113 F g⁻¹, which is comparable to the performance of H-P-L-3M-L-3.8 (121 F g⁻¹) and PMMA-PC-L-S-3.8 (107 F g⁻¹). The specific capacitance value obtained for H-P-L-3M-S-3.8 is well matching with that obtained for the device using the standard nonaqueous liquid electrolyte, 3M LiClO₄/PC. The device with the standard nonaqueous liquid electrolyte is found to be showing mass-specific capacitances of 125 F g⁻¹ and 113 F g⁻¹ when operated at potential windows of 2.0 and 2.5 V, respectively (**Figure 3.12b** and **c**). The mass-specific capacitance obtained for the H-P-L-3M-S-3.8, H-P-L-3M-L-3.8, and PMMA-PC-L-S-3.8 devices obtained at various current densities are given in **Figure 3.11d**. It is observed that the *in situ* processed device shows very high retention (81%) of the specific capacitance as the current density is increased from a lower value of 2 mA cm⁻² to a higher value of 20 mA cm⁻². However, the PMMA-PC-L-S-3.8 system shows a drastic drop in the capacitance at higher current densities leading to poor capacitance retention of just 3 %. The IR drop associated with each device at 2 mA cm⁻² is depicted in **Figure 3.11c**, where ‘I’ and ‘R’ represent the applied current and the

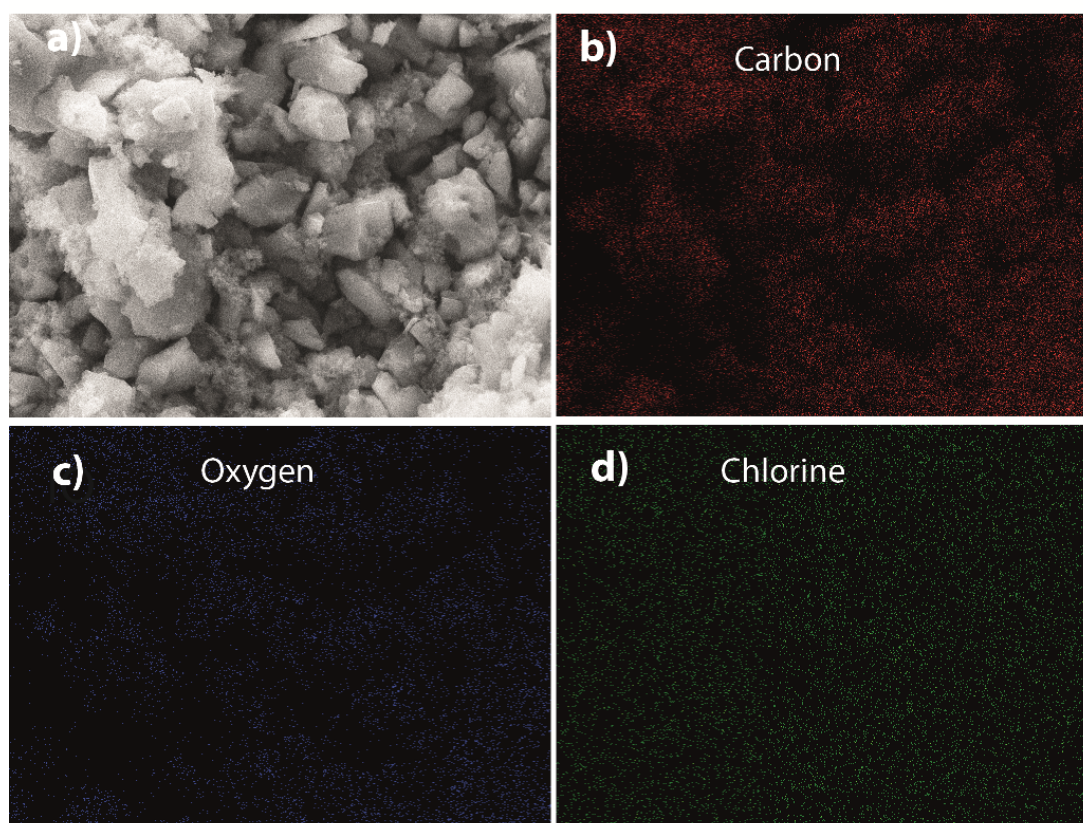


Figure 3.13. EDX mapping of the carbon sample after the *in situ* polymerization: (a) electron microscopy image of carbon portion which is taken after the *in situ* polymerization from the device; (b)-d) elemental mapping of carbon (b), oxygen (c) and chlorine (d) which are corresponding to the area represented in (a). ([*J. Mater. Chem. A*, 2017, 5, 8461-8476] - Reproduced by permission of The Royal Society of Chemistry). ESR, respectively. This clearly shows the advantage of H-P-L-3M-S-3.8 over PMMA-PC-L-S-3.8, where a low ESR is associated with H-P-L-3M-S-3.8 (IR drop of 50 mV) compared to PMMA-PC-L-S-3.8 (IR drop of 180 mV), which are also confirmed by the EIS analysis.

The high capacitance retention in the case of the *in situ* fabricated devices can be attributed to the low ESR associated with H-P-L-3M-S-3.8 as a result of the high conductivity of GPE ($4.7 \times 10^{-3} \text{ S cm}^{-1}$) along with the improved electrode|electrolyte interface formed during the *in situ* GPE generation. The fast ion transport owing to the high ionic conductivity associated with the *in situ* formed GPE also contributes to the excellent power capability of H-P-L-3M-S-3.8. The high ESR observed for PMMA-PC-L-S-3.8 underlines the inefficient electrode|electrolyte interface achieved using the conventional GPE solution. The energy density and power density of the solid-state

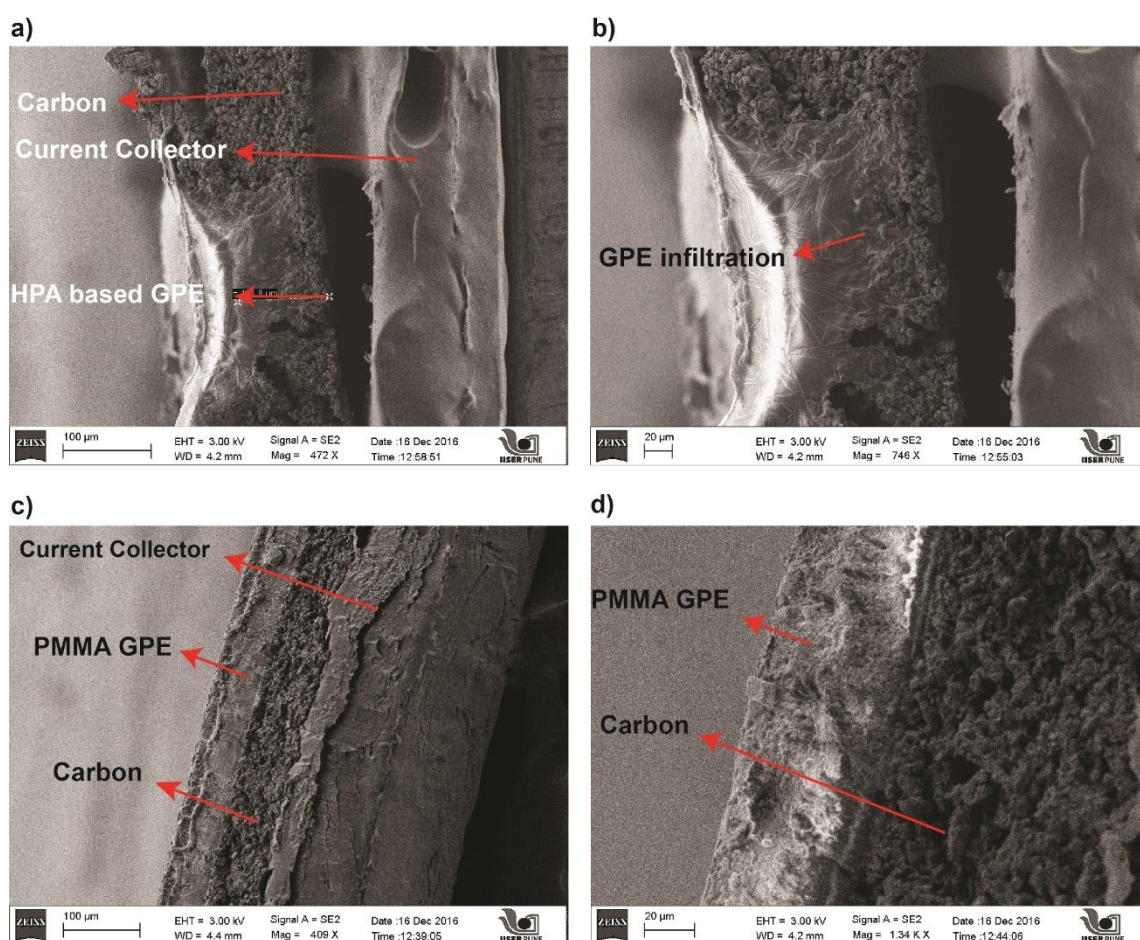


Figure 3.14. (a) and (b) represent the FESEM images of the electrode/electrolyte interface retrieved from the H-P-L-3M-S-3.8 device; (c) and (d) correspond to the same in the case of PMMA-PC-L-3M-S-3.8 device. ([*J. Mater. Chem. A*, 2017, 5, 8461-8476] - Reproduced by permission of The Royal Society of Chemistry).

supercapacitor device (H-P-L-3M-S-3.8) are also calculated and the corresponding Ragone plot is given in **Figure 3.11e**. The device is found to show a maximum energy density of 15.71 Wh kg^{-1} at a power density of 327 W kg^{-1} . The maximum power density obtained is 3550 W kg^{-1} at an energy density of 12.8 Wh kg^{-1} . The cycling stability of the fabricated device (H-P-L-3M-S-3.8) was also studied using the charge-discharge experiments conducted at a current density of 10 mA cm^{-2} (**Figure 3.11f**). The device was found to retain 81% of its initial capacitance even after 9000 continuous charge-discharge cycles. The stability is attributed to the highly interpenetrated GPEs along with the various covalent- and non-covalent interactions operating in the system. These interactions keep the conducting solvent inside the polymer matrix without exudation or evaporation. Thus, the high ionic conductivity of the GPE is preserved even after long

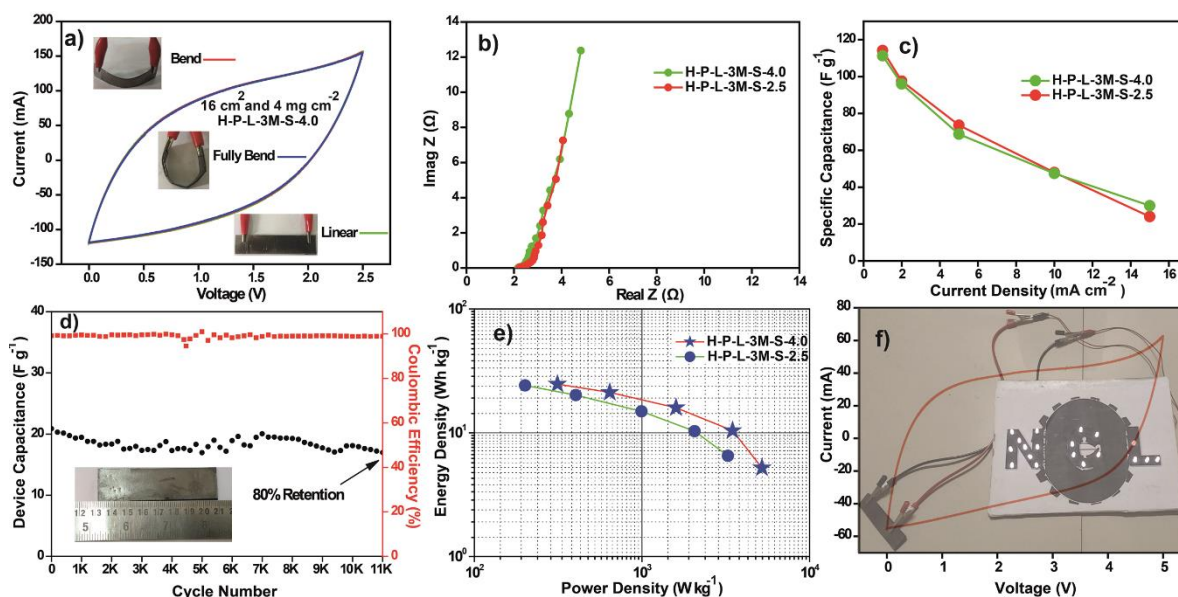


Figure 3.15. (a) CV profiles recorded at a scan rate of 50 mV s^{-1} of H-P-L-3M-S-4.0 under various flexible conditions as shown in the inset images; b) superimposed Nyquist plots obtained from the EIS analysis of H-P-L-3M-S-4.0 and H-P-L-3M-S-2.5; (c) the mass-specific capacitance values measured for H-P-L-3M-S-4.0 and H-P-L-3M-S-2.5 devices as a function of increasing current density values; (d) the cycling stability of the H-P-L-3M-S-4.0 studied by continuous CD cycles at a current density of 15 mA cm^{-2} (the image in the inset shows the dimensions of the H-P-L-3M-S-4.0); (e) combined Ragone plots comparing the energy and power densities of H-P-L-3M-S-2.5 and H-P-L-3M-S-4.0 supercapacitor devices; (f) two H-P-L-3M-S-2.5 devices are connected in series to achieve a maximum voltage of 5.0 V and the corresponding CV plot (the image in the background shows the glowing of 19 LEDs powered by the device). ([*J. Mater. Chem. A*, 2017, 5, 8461-8476] - Reproduced by permission of The Royal Society of Chemistry).

number of cycling. Moreover, the *in situ* generated GPE can help in the effective binding of the active electrode material in the current collector. This prevents the gradual delamination of the electrode material from the current collector on continuous CD cycles, hence, retaining the stability.

Confirmation of improved electrode|electrolyte interface

A small portion of carbon from the device (H-P-L-3M-S-3.8) is subjected to elemental mapping through EDX analysis (**Figure 3.13a-d**) to confirm the desired electrolyte infiltration into the carbon pores. The homogeneous distribution of chlorine and oxygen throughout the carbon region validates the uniform GPE infiltration of the electrolyte inside the carbon pores. However, the high-resolution imaging was restricted due to the

polymer burning. The cross-sectional FESEM image of the H-P-L-3M-S-3.8 device at different magnifications is given in **Figure 3.14a** and **b**, respectively. The extended electrode|electrolyte interface in the case of H-P-L-3M-S-3.8 is visible from **Figure 3.14b**. However, in the case of PMMA-PC-L-S-3.8 (**Figure 3.14c** and **d**), such an extended electrode|electrolyte interface is not observed. The GPE solution is found to be confined in the surface of the carbon-coated electrode. This experimental evidence supports the claim that the *in situ* GPE process provides a better electrode|electrolyte interface than the conventional GPE solutions.

Table 3.1. The electrochemical performances among the GPE based supercapacitor devices already reported in the literature and the devices reported in this work are compared and summarised. ([J. Mater. Chem. A, 2017, 5, 8461-8476] - Reproduced by permission of The Royal Society of Chemistry).

Active Electrode material	GPE used	Details of Device Fabrication	ESR	Specific Capacitance	Ref.
1. YP-80F	Poly (HEMA-co-MMA) with DPHPO4	GPE film is used, Tested the device in Sweaglock Cell, Electrodes pre-soaked with Electrolyte, Electrode area = 1.28 cm ² , Active material loading = 2 mg cm ⁻² .	95 Ω cm ²	123 F g ⁻¹ at 0.78 mA g ⁻¹	11
2. CNT	Silica Nano-Powder with [EMIM][NTf ₂]	GPE solution pressed in between the electrodes, Electrode area = 1 cm ² , Low Active material loading = 0.23 mg cm ⁻² .	30 Ω	135 F g ⁻¹ at 2 A g ⁻¹	21
3. AC	Poly (OEGMA-co-BnMA)	Organic electrolyte swollen GPE film is used, Area of the device = 1.13 cm ² , Mass-loading = Mass-loading=3.1 mg cm ⁻² .	20 Ω cm	24 F g ⁻¹ at 0.8 A g ⁻¹	23
4. AC	PEO-NaTFSI	GPE solution, Electrode area= 1 cm ² , Active material loading 4-5 mg, Device testing details are not provided.	6.8 Ω	25.6 F g ⁻¹ at 200 mA g ⁻¹	65
5. CNT	PS-PEO-PS tri-block copolymer with [EMIM][NTf ₂]	GPE solution spread over electrode, Device area = 1 cm ² , Loading not mentioned.	31.3 Ω	50.5 F g ⁻¹ at 1 A g ⁻¹	66
6. YP-80F	H-P-L-3M-80%	<i>In situ</i> GPE generation, Electrode Area = 16 cm ² , Mass-loading= 4.5 mg cm ⁻²	2.2 Ω	111 F g ⁻¹ at 0.20 A g ⁻¹	This Work

3.3.5 Scalability of the *in situ* process

The scalability of the *in situ* process in SC fabrication is demonstrated by the fabrication of large-area (an active area of = 16 cm²) prototype solid-state flexible supercapacitor devices with two different mass-loading of 2.5 mg cm⁻² and 4.0 mg cm⁻²

², which are respectively designated as H-P-L-3M-S-2.5 and H-P-L-3M-S-4.0. These devices are operated at a potential window of 2.5 V and their electrochemical performances are compared. **Figure 3.15a** represents the superimposed CV profiles (recorded at a scan rate of 50 mVs⁻¹) for the H-P-L-3M-S-4.0 device at various flexible conditions. It is found to retain similar current-voltage characteristics in all the flexible conditions, as depicted in the inset of the figure. This confirms the mechanical flexibility imparted by the *in situ* process to the supercapacitor device. The excellent fatigue resistance associated with the *in situ* formed GPE as already shown in **Figure 3.6c** and **e** helps the device to withstand such large mechanical strain during the flexible conditions without the failure of the device. The superimposed Nyquist plots of H-P-L-3M-S-2.5 and H-P-L-3M-S-4.0 are represented in **Figure 3.15b**. A very low ESR of 2.20 Ω is obtained for both the devices. The ESR value is in close agreement to that of the small area device (H-P-L-3M-S-3.8) as already mentioned in **Figure 3.11b**. The retention of very small ESR even in the scaled-up condition proves the robustness of the device owing to the excellent device fabrication process adopted. This is a key advantage exclusive to the *in situ* polymerization process in achieving an effective electrode|electrolyte interface irrespective of the mass-loading of the active material.

The superimposed plots of the mass-specific capacitance obtained for the scaled-up devices from the CD measurements at various current densities (in the scale of mA cm⁻²) are presented in **Figure 3.15c**. The H-P-L-3M-S-2.5 and H-P-L-3M-S-4.0 are found to show almost similar specific capacitance of 114 and 111 F g⁻¹ at a current density of 1 mA cm⁻². The cycling stability of H-P-L-3M-S-4.0 is studied by continuous CD cycles at a current density of 15 mA cm⁻² (**Figure 3.15d**). It is observed that 80% of the initial capacitance is retained even after 11000 continuous CD cycles with a Coulombic efficiency of 99%. The Ragone-plot for both the devices is also shown in **Figure 3.15e**. The H-P-L-3M-S-4.0 device shows a maximum power density of 3255 W kg⁻¹ at an energy density of 6.51 Wh kg⁻¹. The highest energy density obtained for the device is 24.1 Wh kg⁻¹ at a power density of 200 W kg⁻¹. The process adopted here could help in minimizing the complexity associated with the fabrication of the all-solid-state flexible supercapacitor devices without hampering their performance. This shows the viability of this novel process over the other tedious conventional device fabrication methods. The excellent electrochemical performance is attributed to the electrolyte robustness achieved during the GPE generation during the *in situ* process. The flexibility imparted to the device is also evident. A real-life demonstration is also shown by the

lighting of 19 LEDs using a 5.0 V device (two 2.5 V devices connected in series). The digital image of the demonstration is given in **Figure 3.14f**. The electrochemical performances among the GPE based supercapacitor devices already reported in the literature and the devices reported in this work are compared and summarized in **Table 3.1**.^{11,21,23,65,66}

3.4 Conclusion

In this work, the process of the UV assisted *in situ* GPE generation adopted for the fabrication of a solid-state, nonaqueous, flexible SC devices is found to mimic the electrode|electrolyte interface close in nature to that of a liquid electrolyte. The GPE shows excellent ionic conductivity ($4.7 \times 10^{-3} \text{ S cm}^{-1}$) and mechanical properties. The higher solvent holding capability augmented with the excellent mechanical stability of the GPE arises as a result of the various covalent and non-covalent crosslinks operating in the GPE. The existing trade-off between the higher solvent holding ability of the GPE and the mechanical stability could be minimized to an extent by this work. The solid-state flexible SCs fabricated using the above-mentioned process exhibits very low ESR ($2.20 \text{ } \Omega$) at higher (4.0 mg cm^{-2}) and lower (2.5 mg cm^{-2}) mass-loading of the active electrode material. Thus, it is concluded that an effective electrode|electrolyte interface is achievable irrespective of the electrode mass-loading when the *in situ* process is adopted for the supercapacitor device fabrication. Thus, even thicker electrodes can be used for the supercapacitor device fabrication, which is indeed important in the commercial aspect. A 4 cm^2 device with an electrode mass-loading of 3.8 mg cm^{-2} (H-P-L-3M-S-3.8), fabricated using the *in situ* process, is found to provide a mass-specific capacitance of 113 F g^{-1} , when operated in a potential window of 2.0 V. The process is scaled-up to a large area (16 cm^2) with high mass-loading of 4.0 mg cm^{-2} for the preparation of a solid-state flexible SC device (H-P-L-3M-S-4.0). The device is found to show a capacitance of 111 F g^{-1} at a current density of 1 mA cm^{-2} (0.25 A g^{-1}) when operated at a voltage window of 2.5 V. The same device shows an energy density of 6.51 Wh kg^{-1} at a power density of 3255 W kg^{-1} . Even though in this report we have shown the viability of the process towards the SC design, it can be further extended for the fabrication of other electrochemical devices such as metal-ion batteries, metal-air batteries, etc.

3.5 References

- [1] Conway, B. E. Electrochemical supercapacitors: scientific fundamentals and technological applications, Springer Science & Business Media: 2013.

-
- [2] Zhang, Y.; Feng, H.; Wu, X.; Wang, L.; Zhang, A.; Xia, T.; Dong, H.; Li, X.; Zhang, L. Progress of electrochemical capacitor electrode materials: A review. *International journal of hydrogen energy* 2009, 34 (11), 4889-4899.
- [3] Simon, P.; Gogotsi, Y. Materials for electrochemical capacitors. In *Nanoscience and technology: a collection of reviews from Nature journals*; World Scientific: 2010; pp 320-329.
- [4] Béguin, F.; Presser, V.; Balducci, A.; Frackowiak, E. Carbons and electrolytes for advanced supercapacitors. *Advanced materials* 2014, 26 (14), 2219-2251.
- [5] Xu, K. Nonaqueous liquid electrolytes for lithium-based rechargeable batteries. *Chemical reviews* 2004, 104 (10), 4303-4418.
- [6] Agrawal, R.; Pandey, G. Solid polymer electrolytes: materials designing and all-solid-state battery applications: an overview. *Journal of Physics D: Applied Physics* 2008, 41 (22), 223001.
- [7] Winter, M.; Brodd, R. J., *What are batteries, fuel cells, and supercapacitors?* ACS Publications: 2004.
- [8] Wright, P. V. Polymer electrolytes—the early days. *Electrochimica Acta* 1998, 43 (10-11), 1137-1143.
- [9] Hallinan Jr, D. T.; Balsara, N. P. Polymer electrolytes. *Annual review of materials research* 2013, 43, 503-525.
- [10] Song, J.; Wang, Y.; Wan, C. C. Review of gel-type polymer electrolytes for lithium-ion batteries. *Journal of power sources* 1999, 77 (2), 183-197.
- [11] Łatoszyńska, A. A.; Żukowska, G. Z.; Rutkowska, I. A.; Taberna, P.-L.; Simon, P.; Kulesza, P. J.; Wieczorek, W. Non-aqueous gel polymer electrolyte with phosphoric acid ester and its application for quasi solid-state supercapacitors. *Journal of Power Sources* 2015, 274, 1147-1154.
- [12] Tillmann, S.; Isken, P.; Lex-Balducci, A. Gel polymer electrolyte for lithium-ion batteries comprising cyclic carbonate moieties. *Journal of Power Sources* 2014, 271, 239-244.
- [13] Zhong, C.; Deng, Y.; Hu, W.; Qiao, J.; Zhang, L.; Zhang, J. A review of electrolyte materials and compositions for electrochemical supercapacitors. *Chemical Society Reviews* 2015, 44 (21), 7484-7539.
- [14] Latham, R.; Rowlands, S.; Schlindwein, W. Supercapacitors using polymer electrolytes based on poly (urethane). *Solid State Ionics* 2002, 147 (3-4), 243-248.

- [15] Shao, Y.; Rajput, N. N.; Hu, J.; Hu, M.; Liu, T.; Wei, Z.; Gu, M.; Deng, X.; Xu, S.; Han, K. S. Nanocomposite polymer electrolyte for rechargeable magnesium batteries. *Nano Energy* 2015, 12, 750-759.
- [16] Jin, L.; Howlett, P. C.; Pringle, J. M.; Janikowski, J.; Armand, M.; MacFarlane, D. R.; Forsyth, M. An organic ionic plastic crystal electrolyte for rate capability and stability of ambient temperature lithium batteries. *Energy & Environmental Science* 2014, 7 (10), 3352-3361.
- [17] Membreno, D.; Smith, L.; Shin, K.-S.; Chui, C. O.; Dunn, B. A high-energy-density quasi-solid-state carbon nanotube electrochemical double-layer capacitor with ionogel electrolyte. *Translational Materials Research* 2015, 2 (1), 015001.
- [18] Anothumakkool, B.; Torris AT, A.; Bhange, S. N.; Unni, S. M.; Badiger, M. V.; Kurungot, S. Design of a high performance thin all-solid-state supercapacitor mimicking the active interface of its liquid-state counterpart. *ACS applied materials & interfaces* 2013, 5 (24), 13397-13404.
- [19] Anothumakkool, B.; Torris AT, A.; Veeliyath, S.; Vijayakumar, V.; Badiger, M. V.; Kurungot, S. High-performance flexible solid-state supercapacitor with an extended nanoregime interface through in situ polymer electrolyte generation. *ACS applied materials & interfaces* 2016, 8 (2), 1233-1241.
- [20] Puthusseri, D.; Aravindan, V.; Anothumakkool, B.; Kurungot, S.; Madhavi, S.; Ogale, S. From Waste Paper Basket to Solid State and Li-HEC Ultracapacitor Electrodes: A Value Added Journey for Shredded Office Paper. *Small* 2014, 10 (21), 4395-4402.
- [21] Kang, Y. J.; Chung, H.; Han, C.-H.; Kim, W. All-solid-state flexible supercapacitors based on papers coated with carbon nanotubes and ionic-liquid-based gel electrolytes. *Nanotechnology* 2012, 23 (6), 065401.
- [22] Isken, P.; Winter, M.; Passerini, S.; Lex-Balducci, A. Methacrylate based gel polymer electrolyte for lithium-ion batteries. *Journal of power sources* 2013, 225, 157-162.
- [23] Schroeder, M.; Isken, P.; Winter, M.; Passerini, S.; Lex-Balducci, A.; Balducci, A. An investigation on the use of a methacrylate-based gel polymer electrolyte in high power devices. *Journal of the Electrochemical Society* 2013, 160 (10), A1753.
- [24] Anothumakkool, B.; Bhange, S. N.; Badiger, M. V.; Kurungot, S. Electrodeposited polyethylenedioxythiophene with infiltrated gel electrolyte interface: a close contest of an all-solid-state supercapacitor with its liquid-state counterpart. *Nanoscale* 2014, 6 (11), 5944-5952.

- [25] Meng, C.; Liu, C.; Chen, L.; Hu, C.; Fan, S. Highly flexible and all-solid-state paperlike polymer supercapacitors. *Nano letters* 2010, 10 (10), 4025-4031.
- [26] Kühn, P. T.; Meijer, T. L.; Schiavon, I.; van Poll, M.; van Aken, J.; Groen, S.; Kuijter, R.; van Kooten, T. G.; van Rijn, P. Non-Covalently Stabilized Alginate Hydrogels as Functional Cell Scaffold Material. *Macromolecular bioscience* 2016, 16 (11), 1693-1702.
- [27] Chen, Q.; Yan, X.; Zhu, L.; Chen, H.; Jiang, B.; Wei, D.; Huang, L.; Yang, J.; Liu, B.; Zheng, J. Improvement of mechanical strength and fatigue resistance of double network hydrogels by ionic coordination interactions. *Chemistry of Materials* 2016, 28 (16), 5710-5720.
- [28] Morita, M.; Qiao, J.-L.; Yoshimoto, N.; Ishikawa, M. Application of proton conducting polymeric electrolytes to electrochemical capacitors. *Electrochimica acta* 2004, 50 (2-3), 837-841.
- [29] Wei, J.; Wang, J.; Su, S.; Wang, S.; Qiu, J. Tough and fully recoverable hydrogels. *Journal of Materials Chemistry B* 2015, 3 (26), 5284-5290.
- [30] Lee, T. Y.; Roper, T. M.; Jönsson, E. S.; Guymon, C.; Hoyle, C. Influence of hydrogen bonding on photopolymerization rate of hydroxyalkyl acrylates. *Macromolecules* 2004, 37 (10), 3659-3665.
- [31] Sopeña, S.; Fiorani, G.; Martín, C.; Kleij, A. W. Highly Efficient Organocatalyzed Conversion of Oxiranes and CO₂ into Organic Carbonates. *ChemSusChem* 2015, 8 (19), 3248-3254, DOI: 10.1002/cssc.201500710.
- [32] Yuan, K.; Bian, H.; Shen, Y.; Jiang, B.; Li, J.; Zhang, Y.; Chen, H.; Zheng, J. Coordination number of Li⁺ in nonaqueous electrolyte solutions determined by molecular rotational measurements. *The Journal of Physical Chemistry B* 2014, 118 (13), 3689-3695.
- [33] Johansson, P.; Edvardsson, M.; Adebahr, J.; Jacobsson, P. Mixed solvent and polymer coordination in PAN and PMMA gel polymer electrolytes studied by ab initio calculations and Raman spectroscopy. *The Journal of Physical Chemistry B* 2003, 107 (46), 12622-12627.
- [34] Shakourian-Fard, M.; Kamath, G.; Sankaranarayanan, S. K. Evaluating the Free Energies of Solvation and Electronic Structures of Lithium-Ion Battery Electrolytes. *ChemPhysChem* 2016, 17 (18), 2916-2930.

- [35] Arslanargin, A.; Powers, A.; Beck, T. L.; Rick, S. W. Models of ion solvation thermodynamics in ethylene carbonate and propylene carbonate. *The Journal of Physical Chemistry B* 2016, 120 (8), 1497-1508.
- [36] Giorgini, M. G.; Futamatagawa, K.; Torii, H.; Musso, M.; Cerini, S. Solvation structure around the Li^+ ion in mixed cyclic/linear carbonate solutions unveiled by the Raman noncoincidence effect. *The Journal of Physical Chemistry Letters* 2015, 6 (16), 3296-3302.
- [37] Bhatt, M. D.; Cho, M.; Cho, K. Conduction of Li^+ cations in ethylene carbonate (EC) and propylene carbonate (PC): comparative studies using density functional theory. *Journal of Solid State Electrochemistry* 2012, 16 (2), 435-441.
- [38] Tasaki, K.; Goldberg, A.; Liang, J.-J.; Winter, M. New Insight into Differences in Cycling Behaviors of a Lithium-ion Battery Cell Between the Ethylene Carbonate-and Propylene Carbonate-Based Electrolytes. *ECS Transactions* 2011, 33 (28), 59.
- [39] Kilambi, H.; Stansbury, J. W.; Bowman, C. N. Deconvoluting the impact of intermolecular and intramolecular interactions on the polymerization kinetics of ultrarapid mono (meth) acrylates. *Macromolecules* 2007, 40 (1), 47-54.
- [40] Zhou, D.; Zhou, R.; Chen, C.; Yee, W.-A.; Kong, J.; Ding, G.; Lu, X. Non-volatile polymer electrolyte based on poly (propylene carbonate), ionic liquid, and lithium perchlorate for electrochromic devices. *The Journal of Physical Chemistry B* 2013, 117 (25), 7783-7789.
- [41] Chen, Q.; Chen, H.; Zhu, L.; Zheng, J. Engineering of tough double network hydrogels. *Macromolecular Chemistry and Physics* 2016, 217 (9), 1022-1036.
- [42] Harrass, K.; Krüger, R.; Möller, M.; Albrecht, K.; Groll, J. Mechanically strong hydrogels with reversible behaviour under cyclic compression with MPa loading. *Soft Matter* 2013, 9 (10), 2869-2877.
- [43] Sekhon, S. Conductivity behaviour of polymer gel electrolytes: Role of polymer. *Bulletin of Materials Science* 2003, 26 (3), 321-328.
- [44] Silva, M. M.; Barros, S. C.; Smith, M. J.; MacCallum, J. R. Study of novel lithium salt-based, plasticized polymer electrolytes. *Journal of power sources* 2002, 111 (1), 52-57.
- [45] Kim, D.-W.; Kim, Y.-R.; Park, J.-K.; Moon, S.-I. Electrical properties of the plasticized polymer electrolytes based on acrylonitrile-methyl methacrylate copolymers. *Solid State Ionics* 1998, 106 (3-4), 329-337.
- [46] Tarascon, J.-M.; Gozdz, A.; Schmutz, C.; Shokoohi, F.; Warren, P. Performance of Bellcore's plastic rechargeable Li-ion batteries. *Solid State Ionics* 1996, 86, 49-54.

- [47] Abraham, K.; Alamgir, M. Li⁺-conductive solid polymer electrolytes with liquid-like conductivity. *J. Electrochem. Soc* 1990, 137 (5), 1657.
- [48] Ue, M. Chemical capacitors and quaternary ammonium salts. *Electrochemistry* 2007, 75 (8), 565-572.
- [49] Xu, K.; Ding, M. S.; Jow, T. R. Quaternary onium salts as nonaqueous electrolytes for electrochemical capacitors. *Journal of the electrochemical Society* 2001, 148 (3), A267-A274.
- [50] Huang, L.-Y.; Shih, Y.-C.; Wang, S.-H.; Kuo, P.-L.; Teng, H. Gel electrolytes based on an ether-abundant polymeric framework for high-rate and long-cycle-life lithium ion batteries. *Journal of Materials Chemistry A* 2014, 2 (27), 10492-10501.
- [51] Wang, S.-H.; Kuo, P.-L.; Hsieh, C.-T.; Teng, H. Design of poly (acrylonitrile)-based gel electrolytes for high-performance lithium ion batteries. *ACS applied materials & interfaces* 2014, 6 (21), 19360-19370.
- [52] Kumar, D.; Hashmi, S. Ionic liquid based sodium ion conducting gel polymer electrolytes. *Solid State Ionics* 2010, 181 (8-10), 416-423.
- [53] Prasanth, R.; Aravindan, V.; Srinivasan, M. Novel polymer electrolyte based on cobweb electrospun multi component polymer blend of polyacrylonitrile/poly (methyl methacrylate)/polystyrene for lithium ion batteries—Preparation and electrochemical characterization. *Journal of Power Sources* 2012, 202, 299-307.
- [54] Forsyth, M.; Meakin, P.; MacFarlane, D.; Hill, A. Free volume and conductivity of plasticized polyether-urethane solid polymer electrolytes. *Journal of Physics: Condensed Matter* 1995, 7 (39), 7601.
- [55] Christie, A. M.; Lilley, S. J.; Staunton, E.; Andreev, Y. G.; Bruce, P. G. Increasing the conductivity of crystalline polymer electrolytes. *Nature* 2005, 433 (7021), 50-53.
- [56] Kuo, C.-W.; Huang, C.-W.; Chen, B.-K.; Li, W.-B.; Chen, P.-R.; Ho, T.-H.; Tseng, C.-G.; Wu, T.-Y. Enhanced ionic conductivity in PAN-PEGME-LiClO₄-PC composite polymer electrolytes. *International Journal of Electrochemical Science* 2013, (8), 3834-3850.
- [57] Kuo, C.-W.; Li, W.-B.; Chen, P.-R.; Liao, J.-W.; Tseng, C.-G.; Wu, T.-Y. Effect of plasticizer and lithium salt concentration in PMMA-based composite polymer electrolytes. *International Journal of Electrochemical Science* 2013.
- [58] Seki, S.; Susan, M. A. B. H.; Kaneko, T.; Tokuda, H.; Noda, A.; Watanabe, M. Distinct difference in ionic transport behavior in polymer electrolytes depending on the matrix

- polymers and incorporated salts. *The Journal of Physical Chemistry B* 2005, 109 (9), 3886-3892.
- [59] Pas, S. J.; Ingram, M. D.; Funke, K.; Hill, A. J. Free volume and conductivity in polymer electrolytes. *Electrochimica acta* 2005, 50 (19), 3955-3962.
- [60] Xue, Y.; Quesnel, D. J. Synthesis and electrochemical study of sodium ion transport polymer gel electrolytes. *RSC advances* 2016, 6 (9), 7504-7510.
- [61] Polu, A. R.; Rhee, H.-W.; Kim, D. K. New solid polymer electrolytes (PEO 20–LiTDI–SN) for lithium batteries: structural, thermal and ionic conductivity studies. *Journal of Materials Science: Materials in Electronics* 2015, 26 (11), 8548-8554.
- [62] Perdew, J.; Burke, K.; Ernzerhof, M. Quantum Monte Carlo Calculations for a Large Number of Bosons in a Harmonic Trap. *Physical Review Letters* 1996, 77, 3865-3868.
- [63] Schäfer, A.; Huber, C.; Ahlrichs, R. Fully optimized contracted Gaussian basis sets of triple zeta valence quality for atoms Li to Kr. *The Journal of Chemical Physics* 1994, 100 (8), 5829-5835.
- [64] TURBOMOLE, V., 10: A Development of University of Karlsruhe and Forschungszentrum Karlsruhe GmbH 1989–2007, TURBOMOLE GmbH, since 2007, 2008. 2014.
- [65] Ramasamy, C.; Anderson, M. An activated carbon supercapacitor analysis by using a gel electrolyte of sodium salt-polyethylene oxide in an organic mixture solvent. *Journal of Solid State Electrochemistry* **2014**, 18 (8), 2217-2223.
- [66] Kang, Y. J.; Chun, S.-J.; Lee, S.-S.; Kim, B.-Y.; Kim, J. H.; Chung, H.; Lee, S.-Y.; Kim, W. All-solid-state flexible supercapacitors fabricated with bacterial nanocellulose papers, carbon nanotubes, and triblock-copolymer ion gels. *ACS nano* **2012**, 6 (7), 6400-6406.

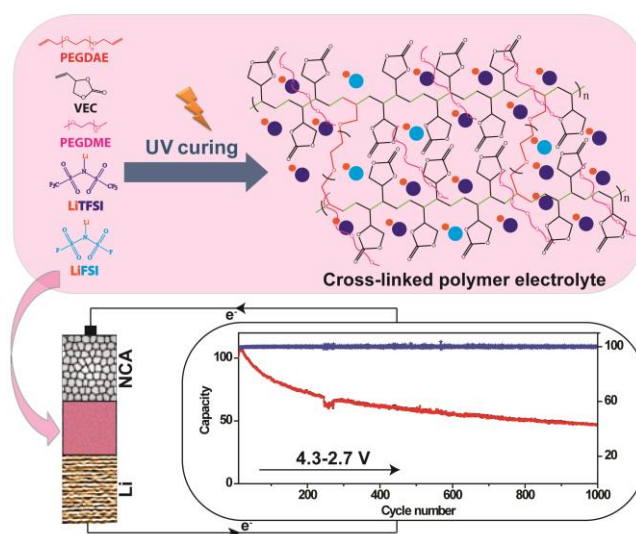
Chapter 4

Dioxolanone Anchored Poly (Allyl Ether)-Based Crosslinked Dual-Salt Polymer Electrolytes for High-Voltage Lithium Metal Batteries

In this chapter, novel crosslinked polymer electrolytes (XPEs) are synthesized by free radical co-polymerization induced by ultraviolet (UV)-light irradiation. The reactive solution is

composed of a difunctional poly(ethylene glycol) diallyl ether oligomer (PEGDAE), a monofunctional reactive diluent 4-vinyl-1,3-dioxolan-2-one (VEC), and a stock solution containing a lithium salt (LiTFSI) dissolved in carbonate-free non-volatile plasticizer, poly(ethylene glycol) dimethyl ether (PEGDME). The resulting polymer matrix can be represented as a linear polyethylene chain functionalized with

cyclic carbonate (dioxolanone) moieties and crosslinked by ethylene oxide units. A series of XPEs are prepared by varying the [O]/[Li] ratio (24 to 3) of the stock solution in the polymer matrix and characterized using TGA-MS, DSC, NMR, and electrochemical techniques. Later, LiFSI salt is incorporated into the electrolyte system to produce a dual-salt XPE that exhibits improved electrochemical performance, a stable interface against lithium metal, and enhanced physicochemical characteristics to be used with high-voltage cathodes. Finally, the XPE films are assembled in a lab-scale lithium metal battery (LMB) configuration with carbon-coated LiFePO₄ (LFP) or LiNi_{0.8}Co_{0.15}Al_{0.05}O₂ (NCA) as a cathode, and galvanostatically cycled at 20, 40 and 60°C. Remarkably, at 20°C, the NCA based lithium metal cells displayed excellent cycling stability and good capacity retention (>50%) even after 1000 cycles.



Contents in this chapter is published in the article: DOI: 10.1021/acsami.9b16348.

Reprinted (adapted) with permission from (ACS Appl. Mater. Interfaces 2020, 12, 1, 567-579).

Copyright (2020) American Chemical Society.

4.1 Introduction

Lithium metal anode based rechargeable batteries (LMBs) are proposed to be the potential candidates over the lower energy-dense state-of-the-art lithium-ion batteries (LIBs).¹ However, the factor impeding the large scale employment of LMBs is associated with the lack of a suitable electrolyte. The conventional carbonate-based liquid electrolytes used in LIBs are not compatible with metallic lithium and can incite the deposition of high surface area lithium (HSAL)³ and related growth of dendrites during the charge/discharge process.⁴ Besides, cross-talk of soluble species from the cathode may harm the Li metal anode.⁵ These unwanted processes lead to performance deterioration and safety hazards, thus, it is inevitable to design suitable electrolytes that can be used against lithium metal anode for the fabrication of safe and reliable LMBs.

In general, solid polymer electrolytes (SPEs) are considered as a safe alternative to the currently used organic carbonate-based liquid electrolytes, especially for LMBs.⁶ Most investigated Li⁺-ion conducting SPEs are consisting of a lithium salt dissolved in a polymer matrix such as polyethylene oxide (PEO) and others,⁷ which often possess low ionic conductivity due to the high crystallinity. An effective strategy to improve the ionic conductivity of the polymer electrolytes is to introduce the concept of quasi-solid-state behavior, which is realized in gel polymer electrolytes (GPEs).⁸ In GPEs, in addition to a solid polymer phase and a lithium salt, a liquid phase is also present. The liquid phase in most cases can be the electrolyte solvent itself and functions also as a plasticizer.⁹ Apart from improved ionic conductivity, the liquid phase in GPEs can induce effective wetting of the electrode surfaces providing an improved electrode-electrolyte interaction as compared to their SPE counterparts. The conventional approach for the preparation of GPE films sequentially follows the synthesis of a suitable polymer matrix, casting it into a free-standing film using a suitable solvent and swelling in a liquid electrolyte.¹⁰ Considering the practical intricacies associated with these tedious processes, the facile production of crosslinked polymer electrolyte (XPE) by ultraviolet (UV)-induced free-radical copolymerization (UV curing) is considered as an effective and solvent-free electrolyte production approach.¹¹ In this method, the polymer electrolytes are prepared from a reactive solution composed of one or more polymerizable monomers or oligomers, conducting salts, plasticizer, and a free-radical initiator by exposing to photo- or thermal energy source. This method is commonly known as the *in situ* synthesis since the generation of polymer electrolyte takes place in a single step unlike multiple steps involved in the classical approach.¹²⁻¹⁴ Additionally, the *in situ* synthesis (direct deposition) is

handy in terms of improving the electrode-electrolyte interface when the polymer electrolyte is directly prepared on an electrode surface in line with the device fabrication.¹¹⁻¹⁴

Several classes of functionalities have been used for the synthesis of XPEs by free-radical induced copolymerization approach, and among them, (meth)acrylate-based monomers are the most explored category.^{15, 16} However, the ester groups in acrylates may passivate the lithium metal surface with the formation of a ketol product. This makes them unsustainable to be used for a prolonged number of charge-discharge cycles against lithium metal anode.¹⁷ Therefore, an alternate approach could be the designing of efficient ester-free polymer electrolyte systems which can be easily processed. The previous attempts in this line have been reported by Cui *et al.* where polyvinylene carbonate (PVCA-SPE) based polymer electrolytes are prepared by in-situ thermal polymerization.^{18, 19} However, the application in LMBs is achieved only using reinforcing the electrolyte with a cellulose-based separator and the preparation of PVCA-SPE takes more than 34 h. Several reports are also available on crosslinked and non-crosslinked poly(ethylene oxide carbonates)-based polymer electrolytes for LMBs.^{20, 21} However, these systems also involve tedious synthesis routes such as ring-opening and condensation polymerization methods. In several recent works, glymes, allyl glycidyl ethers, allyl ethers, etc., are used for the preparation of crosslinked polymer electrolytes.²²⁻²⁴ Most studies are either limited to low-voltage cathodes or do not involve any cycling studies in LMB configuration. From the available literature, it can be seen that polymer electrolyte systems in which both PEO and cyclic carbonate moieties co-exist are rarely reported. An exception is a recent work by Itoh *et al.* in which Li⁺-ion conducting properties of alternating copolymers of vinyl ethers with methoxy oligo(ethyleneoxy)ethyl groups and vinylene carbonate are reported. However, no cycling studies have been carried out in lithium metal cells.²⁵

In this work, novel acrylate-free XPEs consisting of an interesting macromolecular architecture where both the cyclic carbonate and PEO moieties are integrated into a polyethylene-based polymer backbone is developed. The XPE membranes are prepared by photo-crosslinking of monomers *viz.*, poly(ethylene glycol) diallyl ether (PEGDAE), and 4-vinyl-1,3-dioxolan-2-one (VEC) in the presence of a non-volatile carbonate-free plasticizer (poly(ethylene glycol) dimethyl ether (PEGDME) and lithium salts (here LiTFSI and LiFSI are used). The XPE membrane composed of LiTFSI salt alone is represented as single-salt XPE (S-XPE) whereas the other category with both LiTFSI and LiFSI is termed as dual-salt XPE (D-XPE). The applicability of these XPE membranes is demonstrated by fabricating lab-scale lithium metal cells with Li[Ni_{0.8}Co_{0.15}Al_{0.05}]O₂ (NCA) or carbon-coated LiFePO₄ (LFP) as

cathodes. As of our understanding, this is the first report where a copolymer electrolyte matrix consisting of poly(vinyl ethylene carbonate) is crosslinked using ethylene oxide (EO) units and galvanostatically cycled against high-voltage cathodes in LMB configuration.

4.2 Experimental section

4.2.1 Materials

Unless otherwise specified separately, all the materials used in this work were purchased from Sigma Aldrich. For the synthesis of the bifunctional crosslinker oligomer named poly(ethylene glycol) diallyl ether (PEGDAE), allyl bromide, sodium hydride (NaH) and poly(ethylene glycol) 400 (PEG, average $M_n = 400$ Da) were used. Dimethylformamide (DMF), dichloromethane (DCM), and deionized water (Millipore) were used as solvents during the synthesis. 4-Vinyl-1,3-dioxolan-2-one (VEC) was used as the monofunctional monomer. Lithium bis(trifluoromethanesulfonyl)imide (LiTFSI) and lithium bis(fluorosulfonyl)imide (LiFSI) were used as the source of lithium ions. 2-Hydroxy-2-methylpropiophenone (HMPP) was used as the free-radical photo-initiator. The carbonate-free non-volatile plasticizer poly(ethylene glycol) dimethyl ether (PEGDME, average $M_n = 500$ Da) was purchased from Merck. Deuterated acetonitrile (CD_3CN) was used as the solvent for carrying out 1H - and ^{13}C -NMR measurements. Carbon-coated lithium iron phosphate (C-LiFePO₄, LifePower[®]) was purchased from Phostech Lithium Inc. and the binder polyvinylidenedifluoride (PVdF, Solef[®]5130) was from Solvay. Li[Ni_{0.8}Co_{0.15}Al_{0.05}]O₂ (NCA) was procured from Hunan Shanshan Energy Technology Co. Ltd. The carbon black, Super P[®] was purchased from TIMCAL and used as an electron conductive additive.

4.2.2 Synthesis of PEGDAE

The synthesis procedure of PEGDAE oligomer is adapted from the report of Boydston et al.²⁶ In a typical synthesis, 3 g of NaH (75.00 mmol) was added to 20 ml DMF and kept for continuous stirring (1 h) to form a suspension in a two-necked flask placed in an ice bath. A solution of 5 g PEG dissolved in 10 ml DMF (12.50 mmol, 1.25 M) was added dropwise to this suspension under continuous stirring. Later, the reaction mixture was brought back to room temperature (RT) and continuously stirred for another 1 h. The reaction flask was again placed in an ice bath under stirring and 10.80 ml (125 mmol) of allyl bromide was added dropwise and the reaction mixture was stirred further for another 48 h during which the ice bath turned to RT. After 48 h, the ice bath was reinstated under stirring and 5 ml of distilled water was added drop-wise to the reaction mixture. Later, 100 ml of distilled water was further added into the reaction mixture and a combined organic layer was extracted with DCM (6×50ml) followed by drying with sodium sulfate (Na₂SO₄). Finally, the solvent was evaporated under vacuum to

get the crude product and pure PEGDAE was recovered by subsequent washing with hexane and acetone, respectively.

4.2.3 Preparation of polymer electrolyte

The sample preparation was carried out in an environmentally controlled dry-room (100 m², R.H. <0.02% at 20 °C). Before the preparation of the XPE membranes, stock solutions were prepared by dissolving various amounts of LiTFSI in PEGDME (precisely, 0.93, 1.86, 2.80, 4.65, and 7.30 m of LiTFSI in PEGDME, where ‘m’ is the molality of LiTFSI in the solution). The prepared solutions were labeled as Li-P-x, where ‘x’ ranges from 1 to 5 with respect to the ascending order of [O]/[Li] ratio in PEGDME/LiTFSI stock solution (the formulation and [O]_{PEGDME}/[Li] ratios of all LiTFSI/PEGDME bulk solutions are given in **Table 4.1**). [O]_{PEGDME} and [Li] represent the number of moles of oxygen atoms from PEGDME and Li⁺-ions from LiTFSI, respectively. Later, reactive solutions in the ratio of PEGDAE:VEC:Li-P-x in 1:1:2 by weight was prepared. Additionally, 5 wt.% of HMPP initiator was also added to this reactive mixture. The reactive solution was cast in between two Mylar films followed by a photo-polymerization process of 1 h using a UV lamp (Hoenle, UVACUBE 100). After the UV irradiation, the XPE films could be peeled off; later these films were punched into discs for further characterizations. The XPE membranes obtained by using the aforementioned process are termed as S-XPE-x (or simply S-XPEs). Here also ‘x’ has the values from 1 to 5 depending on the [O]/[Li] ratio of the PEGDME/LiTFSI stock solution used. The term ‘S’ indicates that the XPE is prepared using a single-salt, LiTFSI, as the Li⁺-ions source. Similarly, D-XPE-x (or simply D-XPEs) samples were also prepared for comparison purposes where ‘D’ indicates the presence of dual-salt (in D-XPEs, small amounts of LiFSI were added along with LiTFSI). During the preparation of D-XPE-x membranes, 3 wt.% of LiFSI was added to the previously mentioned solution consisting of reactive monomers and Li-P-x (PEGDAE: VEC: Li-P-x= 1: 1: 2 by weight). The second series of the reactive solution was prepared using this mixture by the addition of 5 wt.% of HMPP initiator. The formulations of all the reactive solutions/S-XPE-x samples under investigation and their related [O]/[Li] ratio are given in **Table 4.2**. The same for all the D-XPE-x samples are also provided in **Table 4.3**. For comparison purposes, a crosslinked polymer system that contains PEGDAE:VEC:PEGDME in the absence of lithium salt was also prepared and this sample is labeled as S-XPE-0, where ‘0’ represents the absence of Li⁺-ions. The average thickness of the XPE membranes used here for various investigations is about 200 ± 10 μm.

Table 4.1. The formulation and $[O]_{\text{PEGDME}}/[Li]$ ratios of all the LiTFSI/PEGDME (Li-P-*x*) bulk solutions. (Reprinted (adapted) with permission from (ACS Appl. Mater. Interfaces 2020, 12, 1, 567-579). Copyright (2020) American Chemical Society).

Sample name	molality of LiTFSI (m)	$[O]_{\text{PEGDME}}/[Li]$ ratio
Li-P-1	0.93	24
Li-P-2	1.86	12
Li-P-3	2.8	8
Li-P-4	4.65	5
Li-P-5	7.3	3

Table 4.2. The formulation of the S-XPE-*x* reactive solutions and the related $[O]/[Li]$ ratios. (Reprinted (adapted) with permission from (ACS Appl. Mater. Interfaces 2020, 12, 1, 567-579). Copyright (2020) American Chemical Society).

Sample	No of moles of O from PEGDME $[O]_{\text{PEGDME}}$	No of moles of O from VEC $[O]_{\text{VEC}}$	No of moles of O from PEGDAE $[O]_{\text{PEGDAE}}$	No. of moles of Li ⁺ -ions from LiTFSI [Li]	$[O]^*/[Li]$
S-XPE-1	0.0085	0.006244	0.00445	0.00035	55
S-XPE-2	0.0070	0.006244	0.00445	0.00057	31
S-XPE-3	0.0059	0.006244	0.00445	0.000742	22
S-XPE-4	0.0046	0.006244	0.00445	0.000948	16
S-XPE-5	0.0034	0.006244	0.00445	0.0011	13

Table 4.3. Formulations of the D-XPE-*x* reactive solutions/D-XPEs and the related $[O]/[Li]$ ratios. (Reprinted (adapted) with permission from (ACS Appl. Mater. Interfaces 2020, 12, 1, 567-579). Copyright (2020) American Chemical Society).

Sample	No of moles of O from PEGDME $[O]_{\text{PEGDME}}$	No of moles of O from VEC $[O]_{\text{VEC}}$	No of moles of O from PEGDAE $[O]_{\text{PEGDAE}}$	No of moles of Li ⁺ -ions from LiTFSI & LiFSI [Li]	$[O]^*/[Li]$
D-XPE-1	0.00825	0.00606	0.00432	0.0004924	38
D-XPE-2	0.00681	0.00606	0.00432	0.0007124	24
D-XPE-3	0.00577	0.00606	0.00432	0.0008724	18.5
D-XPE-4	0.00447	0.00606	0.00432	0.0010724	14
D-XPE-5	0.00333	0.00606	0.00432	0.0012434	11

$$[O]^* = [O]_{\text{PEGDME}} + [O]_{\text{VEC}} + [O]_{\text{PEGDAE}} \text{ (in both Table 4.2 and 4.3)}$$

4.2.4 Characterization methods and techniques

Differential scanning calorimetry (DSC) analysis was carried out using the Discovery DSC 2500, instrument (TA instruments). The sample preparation was carried out in a dry room to minimize moisture uptake and contamination. In a typical measurement, the samples were heated from 25 to 100°C and then cooled to –150°C, and then heated again up to 150 °C. The heating and cooling steps were carried out at a scan rate of 10°C min⁻¹ under helium flux. From the DSC thermograms, the glass transition temperature (T_g) values of the respective specimens were extracted. Thermogravimetric analysis (TGA) was carried out using a Discovery TGA 5500 instrument that was additionally equipped with a Discovery Mass Spectrometer (MS). The test was carried out in the presence of helium carrier gas at a flow rate of 25 ml min⁻¹. The MS has the sensitivity to detect compounds and gases in parts per billion (ppb), which was ensured with a quadrupole detection system, including a closed ion source, a triple mass filter, and a dual (Faraday and Secondary Electron Multiplier) detector system. The weight of the sample used for the analysis was less than 2 mg. The ¹H and ¹³C NMR measurements were performed by employing an Avance III HD spectrometer (Bruker, USA) at 400 MHz (¹H) and a broadband probe (PA BBO 400 MHz, Bruker). The solvent used was CD₃CN and SiMe₄ was used as the primary standard.

The ionic conductivity of XPE membranes and LiTFSI/PEGDME bulk solutions were determined by electrochemical impedance spectroscopy (EIS) analysis using an Autolab (PGSTAT204-FRA32M, Metrohm) potentiostat. To do this, the XPE was placed between two stainless steel blocking electrodes (area 1.54 cm²) in a 2032-coin cell assembly. Similarly, the Li-P-x solution-soaked glass fiber separator (200 µl electrolyte, thickness 300 µm, diameter 18 mm) was assembled in between the stainless-steel current collectors of an EL-cell. The coin cells/EL-cells were assembled in a dry room. Before the EIS analysis, the cells were placed inside a climatic chamber (BINDER MK-53). The measurements were carried in the frequency range of 500 kHz to 1 Hz between 0°C and 70°C at open circuit potential (OCP). The impedance responses were taken at every 10 °C interval by maintaining the temperature equilibrium for 2 h. To calculate the ionic conductivity (σ , S cm⁻¹) **Equation 4.1** was used,²² where ' R_b ' is the bulk resistance, ' l ' is the thickness, and ' A ' is the area of the sample:

$$\sigma = lA^{-1}R_b^{-1} \quad (\text{Equation 4.1})$$

The ionic conductivity values obtained at various temperatures were fitted with Vogel–Tamman–Fulcher (VTF) equation (**Equation 4.2**).²² The VTF equation represents the

relationship between viscosity and temperature near T_g of the polymer matrix. **Equation 4.2** is given below:

$$\sigma = A \exp\left(-\frac{E_a}{R(T-T_0)}\right) \quad (\text{Equation 4.2})$$

where A is the pre-exponential factor related to charge carrier concentration, ' σ ' is the ionic conductivity, ' E_a ' is the activation energy (E_a^{VTF}), ' R ' is the gas constant, ' T ' is the experimental temperature and ' T_0 ' is the temperature which is 50 °C below the T_g .

The salt diffusion coefficient of the XPE membranes (D_{Li^+}) was estimated using **Equation 4.3**.²² In this work, the XPE sandwiched lithium symmetrical cells were polarized at 20 mV for 1 h. followed by keeping the cell at OCP until a stable state was achieved. Later, from the plot of the natural logarithm of potential (V) vs. time (t), the D_{Li^+} values were calculated using **Equation 4.3**:

$$\text{Slope} = (\pi^2 D_{\text{Li}^+}) L^{-2} \quad (\text{Equation 4.3})$$

where, the slope is obtained by the linear fitting of the plot of $-\ln(V)$ vs. t , ' L ' is the thickness of the XPE specimen under consideration.

The Li-ion transference number (T_{Li^+}) of the XPEs were measured at 60°C by using combined AC impedance spectroscopy and DC polarization measurements using **Equation 4.4**.²²

$$T_{\text{Li}^+} = \frac{I_S R_S (\Delta V - I_0 R_{ct,0})}{I_0 R_{\Omega,0} (\Delta V - I_S R_{ct,S})} \quad (\text{Equation 4.4})$$

Here, V is the DC polarization voltage (10 mV), I_0 and I_S are the initial and steady-state current responses during the DC polarization, R_0 and $R_{ct,0}$ stand for the bulk resistance and charge transfer resistance, respectively, which is obtained from the Nyquist plot before the DC polarization. Similarly, R_s and $R_{ct,s}$ stand for the bulk and charge transfer resistance obtained after achieving steady-state conditions.

The oxidation stability (anodic stability) of the XPE was evaluated by linear sweep voltammetry (LSV), and the reduction stability (cathodic stability) by employing cyclic voltammetry (CV) using a potentiostat (VMP3, Bio-logic, Switzerland). In both measurements,

a scan rate of 0.1 mVs^{-1} was employed. The LSV tests were run between OCP and 7 V vs. Li|Li^+ , where aluminum (Al) or stainless steel (StSt) was used as the working electrode (Li|XPE|Al or Li|XPE|SS). A limiting current of $1 \mu\text{A cm}^{-2}$ was considered as the onset of the decomposition process and corresponding voltage was considered as the maximum application voltage in the case of LSV measurements. Similarly, the CV was carried out between OCP and $-0.25 \text{ V vs. Li|Li}^+$ with copper (Cu) as the working electrode (Li|XPE|Cu). In both cases, lithium was used as a reference electrode. Galvanostatic lithium plating/stripping measurements were carried out in a symmetric cell configuration *viz.*, Li|XPE|Li. Measurements were carried out at 60°C at a current density of 0.1 mA cm^{-2} (5h Li-plating and 5h Li-stripping).

4.2.5 Quantum chemistry calculations

Intrinsic oxidative stabilities have been computed for PEGDME and various clusters involving PEGDME and Li^+ . The calculations were performed with the Gaussian 16 package²⁷ at different levels of theory: For larger complexes involving a single PEGDME chain with monomers and multiple lithium ions, both the semi-empirical PM6 method²⁸ and density functional theory (DFT) with the range-separated LC- ω PBE functional²⁹ were used in combination with the 6-31+G(d,p) basis set. All calculations were performed using the SMD implicit solvation model³⁰ with the parameters for “ether” contained in Gaussian 16. The oxidation potentials E_{ox} were computed *via* the following equation:³¹

$$E_{\text{ox}} = \frac{G(M^+) - G(M)}{F} - 1.4 \text{ V} \quad (\text{Equation 4.5})$$

where $G(M)$ and $G(M^+)$ are the computed free energies of the non-oxidized and the oxidized molecule or cluster, respectively, F is the Faraday constant, and the shift of 1.4 V relates the absolute free energy differences to the Li|Li^+ scale.^{32, 33} The geometry of the oxidized cluster was re-optimized such that the potentials correspond to adiabatic potentials.³² To validate the semi-empirical PM6 method and the LC- ω PBE function required to computationally tackle the larger clusters, additional calculations with the highly accurate but demanding G4MP2 method¹² were carried out for a PEGDME- Li^+ complex with monomers and a single lithium-ion. While G4MP2 yields $E_{\text{ox}} = 6.7 \text{ V vs. Li|Li}^+$, values of $6.4 \text{ V vs. Li|Li}^+$ and $7.0 \text{ V vs. Li|Li}^+$ were obtained at the PM6 and LC- ω PBE/6-31+G(d,p) level, respectively. Although the

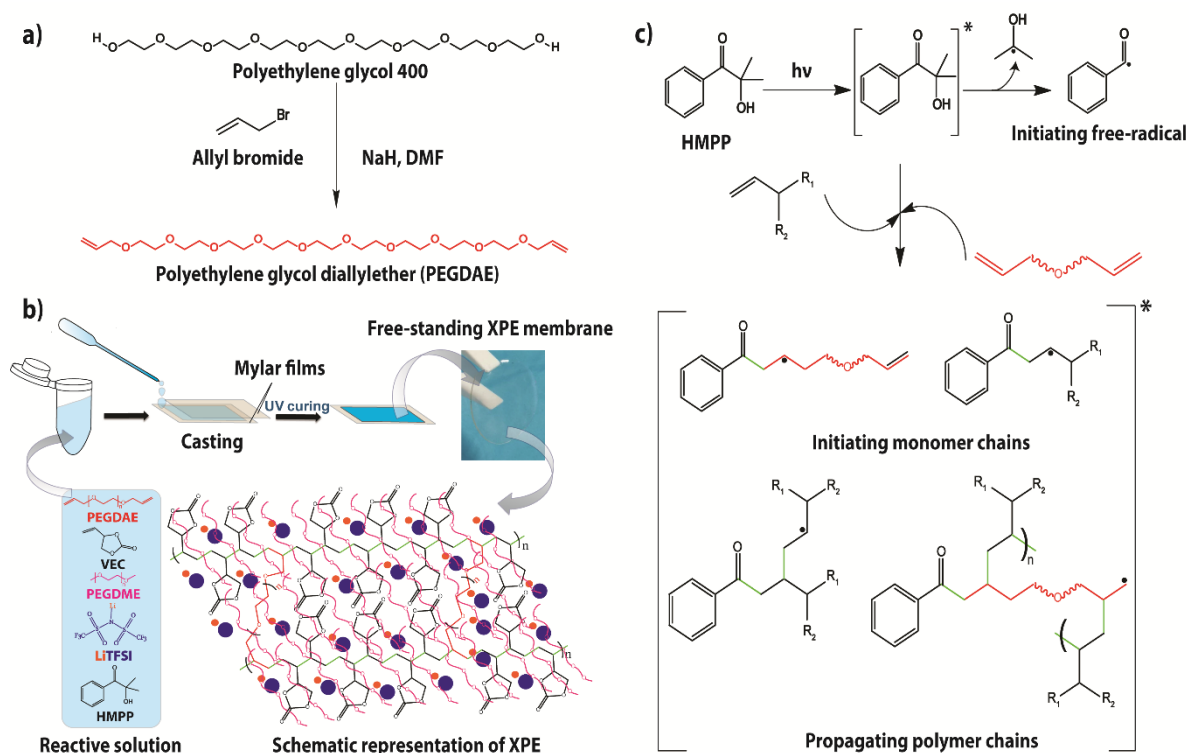


Figure 4.1. (a) The reaction scheme adopted for the synthesis of PEGDAE crosslinker monomer; (b) schematic representation of the preparation of XPE membrane from the reactive solution composed of monomers, plasticizer, lithium salt, and photo-initiator by UV-curing process; (c) representation of the various stages of free-radical polymerization mechanism induced by UV-light. (Reprinted (adapted) with permission from (ACS Appl. Mater. Interfaces 2020, 12, 1, 567-579). Copyright (2020) American Chemical Society).

absolute deviations are in the range of 0.3 V, we therefore have confidence that both computationally expedient methods yield satisfactory results.

4.3 Results and discussion

4.3.1 Synthesis of XPE membranes

The PEGDAE crosslinker used here was synthesized *via* a simple reaction between poly(ethylene glycol), PEG, and allyl bromide in the presence of sodium hydride (NaH).²⁶ The reaction scheme adopted for the synthesis of PEGDAE crosslinker is presented in **Figure 4.1a**. The scheme adopted for the synthesis of XPE membranes is presented in **Figure 4.1b**. Besides, a digital image of one of the representative membranes is shown in **Figure 4.1b** demonstrating its free-standing nature and high dimensional integrity. The photo-polymerization initiation mechanism is depicted in **Figure 4.1c**. Indeed, the photo-initiator absorbs UV-light and excites to a high energy state, which returns to a low energy state by decomposing into reactive free radicals. These free radicals react with an allylic functional group to form an initiating chain

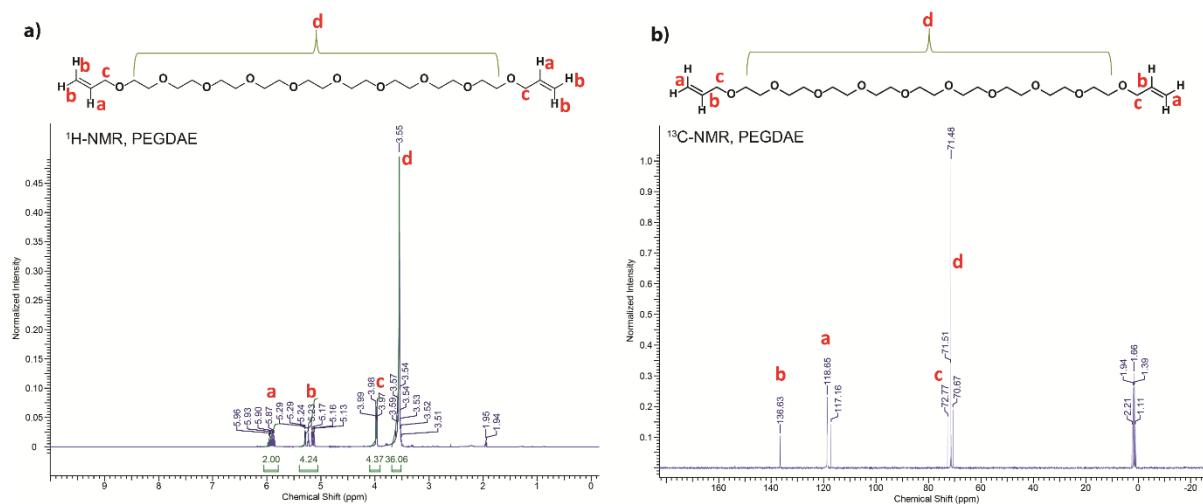


Figure 4.2. (a) The ^1H -NMR spectrum of the oligomer crosslinker PEGDAE; (b) ^{13}C -NMR spectrum of the crosslinker monomer PEGDAE. (Reprinted (adapted) with permission from (ACS Appl. Mater. Interfaces 2020, 12, 1, 567-579). Copyright (2020) American Chemical Society).

which on continued addition (propagation) forms a three-dimensional crosslinked network. Besides, the NMR spectra (^1H and ^{13}C) of PEGDAE are also provided in **Figure 4.2a** and **4.2b**, which confirmed the chemical structure and the purity of the synthesized PEGDAE oligomer. From the ^1H -NMR spectra, the formation of PEGDAE is confirmed. The absence of peaks corresponding to any trace impurities underlines that PEGDAE is obtained in its purest form. Additionally, in the ^1H -NMR spectrum, peaks corresponding to the -OH group is also absent further evidencing the complete conversion of PEG to PEGDAE. For instance, the peaks observed between 5.87-5.96 (m), 5.13-5.29 (m), and 3.97-3.99 ppm (m) are related to the protons from the terminal allyl ether groups (-OCH₂-CH=CH₂). At the same time, the broad peaks between 3.51-3.59 ppm correspond to the remaining 36 protons present in the ethylene oxide (EO) units in PEGDAE. The ^{13}C -NMR spectrum also supports the structure elucidated from the ^1H -NMR spectrum.

Compared to the vinyl monomers such as acrylates, the free radical polymerization of allyl monomers is rather slow. The slow rate of polymerization is owing to the high stability of allyl free radicals, which leads to the inhibition of the propagating chain. The stabilization of allyl free radicals occurs *via* a well-known mechanism of ‘*degradative monomer chain transfer*’ in which the monomer is resonance stabilized by allylic hydrogen abstraction.³⁴ Owing to the low reactivity of the allyl monomers, an irradiation time of 1 h is necessary for achieving a complete monomer to polymer conversion. It is worth noting that the PEGDME used as a plasticizer is an inert molecule and it does not take part in the polymerization process, however, during the process, effectively embedded within the crosslinked polymer matrix.

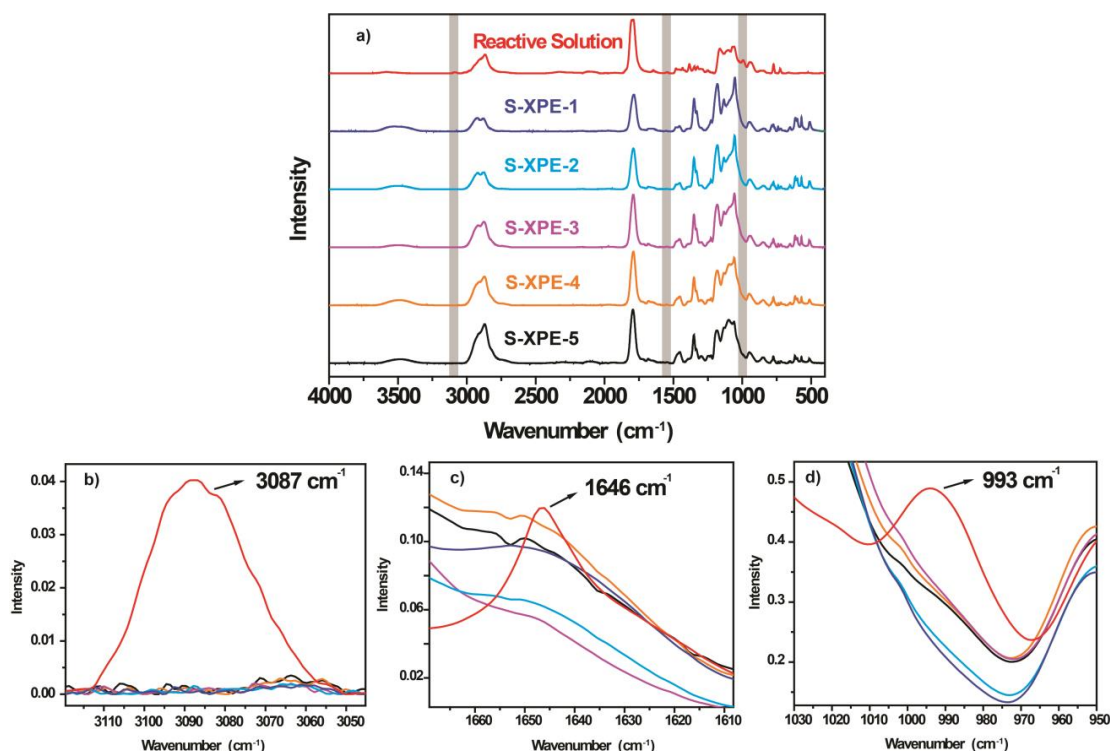


Figure 4.3. ATR-FTIR spectra of the reactive solution and the S-XPE-*x* samples from (a) 400 to 4000 cm^{-1} ; the magnified spectra in the wavenumber regions of (b) 3045–3120 cm^{-1} , (c) 1605–1670 cm^{-1} , and (d) 950–1030 cm^{-1} , representing the disappearance of the peaks corresponding to the -C=C- bonds. (Reprinted (adapted) with permission from (ACS Appl. Mater. Interfaces 2020, 12, 1, 567–579). Copyright (2020) American Chemical Society).

The whole polymerization is carried out in a single step without the use of any processing solvents. The structure of the three-dimensionally crosslinked polymer matrix (**Figure 4.1b**) can be interpreted as a linear polyethylene chain functionalized with cyclic carbonate moiety, which is then crosslinked by ethylene oxide (EO) units. The composition of the LiTFSI/PEGDME bulk solutions (Li-P-*x*), single- (S-XPE-*x*), and dual-salt (D-XPE-*x*) polymer electrolytes are tabulated in **Table 4.1–4.3**. The PEGDME plasticizer acts as a mobile phase within the crosslinked polymer matrix and facilitates lithium ion transport through the synergy arising from the EO units of the polymer matrix and the plasticizer, indeed the carbonyl groups present in the polymer matrix can also take part in the ion transport process.

4.3.2 Characterization of XPEs by ATR-FTIR spectroscopy

The complete conversion of the monomer to polymer is confirmed by ATR-FTIR analysis (**Figure 4.3a–d**). The characteristic peaks at 993 (H-C=CH_2 , alkenyl C-H bend), 3087 (H-C=CH_2 , alkenyl C-H Stretch), and 1646 cm^{-1} (-C=C- , stretching), which are present in the reactive solution are absent in the UV-cured XPEs. This underlines that almost all the monomers are converted to a complete polymer network. The ATR-FTIR peak corresponding

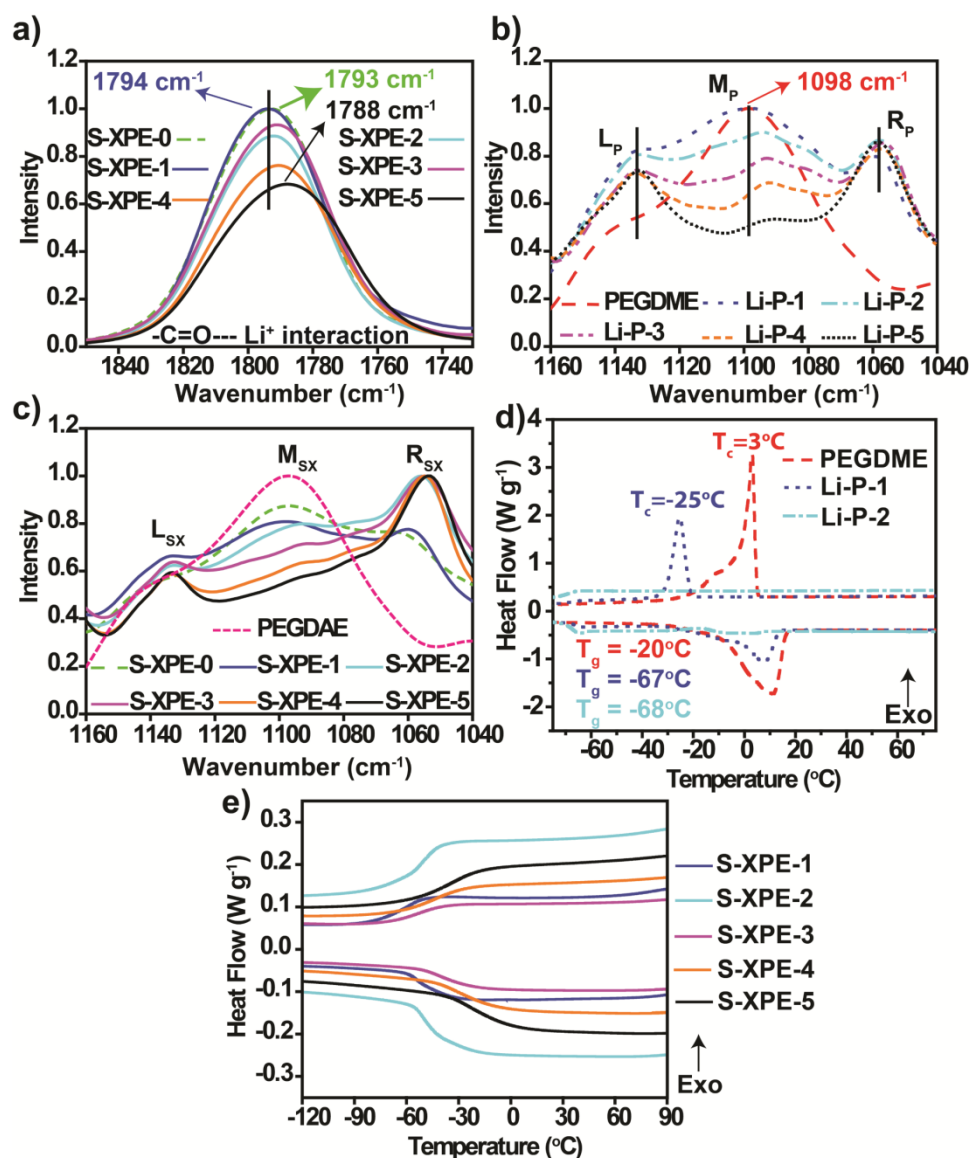


Figure 4.4. ATR-FTIR spectra representing the peak shifts associated with the stretching vibration of (a) $>C=O$, carbonyl group in S-XPE- x samples, (b) $-C-O-C-$ band in Li-P- x samples (L_P , M_P , and R_P), and (c) $-C-O-C-$ band (L_{SX} , M_{SX} , and R_{SX}) in PEGDAE and S-XPE- x samples; (d) DSC thermograms of PEGDME, Li-P-1, Li-P-2 samples, and (e) all S-XPE- x specimens. (Reprinted (adapted) with permission from (ACS Appl. Mater. Interfaces 2020, 12, 1, 567-579). Copyright (2020) American Chemical Society).

to the stretching of the free $>C=O$ groups arising from the cyclic carbonate moieties of the polymer specimen (in the absence of LiTFSI salt, S-XPE-0) is observed in 1793 cm^{-1} (Figure 4.4a). However, with the gradual increment in LiTFSI salt content (from S-XPE-1 to S-XPE-5), the carbonyl peaks undergo a slight redshift. This indicates the interaction of the cyclic carbonate moieties with the Li^+ -ions.³⁵⁻³⁷ However, provided that the shift is very low, it can be elucidated that the solvation of the lithium salt by carbonate groups is not very prominent. Moreover, the absence of split bands in the peaks corresponding to the carbonate further rules

Li-P-1 to Li-P-5

Viscosity



Figure 4.5. Digital images of the inversion tests of Li-P-X specimens showing the increment in viscosity with respect to an increase of LiTFSI content in PEGDME. (Reprinted (adapted) with permission from (ACS Appl. Mater. Interfaces 2020, 12, 1, 567-579). Copyright (2020) American Chemical Society).

out the existence of any sort of significant ion-dipole interactions between Li^+ -ions and carbonyl oxygen.³⁷ The aforementioned observations indicate that the solvation and ion-transport predominantly occur through EO groups in XPE.

It is observed that the position of the peak corresponding to the -C-O-C- stretching vibration in the case of pristine PEGDME (in the absence of LiTFSI salt) appears as a single broad peak centered at 1098 cm^{-1} (represented as M_P in **Figure 4.4b**).³⁸ However, in the case of Li-P-1, a set of two new shoulder peaks are appeared neighboring the broad M_P peak. The triplet peak is directly related to the existence of the EO units in different physicochemical environments in the PEGDME:LiTFSI mixture.^{39, 40} For example, lower-order glymes (triglyme, tetraglyme, etc.) and PEO chains are known to complex with the Li^+ -ions in the crown ether and helix (single and double)-like conformations.⁴¹⁻⁴³ Considering that PEGDME is nothing but a higher-order glyme, which is a structural equivalent to that of PEO, similar conformational changes can be expected in proximity with Li^+ -ions, which is also confirmed by the quantum chemical (QC) calculations (see **Section 4.3.4**). Additionally, the Li^+ -ions can act as intermolecular crosslinkers between the EO units, which further affect the local order of the polymer chains. The subsequent addition of LiTFSI into PEGDME is accompanied by apparent changes in the position and the intensity of the L_P , M_P , and R_P peaks. The changes associated with the peak positions of all the Li-P-x samples are summarized in **Table 4.4** and further explanations are given below. The single peak at 1098 cm^{-1} in between the wavelength region of $1040\text{-}1160\text{ cm}^{-1}$ as observed in the case of PEGDME is subjected to tremendous

changes with the addition of LiTFSI into it. With the addition of LiTFSI into PEGDME (Li-P-1), a set of two new shoulder peaks are appeared neighboring the broad M_P peak at 1098 cm^{-1} . These triplet peaks are positioned at 1133 cm^{-1} (L_P), 1098 cm^{-1} (M_P) and 1059 cm^{-1} (R_P), respectively. From, the nature of these triplet peaks, it is possible to decipher the interaction of the Li^+ ions with the EO units and the accompanying conformational changes that occurred in the system.

Table 4.4. The changes associated with the L_P , M_P , and R_P peak positions of the entire Li-P- x samples and their respective T_g values. (Reprinted (adapted) with permission from (ACS Appl. Mater. Interfaces 2020, 12, 1, 567-579). Copyright (2020) American Chemical Society).

Sample	Peak position (cm^{-1})			T_g ($^{\circ}\text{C}$)
	L_P	M_P	R_P	
Li-P-1	1133	1098	1059	-67
Li-P-2	1133	1094	1058	-68
Li-P-3	1133	1093	1056	-59
Li-P-4	1134	1092	1057	-46
Li-P-5	1133	1091	1058	-30

Table 4.5. The changes associated with the L_{SX} , M_{SX} , and R_{SX} peak positions of the entire series of S-XPE- x samples and their respective T_g values. (Reprinted (adapted) with permission from (ACS Appl. Mater. Interfaces 2020, 12, 1, 567-579). Copyright (2020) American Chemical Society).

Sample	Peak position (cm^{-1})			T_g ($^{\circ}\text{C}$)
	L_{SX}	M_{SX}	R_{SX}	
S-XPE-1	1133	1098	1059	-54
S-XPE-2	1133	1094	1056	-52
S-XPE-3	1133	1093	1054	-41
S-XPE-4	1133	1093	1054	-30
S-XPE-5	1133	1093	1053	-24

The subsequent addition of LiTFSI into PEGDME is accompanied by apparent changes in the position and intensity of the L_P , M_P , and R_P peaks. The redshift observed for the M_P peak as we move from Li-P-1 to Li-P-5, and the R_P peak from Li-P-1 to Li-P-3 indicates an enhanced interaction between the oxygen atom of the EO units and the Li^+ -ions at high salt concentrations. However, in the case of the Li-P-4 and Li-P-5 samples, the effect is reversed

in such a way that the R_P peaks are observed at higher wavenumber values *viz.*, 1057 and 1058 cm^{-1} , respectively. The observed blueshift compared to Li-P-3 may be associated with the reduced interaction between the Li^+ -ions and the EO units as a result of the formation of ion-pair aggregates/ion clustering at very high salt content.⁴⁴

Apart from the peak positions, the intensity of the M_P and R_P peaks in each of the Li-P-x samples can also give valuable information regarding the interaction between the EO and Li^+ -ions. As it can be seen from **Figure 4.4b**, the intensity of the M_P peak is decreased with the successive addition of LiTFSI into PEGDME. At the same time, the R_P peaks are sharp and more or less of the same intensity except for the Li-P-1 sample. The reduction in the M_P peak intensity is associated with the decreased amount of free EO units in the respective samples owing to the concomitant enhancement in the coordination of more EO units with the Li^+ ions. The evolution of sharp R_P peaks in the case of the Li-P-2 to Li-P-5 samples compared to Li-P-1 is directly related to the reduction in the M_P peak intensity, where the intensity of the R_P peak corresponds to the amount of interacting EO units.

Followed by contemplating the trends in ATR-FTIR spectrum of the Li-P-x samples, similar wavelength regions in the S-XPE-x samples are also analyzed (**Figure 4.4c**). As already seen in the case of Li-P-1, the appearance of triplets in the case of S-XPE-0 is also due to the conformational changes induced in the polymer matrix. However, in the case of S-XPE-0, the conformational changes are induced using chemical crosslinks (interpenetrated networks of crosslinked PEGDAE (X-PEGDAE) through PEGDME matrix) rather than LiTFSI salt-induced physical crosslinks. Considering the ATR-FTIR spectra of the S-XPE-1 and -2 samples, it can be seen that the triplet peaks are retained with considerable intensity. The presence of intense M_{SX} peaks, which indicates the presence of a significant amount of free EO units in S-XPE-1 and -2. The diminished peak intensity in the case of S-XPE-3, -4, and -5 samples indicates that the amount of free EO chains is reduced in the presence of high salt concentrations. This is because the EO chains from X-PEGDAE are also utilized for complexing with the Li^+ -ions. This reduces the plasticizing effect induced by the EO units from X-PEGDAE making the polymer matrix stiff. The changes associated with the peak positions of all the S-XPE-x samples are summarized in **Table 4.5**. In the region between 1040 and 1160 cm^{-1} , the ATR-FTIR spectrum of the crosslinker (PEGDAE, **Figure 4.4c**) looks similar to that of PEGDME with a broad peak centered at 1098 cm^{-1} . This is obvious considering the structural similarity of both the molecules except at their terminals. Interestingly, in the case of S-XPE-0, a broad triplet is observed with peak maximums at 1144 (L_{SX}), 1098 (M_{SX}) and 1060 cm^{-1}

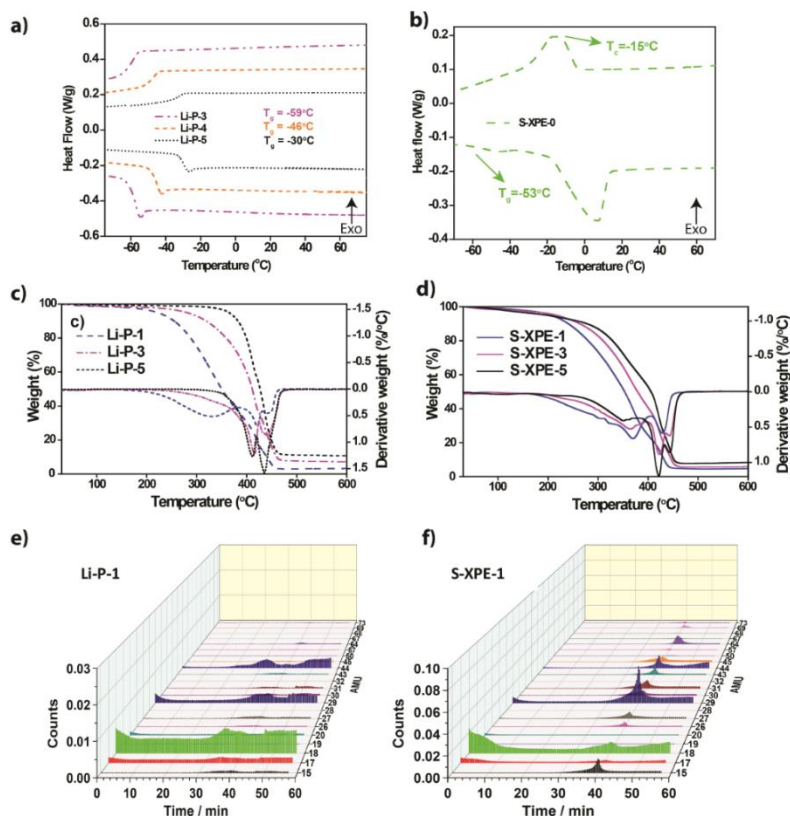


Figure 4.6. DSC thermograms of (a) Li-P-1, Li-P-2, and Li-P-3, and (b) S-XPE-0 samples; TGA profiles of (c) Li-P- x ($x=1,3$ and 5), and (d) S-XPE- x ($x=1, 3$ and 5) samples; AMU of the products released during the TGA–MS analysis. The graph is reported as the ion current vs. test time for different molecules expelled during the TGA analysis of (e) Li-P-1 salt, and (f) S-XPE-1. (Reprinted (adapted) with permission from *ACS Appl. Mater. Interfaces* 2020, 12, 1, 567-579). Copyright (2020) American Chemical Society).

(R_{SX}), respectively. This is already explained in the main text utilizing the chemical crosslinks induced by X-PEGDAE. The triplet peaks are retained with the introduction of LiTFSI to form the XPEs. In the case of S-XPE-1 and -2, the intensity of the triplet peak is rather high compared to S-XPE-3,4 and 5. The physical observation of the increase in viscosity of the PEGDME solution with higher LiTFSI content further supports the aforementioned claims on the evolution of the ordered polymer matrix through physical crosslinks (see digital images of the inversion tests in **Figure 4.5**).

The ATR-FTIR spectra of the Li-P- x and S-XPE- x samples also exhibit triplets similar to that of the PEO matrix.^{37, 45, 46} In PEO and related blends, these peaks are generally attributed to their crystalline nature and inter- or intramolecular interaction of EO with other species present in the polymer matrix. Unfortunately, there are not many reports available in the literature regarding the interactions of Li^+ -ions with higher-order glymes such as PEGDME as

used in this work. To support our findings, we have carried out quantum chemistry (QC) calculations of PEGDME-Li⁺ clusters and the results are reported in the following sections.

4.3.3 Thermal analysis

The differential scanning calorimetry (DSC) profile (**Figure 4.4d**) of pure PEGDME shows a sharp peak of crystallization (T_c) at 3°C during the cooling cycle, which is attributed to the transition of liquid PEGDME to a solid phase accompanied by the rearrangement and

Table 4.6. Summary of ionic conductivity, transference number (T_{Li^+}), diffusion coefficient (D_{Li^+}), activation energy (E_a^{VTF}), and anodic stabilities values of the entire series of S-XPE-x samples. (Reprinted (adapted) with permission from (ACS Appl. Mater. Interfaces 2020, 12, 1, 567-579). Copyright (2020) American Chemical Society).

Sample	Ionic Conductivity (mS cm ⁻¹)		T_{Li^+}	D_{Li^+} (cm ² s ⁻¹)	E_a^{VTF} (kJ mol ⁻¹)	Anodic stability (V) vs. (Li Li ⁺)
	30°C	60°C				
S-XPE-1	0.045	0.24	0.33	3.51×10^{-8}	10.48	4.2
S-XPE-2	0.03	0.20	0.25	3.40×10^{-8}	10.93	4.3
S-XPE-3	0.012	0.09	0.22	2.60×10^{-8}	10.38	4.5
S-XPE-4	0.005	0.053	0.14	1.78×10^{-8}	9.50	4.9
S-XPE-5	0.001	0.02	0.11	1.37×10^{-8}	10.27	5.1

crystallization of the EO chains.²² During the heating cycle, an endothermic peak corresponding to the melting (T_m) of the crystalline phase is observed at 11.7°C along with a glass transition temperature (T_g) value of -20°C. Considering the DSC thermogram, it can be concluded that the PEGDME is a viscous liquid at 20°C. The nature of the thermogram changes with the addition of LiTFSI salt in PEGDME (**Figure 4.4d**). It is observed that the T_c of Li-P-1 is reduced and shifted towards lower temperatures noted as 3°C for Li-P-0 and -25°C for Li-P-1. A concomitant decrease in T_m is also observed. A very low T_g value of -67°C underlines increased mobility of the liquid phase in Li-P-1 as compared to that of Li-P-0.

The interactions between EO and the Li⁺-ion induce significant differences in the DSC profiles of other Li-P-x samples as well. Most importantly, the peak corresponding to T_c is absent in the case of Li-P-2 (**Figure 4.4d**), as the crystallization of the EO chains is completely hindered due to the complexation of the EO units with the Li⁺-ions. Ultimately, the T_g value of Li-P-2 is as low as -68°C, which emphasizes the presence of amorphous character similar to that of Li-P-1. However, at very high salt concentrations (Li-P-3, Li-P-4, and Li-P-5), the T_g values are found to be largely increased due to the formation of several physical crosslinks leading to a higher viscosity, which imparts stiffness to the plasticizer chains by the inter-chain

complexation of the PEGDME molecules by the Li^+ -ions. The T_g value of Li-P-3 is increased to -59°C , and in the case of Li-P-4 and Li-P-5, the values are -46 and -30°C , respectively (**Figure 4.6a** and **Table 4.4**).

In the case of the S-XPE-x samples, the DSC thermograms do not exhibit any T_c peaks, which cement the effect of lithium salt in preventing the crystallization of the EO chains (**Figure 4.4e**). The T_g values of S-XPEs are in accordance with the trends observed from the ATR-FTIR and DSC data of the Li-P-x samples. In the case of the S-XPE-1 and -2 samples, which possess a comparatively greater number of free EO units, the T_g values are found to be at -54 and -52°C , respectively. All the while, other samples having a lower content of free EO units exhibit high T_g values (**Table 4.6**). DSC thermogram corresponding to S-XPE-0 is presented in **Figure 4.6b** and the persistence of the T_c peak in S-XPE-0 evidence that the presence of lithium salt is inevitable to hinder the crystallization of the EO chains. However, the shift of the T_c and T_g values to the lower temperature regions (compared to PEGDME) in the case of S-XPE-0 indicates the effect of UV induced chemical crosslinks in improving the amorphous character.

The thermogravimetric analyses (TGA) of the Li-P-x and S-XPE-x samples are provided in **Figures 4.6c** and **d** respectively. The lithium salt-free samples, *viz.*, Li-P-0 and S-XPE-0, displayed thermal stability of 180°C , whereas the Li-P-5 and S-XPE-5 samples are stable above 300 and 250°C , respectively. Here, the gradual increment in the thermal stability of both Li-P-x and S-XPE-x with increased LiTFSI content is directly associated with the enhanced degree of physical and chemical crosslinks induced which also increases the viscosity of the respective systems. In the case of Li-P-1, three major weight loss regions are observed. It can be seen from the derivative plot that the broad weight losses that occurred in the region between 180 - 380°C correspond to the evaporation/degradation of PEGDME molecules present in Li-P-1.²² The inflection point associated with this process is recorded to be at 329°C . Interestingly, in the case of Li-P-3, the degradation associated with the PEGDME molecule is suppressed whereas the peak is completely disappeared in the Li-P-5 sample. In other words, the onset of thermal degradation at 180°C in the case of Li-P-1 is significantly improved to about 300°C in the case of Li-P-5. This proves the favorable effect of higher salt content in improving the thermal stability of the Li-P-x samples. This further supports the claims regarding the changes in the physicochemical properties of PEGDME utilizing the interactions with the Li^+ -ions. The peaks beyond 400°C in the case of the Li-P-x specimens are associated with the decomposition of LiTFSI.⁴⁷ In the case of the S-XPE-x samples, the degradation peaks

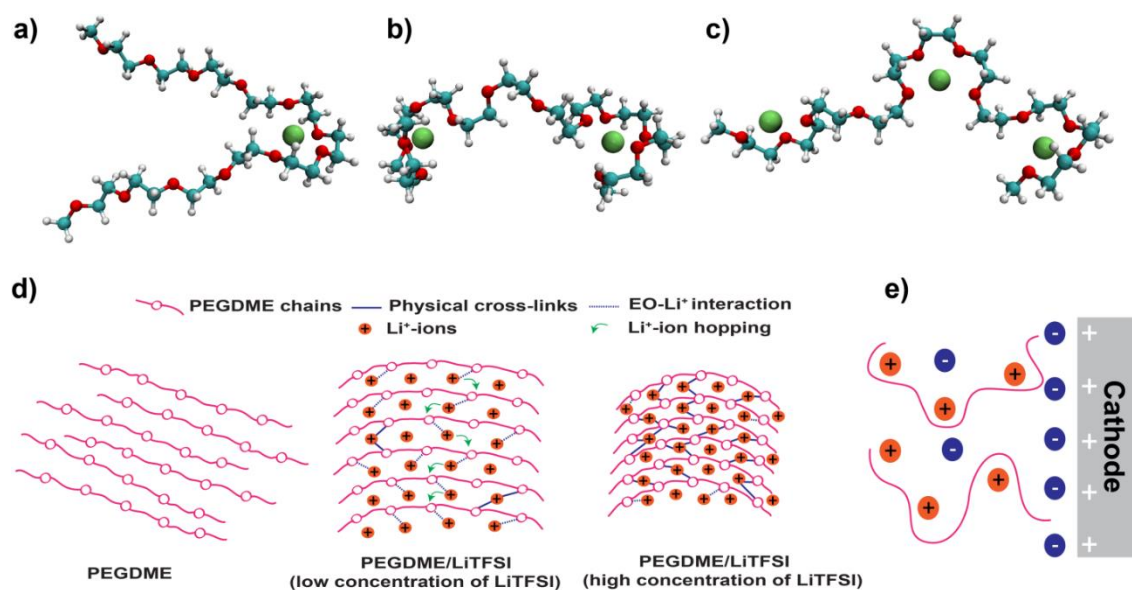


Figure 4.7. Optimized geometries from quantum chemistry calculations of clusters in which PEGDME coordinates to (a) one, (b) two, and (c) three Li⁺ ions (colour codes: green - Li⁺, blue - carbon, red - oxygen, white - hydrogen). The progressive coordination of lithium ions to PEGDME results in conformational changes of the backbone as well as an increase in the intrinsic oxidative stability; (d) schematic representation of the conformational changes occurred in PEGDME chains in the absence and at various concentration of LiTFSI salt; (e) the putative double-layer structure at the cathode/electrolyte interface leading to an additional increase of the oxidation potential. (Reprinted (adapted) with permission from (ACS Appl. Mater. Interfaces 2020, 12, 1, 567-579). Copyright (2020) American Chemical Society).

corresponding to the PEGDME molecules are not very prominent. However, considering the onset of degradation at 180°C similar to the case of Li-P-1, it can be concluded that PEGDME degradation is occurring in the case of S-XPE-1 as well. In the case of the S-XPE samples also, the onset of PEGDME degradation is found to be increased with an increase in the LiTFSI content. Hence, the maximum thermal stability is exhibited by S-XPE-5 which is up to 250°C. This value is 50°C less than the thermal stability of the Li-P-5 sample and could be contributed from the degradation of the crosslinked polymer matrix, which is coupled with the degradation of PEGDME. Additionally, an inflection point at 368°C is observed in the case of S-XPE-1 which could be due to the degradation of poly(vinyl ethylene carbonate) chains present in the crosslinked polymer matrix.^{18, 48} In the case of S-XPE-x specimens also, the weight losses beyond 400°C are attributed to LiTFSI decomposition.

The TGA data is further supported by temperature-dependent mass spectrometry (MS) analysis (**Figure 4.6e** and **f**), which is consistent with the role of lithium salt in increasing the

overall thermal stability. In both cases, as evidenced by the MS spectra, water is expelled until 130°C for both Li-P-1 and S-XPE-1. Water was also evaporated from the system above 330°C due to the decomposition of the ether molecules. Small amounts of hydrocarbons are also escaped from both the samples only above 300°C. The main decomposition products of the LiTFSI salt were the fluorinated carbons such as CF₃, and CF₂ at respective AMUs above 300°C. Thus, it can be concluded that the TGA results obtained are in agreement with the MS data with respect to assigning the stages of the sample decomposition.

4.3.4 Quantum chemical calculations

Selected optimized conformations of the PEGDME-Li⁺-ion clusters are displayed in **Figures 4.7a-c**. In addition to the motifs displayed in **Figures 4.7a-c**, also the coordination of a single lithium-ion by two PEGDME chains seems possible.^{49, 50} Even though the QC calculations cannot fully assess the conformational phase space of longer chains, we note a significant change in local conformation upon coordination of the Li⁺-ions. Such conformational changes can have a significant impact on the local order associated with the polymer chains as explained below.

In the absence of any Li⁺-ions, the PEGDME molecules are randomly aligned in a linear fashion, which is perturbed once the Li⁺-ions are introduced into the system. In the presence of the Li⁺-ions, the PEGDME chains are coiled around the Li⁺-ions contributing to the formation of the PEGDME-Li⁺ complexes. In the case of the specimens with low salt concentrations such as Li-P-1 and -2, these complexes are isolated leaving vacant space (or free volume) between two successive PEGDME chains facilitating the transport of the Li⁺-ions by segmental motion. However, with further salt addition (as in the case of Li-P-3, -4 and -5), the coiling effect is increased. Moreover, when two PEGDME chains come close to each other, more and more physical crosslinks are generated between them using the Li⁺-ions. This reduces the free volume available for the ion-transport and arrests the segmental motion of the PEGDME chains. The overall effect of these interacting PEGDME chains contributes to the enhancement in crystalline-like properties as reflected from the increased T_g . Therefore, it can be concluded that the Li-P-1 and Li-P-2 samples possess a very low amount of ordered conformations in an amorphous rich phase. This phenomenon is schematically shown in **Figures 4.7d** and it directly influences the ion transport mechanism as explained in **Section 4.4.1**. Additionally, **Figure 4.7e** represents the organization of ions at the electrode-electrolyte interface inside a real cell. The importance of such an electrode-electrolyte interface in deciding the oxidation stability of the XPE is explained in **Section 4.4.2**.

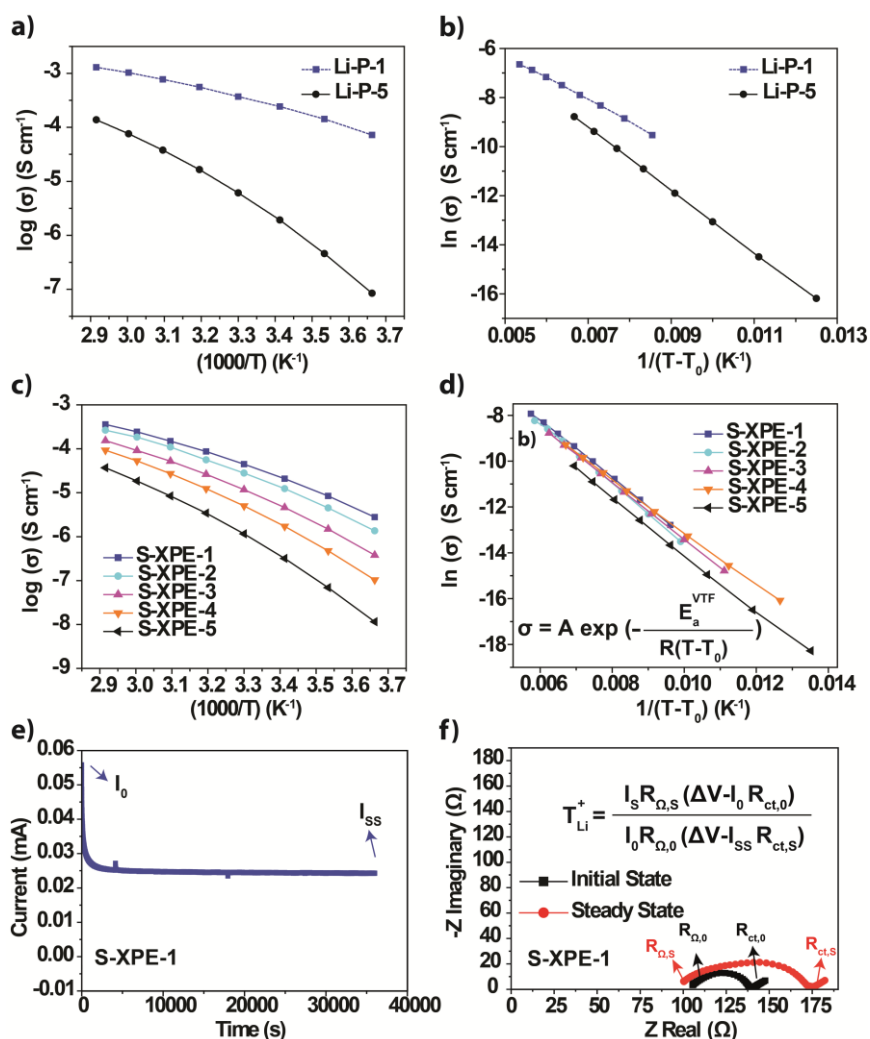


Figure 4.8. (a) Ionic conductivity vs. temperature plots of the Li-P-1 and -5 samples; (b) VTF fit of the same plots of Figure 4.8a using Equation 4.2 for the calculation of the activation energy (E_a^{VTF}); (c) plots representing the ionic conductivity values of the S-XPE-*x* membranes as a function of temperature between 0 and 70°C; (d) Vogel–Tammann–Fulcher (VTF) fit of Figure 4.8c; determination of Li^+ -ion transference number (T_{Li}^+) using (e) chronoamperometry and (f) EIS measurements at 60 °C for a Li/S-XPE-1/Li symmetric cell. (Reprinted (adapted) with permission from (ACS Appl. Mater. Interfaces 2020, 12, 1, 567-579). Copyright (2020) American Chemical Society).

4.3.5 Ionic conductivity and related characteristics

The plots representing the ionic conductivity values of the S-XPEs between 0 and 70°C are presented in **Figure 4.8a**. The ionic conductivity values of S-XPEs are decreasing as a function of an increase in salt concentration. The S-XPE-1 sample exhibits a maximum ionic conductivities of 0.045 and 0.24 mS cm⁻¹ at 30 and 60°C, respectively. Similarly, for the S-XPE-2 membrane, the ionic conductivity value is 0.03 mS cm⁻¹ at 30°C. The high ionic conductivity values of the S-XPE-1 and -2 specimens can be directly correlated with the lowest

T_g values obtained as compared to the other S-XPEs. As expected, the lowest ionic conductivity of 0.001 mS cm^{-1} is exhibited by S-XPE-5 at 30°C , which is in agreement with the highest T_g value of -15°C and also the high viscosity. The ionic conductivity values of all the S-XPEs are summarized in **Table 4.6**.

To understand the ion transport mechanism, the activation energy values of the S-XPE-x membranes are calculated. The plot in **Figure 4.8a** is fit with Vogel–Tammann–Fulcher (VTF) equation (**Figure 4.8b, Equation 4.2**).²² The activation energy (E_a^{VTF}) values associated with S-XPE specimens lie within the error margin of $\approx 10.31 \pm 0.34 \text{ kJ mol}^{-1}$ irrespective of the composition (**Table 4.6**). The E_a^{VTF} values of the S-XPE membranes are compared with the E_a^{VTF} values of the Li-P-x solutions. For this purpose, the two solutions with low and high Li^+ -ion concentrations *viz.*, Li-P-1, and Li-P-5 are chosen. The ionic conductivity *vs.* temperature plots of the Li-P-1 and -5 samples are presented in **Figure 4.8c**. The VTF fit of the same plot is provided in **Figure 4.8d**. The E_a^{VTF} values associated with the aforementioned solutions are 7.5 and $10.60 \text{ kJ mol}^{-1}$, respectively. Interestingly, the E_a^{VTF} value of the Li-P-5 is higher than Li-P-1 and lies within the error margin of the S-XPE membranes. This indirectly indicates that the Li^+ -ion transport mechanism in PEGDME is directly dependent on the salt concentration.

As it is evident from **Figure 4.7d**, the physical crosslinks present in the polymer assisted by Li^+ -ions are responsible for arresting the segmental motion of the EO units. In the case of Li-P-1, such physical crosslinks are less in number due to the low concentration of the Li^+ -ions.⁵¹ However, facile coordination between the EO units and Li^+ -ions is possible.^{52, 53} The less number of physical crosslinks leave a significant amount of free volume between the polymer chains so that persistent segmental motion is favored. Hence, the motion of the polymer chains can assist the easy hopping of the Li^+ -ions from one coordination site to another, or in other words, the ion transport is coupled with the segmental motion of the polymer chains. This process is energetically favorable, and it is considered as the most effective Li^+ -ion transport mechanism.⁵⁴ Considering the low E_a^{VTF} value of Li-P-1, it can be concluded that Li^+ -ion transport occurs *via* the free volume model as explained above. Any deviation from the aforementioned ion transport model may lead to high E_a^{VTF} value as obtained in the case of the S-XPE membranes and PEGDME liquid-phase at high salt concentrations.

In the presence of higher salt content, the LiTFSI/PEGDME solution behaves similarly to that of a chemically crosslinked S-XPE membrane. High LiTFSI content in the electrolyte results in an increased degree of physical crosslinks between the PEGDME chains. This also means that the number of simple EO- Li^+ coordination sites are reduced in the polymer

electrolyte since a good number of the EO units are involved in physical crosslinks. Such physical or chemical crosslinks make the polymer chains stiffer thereby diminishing their segmental motion and availability of the coordination sites for inter-chain Li^+ -ion hopping. Therefore, it can be concluded that the S-XPE membranes as well as highly concentrated LiTFSI/PEGDME solutions follow more or less similar Li^+ -ion transport mechanisms which are partially decoupled from the segmental motion of the polymer chains. This in turn results in an increment in the E_a^{VTF} values compared to that of Li-P-1 in which the Li^+ -ion transport is coupled with the polymer chain segmental motion. This decoupling could be the reason for the comparatively low ionic conductivity observed for the XPE membranes than the targeted value of $10^{-3} \text{ S cm}^{-1}$ at RT. However, in the recent reports by Bresser *et al.* and Agapov *et al.*, decoupling of ionic conductivity and segmental motion is proposed to be an unconventional strategy for improving Li^+ -ion mobility in polymer electrolytes.^{55, 56} Despite the decoupled ionic conductivity and segmental motion, the low ionic conductivity of the XPEs as observed in the current work is indeed due to the absence of well-defined ion transport channels due to high degree of physical and chemical crosslinks.

The Li^+ -ion transference number (T_{Li^+}) associated with the S-XPE samples is calculated using the DC-polarization method as reported by Abraham *et al.*⁵⁷ A high transference number is desirable for polymer electrolytes to prevent the buildup of anion concentration gradient, which may lead to salt precipitation and decomposition.²² At the same time, polymer electrolytes with high transference number have already proven to suppress HSAL,³ such as dendrite deposition.⁹ Data corresponding to chronoamperometry and impedance measurements at 60 °C on the S-XPE-1 membrane (in Li|S-XPE-1|Li configuration) are provided in **Figures 4.8e** and **f**, respectively. The T_{Li^+} values achieved for all the S-XPE-x membranes are provided in **Table 4.6**. The highest transference number value of 0.33 is exhibited by S-XPE-1. The presence of higher wt.% of PEGDME in the S-XPE-1 sample can loosen the interaction of Li^+ with the oxygen atoms from the EO chains present in the crosslinker units. This results in more Li^+ -ions available for facile charge carriage through the PEGDME liquid-phase contributing to a high transference number.

The reduction in the T_{Li^+} values at a high concentration of lithium salt is obvious due to an increased number of physical crosslinks leading to increased viscosity as already explained in the previous section (**Section 3.3**), which reduces the mobility of the Li^+ -ions. The lithium-ion diffusion coefficients (D_{Li^+}) of the S-XPEs are determined by using the method suggested

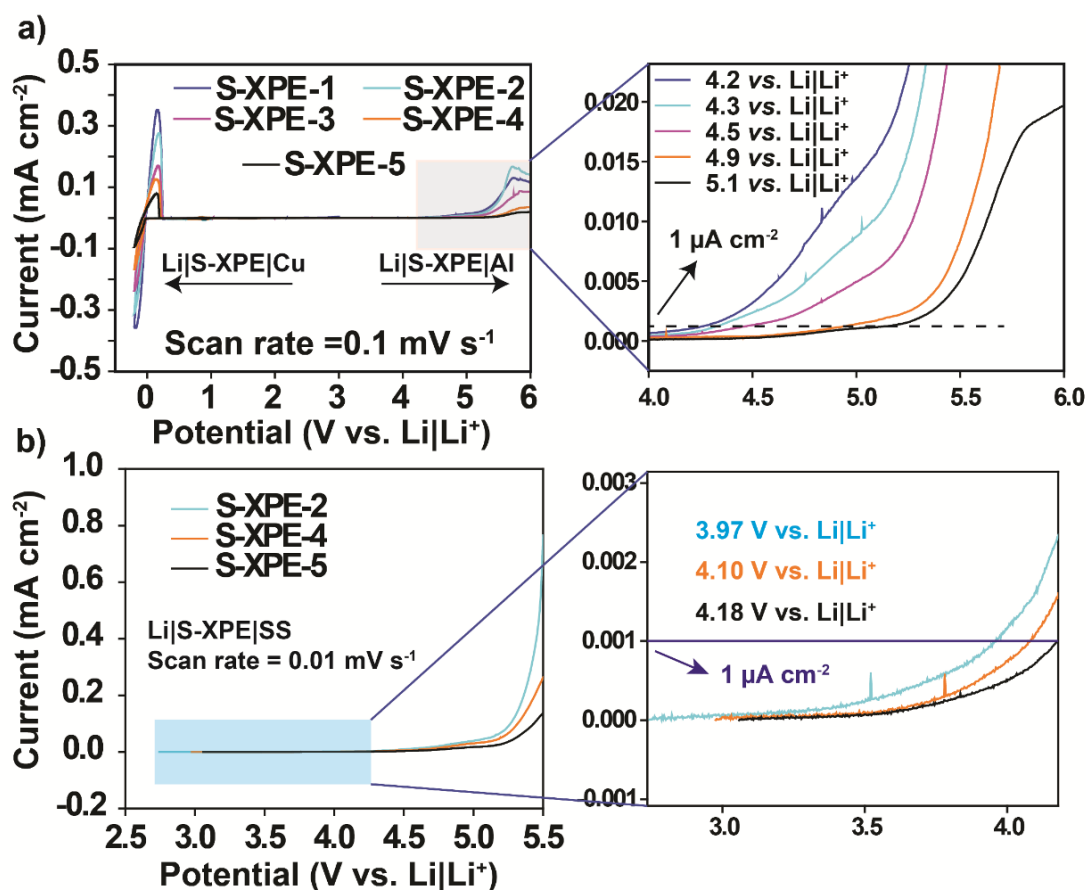


Figure 4.9. (a) Determination of the electrochemical stability window (ESW) of S-XPE-*x* membranes. The Current vs. Potential curves associated with the oxidation and reduction stability of the S-XPE membranes against Al and Cu non-blocking electrodes, respectively, are presented; (b) determination of oxidation stability of S-XPE-*x* membranes against stainless steel (StSt) as the working electrode. (Reprinted (adapted) with permission from (ACS Appl. Mater. Interfaces 2020, 12, 1, 567-579). Copyright (2020) American Chemical Society).

by Ma *et al* (Table 4.6).⁵⁸ The highest D_{Li^+} value of $3.51 \times 10^{-8} \text{ cm}^2 \text{ s}^{-1}$ is exhibited by S-XPE-1 whereas S-XPE-2 possessed a value of $3.4 \times 10^{-8} \text{ cm}^2 \text{ s}^{-1}$. This means that the D_{Li^+} value is decreased at a higher salt concentration, which is in agreement with the observed ionic conductivity and transference number.

4.3.6 Electrochemical stability window (ESW)

The oxidation stability of the S-XPEs is analyzed at 60°C against a working electrode (Al and stainless steel (StSt)) by LSV experiments. The results are shown in Figure 4.9a. During the anodic scan towards higher potential values, the onset of the current is directly related to the oxidative decomposition of the electrolyte. Here, the limiting oxidation current is set to be 1 μA cm⁻². The concentration of LiTFSI is found to have an influential role in deciding the oxidative stability of the S-XPEs. It is observed that the oxidation stability value of the S-XPE is increased as a function of an increase in salt concentration (Table 4.6). When S-XPE-1

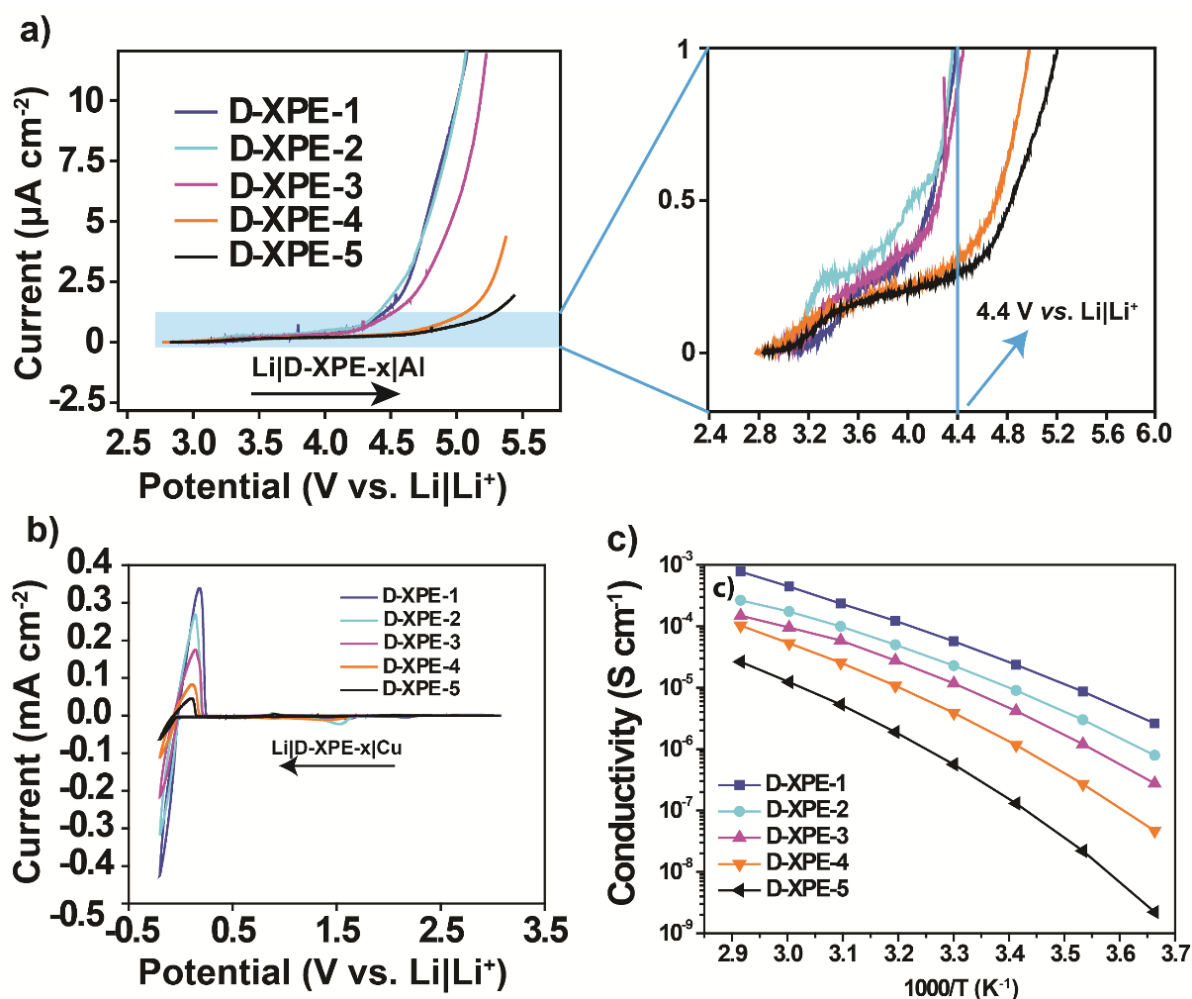


Figure 4.10. (a) Current vs. potential (vs. $\text{Li}|\text{Li}^+$) plots representing the oxidation stability of the D-XPE-x samples against Al; (b) current vs. potential (vs. $\text{Li}|\text{Li}^+$) plots representing the reduction stability of the D-XPE-x samples against Cu; (c) the plots representing the change in ionic conductivity of the D-XPE-x specimen with respect to temperature. (Reprinted (adapted) with permission from (ACS Appl. Mater. Interfaces 2020, 12, 1, 567-579). Copyright (2020) American Chemical Society).

exhibited stability of 4.2 V vs. $\text{Li}|\text{Li}^+$, the oxidation stability of S-XPE-5 is found to be ≈ 5.1 V vs. $\text{Li}|\text{Li}^+$. In the case of other S-XPEs, the oxidation stability recorded is 4.3, 4.5, and 4.9 V vs. $\text{Li}|\text{Li}^+$, respectively for the S-XPE-2, -3, and -4 samples. In other words, if one looks at the sudden increase (onset potential) in the current density then all the samples evaluated here show oxidation stability above 5 V vs. $\text{Li}|\text{Li}^+$, which is also dependent on the TFSI⁻ anion concentration. The increase of the oxidative stability with the LiTFSI concentration can be rationalized with several arguments. For instance, the intrinsic oxidative stability of the PEGDME- Li^+ complex is increased by the progressive coordination of the lithium ions. This is verified by the calculation of the oxidative stabilities of the individual clusters by QC

calculation in **Figures 4.7a-c**. For instance, the PM6 calculations estimate values of 5.4 V vs. Li|Li⁺ for isolated PEGDME, whereas this value increases to 6.2 V vs. Li|Li⁺, 9.0 V vs. Li|Li⁺ and 9.0 V vs. Li|Li⁺ for the PEGDME coordinating to one, two or three lithium ions, respectively. Comparable values of 5.8 vs. Li|Li⁺ and 6.2 vs. Li|Li⁺ values are found for PEGDME and PEGDME-Li⁺ (i.e. coordinating to a single lithium-ion) at the LC- ω PBE/6-31+G(d,p) level. It has to be mentioned, however, that these values might be significantly lowered by the presence of anions in the bulk electrolyte or when taking electrochemical decomposition reactions (the deprotonation of the oxidized cluster that stabilizes the electron-hole) into account.^{31,32}

In addition to an increase in intrinsic electrochemical stability, a higher salt concentration additionally leads to an effective exclusion of all the ether molecular species except the anions from the first electrolyte layer in contact (inner-Helmholtz layer) with the cathode (**Figure 4.7e**).³² Since the TFSI anion is rather stable, the increased oxidative stability at high LiTFSI concentrations could thus be rationalized by the formation of a surface layer such as cathode electrolyte interphase (CEI), which is comparable to the stabilization of the so-called water-in-salt electrolytes.⁵⁹ The dependence of high LiTFSI content in an electrolyte suppressing the dissolution of the Al electrode by the formation of a surface layer is reported by several authors.⁶⁰⁻⁶⁴ It is known that conventional electrolytes with a low concentration of LiTFSI such as S-XPE-1 (or Li-P-1) enhance the Al current collector dissolution at higher potentials in liquid (low viscous) state.⁶⁵ The reaction product (Al(TFSI)₃) is soluble in the case of the liquid electrolytes (especially, for carbonate-based liquid electrolytes) leading to the gradual dissolution of Al,⁶³ however, it is not soluble when the polymer electrolytes are used. This insoluble product may act as a surface protection layer and extends the overall continuous oxidation process when Al is used as the working electrode. Also, at higher potentials, decomposition of the TFSI⁻ anion can induce the formation of LiF/AlF₃/AlOF₃ over the Al electrode and extend the decomposition potential of the electrolyte. This scenario is similar when a polymer or highly concentrated electrolytes are employed.⁶⁶⁻⁶⁸ In both processes, the type of salt and its concentration play a critical role when Al is used as the working electrode.

The oxidation stability of the XPEs against the StSt electrodes is also as determined. The results are presented in **Figure 4.9b**. If one considers the limiting current as 1 $\mu\text{A cm}^{-2}$, the obtained oxidation stability values are lower than the values obtained from the Al-based working electrode. A higher oxidation current value is observed before the large onset of the respective current density, which indicates that the formation of Al(TFSI)₃ and related passivation is not occurring in the case of StSt, indeed a decomposition of the TFSI⁻ anion may

occur.⁶⁹ In the case of StSt, a current density of $6.8 \mu\text{A cm}^{-2}$ is observed for S-XPE-2 at 4.4 V vs. Li|Li⁺, which is about at least 6 times larger than what we observed on an Al electrode. This extra current could be coming from the partial decomposition of the polymer electrolyte components or the TFSI⁻ anions. However, the real onset of current density is observed only above 5.0 V vs. Li|Li⁺ for all the analyzed samples. These results are in agreement with the results achieved here when Al is used as the working electrode and also with the other reported values,⁶⁹ which indicate that the S-XPEs are stable above 4.2 V vs. Li|Li⁺.

To determine the reduction stability of the S-XPEs, cyclic voltammetry analysis was employed at 60°C against Cu as the working electrode (**Figure 4.9a**). Clear and well-defined peaks corresponding to the plating and stripping process of lithium are observed for all S-XPEs. It is observed that the current density corresponding to the plating and stripping processes is the highest for the S-XPE-1 based cell, whereas it is the lowest for S-XPE-5. This reduced current intensity is directly related to the facile transport of Li⁺-ions through the S-XPE-1 sample as compared to other S-XPE counterparts. The current consumed during the lithium plating and the current generated during the stripping process is directly proportional to the lithium ions available at the working electrode, which in turn is an indication of higher ion mobility. No other peaks are observed between the open circuit potential (OCP) and 0 V vs. Li|Li⁺ indicates the purity of the crosslinked electrolytes and the synthesized materials.

Table 4.7. Ionic conductivity and anodic stability values of the entire series of D-XPE-*x* specimens. (Reprinted (adapted) with permission from (ACS Appl. Mater. Interfaces 2020, 12, 1, 567-579). Copyright (2020) American Chemical Society).

Sample	Ionic Conductivity (mS cm ⁻¹)		Transference No. (T _{Li⁺})	Anodic stability (vs. Li Li ⁺)
	30°C	60°C		
D-XPE-1	0.06	0.44	0.31	4.4
D-XPE-2	0.023	0.17	0.26	4.4
D-XPE-3	0.012	0.095	0.19	4.5
D-XPE-4	0.004	0.06	0.14	5
D-XPE-5	0.0006	0.012	0.11	5.2

From the above experiments, it is concluded that, for high voltage applications beyond 4.3 V, the S-XPEs with high LiTFSI content is suitable. To check with the possibility of further

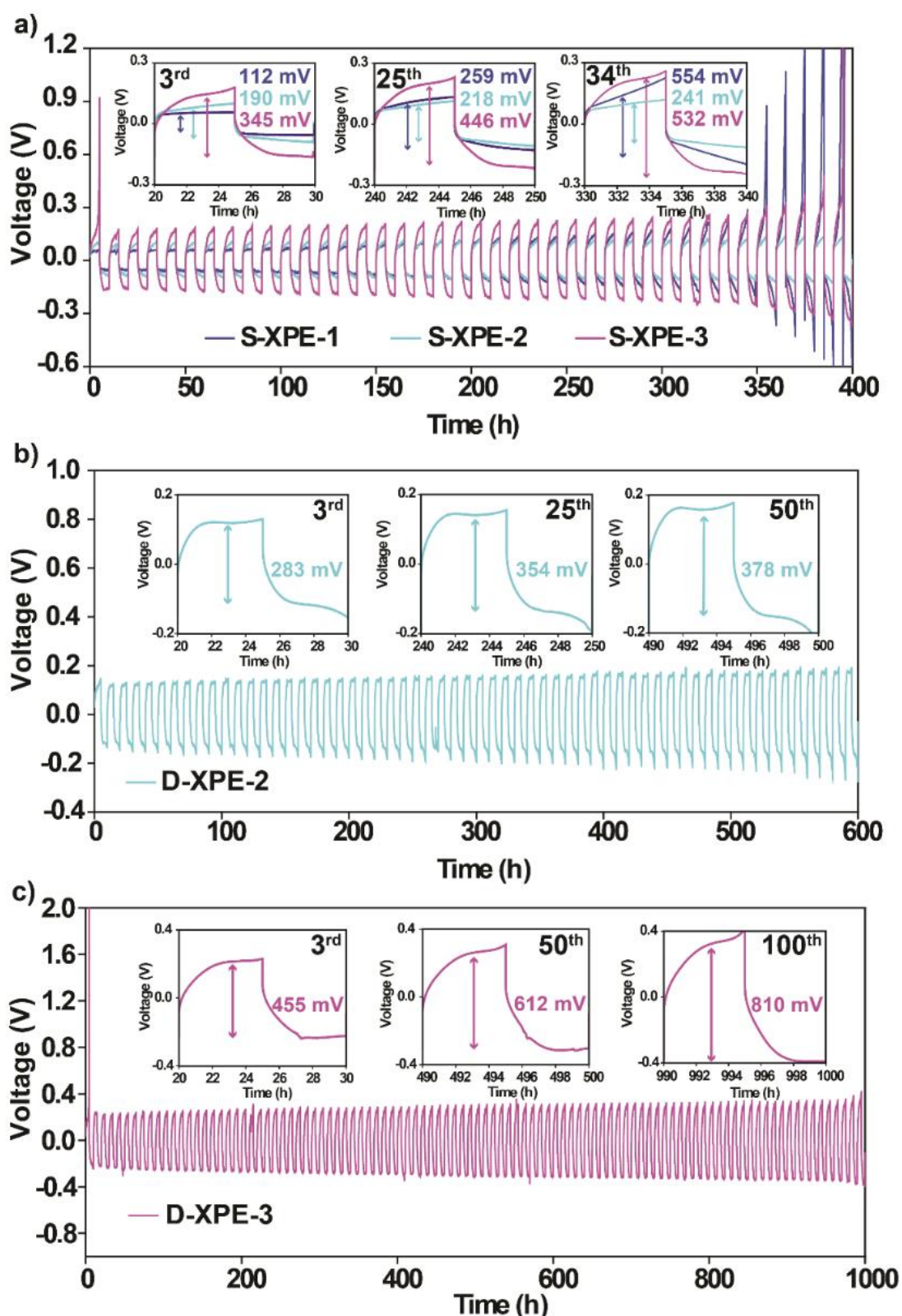


Figure 4.11. Voltage vs. time plot obtained from lithium plating and stripping cycles of lithium symmetric cells constructed with the (a) S-XPE-1, S-XPE-2, and S-XPE-3, (b) D-XPE-2, and (c) D-XPE-3 membranes when a current rate of 0.1 mA cm^{-2} for 5 h has been used. (Reprinted (adapted) with permission from (ACS Appl. Mater. Interfaces 2020, 12, 1, 567-579). Copyright (2020) American Chemical Society).

improving the oxidation stability, an additional 3 wt.% of LiFSI salt is introduced into the formulations and the obtained samples are termed as dual-salt XPEs (D-XPEs). Dual-salt electrolyte systems are well-known to enhance the interfacial/interphasial stability between the electrode and electrolyte depending on the type of lithium salt and its quantity and few reports also suggest their capability to improve the ESW of the electrolyte.^{16, 67, 70-72} The plots corresponding to the oxidation stability of all the D-XPE-x membranes are reported in **Figure 4.10a**. Compared to S-XPE-1, the D-XPE-1 membrane displayed significant improvement in the oxidation stability from 4.2 to 4.4 V vs. Li|Li⁺. In all other cases, the oxidation stability value of D-XPE membranes either remained the same or improved slightly by an additional 0.1 V compared to the S-XPE-x counterparts. As already proved by the QC studies, the screening of molecular species by means of the inner-Helmholtz layer occupied by the TFSI⁻ anions helps in improving the oxidation stability in high concentrated single-salt polymer electrolytes. With the inclusion of relatively small-sized FSI⁻ anions, we hypothesize that the inner-Helmholtz layer is modified and protects the cathode surface much effectively from the species prone to oxidation resulting in better oxidation stability values. The plots corresponding to the reduction stability of D-XPEs are provided in **Figure 4.10b**. Also, the plot representing the change in ionic conductivity with respect to temperature is provided in **Figure 4.10c**. **Table 4.7** summarizes the ionic conductivity, T_{Li^+} and oxidation stability values of all D-XPEs under investigation.

4.3.7 Galvanostatic lithium plating/stripping

To evaluate the performance of S-XPEs in LMBs, we have performed galvanostatic plating/stripping of lithium in Li|S-XPE|Li symmetric cells. A current density of 0.1 mA cm⁻² was applied for 5 h per half cycle, thus a total areal capacity of 0.5 mAh cm⁻² was deposited and extracted. The voltage vs. time response of S-XPEs is presented in **Figure 4.11a**. In the case of the Li|S-XPE-1|Li cell, the cumulative overvoltage value for the plating and stripping process is 112 mV in the 3rd cycle. However, the overvoltage values are gradually getting larger with an increase in the number of cycles. If one notices the plating and stripping profile of S-XPE-1 at different time intervals, it is evident that the diffusion of lithium ions is changing the plating/stripping characteristics, which may be induced by a change in the solid electrolyte interphase (SEI) layer thickness.⁷³ In the 25th cycle, the value is increased to 259 mV and 554 mV in the 34th cycle. In other words, about 400% increment in the overvoltage value is observed within the 35th cycle as compared to that of the 3rd cycle. These changes in overvoltage values are attributed to the incapability of the S-XPE-1 membrane to form a thin and effective SEI layer. The inability of low concentrated electrolytes to sustain stable and thin

SEI layer leading to an HSAL/dendrite induced cell failure is well known.^{74, 75} Despite the aforementioned limitations, the Li|S-XPE-1|Li cell could be cycled for 400 h without any cell failure.

The performance of S-XPE-2 is observed to be superior to that of S-XPE-1. Although a cumulative overvoltage value of 190 mV is observed in the 3rd cycle, the increment in the overvoltage value in the subsequent cycles is lower as compared to that of S-XPE-1. For instance, in the 25th cycle, the overvoltage value is just 218 mV whereas in the 34th cycle it is only 241 mV (27% increment in overvoltage as compared to the 3rd cycle). Concomitantly, the Li|S-XPE-2|Li cell displays excellent stability for more than 500 h. The retention of similar overvoltage values throughout the plating/stripping processes as well as the improved cycling stability proves the formation of an effective SEI for the S-XPE-2 membrane. As already explained, an increase in the LiTFSI content of S-XPE-2 is, in fact, the rationale behind the improved interfacial stability/interphase behavior of S-XPE-2.

In the case of the S-XPE-3 membrane, a very high overvoltage value of 345 mV in the 3rd cycle is observed, which is higher than those of the S-XPE-1 and S-XPE-2 samples. Later, the value increases to 446 and 532 mV in the 25th and 34th cycles, respectively. This corresponds to a 53% increment in the overvoltage at the 34th cycle as compared to the same in the 3rd cycle. This cell could also be cycled beyond 400 h. It is worth mentioning that the percentage increment in the overvoltage value associated with the S-XPE-3 membrane is lower compared to that of the S-XPE-1 counterpart. This suggests, that the SEI formed in the case of S-XPE-3 is much effective than that of S-XPE-1. However, the low ionic conductivity limits the potential of S-XPE-3 to be employed for practical applications. Similarly, in the case of S-XPE-4 and S-XPE-5, the plating/stripping experiment could not be carried out successfully beyond a single cycle owing to the constraints associated with low ionic conductivity, limited electrode wettability (contact) and the toughness of the membrane, and hence the data are not presented.⁶⁰ Increased toughness and insufficient contact at the lithium metal-polymer electrolyte interface leading to a high polarization overvoltage, thus the inability to maintain an insufficient continuous contact during the operation results in cell failure.

The aforementioned results suggest that the S-XPE-2 membrane could be a suitable choice for the LMBs among the single-salt polymer electrolytes with long-term cycling stability. Considering this fact, the galvanostatic plating/stripping characteristics of the related Li|D-XPE-2|Li cell are also studied. The impact of LiFSI as an additive in the LiTFSI based electrolytes to increase the effectiveness of the SEI is already known.⁷⁶ The voltage *vs.* time

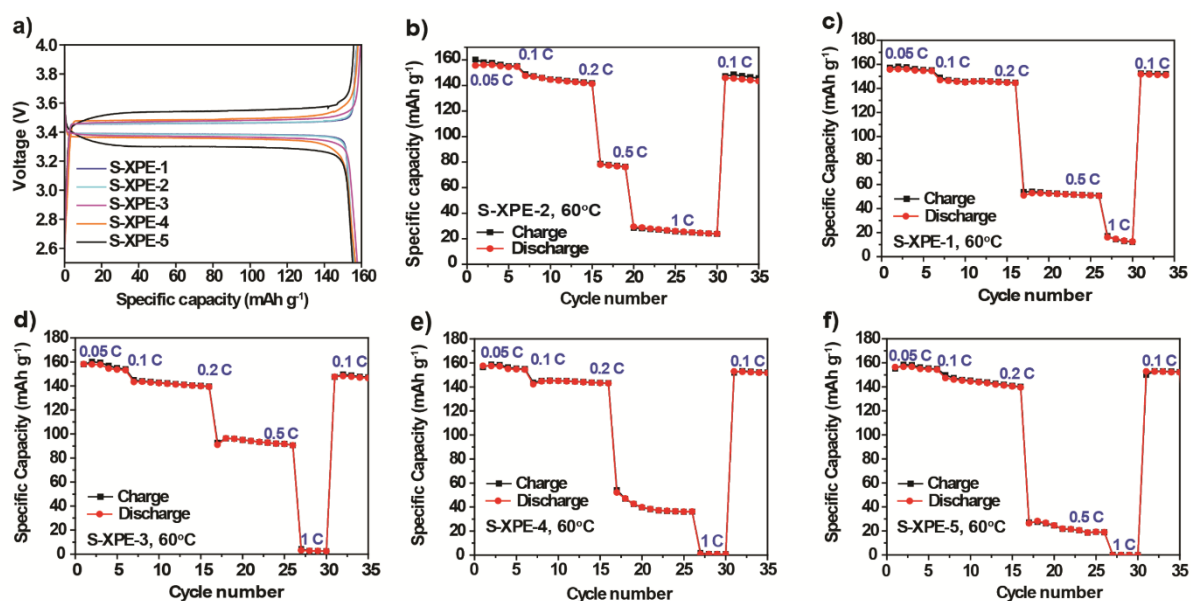


Figure 4.12. (a) Galvanostatic charge-discharge profiles of LFP|S-XPE-*x*|Li cells (60°C) at 0.05 C current rate. (b)-(c) The specific capacity vs. cycle number plot corresponding to the entire LFP|S-XPE-*x*|Li cells (60°C) at different C-rates. (Reprinted (adapted) with permission from *ACS Appl. Mater. Interfaces* 2020, 12, 1, 567-579). Copyright (2020) American Chemical Society).

response profile of the cell for 600 h is presented in **Figure 4.11b**. In the 3rd cycle, the overvoltage is calculated to be 283 mV. On direct comparison with the Li|S-XPE-2|Li cell, it can be seen that the 3rd cycle overvoltage value associated with the Li|D-XPE-2|Li cell is slightly high. However, the 25th cycle overvoltage shows only a 25% increment to a value of 354 mV, and even at the 50th cycle, the overvoltage value is 378 mV. This overvoltage at the 50th cycle corresponds to a 33% increment as compared to the 3rd cycle overpotential of the same sample. If the 50th cycle overvoltage of Li|S-XPE-2|Li alone is considered (**Figure 4.11a**), the increment is $\approx 48\%$ compared to the same at its 3rd cycle. Therefore, it can be concluded that the rate of increment in the overvoltage value associated with the D-XPE-2 membrane is minimal as compared to the S-XPE-2 counterpart. This underlines the formation of an effective SEI layer for D-XPE-2 owing to the presence of LiFSI salt as compared to that of S-XPE-2.⁷⁷

78

The superiority of the dual-salt XPEs is further reflected in the plating/stripping profile of the Li|D-XPE-3|Li cell (**Figure 4.11c**). In this case, the cell displayed excellent stability for 1000 h as compared to Li|S-XPE-3|Li, despite exhibiting high overvoltage values. The 2nd, 50th and 100th cycle overvoltage values associated with the cell are 455, 612, and 810 mV, respectively. This means a 34% increase in the 50th cycle and a 78% increase in the 100th cycle.

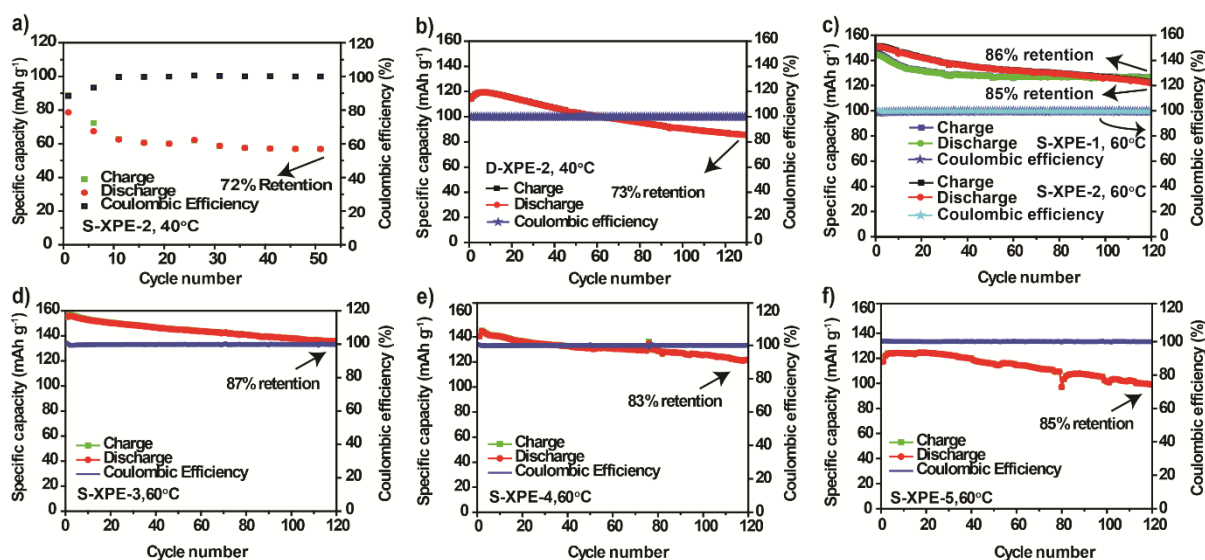


Figure 4.13. The long-term cycling stability of (a) LFP/S-XPE-2/Li, and (b) LFP/D-XPE-2/Li cells at 0.2C and 40°C at 0.2 C current rate; the long-term cycling stability of (c) LFP/S-XPE-1/Li and LFP/S-XPE-2/Li cells, (d) LFP/S-XPE-3/Li, (e) LFP/S-XPE-4/Li, and (f) LFP/S-XPE-4/Li cells at 0.2C and 60°C. (Reprinted (adapted) with permission from (ACS Appl. Mater. Interfaces 2020, 12, 1, 567-579). Copyright (2020) American Chemical Society).

Considering the above results, the superiority of the D-XPE membranes over the S-XPE membranes in terms of interfacial stability with the lithium metal anode is confirmed.¹¹¹ In addition, the high ESW of the D-XPE membrane as explained in the previous section provides a superior edge over the S-XPE-2 in terms of practicality.

4.3.8 Performance of XPE membranes in LMBs

To demonstrate the suitability of the synthesized XPE membranes, several lab-scale LMBs are fabricated. Both LFP and NCA cathodes are used for this purpose. For the fabrication of the LFP based lithium metal polymer cells that operate at a voltage range of 2.5-4 V vs. Li|Li⁺, the S-XPE-x membranes are used. In the case of high voltage NCA based cells that operate in the range of 2.7 V-4.3 V vs. Li|Li⁺, D-XPEs with high oxidation stability is used. The cells are cycled at 60, 40, and 20°C. **Figure 4.12a** represents the galvanostatic charge-discharge profiles (3rd cycle) corresponding to LFP/S-XPE-x/Li cells at 0.05 C (60°C). It is observed that all the cells display a discharge capacity of about 156 mAhg⁻¹, close to the practical specific capacity of the LFP cathodes (160 mAhg⁻¹) provided by the supplier. However, it can be also seen that the voltage gap between the charge and discharge plateau is higher in the case of S-XPE-3, -4, and -5 as compared to S-XPE-1 and -2 based cells. This is in accordance with the diffusion coefficient and lithium plating/stripping responses of the XPEs as provided in **Table 4.6**.

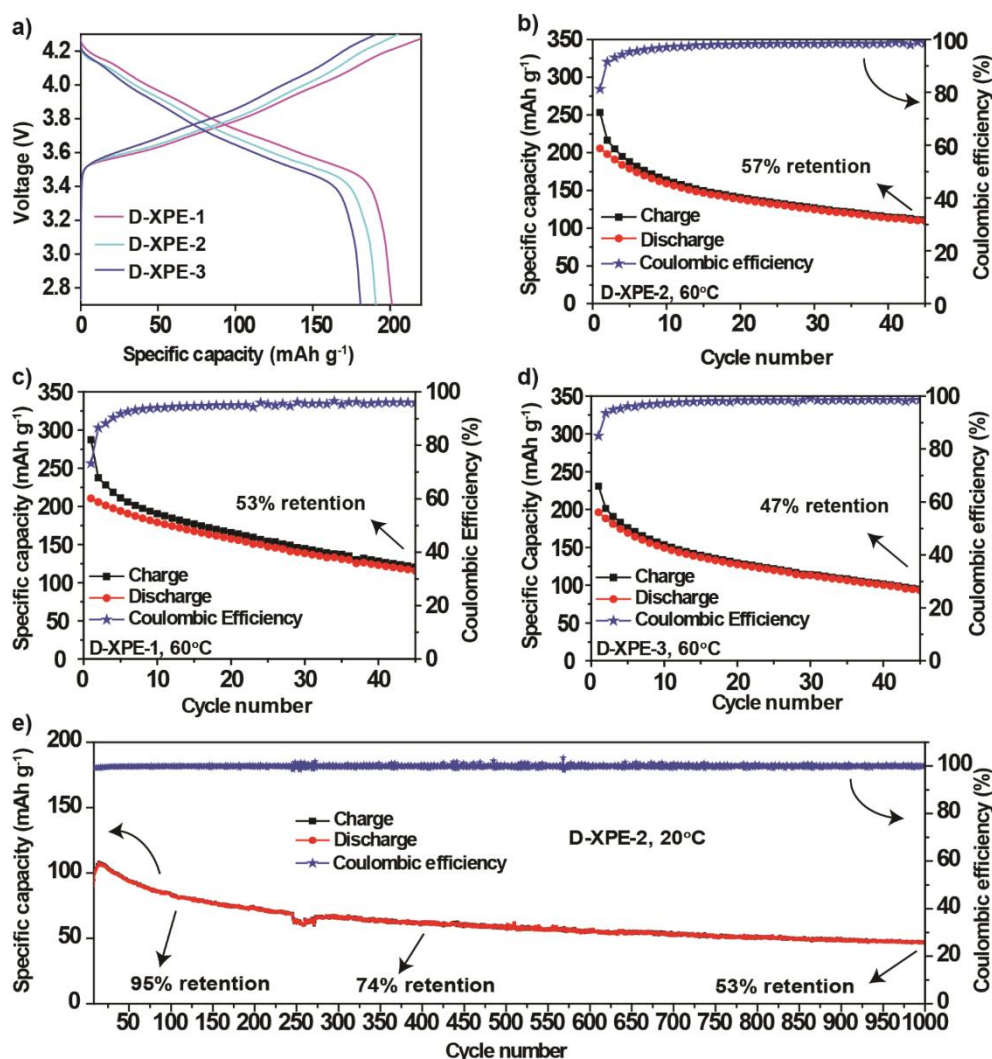


Figure 4.14. (a) Galvanostatic charge-discharge profiles corresponding to the NCA|D-XPE- x |Li cells at 0.1C (60°C); long term cycling stability profiles of (b) NCA|D-XPE-2|Li, (c) NCA|D-XPE-1|Li, and (d) NCA|D-XPE-3|Li at 0.1C and 60°C; (e) long term cycling stability profile of NCA|D-XPE-2|Li at 0.1C and 20°C. (Reprinted (adapted) with permission from *ACS Appl. Mater. Interfaces* 2020, 12, 1, 567-579). Copyright (2020) American Chemical Society.

The specific capacity vs. cycle number plots corresponding to the LFP|S-XPE-2|Li (60°C) at various C-rates are presented in **Figure 4.11b-f**. It is observed that the LFP cells of S-XPE-1 and S-XPE-2 (**Figure 4.12a**) exhibited good cycling stability at 0.2 C (60°C) with more than 85% retention of the initial capacity even after 120 charge-discharge cycles. The specific capacity vs. cycle number plot associated with the other LFP|S-XPE- x |Li cells at 60°C is presented in **Figure 4.12b-e**. At 40°C, the LFP|S-XPE-2|Li cell (**Figure 4.13a**) found to deliver very low cycling stability (only 72% retention with respect to the initial capacity after 40 cycles) with gradual capacity fading. The capacity fading can be attributed to the limitations associated with the S-XPE membrane where the interfacial stability with lithium-metal anode

is inferior as already been noticed from the plating/stripping investigations. However, this intricacy at low temperatures is found to be solved by the use of a D-XPE membrane. As it can be seen from **Figure 4.13b**, at 40°C, unlike the LFP|S-XPE-2|Li cell, the LFP|D-XPE-2|Li cell is characterized by 73% retention with respect to the initial capacity for over 130 cycles at 0.2C. This improved cycling stability is in accordance with the results obtained from the plating/stripping analysis of the D-XPE-2 membrane providing better electrode-electrolyte interfacial stability inside the cell. Finally, the cycling stability of the other LFP|S-XPE-x|Li cells at 60°C is presented in **Figure 4.13c-f**, which are displaying $\approx 85\%$ retention of the initial capacity after 120 cycles. Therefore, it can be concluded that the S-XPE membranes perform well with the LFP cathodes at 60°C and the cycling performance at low temperatures such as 40°C can be improved using D-XPE membrane. It is also important to optimize the anode side of the cell for improved cell performance while using the LFP based cathodes. Considering the better interfacial/interphasial properties and ESW of the D-XPE membranes, the NCA|D-XPE-x|Li cells are fabricated and cycled at 60 and 20°C.

The galvanostatic charge-discharge profiles corresponding to the NCA|D-XPE-x|Li cells at 0.1 C (60°C) are presented in **Figure 4.14a**. All the cells exhibited discharge capacities above 180 mAhg⁻¹ and a maximum capacity of 200 mAh g⁻¹ is obtained with the D-XPE-1 based NCA||Li cell. However, the long-term cycling stability of the D-XPE-x membrane-based cells at 60°C is found to be lower. It should be noted that the low Coulombic efficiency values observed in the initial cycles are associated with the formation cycles of the battery cell, which stabilizes once stable interphase is achieved. For instance, the NCA|D-XPE-2|Li cell shows the maximum capacity retention of 57 % of the initial capacity after 45 cycles (**Figure 4.14b**). At the same time, the D-XPE-1 (**Figure 4.14c**) and D-XPE-3 (**Figure 4.14d**) membrane-based cells displayed capacity retention of 53 and 47%, respectively. Despite the inferior performance of the D-XPE-x membranes at 60°C, the D-XPE-2 membrane exhibited excellent cycling stability when operated at a lower temperature of 20°C (**Figure 4.14e**). The cell displayed a maximum capacity of 110 mAh g⁻¹ with retention of $\approx 95\%$ of the initial capacity over 100 cycles. It is worth mentioning that the capacity retention even after 1000 cycles is 53% of the initial capacity. The improvement in cycling stability sheds light on the conclusion that the degradation of XPE induced by NCA particles or high voltage is reduced at a lower temperature and the cycling of other high-voltage cathodes against the polymer electrolytes is an important parameter to be investigated further. The above results indicate that the reported S-XPE and D-XPEs are promising candidates for LMBs and a dual-salt approach could be a game-changer for already existing and well-investigated polymer matrices. Also, it is envisaged that judicious

modifications in the structure of the polymer matrix can help in improving the performance of XPEs while providing an opportunity to extend its applicability to SPEs.

4.4 Conclusion

In this work, the synthesis of a series of novel Li⁺-ion conducting single (S-) and dual (D-) salt crosslinked polymer electrolyte (XPE) membranes are reported based on a polymer matrix composed of poly(vinyl ethylene carbonate) crosslinked by EO units and plasticized by a high boiling oligomer poly(ethylene glycol dimethyl ether) (PEGDME). In S-XPE membranes, LiTFSI alone acts as a source of Li⁺-ions whereas the D-XPE membranes consist of LiFSI in addition to LiTFSI. QC calculations, thermal and ATR-FTIR spectroscopy analyses provided insights regarding the interactions between the Li⁺-ions and EO units in the XPE membranes. The ESW of the S- and D-XPE membranes are found to be increased as a function of salt concentration; indeed, a higher salt concentration favors wider oxidation stability. Wide electrochemical stability of 5.1 and 5.2 V vs. Li|Li⁺ is achieved for the S-XPE and D-XPE membranes, respectively. It has been understood that the concentration of salt plays an important role in the oxidation stability of the XPE and the cycling stability of the LMB full cells. However, more studies are required for the mechanistic understanding. Hence obtained XPEs are then used for the fabrication of lab-scale LMB unit-cells. The D-XPE membranes are found to be compatible with LiFePO₄ as well as high-voltage NCA cathodes. At 20°C, the dual salt-based membrane in a LiNi_{0.8}Co_{0.15}Al_{0.05}O₂ based high voltage cell retained 95% of its initial capacity after 100 cycles all-the-while exhibiting 53% of capacity retention after 1000 cycles. It is expected that the performance of the reported XPEs can be further improved by tuning the molecular weight of the allyl ether-based oligomer crosslinker, and at the same time the application of the reported polymer matrix can be extended to SPEs.

4.5 References

- [1] Winter, M.; Barnett, B.; Xu, K., *Before Li Ion Batteries*. Chemical Reviews 2018, 118 (23), 11433-11456.
- [2] Placke, T.; Kloepsch, R.; Dühnen, S.; Winter, M., *Lithium ion, lithium metal, and alternative rechargeable battery technologies: the odyssey for high energy density*. Journal of Solid State Electrochemistry 2017, 21 (7), 1939-1964.
- [3] Ryou, M.-H.; Lee, Y. M.; Lee, Y.; Winter, M.; Bieker, P., *Mechanical Surface Modification of Lithium Metal: Towards Improved Li Metal Anode Performance by Directed Li Plating*. Advanced Functional Materials 2015, 25 (6), 834-841.
- [4] Li, L.; Li, S.; Lu, Y., *Suppression of dendritic lithium growth in lithium metal-based batteries*. Chemical Communications 2018, 54 (50), 6648-6661.

- [5] Betz, J.; Brinkmann, J.-P.; Nölle, R.; Lürenbaum, C.; Kolek, M.; Stan, M. C.; Winter, M.; Placke, T., Cross Talk between Transition Metal Cathode and Li Metal Anode: Unraveling Its Influence on the Deposition/Dissolution Behavior and Morphology of Lithium. *Advanced Energy Materials* 2019, 9 (21), 1900574.
- [6] Nair, J. R.; Imholt, L.; Brunklaus, G.; Winter, M., Lithium Metal Polymer Electrolyte Batteries: Opportunities and Challenges. *The Electrochemical Society Interface* 2019, 28 (2), 55-61.
- [7] Xue, Z.; He, D.; Xie, X., Poly(ethylene oxide)-based electrolytes for lithium-ion batteries. *Journal of Materials Chemistry A* 2015, 3 (38), 19218-19253.
- [8] Cheng, X.; Pan, J.; Zhao, Y.; Liao, M.; Peng, H., Gel Polymer Electrolytes for Electrochemical Energy Storage. *Advanced Energy Materials* 2018, 8 (7), 1702184.
- [9] Porcarelli, L.; Shaplov, A. S.; Bella, F.; Nair, J. R.; Mecerreyes, D.; Gerbaldi, C., Single-Ion Conducting Polymer Electrolytes for Lithium Metal Polymer Batteries that Operate at Ambient Temperature. *ACS Energy Letters* 2016, 1 (4), 678-682.
- [10] Liang, S.; Yan, W.; Wu, X.; Zhang, Y.; Zhu, Y.; Wang, H.; Wu, Y., Gel polymer electrolytes for lithium ion batteries: Fabrication, characterization and performance. *Solid State Ionics* 2018, 318, 2-18.
- [11] Nair, J. R.; Gerbaldi, C.; Meligrana, G.; Bongiovanni, R.; Bodoardo, S.; Penazzi, N.; P.Reale; Gentili, V., UV-cured methacrylic membranes as novel gel-polymer electrolyte for Li-ion batteries. *Journal of Power Sources* 2008, 178 (2), 751-757.
- [12] Vijayakumar, V.; Anothumakkool, B.; Torris A. T, A.; Nair, S. B.; Badiger, M. V.; Kurungot, S., An all-solid-state-supercapacitor possessing a non-aqueous gel polymer electrolyte prepared using a UV-assisted in situ polymerization strategy. *Journal of Materials Chemistry A* 2017, 5 (18), 8461-8476.
- [13] Gerbaldi, C.; Nair, J. R.; Meligrana, G.; Bongiovanni, R.; Bodoardo, S.; Penazzi, N., UV-curable siloxane-acrylate gel-copolymer electrolytes for lithium-based battery applications. *Electrochimica Acta* 2010, 55 (4), 1460-1467.
- [14] Nair, J. R.; Shaji, I.; Ehteshami, N.; Thum, A.; Diddens, D.; Heuer, A.; Winter, M., Solid Polymer Electrolytes for Lithium Metal Battery via Thermally Induced Cationic Ring-Opening Polymerization (CROP) with an Insight into the Reaction Mechanism. *Chemistry of Materials* 2019, 31 (9), 3118-3133.

- [15] Cho, Y.-G.; Hwang, C.; Cheong, D. S.; Kim, Y.-S.; Song, H.-K., Gel/Solid Polymer Electrolytes Characterized by In Situ Gelation or Polymerization for Electrochemical Energy Systems. *Advanced Materials* 2019, 31 (20), 1804909.
- [16] Li, S.; Chen, Y.-M.; Liang, W.; Shao, Y.; Liu, K.; Nikolov, Z.; Zhu, Y., A Superionic Conductive, Electrochemically Stable Dual-Salt Polymer Electrolyte. *Joule* 2018, 2 (9), 1838-1856.
- [17] Zhou, Y. F.; Xie, S.; Ge, X. W.; Chen, C. H.; Amine, K., Preparation of rechargeable lithium batteries with poly(methyl methacrylate) based gel polymer electrolyte by in situ γ -ray irradiation-induced polymerization. *Journal of Applied Electrochemistry* 2004, 34 (11), 1119-1125.
- [18] Chai, J.; Liu, Z.; Zhang, J.; Sun, J.; Tian, Z.; Ji, Y.; Tang, K.; Zhou, X.; Cui, G., A Superior Polymer Electrolyte with Rigid Cyclic Carbonate Backbone for Rechargeable Lithium Ion Batteries. *ACS Applied Materials & Interfaces* 2017, 9 (21), 17897-17905.
- [19] Chai, J.; Liu, Z.; Ma, J.; Wang, J.; Liu, X.; Liu, H.; Zhang, J.; Cui, G.; Chen, L., In Situ Generation of Poly (Vinylene Carbonate) Based Solid Electrolyte with Interfacial Stability for LiCoO₂ Lithium Batteries. *Advanced Science* 2017, 4 (2), 1600377.
- [20] Morioka, T.; Nakano, K.; Tominaga, Y., Ion-Conductive Properties of a Polymer Electrolyte Based on Ethylene Carbonate/Ethylene Oxide Random Copolymer. *Macromolecular Rapid Communications* 2017, 38 (8), 1600652.
- [21] Meabe, L.; Huynh, T. V.; Mantione, D.; Porcarelli, L.; Li, C.; O'Dell, L. A.; Sardon, H.; Armand, M.; Forsyth, M.; Mecerreyes, D., UV-crosslinked poly(ethylene oxide carbonate) as free standing solid polymer electrolyte for lithium batteries. *Electrochimica Acta* 2019, 302, 414-421.
- [22] Porcarelli, L.; Gerbaldi, C.; Bella, F.; Nair, J. R., Super Soft All-Ethylene Oxide Polymer Electrolyte for Safe All-Solid Lithium Batteries. *Scientific Reports* 2016, 6, 19892.
- [23] Barteau, K. P.; Wolffs, M.; Lynd, N. A.; Fredrickson, G. H.; Kramer, E. J.; Hawker, C. J., Allyl Glycidyl Ether-Based Polymer Electrolytes for Room Temperature Lithium Batteries. *Macromolecules* 2013, 46 (22), 8988-8994.
- [24] Pesko, D. M.; Webb, M. A.; Jung, Y.; Zheng, Q.; Miller, T. F.; Coates, G. W.; Balsara, N. P., Universal Relationship between Conductivity and Solvation-Site

- Connectivity in Ether-Based Polymer Electrolytes. *Macromolecules* 2016, 49 (14), 5244-5255.
- [25] Itoh, T.; Fujita, K.; Inoue, K.; Iwama, H.; Kondoh, K.; Uno, T.; Kubo, M., Solid polymer electrolytes based on alternating copolymers of vinyl ethers with methoxy oligo(ethyleneoxy)ethyl groups and vinylene carbonate. *Electrochimica Acta* 2013, 112, 221-229.
- [26] Lu, P.; Alrashdi, N. M.; Boydston, A. J., Bidirectional metal-free ROMP from difunctional organic initiators. *Journal of Polymer Science Part A: Polymer Chemistry* 2017, 55 (18), 2977-2982.
- [27] Frisch, M.; Trucks, G.; Schlegel, H.; Scuseria, G.; Robb, M.; Cheeseman, J.; Scalmani, G.; Barone, V.; Petersson, G.; Nakatsuji, H., *Gaussian 16 Rev. B. 01*, 2016. Wallingford, CT.
- [28] Stewart, J. J., Optimization of parameters for semiempirical methods V: modification of NDDO approximations and application to 70 elements. *Journal of Molecular modeling* 2007, 13 (12), 1173-1213.
- [29] Vydrov, O. A.; Scuseria, G. E., Assessment of a long-range corrected hybrid functional. *The Journal of chemical physics* 2006, 125 (23), 234109.
- [30] Marenich, A. V.; Cramer, C. J.; Truhlar, D. G., Universal solvation model based on solute electron density and on a continuum model of the solvent defined by the bulk dielectric constant and atomic surface tensions. *The Journal of Physical Chemistry B* 2009, 113 (18), 6378-6396.
- [31] Borodin, O.; Olguin, M.; Spear, C. E.; Leiter, K. W.; Knap, J., Towards high throughput screening of electrochemical stability of battery electrolytes. *Nanotechnology* 2015, 26 (35), 354003.
- [32] Borodin, O.; Ren, X.; Vatamanu, J.; von Wald Cresce, A.; Knap, J.; Xu, K., Modeling Insight into Battery Electrolyte Electrochemical Stability and Interfacial Structure. *Accounts of Chemical Research* 2017, 50 (12), 2886-2894.
- [33] Curtiss, L. A.; Redfern, P. C.; Raghavachari, K., Gaussian-4 theory using reduced order perturbation theory. *The Journal of chemical physics* 2007, 127 (12), 124105.
- [34] Matsumoto, A.; Kumagai, T.; Aota, H.; Kawasaki, H.; Arakawa, R., Reassessment of Free-Radical Polymerization Mechanism of Allyl Acetate Based on End-Group Determination of Resulting Oligomers by MALDI-TOF-MS Spectrometry. *Polymer Journal* 2008, 41, 26.

- [35] Borodin, O.; Smith, G. D., LiTFSI Structure and Transport in Ethylene Carbonate from Molecular Dynamics Simulations. *The Journal of Physical Chemistry B* 2006, 110 (10), 4971-4977.
- [36] Tominaga, Y.; Yamazaki, K.; Nanthana, V., Effect of anions on lithium ion conduction in poly (ethylene carbonate)-based polymer electrolytes. *Journal of the Electrochemical Society* 2015, 162 (2), A3133-A3136.
- [37] Sim, L. H.; Gan, S. N.; Chan, C. H.; Yahya, R., ATR-FTIR studies on ion interaction of lithium perchlorate in polyacrylate/poly(ethylene oxide) blends. *Spectrochimica Acta Part A: Molecular and Biomolecular Spectroscopy* 2010, 76 (3), 287-292.
- [38] Dai, Z.; Aboukeila, H.; Ansaloni, L.; Deng, J.; Giacinti Baschetti, M.; Deng, L., Nafion/PEG hybrid membrane for CO₂ separation: Effect of PEG on membrane micro-structure and performance. *Separation and Purification Technology* 2019, 214, 67-77.
- [39] Matsuura, H.; Miyazawa, T.; Machida, K., Infrared spectra of poly(ethylene glycol) dimethyl ethers in the crystalline state. *Spectrochimica Acta Part A: Molecular Spectroscopy* 1973, 29 (5), 771-779.
- [40] Krishnan, K.; Krishnan, R. In *Raman and infrared spectra of ethylene glycol*, Proceedings of the indian academy of sciences-section A, Springer: 1966; p 111.
- [41] Ueno, K.; Tatara, R.; Tsuzuki, S.; Saito, S.; Doi, H.; Yoshida, K.; Mandai, T.; Matsugami, M.; Umebayashi, Y.; Dokko, K.; Watanabe, M., Li⁺ solvation in glyme–Li salt solvate ionic liquids. *Physical Chemistry Chemical Physics* 2015, 17 (12), 8248-8257.
- [42] Chen, Z.; FitzGerald, P. A.; Warr, G. G.; Atkin, R., Conformation of poly(ethylene oxide) dissolved in the solvate ionic liquid [Li(G4)]TFSI. *Physical Chemistry Chemical Physics* 2015, 17 (22), 14872-14878.
- [43] Gitelman, L.; Israeli, M.; Averbuch, A.; Nathan, M.; Schuss, Z.; Golodnitsky, D., Polymer geometry and Li⁺ conduction in poly(ethylene oxide). *Journal of Computational Physics* 2008, 227 (18), 8437-8447.
- [44] Molinari, N.; Mailoa, J. P.; Kozinsky, B., Effect of Salt Concentration on Ion Clustering and Transport in Polymer Solid Electrolytes: A Molecular Dynamics Study of PEO–LiTFSI. *Chemistry of Materials* 2018, 30 (18), 6298-6306.

- [45] Xu, X.; Jiang, L.; Zhou, Z.; Wu, X.; Wang, Y., Preparation and Properties of Electrospun Soy Protein Isolate/Polyethylene Oxide Nanofiber Membranes. *ACS Applied Materials & Interfaces* 2012, 4 (8), 4331-4337.
- [46] Jones, D. S.; Tian, Y.; Li, S.; Yu, T.; Abu-Diak, O. A.; Andrews, G. P., The Use of Binary Polymeric Networks in Stabilizing Polyethylene Oxide Solid Dispersions. *Journal of Pharmaceutical Sciences* 2016, 105 (10), 3064-3072.
- [47] He, R.; Echeverri, M.; Ward, D.; Zhu, Y.; Kyu, T., Highly conductive solvent-free polymer electrolyte membrane for lithium-ion batteries: Effect of prepolymer molecular weight. *Journal of Membrane Science* 2016, 498, 208-217.
- [48] Yoshida, Y.; Endo, T., Radical polymerization behavior and thermal properties of vinyl ethylene carbonate derivatives bearing aromatic moieties. *Polymer* 2016, 102, 167-175.
- [49] Diddens, D.; Heuer, A.; Borodin, O., Understanding the Lithium Transport within a Rouse-Based Model for a PEO/LiTFSI Polymer Electrolyte. *Macromolecules* 2010, 43 (4), 2028-2036.
- [50] Chatteraj, J.; Diddens, D.; Heuer, A., Effects of ionic liquids on cation dynamics in amorphous polyethylene oxide electrolytes. *The Journal of chemical physics* 2014, 140 (2), 024906.
- [51] Meyer, W. H., Polymer Electrolytes for Lithium-Ion Batteries. *Advanced Materials* 1998, 10 (6), 439-448.
- [52] Long, L.; Wang, S.; Xiao, M.; Meng, Y., Polymer electrolytes for lithium polymer batteries. *Journal of Materials Chemistry A* 2016, 4 (26), 10038-10069.
- [53] Forsyth, M.; Meakin, P.; MacFarlane, D. R.; Hill, A. J., Free volume and conductivity of plasticized polyether-urethane solid polymer electrolytes. *Journal of Physics: Condensed Matter* 1995, 7 (39), 7601-7617.
- [54] Brooks, D. J.; Merinov, B. V.; Goddard, W. A.; Kozinsky, B.; Mailoa, J., Atomistic Description of Ionic Diffusion in PEO–LiTFSI: Effect of Temperature, Molecular Weight, and Ionic Concentration. *Macromolecules* 2018, 51 (21), 8987-8995.
- [55] Bresser, D.; Lyonnard, S.; Iojoiu, C.; Picard, L.; Passerini, S., Decoupling segmental relaxation and ionic conductivity for lithium-ion polymer electrolytes. *Molecular Systems Design & Engineering* 2019.

- [56] Agapov, A. L.; Sokolov, A. P., Decoupling Ionic Conductivity from Structural Relaxation: A Way to Solid Polymer Electrolytes? *Macromolecules* 2011, 44 (11), 4410-4414.
- [57] Abraham, K.; Jiang, Z.; Carroll, B., Highly conductive PEO-like polymer electrolytes. *Chemistry of materials* 1997, 9 (9), 1978-1988.
- [58] Ma, Y.; Doyle, M.; Fuller, T. F.; Doeff, M. M.; De Jonghe, L. C.; Newman, J., The measurement of a complete set of transport properties for a concentrated solid polymer electrolyte solution. *Journal of The Electrochemical Society* 1995, 142 (6), 1859-1868.
- [59] Suo, L.; Borodin, O.; Gao, T.; Olguin, M.; Ho, J.; Fan, X.; Luo, C.; Wang, C.; Xu, K., "Water-in-salt" electrolyte enables high-voltage aqueous lithium-ion chemistries. *Science* 2015, 350 (6263), 938-943.
- [60] Zheng, J.; Lochala, J. A.; Kwok, A.; Deng, Z. D.; Xiao, J., Research Progress towards Understanding the Unique Interfaces between Concentrated Electrolytes and Electrodes for Energy Storage Applications. *Advanced Science* 2017, 4 (8), 1700032.
- [61] McOwen, D. W.; Seo, D. M.; Borodin, O.; Vatamanu, J.; Boyle, P. D.; Henderson, W. A., Concentrated electrolytes: decrypting electrolyte properties and reassessing Al corrosion mechanisms. *Energy & Environmental Science* 2014, 7 (1), 416-426.
- [62] Wang, J.; Yamada, Y.; Sodeyama, K.; Chiang, C. H.; Tateyama, Y.; Yamada, A., Superconcentrated electrolytes for a high-voltage lithium-ion battery. *Nature Communications* 2016, 7, 12032.
- [63] Meister, P.; Qi, X.; Kloepsch, R.; Krämer, E.; Streipert, B.; Winter, M.; Placke, T., Anodic Behavior of the Aluminum Current Collector in Imide-Based Electrolytes: Influence of Solvent, Operating Temperature, and Native Oxide-Layer Thickness. *ChemSusChem* 2017, 10 (4), 804-814.
- [64] Heckmann, A.; Thienenkamp, J.; Beltrop, K.; Winter, M.; Bruncklaus, G.; Placke, T., Towards high-performance dual-graphite batteries using highly concentrated organic electrolytes. *Electrochimica Acta* 2018, 260, 514-525.
- [65] Zhang, S. S.; Jow, T. R., Aluminum corrosion in electrolyte of Li-ion battery. *Journal of Power Sources* 2002, 109 (2), 458-464.

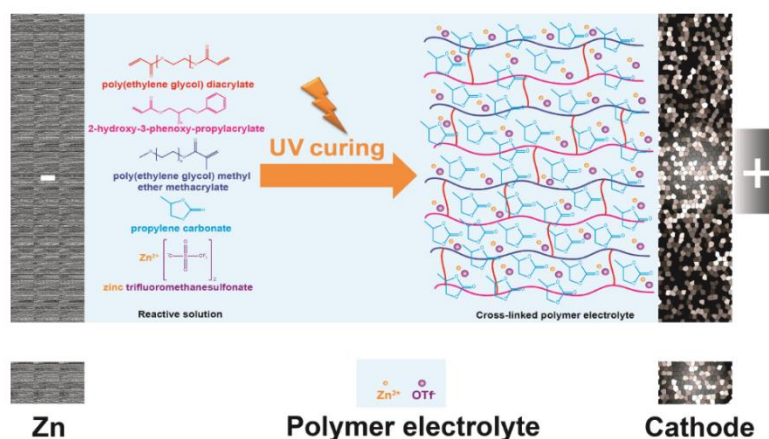
- [66] Krämer, E.; Passerini, S.; Winter, M., Dependency of aluminum collector corrosion in lithium ion batteries on the electrolyte solvent. *ECS Electrochemistry Letters* 2012, 1 (5), C9-C11.
- [67] Yamada, Y.; Chiang, C. H.; Sodeyama, K.; Wang, J.; Tateyama, Y.; Yamada, A., Corrosion Prevention Mechanism of Aluminum Metal in Superconcentrated Electrolytes. *ChemElectroChem* 2015, 2 (11), 1687-1694.
- [68] Kimura, K.; Motomatsu, J.; Tominaga, Y., Highly concentrated polycarbonate-based solid polymer electrolytes having extraordinary electrochemical stability. *Journal of Polymer Science Part B: Polymer Physics* 2016, 54 (23), 2442-2447.
- [69] Zhang, H.; Chen, F.; Lakuntza, O.; Oteo, U.; Qiao, L.; Martinez-Ibañez, M.; Zhu, H.; Carrasco, J.; Forsyth, M.; Armand, M., Suppressed Mobility of Negative Charges in Polymer Electrolytes with an Ether-Functionalized Anion. *Angewandte Chemie International Edition* 0 (0).
- [70] Kerner, M.; Plylahan, N.; Scheers, J.; Johansson, P., Ionic liquid based lithium battery electrolytes: fundamental benefits of utilising both TFSI and FSI anions? *Physical Chemistry Chemical Physics* 2015, 17 (29), 19569-19581.
- [71] Fan, W.; Li, N.-W.; Zhang, X.; Zhao, S.; Cao, R.; Yin, Y.; Xing, Y.; Wang, J.; Guo, Y.-G.; Li, C., A Dual-Salt Gel Polymer Electrolyte with 3D Crosslinked Polymer Network for Dendrite-Free Lithium Metal Batteries. *Advanced Science* 2018, 5 (9), 1800559.
- [72] Zhao, Q.; Chen, P.; Li, S.; Liu, X.; Archer, L. A., Solid-state polymer electrolytes stabilized by task-specific salt additives. *Journal of Materials Chemistry A* 2019, 7 (13), 7823-7830.
- [73] Winter, M., The solid electrolyte interphase—the most important and the least understood solid electrolyte in rechargeable Li batteries. *Zeitschrift für physikalische Chemie* 2009, 223 (10-11), 1395-1406.
- [74] Suo, L.; Hu, Y.-S.; Li, H.; Armand, M.; Chen, L., A new class of Solvent-in-Salt electrolyte for high-energy rechargeable metallic lithium batteries. *Nature Communications* 2013, 4, 1481.
- [75] Jeong, S.-K.; Seo, H.-Y.; Kim, D.-H.; Han, H.-K.; Kim, J.-G.; Lee, Y. B.; Iriyama, Y.; Abe, T.; Ogumi, Z., Suppression of dendritic lithium formation by using concentrated electrolyte solutions. *Electrochemistry Communications* 2008, 10 (4), 635-638.

-
- [76] Liu, P.; Ma, Q.; Fang, Z.; Ma, J.; Hu, Y.-S.; Zhou, Z.-B.; Li, H.; Huang, X.-J.; Chen, L.-Q., Concentrated dual-salt electrolytes for improving the cycling stability of lithium metal anodes. *Chinese Physics B* 2016, 25 (7), 078203.
- [77] Camacho-Forero, L. E.; Balbuena, P. B., Elucidating electrolyte decomposition under electron-rich environments at the lithium-metal anode. *Physical Chemistry Chemical Physics* 2017, 19 (45), 30861-30873.
- [78] Philippe, B.; Dedryvère, R.; Gorgoi, M.; Rensmo, H.; Gonbeau, D.; Edström, K., Improved Performances of Nanosilicon Electrodes Using the Salt LiFSI: A Photoelectron Spectroscopy Study. *Journal of the American Chemical Society* 2013, 135 (26), 9829-9842.

Chapter 5

An *In Situ* Crosslinked Nonaqueous Polymer Electrolyte for Zinc-Metal Polymer Batteries and Hybrid Supercapacitors

This work reports the first examples of nonaqueous zinc-ion conducting polymer electrolyte (ZIP) membranes synthesized using an ultraviolet (UV)-light induced photo-polymerization technique, with room temperature (RT) ionic conductivity in the order of $10^{-3} \text{ S cm}^{-1}$. The ZIP demonstrated excellent physicochemical and electrochemical properties, including an electrochemical stability window of $> 2.4 \text{ V vs. Zn|Zn}^{2+}$ and dendrite-free plating/stripping processes in symmetric Zn||Zn cells. Besides, an *in situ* process is developed to produce ZIP, which is adopted for the first time to fabricate a nonaqueous zinc-metal polymer battery ((ZMPB), $\text{VOPO}_4|\text{i-ZIP|Zn}$) and zinc-metal hybrid polymer supercapacitor ((ZMPS), activated carbon|i-ZIP|Zn) cells. The VOPO_4 cathode



employed in ZMPB possess a layered morphology, exhibiting a high average operating voltage of $\approx 1.2 \text{ V}$. As compared to the conventional *ex situ* process assisted cell assembling approaches, the *in situ* processing of the cell is simple. Also, the *in situ* process enhances the overall electrochemical performance, which enables the widespread intrusion of ZMPBs and ZMPSs into the application domain. Indeed, considering the promising aspects of the proposed ZIPs and its easy processability, this work opens up a new direction for the emergence of the zinc-based energy storage technologies.

Contents in this chapter is published in the article: DOI: 10.1002/sml.202002528.

Reprinted (adapted) with permission from (Small, 2020, vol. 16, no 35, p. 2002528).

Copyright © 2020 John Wiley & Sons, Ltd

5.1 Introduction

Despite the advancements in the field of lithium-ion batteries (LIBs), which revolutionized our daily life for the past several decades, it is clear that a single technology alone cannot rely on all kinds of applications. Concomitant development of other types of energy storage technologies is also important to fuel the concept of ‘technology diversity’ and its competence. In line with this, so-called ‘post-lithium technologies’ are receiving tremendous attention toward realizing affordable and alternate rechargeable energy storage devices.^{1, 2} In recent times, rechargeable energy storage devices employing zinc-metal as the anode (negative electrode) in combination with a zinc-ion (Zn^{2+}) conducting (aqueous/nonaqueous) liquid electrolyte and a suitable cathode (positive electrode) have gathered immense attention among electrochemists.^{3, 4} The relatively abundant supply of zinc, its low cost, stability, and safety (owing to less reactivity with water and other solvents) make the Zn-based systems attractive, perhaps even more than the other post-lithium technologies based on Na, Mg, etc.^{1, 5}

Since zinc-metal is directly employed as the anode, such systems can be called ‘zinc-metal cells.’ Among the zinc-metal cells, zinc-metal batteries (ZMBs) and zinc-metal hybrid supercapacitors (ZMSCs) are the most popular choices. Both ZMBs and ZMSCs are characterized by similar electrochemical reactions taking place at the anode: reversible plating and stripping of Zn during the charge/discharge processes.⁶⁻⁸ Indeed, the electrochemical processes (see **Figure 5.1a**) at the cathode are different in which the ZMB follows the insertion/de-insertion (similar to alkali-metal ion batteries), whereas the ZMSC is identified by the simple adsorption/desorption (similar to supercapacitors) of ions.⁹⁻¹¹ While ZMBs can be employed as high-energy devices, the potential of ZMSCs is relevant in terms of compensating any practical trade-offs in power capability.⁹ Therefore, investing the current ‘know-how’ regarding the energy storage devices toward improving the zinc-metal electrochemistry for rechargeable devices is rather important.

If the available reports are considered, zinc-ion conducting liquid (aqueous) electrolytes dominate the arena of zinc-metal cells.^{12, 13} The use of aqueous electrolytes is often constrained by the O_2 evolution reaction (OER) occurring at 1.98V vs. $\text{Zn}|\text{Zn}^{2+}$, which limits the operating voltage of the battery cell.^{5, 14, 15} Recently, highly concentrated aqueous electrolytes (e.g., water-in-salt electrolytes) are employed for improving the operating voltage of ZMBs beyond 2 V vs. $\text{Zn}|\text{Zn}^{2+}$.¹⁵⁻¹⁷ However, the

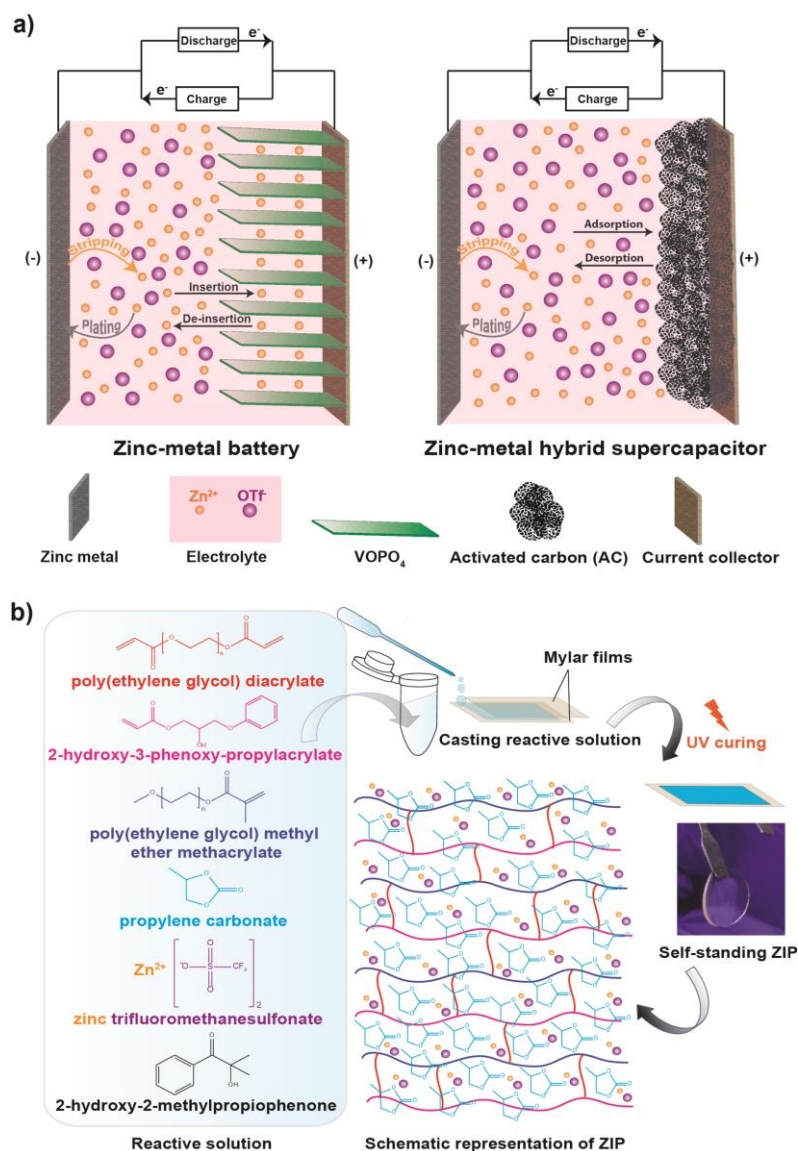


Figure 5.1. (a) The operating mechanism of a zinc-metal battery and zinc-metal hybrid supercapacitor where VOPO_4 and activated carbon (AC) are used as the positive electrodes, respectively; (b) the scheme representing the various components used for the UV-light induced synthesis of the zinc-ion conducting polymer electrolytes (ZIPs) (the digital image of a representative ZIP sample is also provided that exhibits self-standing behavior and transparency). Reprinted (adapted) with permission from (Small, 2020, vol. 16, no 35, p. 2002528). Copyright © 2020 John Wiley & Sons, Ltd.

water-in-salt electrolytes compromise the economic-aspects due to the high salt content. Moreover, the scarcity of high-voltage cathodes also hampers the prospect of realizing aqueous zinc-metal cells, especially ZMBs, with high average operating voltage (E_{av}).³ For example, when V_2O_5 is used as the cathode material, E_{av} is always <1 V, and if the material is changed to MnO_2 , then the voltage can be increased to 1.30 V.^{3, 4, 14} There are reports where Prussian blue-based cathodes are used for the fabrication of aqueous-

ZMBs with E_{av} of 1.70 V; however, they have a limitation concerning their low deliverable specific capacity (less than 100 mAh g^{-1}).^{5, 13, 18} Therefore, the current research in zinc-metal cells should progress towards achieving better suitable electrolytes in terms of ionic conductivity, oxidation stability and safety, and compatible cathode materials with high-voltage operability.

Unlike aqueous electrolytes, nonaqueous solvent-based electrolytes possess improved electrochemical stability,¹⁹⁻²¹ which can be suitably adapted in the high-voltage battery and supercapacitor chemistries, including zinc-metal cells. Recently, Burrell *et al.* reported acetonitrile (ACN) and propylene carbonate (PC)-based nonaqueous electrolytes, which favor reversible plating and stripping of Zn^{2+} ions. Indeed, this electrolyte has demonstrated high electrochemical stability of $> 3.0 \text{ V vs. Zn|Zn}^{2+}$ (Pt as a working electrode),²² which opened up the possibility to design organic solvent-based electrolytes for high-voltage zinc-metal cells. In line with this, Gewirth *et al.* have proposed several spinel structured cathode materials (ZnCo_2O_4 and $\text{ZnNi}_x\text{Mn}_x\text{Co}_{2-2x}\text{O}_4$) compatible with ACN-based liquid electrolytes for high-voltage nonaqueous ZMBs with E_{av} reaching up to of 1.50 V.²³ In separate reports, Hong *et al.*, and Vaughney *et al.*, demonstrated the use of nickel hexacyanoferrate ($E_{av} \approx 1.20 \text{ V}$)²⁴ and $\delta\text{-MnO}_2$ ($E_{av} \approx 1.25 \text{ V}$),²⁵ respectively as active cathode materials. Apart from the ACN-based electrolytes, it is expected that organic carbonate solvent-based liquid electrolytes can also be suitable for the zinc-metal cells considering their intrinsic features such as high boiling point, low flash-point, low viscosity, high dielectric constant and low-toxicity, improving the cell-safety aspects even though they are rarely explored. Despite these benefits, it should be noted that significant improvement in terms of E_{av} or electrochemical performance metrics in par with the aqueous zinc-metal cells is yet to be attained with their nonaqueous counterparts.

Since the field of nonaqueous zinc-metal cells is slowly evolving, considerable attention should be given toward the transition in electrolyte chemistry from liquid to solid-like systems, which can guarantee safe operability, flexibility, and higher energy density. Nonaqueous zinc-ion conducting polymer electrolytes (ZIPs) are anticipated to address these challenges, which may emerge during the ZMB/ZMSC development or commercialization. Zinc-metal cells employing polymer electrolytes can be called as ‘zinc-metal polymer cells’ in general. There are enormous amounts of literature reports related to nonaqueous polymer electrolytes, which can conduct monovalent metal ions

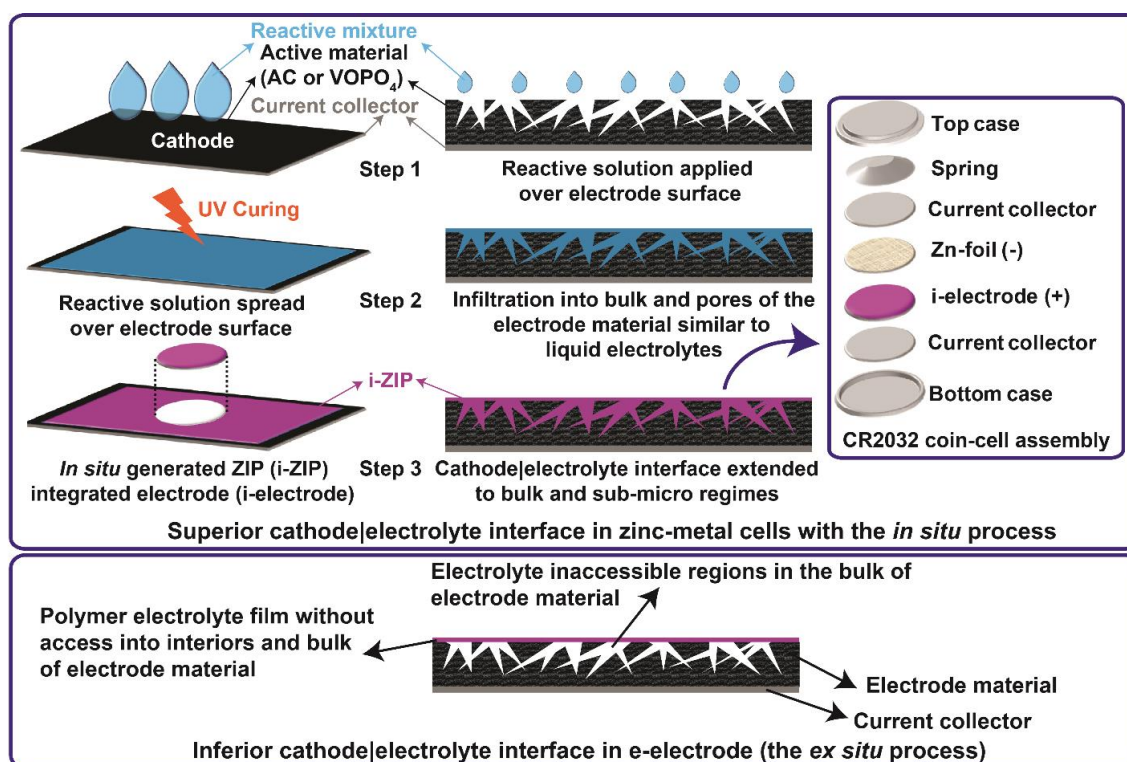


Figure 5.2. The processing steps involving in the *in situ* process for the fabrication of the zinc-metal polymer cells and the schematic illustration of the difference between the cathode|electrolyte interfaces achieved in the case of the *in situ* and *ex situ* processes. Reprinted (adapted) with permission from (Small, 2020, vol. 16, no 35, p. 2002528). Copyright © 2020 John Wiley & Sons, Ltd.

such as Li^+ and Na^+ ions for alkali-metal ion batteries,²⁶⁻²⁸ nevertheless, ZIPs are rarely explored. In this respect, solid- or quasi-solid-state ZIPs can facilitate the realization of zinc-metal polymer cells (zinc-metal polymer batteries (ZMPBs) and zinc-metal hybrid polymer supercapacitors (ZMPSs)), which can be easily integrated into flexible and printed electronic devices or large-scale energy grids. Moreover, compared to the liquid electrolytes, ZIPs may ensure safer operation of the device by eliminating the risk of leakage and fire hazards, especially if one considers nonaqueous liquid electrolytes for the high-voltage zinc-metal cells.

In this work, for the first time, we are reporting the preparation of crosslinked ZIPs by ultraviolet (UV)-light assisted free-radical polymerization and concomitant fabrication of nonaqueous zinc-metal polymer cells (**Figure 5.1b** and **5.2**) through the *in situ* process. The superior cathode|electrolyte interface achieved in the case of the *in situ* processed cells is demonstrated through electrochemical impedance spectroscopy (EIS) and computed tomography (CT) analyses. For instance, the ZMPB (VOPO_4 is used as the cathode) fabricated using the *in situ* process delivered a specific capacity of

$\approx 60 \text{ mAh g}^{-1}$ (0.20 Ag^{-1}) with retention of 63% after 50 cycles. This value is higher than that obtained for the *ex situ* processed ZMPB ($\approx 40 \text{ mAh g}^{-1}$ with 48% retention) as well as a liquid electrolyte-based ZMB ($\approx 23 \text{ mAh g}^{-1}$ with 36% retention). The high E_{av} (1.20 V) and energy density (96 Wh kg^{-1}) associated with the ZMPB are also worth mentioning. Additionally, the high cycling stability over 600 cycles achieved for the ZMPS (AC is used as the cathode) further underlines the broad applicability of ZIP and the *in situ* process towards realizing efficient zinc-metal cells.

5.2 Experimental Section

5.2.1 Materials

Unless otherwise specified separately, all materials used in this work were purchased from Sigma Aldrich. For the synthesis of the crosslinked polymer electrolyte, the acrylate monomers *viz.*, 2-hydroxy-3-phenoxypropyl acrylate (HPA), poly(ethylene glycol) diacrylate (700 Da, PEGDA), poly(ethylene glycol) methyl ether methacrylate (1100 Da, PEGMA) were used. As a photo-initiator, 2-hydroxy-2-methylpropiophenone (HMPP) was used. Propylene carbonate (PC) was used as the plasticizer and zinc trifluoromethanesulfonate ($\text{Zn}(\text{OTf})_2$) as the ion-conducting salt. For the reparation of $\text{VOPO}_4 \cdot 2\text{H}_2\text{O}$, ammonium vanadate (NH_4VO_3) purchased from Sisco Research Laboratories Pvt. Ltd. was used as the precursor. Phosphoric acid (H_3PO_4 , 85 wt. % in H_2O) was purchased from Thomas Baker (Chemicals) Pvt. Ltd. Activated Carbon (AC, YP-80F) used in this study was procured from Kuraray Chemical Co., Japan. Carbon black (Super P®) was purchased from Alfa Aesar and used as the conductive electrode additive. Polyvinylidene difluoride (PVdF, Kynar®) was used as the electrode binder and Grafoil® (GrafTech) was used as the current collector substrate on which the electrode materials were coated. For the preparation of the electrode-slurry, N-methyl-2-pyrrolidone (NMP) was used as the solvent. Zinc-metal foils (50 μm) and glass fibre (Grade GF/F) were supplied by Global NanoTech Pvt. Ltd. The laboratory-grade UV chamber used for polymerization contains 8 fluorescent lamps in a metallic chamber (Model: OSRAM L BL UVA 15 W/78).

5.2.2 Preparation of polymer electrolyte membranes

In a typical synthesis procedure, a bulk solution containing 30 wt. % of the acrylate monomers (PEGDA: PEGMA: HPA in the ratio of 1: 9.5: 9.5 by weight) in PC was prepared. Here onwards, the aforementioned bulk solution is termed as PMH-C-3070. Later, PMH-C-3070 was used to prepare 5, 10, 15, and 20 wt. % of $\text{Zn}(\text{OTf})_2$ salt solutions which are further represented as PMH-C-3070-x. Here, 'x' represents the wt. % of the zinc salt present in the PMH-C-3070 stock-solution. Later, the reactive or precursor solution was prepared from PMH-

C-3070-x stock solution with 5 wt. % of the HMPP initiator. Hence, the formed reactive mixture was cast between two Mylar Films, soon this setup was subjected to UV-irradiation for 15 min (**Figure 5.1b**). Depending on the wt. % ('x') of the Zn(OTf)₂ salt in the PMH-C-3070-x solution, the obtained polymer electrolytes (ZIP) are termed as 'ZIP-x'. In **Table 5.1**, the composition of ZIP-x samples along with their [O]/[Zn²⁺] ratio is provided in detail. ZIP-0 membrane as well as 0.08 m solution of Zn(OTf)₂ in the PC-based liquid electrolyte (represented as 'liquid') is also used for several comparison studies.

Table 5.1. Composition of the ZIP-x samples along with their corresponding [O]/[Zn²⁺] ratio.

* [O] = number of moles of oxygen and [Zn²⁺] = number of moles of Zn²⁺-ions. Reprinted (adapted) with permission from (Small, 2020, vol. 16, no 35, p. 2002528). Copyright © 2020 John Wiley & Sons, Ltd.

Sample	PEGDA (wt. %)	PEGMA (wt. %)	HPA (wt. %)	PC (wt. %)	HMPP (wt. %)	Zn(OTf) ₂ (wt. %)	molality (m)	*[O]/[Zn ²⁺] ratio
ZIP-5	1.35	13	13	63.18	5	4.5	0.13	199
ZIP-10	1.28	12.2	12.2	59.85	5	9.5	0.28	89
ZIP-15	1.21	11.5	11.5	56.53	5	14.25	0.46	56
ZIP-20	1.14	10.83	10.83	53.20	5	19	0.65	40

5.2.3 Synthesis of vanadyl phosphate cathode (VOPO₄·2H₂O)

VOPO₄·2H₂O nano-sheets were synthesized by adopting a simple reflux method. Ammonium metavanadate was used as the precursor for the synthesis. In a typical method, 1.5 g of NH₄VO₃ was dissolved in a mixture of H₃PO₄ and deionized water (13.30 ml and 6.77 ml respectively) followed by sonication for 20 min. This mixture was later transferred into a 250 ml round-bottom flask. The solution was refluxed with constant stirring at a temperature of 110°C for 16 h. After the completion of the reaction, the color of the solution was changed from orange to greenish-yellow. The obtained material was later washed thrice in a centrifuge at 1000 rpm, for 5 min. The collected material was filtrated and dried overnight. The scheme adopted for the synthesis of VOPO₄·2H₂O and the digital image of the final product obtained are presented in **Figure 5.5**.

5.2.4 Electrode coating and fabrication of zinc-metal cells

Polymer electrolyte-based lab-scale non-aqueous zinc-metal battery (ZMPB) and non-aqueous zinc-metal hybrid polymer supercapacitor (ZMPS) cells were prepared by using VOPO₄·2H₂O (VOPO₄) and activated carbon (AC) as the cathodes, respectively. The cathode electrode is composed of active material (AC or VOPO₄), binder (PVdF), and carbon black as

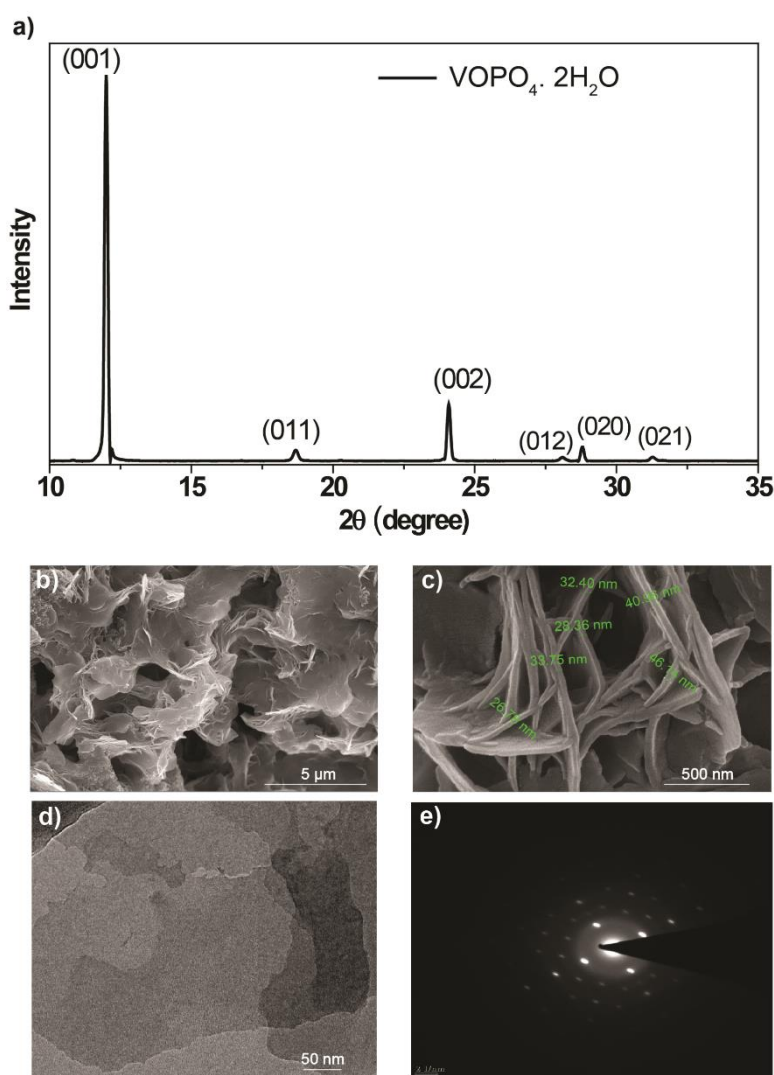


Figure 5.3. (a) P-XRD profile of the obtained $\text{VOPO}_4 \cdot 2\text{H}_2\text{O}$ sample; (b) and (c) show the FESEM images $\text{VOPO}_4 \cdot 2\text{H}_2\text{O}$ at different magnifications; (d) the TEM image and (e) SAED pattern associated with the as synthesized $\text{VOPO}_4 \cdot 2\text{H}_2\text{O}$. Reprinted (adapted) with permission from (Small, 2020, vol. 16, no 35, p. 2002528). Copyright © 2020 John Wiley & Sons, Ltd.

the conductive additive. For the preparation of the electrode, a slurry composed of the active material, PVdF, and Super P in a weight ratio of 90:5:5 in NMP solvent was prepared by probe sonication for 30 min. The obtained slurry was then cast on to a Grafoil substrate coated using a bar-coater followed by an overnight drying step at 60°C . Later, the coated electrodes were subjected to hot-pressing at 60°C for 15 min for ensuring an effective packing and integration of the electrode material on Grafoil® substrate. AC and VOPO_4 electrodes with high mass-loading values of 2 and 3 mg cm^{-2} were achieved, respectively. These electrodes are later used for the fabrication of ZMPBs and ZMPSs by *in situ* process.

The fabrication of ZMPBs and ZMPS cells was carried out by means of an *in situ* process. The details are schematically represented in **Figure 5.2**. In this process, the polymer electrolyte precursor solution (reactive solution of ZIP-20) was directly coated over the electrode surface and subjected to UV-irradiation for 15 min. The formed polymer electrolyte integrated electrode is termed as ‘i-electrode’ where ‘i’ refers to the *in situ* polymerization. Later, circular discs of i-electrode (11 mm diameter) were punched out and used for the fabrication of ZMPB or ZMPS against a Zn-metal anode (11 mm diameter) in a CR2032 coin-cell (two-electrode assembly). In these cells, the *in situ* generated polymer electrolyte plays the role of the separator as well. The *in situ* processed zinc-metal cells are denoted by VOPO₄|i-ZIP-x|Zn or AC|i-ZIP-x|Zn, where ‘i-ZIP-x’ represents the ZIP generated in the *in situ* process with ‘x’ wt.% of zinc-salt.

For comparison purposes, ZIP film- and liquid electrolyte-based zinc-metal cells were also prepared. The ZIP film-based ZMPB is represented as VOPO₄|ZIP-x|Zn. They are prepared by keeping the ZIP film between the respective electrodes (Zn and VOPO₄) in a CR2032 coin-cell assembly. In the case of the liquid electrolyte-based cells (represented as VOPO₄|liquid|Zn), a glass-fiber separator soaked in 0.08 m Zn(OTf)₂/PC was used for the cell fabrication in the CR2032 coin-cell assembly.

5.2.5 Characterization methods and techniques

Differential scanning calorimetry (DSC) analysis was carried out using the Discovery DSC 2500, instrument (TA instruments). The DSC samples were prepared out in a dry room to minimize moisture uptake and contamination. The samples were first cooled down from the temperature of 25 to –150°C followed by heating up to 150°C. The cooling and heating steps were conducted at a scan-rate of 10°C min⁻¹. All the processes were carried out under continuous helium flux. From the DSC thermograms, the glass transition temperature (T_g) values of the respective specimens were extracted.

The morphology of the VOPO₄·2H₂O sample was analyzed with a field emission scanning electron microscope (FESEM) instrument (Nova Nano SEM 450). Powder X-ray diffraction (P-XRD) data of the same samples were collected using a Rigaku, MicroMax007HF with a high-intensity Microfocus rotating anode X-ray generator in the 2θ range between 2° and 80° (Cu Kα ($\lambda = 1.54 \text{ \AA}$)). A Tecnai T-20 instrument equipped with energy-dispersive X-ray spectroscopy (EDS) detector was used for the transmission electron microscopy (TEM) imaging (accelerating voltage of 200 kV). For characterizing the surface morphology of the

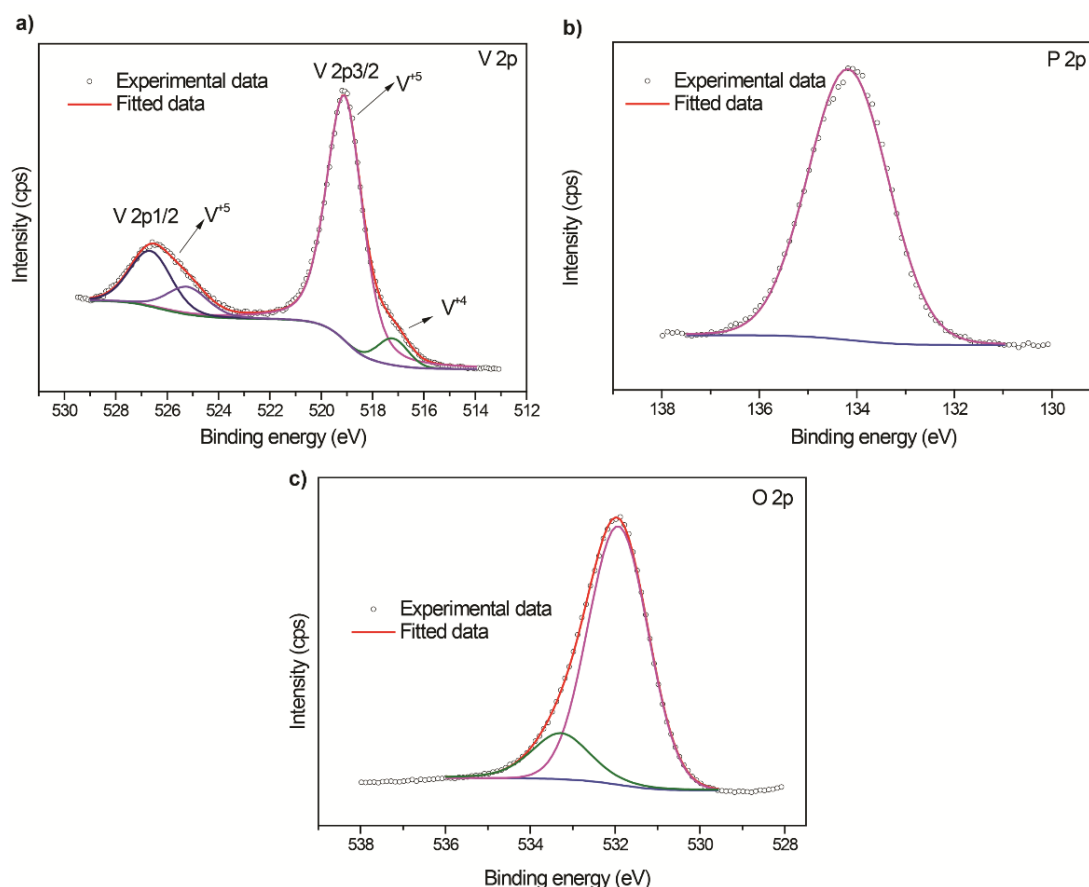


Figure 5.4. XPS profiles of the $\text{VOPO}_4 \cdot 2\text{H}_2\text{O}$ sample representing the regions indicating the presence of (a) V, (b) P, and (c) O. Reprinted (adapted) with permission from (Small, 2020, vol. 16, no 35, p. 2002528). Copyright © 2020 John Wiley & Sons, Ltd.

polymer electrolyte membranes, environmental SEM (ESEM) analysis was carried out with a Quanta 200 3D instrument.

Uni-axial and compression studies of the polymer electrolytes were carried out using a universal testing machine (UTM) (Model: Instron 5943, Instron Ltd., MA, USA), equipped with 1 kN load cell. For this purpose, the polymer electrolytes (ZIP-x) were prepared in the cylindrical form with 15 mm diameter and 12 mm height. A cross-head speed of 2 mm min^{-1} is fixed to carry out the uni-axial compression measurements, until a fracture was detected. Compressive stress and strain were recorded, calculated, and plotted for every sample. Young's modulus was measured from the initial slope of the stress-strain curve. Toughness characterizes the work required to fracture the sample per unit volume, was calculated from the area below the stress-strain curve until fracture.

Non-destructive 3D micro-tomography imaging of the electrodes was performed by X-ray micro-computed tomography (micro-CT) using Xradia Versa 510 X-ray Microscope (Zeiss X-ray Microscopy, USA). The electrodes were kept in between the X-ray source and detector

assembly. The detector assembly consists of a scintillator, objective lens, and a CCD camera. The X-ray source was ramped up to 50 kV at 3 W. The tomographic image acquisitions were completed by acquiring 3201 projections over 360° of rotation with a pixel size of 1.7 microns. Besides, projections without the samples in the beam (reference images) were also collected and averaged. The filtered back-projection algorithm was used for reconstruction of the projections to generate two-dimensional (2D) virtual cross-sections of the specimens. Image processing software, Dragonfly Pro Version 3.6 (Object Research Systems, Montreal, Canada) was used to generate a volume-rendered three-dimensional (3D) image of the electrodes after de-noising 2D images with appropriate image filters.

Electrochemical impedance spectroscopy (EIS) analysis in a Biologic VMP-3 potentiostat was used to determine the ionic conductivity of the ZIP-x membranes. To do this, the ZIP-x membranes (area 1.34 cm²) were placed between two stainless steel blocking electrodes in a CR2032-coin cell assembly. Before the EIS analysis, the cells were placed inside a climatic chamber (ESPEC SH-241). The measurements were carried out in the temperature range of 10°C and 60°C, and in the frequency range of 1 MHz to 1 Hz, at open-circuit voltage (OCV). The impedance responses were taken at every 10°C interval by maintaining the temperature equilibrium for 2 h. To calculate the ionic conductivity (σ , S cm⁻¹), the **Equation 5.1** was used,¹ where ' R_b ' is the bulk resistance, ' l ' is the thickness, and ' A ' is the area of the sample.

$$\sigma = lA^{-1}R_b^{-1} \quad (\text{Equation 5.1})$$

Vogel–Tamman–Fulcher (VTF) equation (**Equation 5.2**) was used to fit the ionic conductivity values obtained at various temperatures.² The VTF equation is significant in polymer electrolytes since it provides insights into the relationship between the viscosity and the temperature near the T_g of the polymer matrix.

$$\sigma = A \exp\left(-\frac{E_a}{R(T-T_0)}\right) \quad (\text{Equation 5.2})$$

where A is the pre-exponential factor related to charge carrier concentration, ' σ ' is the ionic conductivity, ' E_a ' is the activation energy (E_a^{VTF}), ' R ' is the gas constant, ' T ' is the experimental temperature and ' T_0 ' is the temperature which is 50 °C below the T_g .

The oxidation stability (anodic stability) of the ZIP-x membranes and the liquid electrolyte were evaluated by linear sweep voltammetry (LSV), and the reduction stability

(cathodic stability) by employing the cyclic voltammetry (CV) technique using a potentiostat (VMP3, Biologic). In both the measurements, a scan rate of 0.1 mVs^{-1} was employed. The LSV tests were run between OCP and $3.0 \text{ V vs. Zn|Zn}^{2+}$, where stainless steel (SS) was used as the working electrode (SS|ZIP-x|Zn and SS|liquid|Zn). Later, a tangent was plotted and the anodic stability values were determined from the onset of a continuous current flow. Similarly, the CV was carried out between OCP and $-0.26 \text{ V vs. Zn|Zn}^{2+}$ with SS as the working electrode (SS|ZIP-x|Zn). In both cases, Zn-metal was used as the reference electrode. Galvanostatic zinc plating/stripping measurements were carried out in a symmetric cell with a configuration of Zn|ZIP-x|Zn. All the measurements were carried out at 27°C at a current density of 0.1 mA cm^{-2} (0.5 h for Zn-plating and 0.5 h for Zn-stripping).

The ZMPB and ZMPS devices fabricated by the *in situ* processes were subjected to electrochemical characterizations in VMP3, Biologic potentiostat. The galvanostatic charge-discharge (GCD) and CV studies of the ZMPB cells were carried out between 0.50 to 2.0 V. In the case of ZMPS, the same studies were carried out in the range of 0.20 to 2.0 V. Here also, all the studies were conducted at 27°C . The specific capacity of the ZMPBs and ZMPSs was normalized with the mass-loading of the active cathode material.

5.3 Results and discussion

As shown in **Figure 5.1b**, we use a reactive mixture consisting of three types of acrylate monomers *viz.*, 2-hydroxy-3-phenoxypropyl acrylate (HPA), poly(ethylene glycol) diacrylate (700 Da, PEGDA), and poly(ethylene glycol) methyl ether methacrylate (1100 Da, PEGMA) in the presence of zinc salt (zinc trifluoromethanesulfonate, $\text{Zn}(\text{OTf})_2$), active plasticizer/solvent (PC), and a photo-initiator (2-hydroxy-2-methylpropiophenone (HMPP)). The reactive mixture, when subjected to an irradiation of UV-light, undergoes free-radical polymerization leading to a three-dimensionally cross-linked terpolymer network (see the schematic of ZIP structure in **Figure 5.1b**) to give rise to a series of ZIPs (ZIP-x, where 'x' refers to the wt.% of the zinc-salt in each ZIPs) with solid-like characteristics (see the photograph of the free-standing membrane in **Figure 5.1b**).

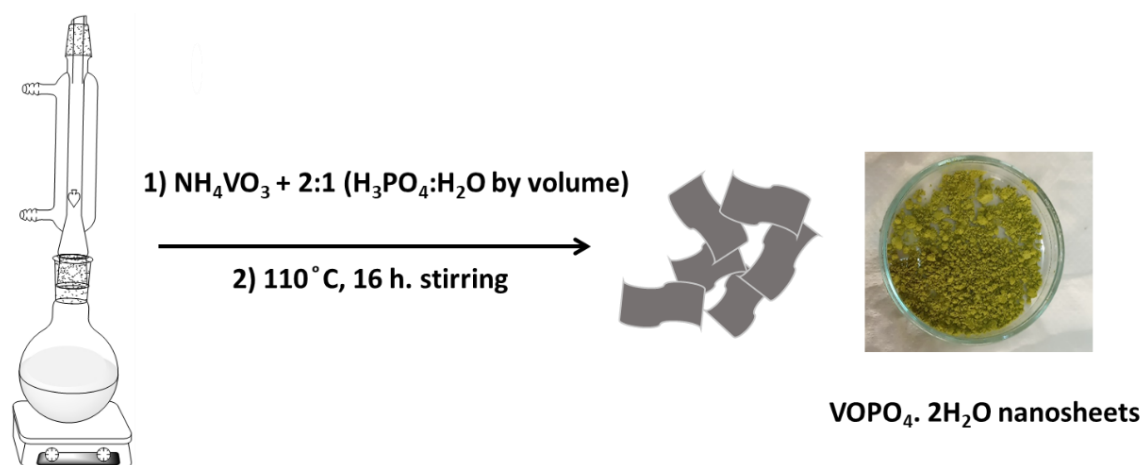


Figure 5.5. The scheme adopted for the synthesis of the $\text{VOPO}_4 \cdot 2\text{H}_2\text{O}$ nano-sheets. The digital image of the obtained sample is also provided. Reprinted (adapted) with permission from (Small, 2020, vol. 16, no 35, p. 2002528). Copyright © 2020 John Wiley & Sons, Ltd.

The compatibility of the acrylate monomers such as HPA with PC to be used in lithium-ion conducting based polymer electrolyte systems is already explored in our previous works as well as by several other researchers.^{29, 30} Indeed, high molecular weight acrylate monomers such as PEGMA is already known to internally plasticize the polymer matrix.³¹ Similarly, the di-functionalized monomer (PEGDA) acts as a crosslinker, which contributes to the free-standing nature, maneuverability, and plasticizer retention, resulting in the formation of a stable and leak-free polymer electrolyte.³⁰ Additionally, it is found that the acrylate monomers facilitate the solubility of the $\text{Zn}(\text{OTf})_2$ salt in the polymer matrix, which is otherwise less-soluble when PC alone is used as a solvent. For example, the reactive mixture could be employed to realize a bulk solution with the zinc-salt concentration as high as *ca.* 0.65 m, whereas the concentration is restricted to *ca.* 0.08 m when PC alone is used for solubilizing the zinc salt (concentration of $\text{Zn}(\text{OTf})_2$ in various ZIPs along with $[\text{O}]/[\text{Zn}^{2+}]$ ratio is tabulated in **Table 5.1**). This difference in solubility proves that PC alone is not a suitable solvent for $\text{Zn}(\text{OTf})_2$, however, in the presence of a suitable co-solvent such as the ether-based acrylate oligomers, the solubility can be improved.³² Indeed, such an approach can provide an opportunity to realize ZIPs.

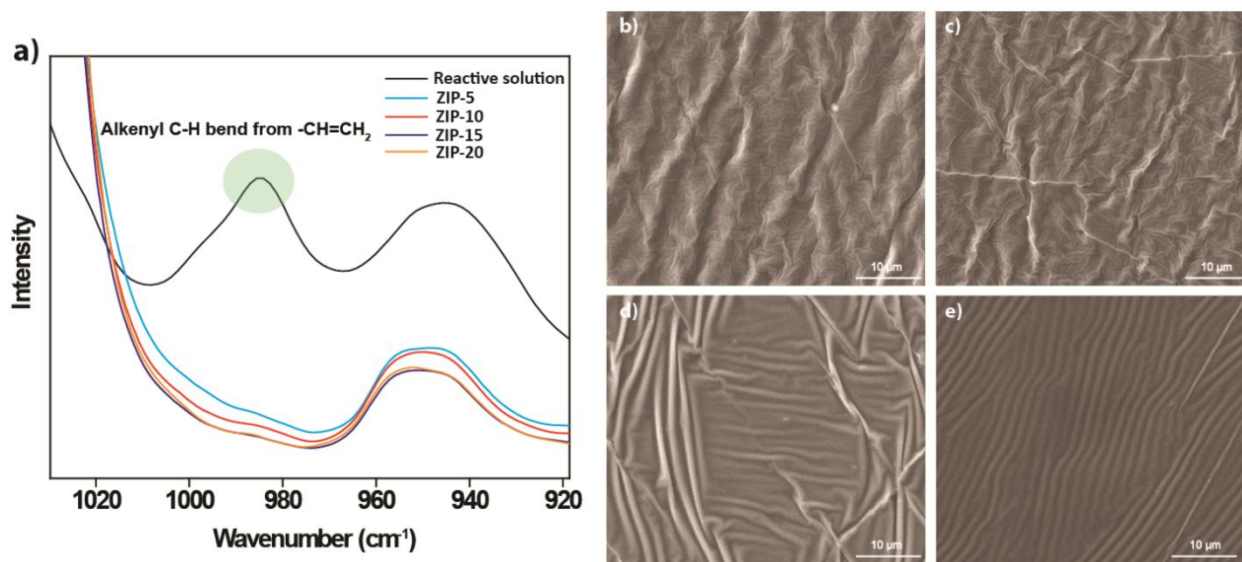


Figure 5.6. (a) ATR-FTIR spectra representing the absence of the $-C=C-$ peak for the crosslinked ZIP- x specimens compared to the unreacted reactive mixture; SEM images of the ZIP- x membranes: (b) ZIP-5, (c) ZIP-10, (d) ZIP-15, and (e) ZIP-20. Reprinted (adapted) with permission from (Small, 2020, vol. 16, no 35, p. 2002528). Copyright © 2020 John Wiley & Sons, Ltd.

The conversion of the reactive mixture to a crosslinked polymer electrolyte is directly achieved over the electrode surface during the fabrication of ZMPB/ZMPS by the *in situ* process (**Figure 5.2**). The polymerization over the electrode helps in achieving conformally coated ZIPs that are integrated into the electrode (called ‘i-electrode’), which is available soon after the process, hence, can be employed directly for the cell fabrication. This method simplifies the device fabrication, at the same time, improving the electrode|electrolyte interface and related electrochemical performance.³³⁻³⁵ Note that, here, the term ‘electrode|electrolyte interface’ refers to the contact between the electrode and electrolyte inside the electrochemical cell and within the electrode. When the electrode under consideration is the cathode, it can be called as ‘cathode|electrolyte interface.’ A good electrode|electrolyte interface always indicates to intimate and extended contact between the electrode and electrolyte, which is highly desirable for maximum active material utilization and optimum electrochemical performance.

As displayed in **Figure 5.2**, the reactive mixture containing monomers and oligomers being in a liquid-state can easily infiltrate into the bulk and sub-micro regimes of the electrode material. During UV-curing, the regions accessed by the reactive mixture will be converted into ZIP; thus, an intimate cathode|electrolyte interface is ensured. Such

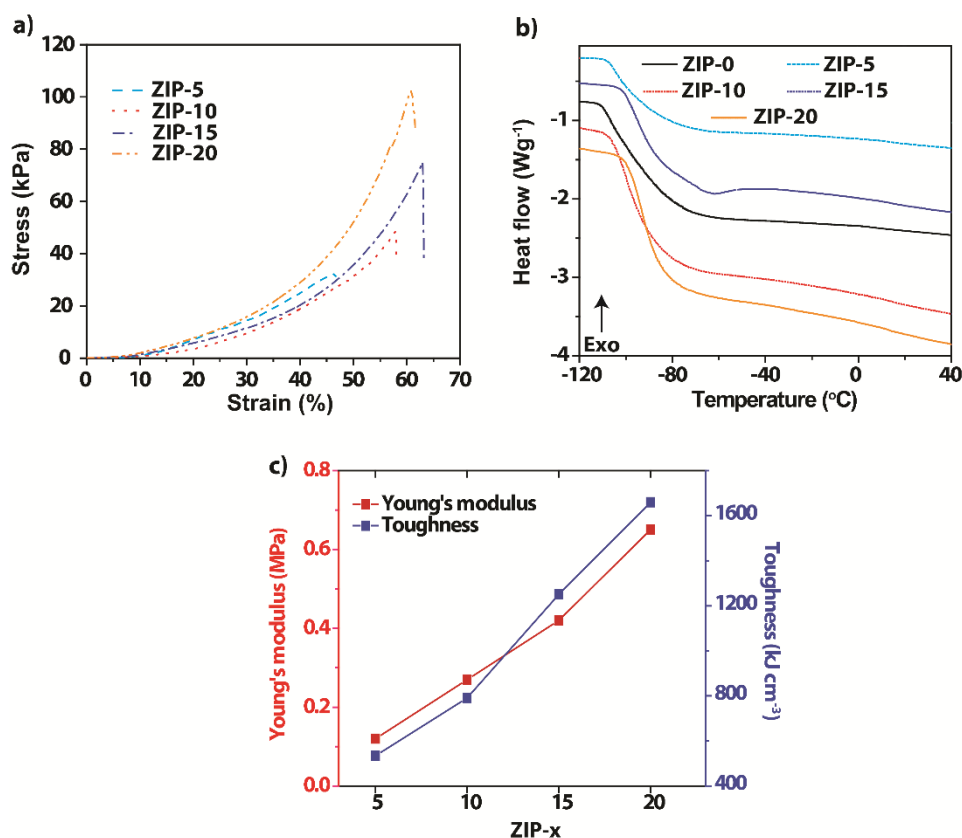


Figure 5.7 (a) Stress vs. strain plots associated with the ZIP-*x* samples showing the mechanical properties under compression mode; (b) DSC profiles of the ZIP-*x* membranes; (c) plots representing Young's modulus and toughness of ZIPs under investigation. Reprinted (adapted) with permission from (Small, 2020, vol. 16, no 35, p. 2002528). Copyright © 2020 John Wiley & Sons, Ltd.

interface integrity cannot be achieved if the ZIP is prepared as a separate film and then assembled in the sandwich configuration as it is the case with the conventional approach, where a cathode, an electrolyte, and an anode are kept one over the other. This conventional approach is popularly known as the 'ex situ process', and in this work, the ZIP film-based electrode is called as the 'e-electrode'. The cathode|electrolyte interface in an e-electrode is also displayed in **Figure 5.2**.

To fabricate ZMPB and ZMPS, vanadyl phosphate (VOPO₄) and commercially available AC (with a surface area of ≈ 2200 m² g⁻¹, which is enriched with nano- and micro-pores) is used as the cathode materials, respectively.^{29, 34} The high-voltage operability of VOPO₄ in ZMBs is recently receiving attention owing to the presence of the phosphate group linked to vanadium-ion center, which is reported to expand the cation intercalation voltage (due to inductive effect) compared to oxides.³⁶⁻³⁸ Here, the synthesis of VOPO₄ is performed using a simple reflux method. The powder X-ray

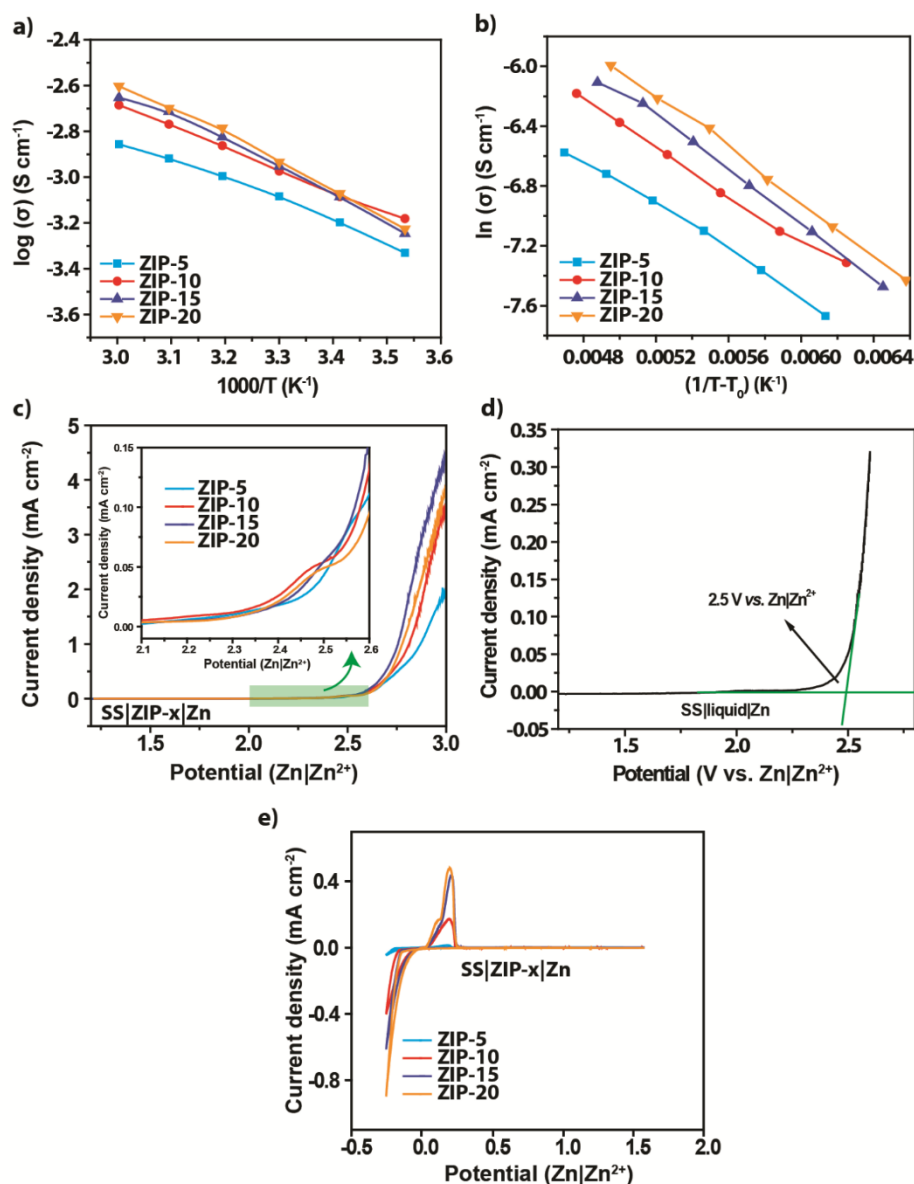


Figure 5.8. (a) Ionic conductivity vs. temperature plots associated with the ZIP-*x* membranes between 10 and 60°C; (b) Vogel–Tammann–Fulcher (VTF) fit of the ionic conductivity vs. temperature data using Equation 5.2 for the calculation of activation energy (E_a^{VTF}); voltammetric determination of (c) oxidation stability of the ZIP-*x* membranes and (d) liquid electrolyte; (e) voltammetric determination of reduction stability of ZIP-*x* membranes. Reprinted (adapted) with permission from (Small, 2020, vol. 16, no 35, p. 2002528). Copyright © 2020 John Wiley & Sons, Ltd.

diffraction (PXRD) profile obtained for the synthesized powder is displayed in (**Figure 5.3a**). The peaks representing the (001), (011), (002), (012), (020), and (021) planes match with the previous reports confirming the formation of the VOPO₄·2H₂O phase.^{36,39} Field emission scanning electron microscope (FESEM) images of the as-synthesized VOPO₄·2H₂O sample are shown in **Figure 5.3b** and **c**. From the FESEM

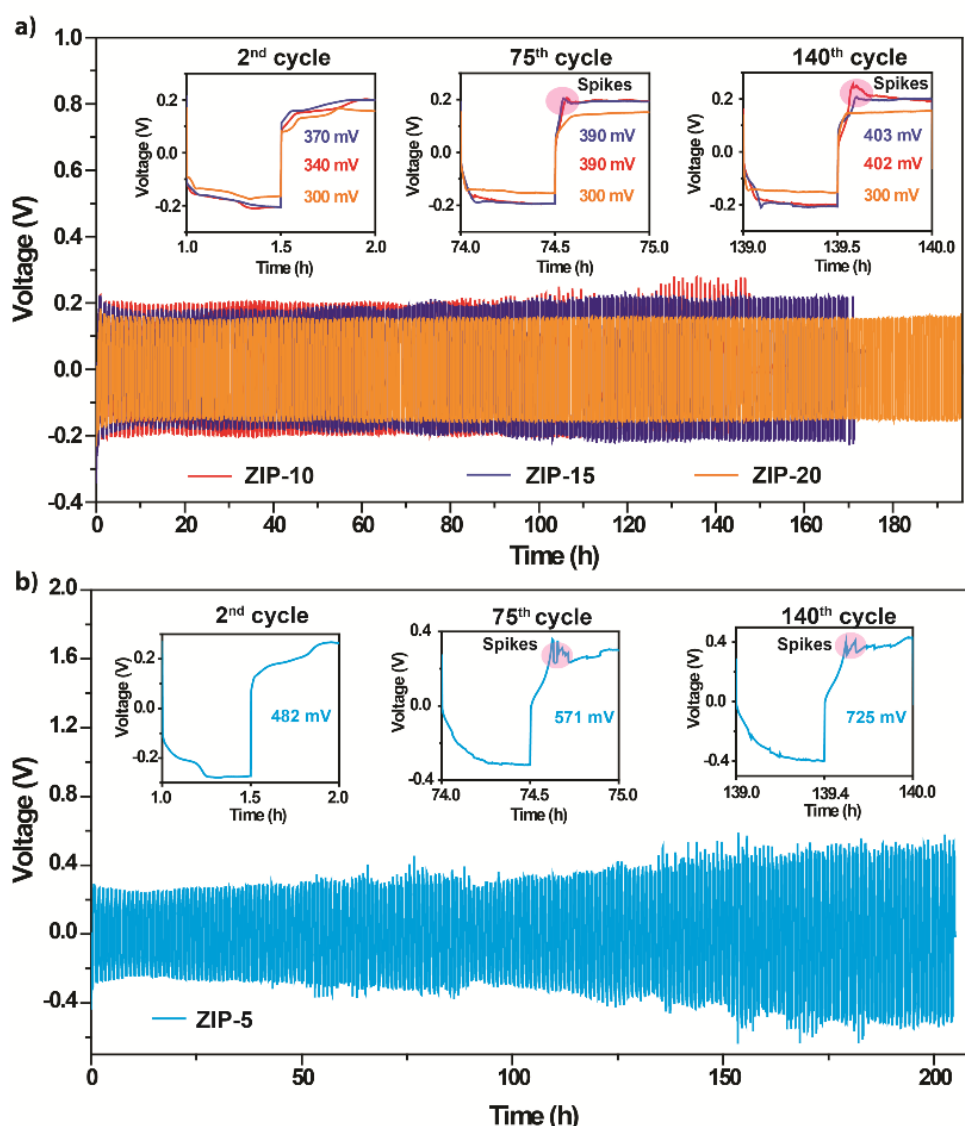


Figure 5.9. (a) Galvanostatic plating/stripping profiles of the ZIP- x ($x = 10, 15,$ and 20) membranes in symmetric Zn//Zn cell, where the voltage vs. time behavior at 2nd, 75th, and 140th cycles are shown in the corresponding insets; (b) Voltage vs. time profile obtained from the long-term galvanostatic plating/stripping process of a Zn/ZIP-5/Zn cell at a current density of 0.1 mA cm^{-2} . Reprinted (adapted) with permission from (Small, 2020, vol. 16, no 35, p. 2002528). Copyright © 2020 John Wiley & Sons, Ltd.

images, it is clear that the synthesized $\text{VOPO}_4 \cdot 2\text{H}_2\text{O}$ possesses nanosheet-like morphology. In addition to the FESEM images, the transmission electron microscopy (TEM) image and the bright spots in the selected area electron diffraction (SAED) pattern (Figure 5.3d and e, respectively) further confirm the layered nature and high-crystallinity of the sample, respectively. Finally, the oxidation states of the various elements in $\text{VOPO}_4 \cdot 2\text{H}_2\text{O}$ is confirmed through X-ray photoelectron spectroscopy (XPS) analysis (Figure 5.4a-c). The peaks at 519.1 (V2p_{3/2}) and 526.5 eV (V2p_{1/2})

correspond to the V^{5+} oxidation state, and if one closely observes, a small quantity of V^{4+} can also be observed (peak at 517.2 eV).^{36, 40} Similarly, the peak at 134.2 eV is associated with the P2p energy level indicating a pentavalent tetra-bonded P.⁴⁰ The peak originating from the oxygen O2p energy level at 531.9 eV is also visible (for further clarity, the scheme adopted for the synthesis of $VOPO_4$ is also presented in **Figure 5.5**).⁴¹

The completion of the polymerization of the reactive mixture is confirmed through ATR-FTIR analysis (**Figure 5.6a**). The absence of the $-C=C-$ peak in the case of the ZIP-x specimens indicates the complete conversion of the monomers to the polymers. The surface morphology of the ZIP-x membranes is studied by environmental SEM (ESEM) analysis, and it was observed that the low-salt containing membranes such as ZIP-5 (**Figure 5.6b**) and ZIP-10 (**Figure 5.6c**) possess a wrinkled surface. A gradual increase in the salt content, as in the case of ZIP-15 and 20 (**Figure 5.6d** and **5.6e**, respectively), rather transformed their surface micro-structure from wrinkled to smooth.

Table 5.2. Summary of ionic conductivity (σ), T_g , and activation energy (E_a^{VTF}) values of the entire series of the ZIP-x samples. Reprinted (adapted) with permission from (Small, 2020, vol. 16, no 35, p. 2002528). Copyright © 2020 John Wiley & Sons, Ltd.

Sample	Compressive strength (kPa)	Ionic Conductivity (σ) (mS cm ⁻¹)		T_g (°C)	E_a^{VTF} (kJ mol ⁻¹)
		30°C	60°C		
ZIP-5	32	0.82	1.3	-103	6.31
ZIP-10	49	1.0	2.0	-100	6.44
ZIP-15	75	1.1	2.2	-95	7.36
ZIP-20	102	1.2	2.5	-92	7.39

From the compressive stress vs. strain plots (**Figure 5.7a**), ZIP-20 is found to exhibit the highest compressive strength with 70% and 30 % increase in compressive stress and strain, respectively, compared to that of ZIP-5. The compressive strength values associated with all ZIPs under investigation are summarized in **Table 5.2**. From the differential scanning calorimetry (DSC) analysis (**Figure 5.7b**), no peaks corresponding to crystallization (T_c) are observed, which indicates that the ZIPs are fully

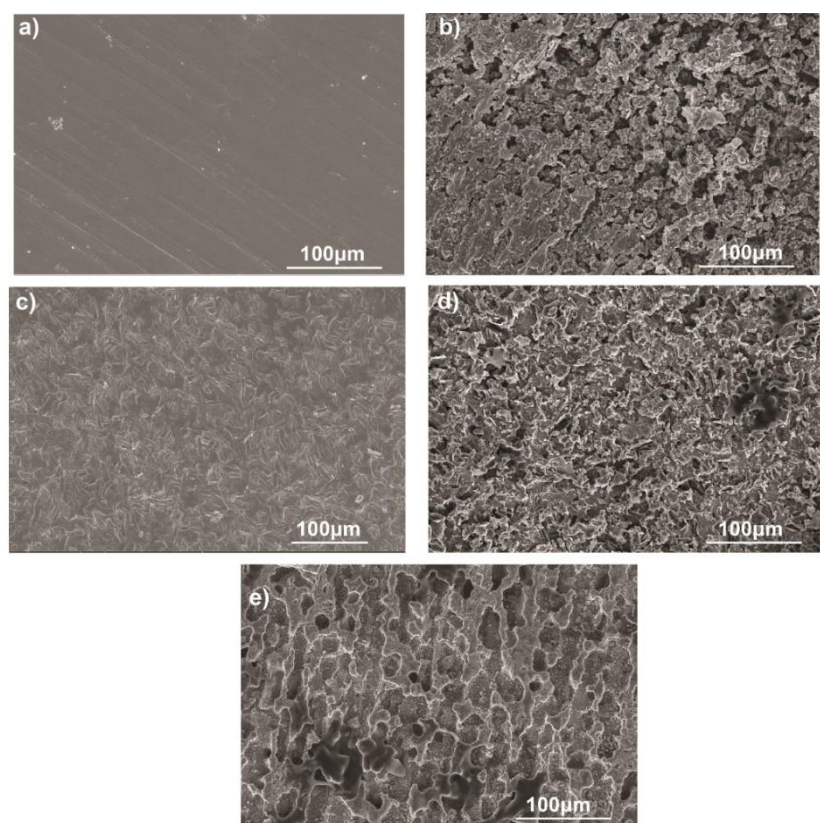


Figure 5.10. FESEM images of (a) the pristine zinc-metal surface; working electrodes retrieved from the (b) Zn|ZIP-5|Zn, (c) Zn|ZIP-20|Zn, d) Zn|ZIP-10|Zn, and e) Zn|ZIP-15|Zn cells after the galvanostatic plating/stripping experiments. Reprinted (adapted) with permission from (Small, 2020, vol. 16, no 35, p. 2002528). Copyright © 2020 John Wiley & Sons, Ltd.

amorphous. Amongst the investigated ZIP samples, the T_g of ZIP-0 is found to be as low as -106°C . Interestingly, with the gradual addition of zinc-salt into the polymer matrix, the T_g values increased up to -92°C for ZIP-20 (**Table 5.2**). This increase (of 14°C) in T_g is observed due to the complexation interactions between the functional groups (carbonyl groups and ethylene oxide moieties) of polymer chains and Zn^{2+} ions.^{42, 43} Such interactions bring the polymer chains closer to each other, hence providing an increased degree of order and rigidity within the electrolyte matrix, unlike a salt-free ZIP-0 sample. These polymer and cation interactions can reinforce the ZIP samples from breaking when they are subjected to external pressure, as reflected from the high compressibility observed for ZIP-20 (**Figure 5.7a**). Additionally, Young's modulus and toughness of the ZIPs are also compiled and presented in **Figure 5.7c**. All these data indicate the improved mechanical stability of ZIPs with an increase in the zinc-salt concentration.

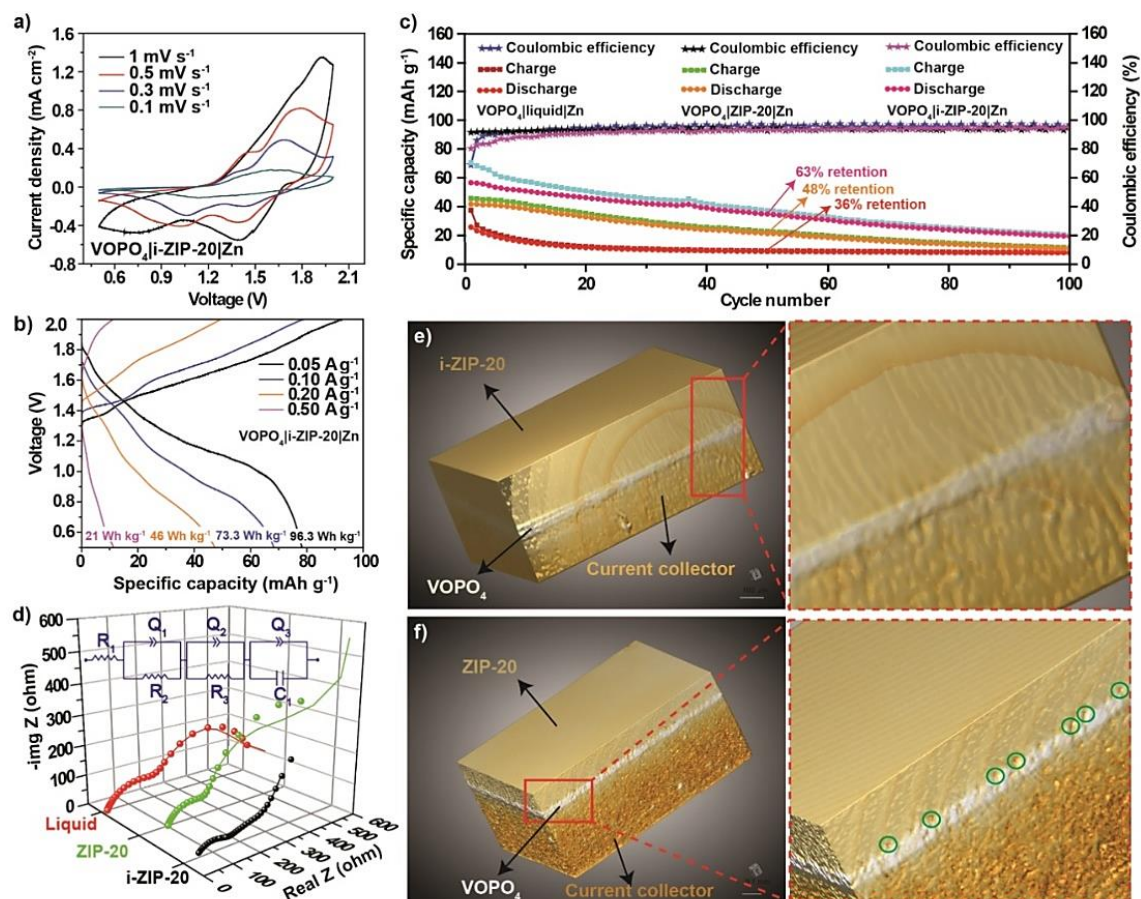


Figure 5.11. Electrochemical characterization of the fabricated ZMPB cell ($\text{VOPO}_4/\text{i-ZIP-20}/\text{Zn}$) by in situ process: (a) the CV profiles recorded at various scan-rates, (b) voltage vs. specific capacity plots obtained from the GCD measurement recorded at various current-densities, (c) long-term cycling stability data recorded at a current density of 0.20 Ag^{-1} for the three types of the VOPO_4 based ZMPB cells where, the liquid electrolyte soaked membrane, ZIP-20, and i-ZIP were used as the electrolytes along with their respective Coulombic efficiencies, and (d) Nyquist plots obtained from the EIS analysis of the $\text{VOPO}_4/\text{liquid}/\text{Zn}$, $\text{VOPO}_4/\text{ZIP-20}/\text{Zn}$ and $\text{VOPO}_4/\text{i-ZIP-20}/\text{Zn}$ cells with the corresponding Randles equivalent circuit model fit. R_1 , R_2 , and R_3 in the equivalent circuit model represent bulk resistance (R_b), interfacial resistance (R_i), and charge transfer resistance (R_{ct}), respectively. Q_1 , Q_2 , and Q_3 represent the constant-phase element components used in the equivalent circuit for the fit; volume rendered 3D Computed Tomography (CT)-images representing the cathode/electrolyte interface in the (e) i-electrode of a $\text{VOPO}_4/\text{i-ZIP-20}/\text{Zn}$ cell and (f) the e-electrode of a $\text{VOPO}_4/\text{ZIP-20}/\text{Zn}$ cell. Reprinted (adapted) with permission from (Small, 2020, vol. 16, no 35, p. 2002528). Copyright © 2020 John Wiley & Sons, Ltd.

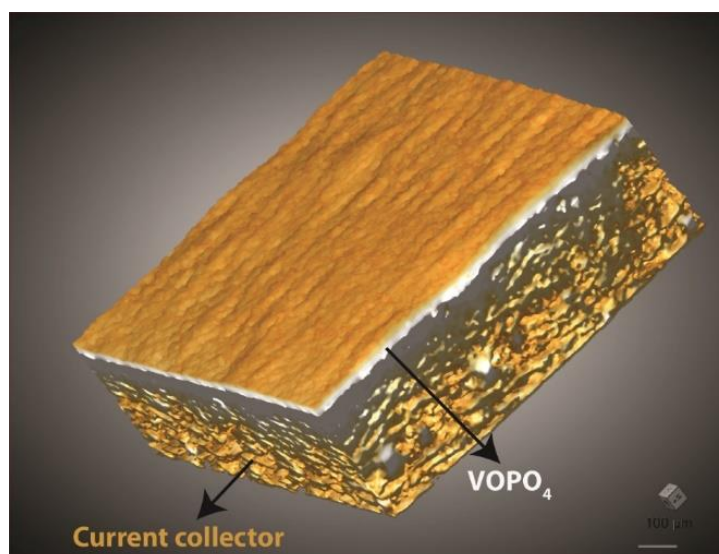


Figure 5.12. Volume rendered 3D CT-image representing the components of the pristine VOPO_4 electrode. Reprinted (adapted) with permission from (Small, 2020, vol. 16, no 35, p. 2002528). Copyright © 2020 John Wiley & Sons, Ltd.

Ionic conductivity (σ) measurements of the ZIP samples are performed at temperatures ranging from 10 to 60°C. The σ vs. temperature plot is presented in **Figure 5.8a**. A ZIP with low T_g value is always preferred since the amorphous regions in a polymer electrolyte facilitate ion conduction by an improved segmental motion of the polymer chains.^{35, 44} This criterion is satisfied in the case of ZIPs as they exhibit a very low T_g value of < -90°C (**Table 5.2**). Despite exhibiting the lowest T_g value, the ionic conductivity possessed by ZIP-5 at 30°C is as low as 0.8 mS cm⁻¹ due to the very low salt content present in it. Hence, a synergistic combination of low T_g value and moderate salt concentrations are preferable for achieving high ionic conductivity in ZIPs. It is worth mentioning that ZIP-10, 15, and 20 exhibits almost similar σ values (~1 mS cm⁻¹) at 30°C (**Table 5.2**). The concomitant increment in T_g value as a function of an increase in the salt concentration is responsible for such a minimal improvement in the σ of ZIP membranes irrespective of the high-salt content as we move from ZIP-10 to ZIP-20.

Followed by the temperature-dependent ionic conductivity measurements, the obtained data is subjected to Vogel-Tamman-Fulcher (VTF) fit (**Figure 5.8b**) to determine the activation energy (E_a^{VTF}) for ion conduction.^{35, 44} ZIP-5 exhibits the lowest E_a^{VTF} value of 6.31 kJ mol⁻¹, whereas a slight increment in E_a^{VTF} values is observed for the other ZIPs as a function of the increase in salt content (**Table 5.2**). The segmental motion of the polymer chains facilitates the ion species transport from one site to another, which helps in reducing the activation energy for ion conduction

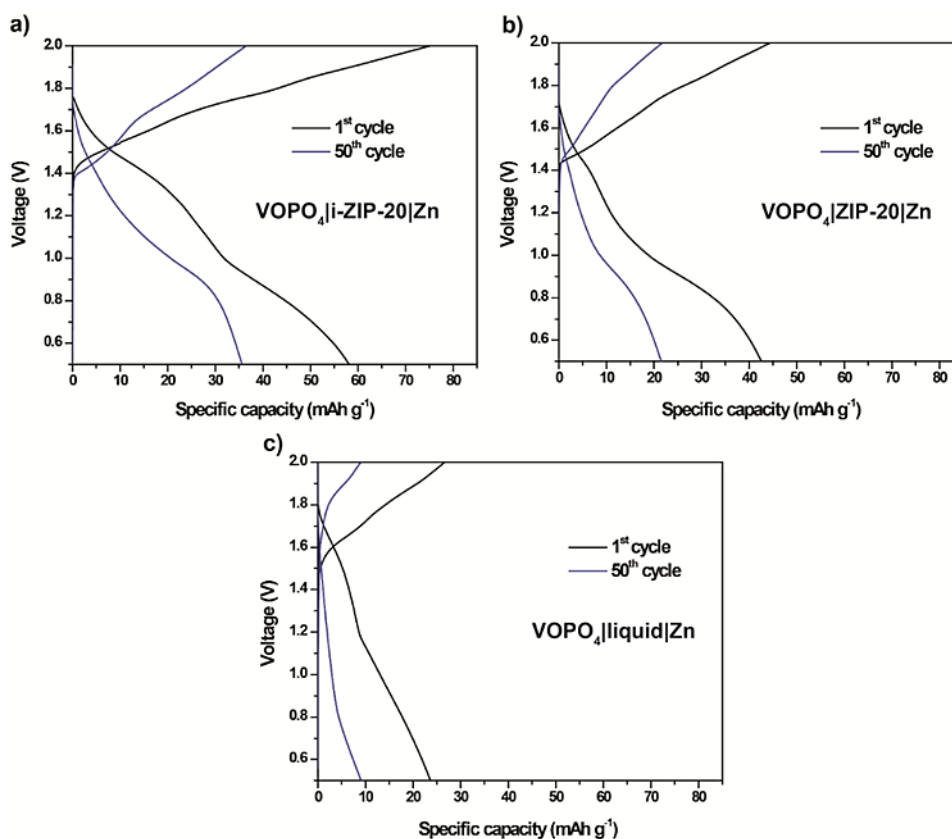


Figure 5.13. GCD plots representing the 1st and 50th cycle capacity of the (a) VOPO₄|i-ZIP-20|Zn, (b) VOPO₄|ZIP-20|Zn, and (c) VOPO₄|liquid|Zn cells. Reprinted (adapted) with permission from (Small, 2020, vol. 16, no 35, p. 2002528). Copyright © 2020 John Wiley & Sons, Ltd.

compared to the simple hopping mechanism. The slight increment in the E_a^{VTF} values for an increase in the salt content is associated with the reduced degree of polymer chain dynamics in the respective ZIPs.

The oxidation stability of the ZIPs is analyzed by linear sweep voltammetry (LSV), where, stainless steel (SS) was used as the working electrode in the SS|ZIP-x|Zn cell configuration. All the ZIP-x membranes exhibited an anodic stability value of ≈ 2.5 V vs. Zn|Zn²⁺ (**Figure 5.8c**). The obtained oxidation stability values are matching with that of the nonaqueous liquid electrolyte (0.08 m Zn(OTf)₂ in PC, **Figure 5.8d**). Similarly, the reduction stability (SS was used as the working electrode in the SS|ZIP-x|Zn cell configuration) of the ZIP-x membranes is also determined, and well-defined peaks corresponding to the plating and stripping of zinc-ions is observed (**Figure 5.8e**). Moreover, it can be seen that the plating/stripping current density is directly proportional to the amount of the zinc-salt present in ZIP-x. This higher current density proves that a high salt concentration in ZIP facilitates a higher amount of zinc-ion deposition or extraction during the plating/stripping process. This observation underlines the

formation of a better interface between zinc-metal and ZIP-20 as a result of a high amount of the salt present in it.

The interfacial stability and compatibility of ZIPs against the zinc-metal electrodes are further validated by the constant current (galvanostatic) plating/stripping experiment in a Zn|ZIP-x|Zn cell (**Figure 5.9a**). Compared to the cells with low salt content (ZIP-5 to 15, the plating/stripping profile associated with the Zn|ZIP-5|Zn cell is separately presented in **Figure 5.9b**), the E_{ov} value associated with the ZIP-20 based cell in the 2nd cycle is found to be only 300 mV, which remained steady for more than 195 cycles. The gradual increase in the E_{ov} values with an increase in the number of the plating/stripping cycles implies that the low-salt ZIPs are not able to maintain a stable solid electrolyte interphase (SEI) layer with the zinc-metal surface. Additionally, for the ZIP-5, 10, and 15 samples, a gradual appearance of voltage-spikes is observed during the plating process, which is absent in the case of ZIP-20 throughout the cycling. Such voltage-spikes can be attributed to the uneven zinc-deposition leading to the formation of pores on the surface of the metal electrodes. Hence, it can be concluded that ZIP-20 displays superior interfacial stability against the zinc-metal surface for many numbers of the plating/stripping cycles, which can be accredited to the presence of a higher and an optimum amount of the salt-content in it.

Additionally, the FESEM images of the surface of the zinc-metal working electrodes after the plating/stripping analysis are also collected. Smooth and uniform surface morphology of the pristine zinc-metal can be observed in **Figure 5.10a**. In the case of the Zn|ZIP-5|Zn cell (**Figure 5.10b**), the surface morphology of the working-electrode is rather irregular and porous, whereas, in the case of the Zn|ZIP-20|Zn (**Figure 5.10c**), a uniform zinc-metal deposition devoid of pores can be witnessed. In the case of Zn|ZIP-10|Zn (**Figure 5.10d**) and Zn|ZIP-15|Zn (**Figure 5.10e**) cells, the nature of the zinc-metal deposition is inferior compared to that of the ZIP-20 membrane-based cell, where, a porous morphology is detected. As already mentioned, the voltage spikes are directly associated with the evolution of porous morphology on the zinc-metal surface when low-salt membranes are used as separators. Hence, it is concluded that among the ZIP-x membranes investigated, the ZIP-20 exhibits suitable features so that it can be used for the fabrication of ZMPBs and ZMPSs.

A ZMPB fabricated by the *in situ* process (as shown in **Figure 5.2**) is denoted as VOPO₄|i-ZIP-x|Zn, where ‘i-ZIP-x’ represents the *in situ* generated ZIP with ‘x’ wt. % of the zinc-salt. The CV profiles of the VOPO₄|i-ZIP-20|Zn cell recorded at various

scan-rates are presented in **Figure 5.11a**, which indicates that the VOPO₄ cathode can be operated within a voltage window of 0.5-2.0 V vs Zn|Zn²⁺. The galvanostatic charge-

Table 5.3. Performance comparison of the nonaqueous electrolyte-based zinc-metal batteries in the existing literature reports. Reprinted (adapted) with permission from (Small, 2020, vol. 16, no 35, p. 2002528). Copyright © 2020 John Wiley & Sons, Ltd.

Electrode	Electrolyte	Average voltage (E _{av})	Specific capacity	Cycling stability	Reference
Potassium nickel hexacyanoferrate	0.5 M Zn(ClO ₄) ₂ /Acetonitrile as liquid electrolyte	1.19 V	55.6 mAh g ⁻¹ at 0.2C (0.011 A g ⁻¹)	90% retention after 10 cycles at 0.2C	24
MnO ₂	0.5 M Zn(TFSI) ₂ /Acetonitrile liquid electrolyte	1.25 V	123 mAh g ⁻¹ at 0.04 C (0.012 Ag ⁻¹)	≈ 80% retention after 10 cycles at 0.04C	25
PPy-VOPO ₄	1M Zn(OTf) ₂ /Acetonitrile liquid electrolyte	1.1 V	20 mAhg ⁻¹ at 0.003 Ag ⁻¹	-	36
V ₃ O ₇ ·H ₂ O	0.25 M Zn(OTf) ₂ /Acetonitrile liquid electrolyte	0.9 V at 5 th cycle and 0.75 V at 50 th cycle	50 mAh g ⁻¹ V at 5 th cycle and 150 mAh g ⁻¹ at 50 th cycle (0.005 A g ⁻¹)	17% drop in average voltage after 50 cycles	45
Bilayered hydrated V ₂ O ₅	0.5 M Zn(TFSI) ₂ /Acetonitrile liquid electrolyte	< 0.9V	≈ 170 mAh g ⁻¹ at 0.1C (0.014 A g ⁻¹)	100% retention after 120 cycles	46
VOPO ₄ ·2H ₂ O	<i>In situ</i> generated ZIP with 0.65 m Zn(OTf) ₂ salt Gel polymer electrolyte	1.2 V	78 mAhg ⁻¹ at 0.05 A g ⁻¹	63% retention after 50 cycles at 0.20 Ag ⁻¹	This Work

discharge (GCD) profiles of the VOPO₄|i-ZIP-20|Zn cell are summarized in **Figure 5.11b**. The cell displayed a high specific capacity of 78 mAh g⁻¹ (at 0.05 Ag⁻¹), which is comparable with several other nonaqueous liquid electrolyte-based ZMBs (summarized in **Table 5.3**).^{15, 24, 25, 36, 45, 46} At the same current density, the cell delivers an E_{av} of 1.2 V with a specific energy density of 96 Wh kg⁻¹ (the specific energy density values at different current densities are also presented in **Figure 5.11b**). Considering the high VOPO₄ mass-loading of 3 mg cm⁻², the obtained specific capacity, E_{av}, and energy density values are promising, especially when a non-lithium-based battery system is considered here.

Additionally, the cycling stability of the VOPO₄|i-ZIP-20|Zn (**Figure 5.11c**) is compared with a cell using the liquid electrolyte (glass-fiber separator soaked in 0.08 m Zn(OTf)₂/PC) and a ZIP film-based cell made by the *ex situ* process as in **Figure 5.2**. These cells are addressed as VOPO₄|liquid|Zn, and VOPO₄|ZIP-20|Zn, respectively. The

VOPO₄|i-ZIP-20|Zn cell is operated for more than 100 cycles; in particular, the cell demonstrated a specific capacity retention of 63% over 50 GCD cycles at 0.20 Ag⁻¹. However, in the liquid electrolyte and the *ex situ* cases, the cycling stability, as well as the specific capacity values, are found to be far inferior to the VOPO₄|i-ZIP-20|Zn cell. The low cycling stability of VOPO₄ in the liquid electrolyte is similar to the previous report from Verma *et al.*, which also emphasizes the importance of the electrolyte tuning for achieving improved cycling stability by imparting structural integrity to the cathode materials.³⁶ Here, the better electrochemical performance associated with the VOPO₄|i-ZIP-20|Zn and VOPO₄|ZIP-20|Zn cells confirms the strength displayed by the polymer electrolytes in improving the electrochemical performance of the nonaqueous ZMBs.

The improved electrochemical performance of the VOPO₄|i-ZIP-20|Zn cell is further rationalized by electrochemical impedance spectroscopy (EIS) analysis (the Nyquist plots of the cells at an OCV of 0.5 V after the completion of the two discharge cycles are reported between 1 MHz to 100 mHz). The impedance spectra are fitted with Randles equivalent circuit model, and the corresponding circuits, curves, and values are summarized in **Figure 5.11d** and **Table 5.4**. Here, R_b (bulk resistance) denotes the equivalent series resistance (ESR) of the electrochemical cell, whereas R_i and R_{ct} represent the interfacial/interphasial and charge-transfer resistance values, respectively. The R_b value is mainly contributed by the electrolyte and Ohmic resistance of the cell components.⁴⁷ The low R_b value associated with the VOPO₄|liquid|Zn cell compared to

Table 5.4. Summary of the Nyquist plots fitted with Randles equivalent circuit model for the various zinc-metal cells under investigation. Reprinted (adapted) with permission from (Small, 2020, vol. 16, no 35, p. 2002528). Copyright © 2020 John Wiley & Sons, Ltd.

Cell	R _b (Ω)	R _i (Ω)	R _{ct} (Ω)
VOPO ₄ liquid Zn	21	214	290
VOPO ₄ ZIP-20 Zn	103	156	687
VOPO ₄ i-ZIP-20 Zn	41	105	215

the other cells is arising from the low-viscosity of the liquid electrolyte, which efficiently wet both the anode and cathode surfaces. If one compares the VOPO₄|i-ZIP-

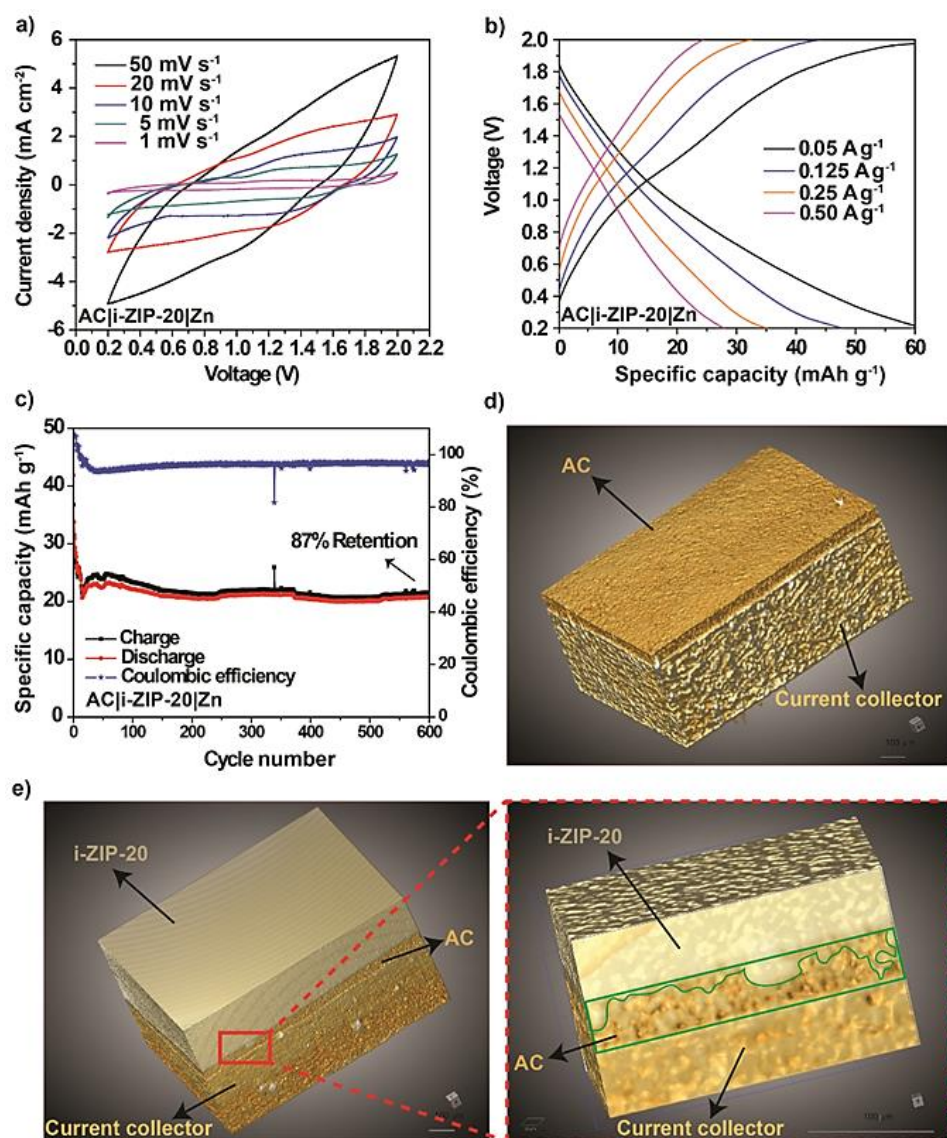


Figure 5.14. Electrochemical characterization of the *in situ* processed ZMPS (AC|i-ZIP-20|Zn) cell: (a) CV profiles recorded at various scan-rates, (b) voltage vs. specific capacity plots obtained from the GCD measurements recorded at various current-densities, and (c) specific capacity vs. cycle number plots showing the long-term stability measured at a current density of 0.50 Ag^{-1} along with their Coulombic efficiencies; volume rendered 3D Computed Tomography (CT)-images of (d) the pristine AC electrode and (e) the cathode-electrolyte interface in the *i*-electrode of AC|i-ZIP-20|Zn cell. Reprinted (adapted) with permission from (Small, 2020, vol. 16, no 35, p. 2002528). Copyright © 2020 John Wiley & Sons, Ltd.

20|Zn and VOPO_4 |ZIP-20|Zn cells, the R_b value is low for the former owing to a better cathode|electrolyte interface achieved in the *in situ* process (Figure 5.2).

The R_i value is mainly associated with the interfacial/interphasial stability of the anode which is formed when the electrolyte comes in contact with the anode. Indeed,

many reports suggest the relationship of R_i with the solid SEI layer at the anode.⁴⁷⁻⁴⁹ As already proved from the plating/stripping experiments, the stability of the SEI layer over the zinc-metal anode depends on the concentration of the zinc-salt used in the electrolyte. Therefore, a low R_i value associated with a ZIP-based zinc-metal cell is attributed to a high concentration of the zinc-salt (≈ 0.65 m) compared to the liquid electrolyte (≈ 0.08 m). The R_{ct} value is generally correlated with the charge-transfer reactions taking place at the electrode|electrolyte interfaces. To retain a low R_{ct} value, the electrolyte infiltration should be extended to the bulk and sub-micro regimes of the electrode material. As mentioned above, the *in situ* process ensures an efficient cathode|electrolyte interface, which is comparable to that of a conventional liquid electrolyte. This improved and extended contact between the electrode and electrolyte helps in achieving low R_{ct} values for VOPO₄|i-ZIP-20|Zn and VOPO₄|liquid|Zn cells, whereas the VOPO₄|ZIP-20|Zn configuration displays about three-times higher R_{ct} value (**Table 5.4**). Ultimately, the better electrochemical performance, as observed in the case of the *in situ* fabricated ZMPB, is supported by a better cathode|electrolyte interface in combination with a high ion-conducting ZIP that possesses an optimum zinc-salt concentration, all the while imparting structural stability to the active electrode materials.

The cathode-electrolyte interface in VOPO₄|i-ZIP-20|Zn and VOPO₄|ZIP-20|Zn cells is further visualized by using computed tomography (CT)-imaging (**Figure 5.11e** and **f**) technique. The three layers *viz.*, current collector, VOPO₄, and i-ZIP-20 are visible in the i-electrode represented in **Figure 5.11e**. Additionally, the magnified region indicates an intimate cathode-electrolyte interface developed between VOPO₄ and the i-ZIP-20 as a beneficial result of the *in situ* process. On the other hand, an inferior cathode|electrolyte interface, as observed in the case of ZIP-20 film-based cell (the *ex situ* process), which is evidenced by the CT-image represented in **Figure 5.11f**. In the magnified region, several pits are observed at the interface between the ZIP-film and the electrode materials (marked in green circles), unlike the smooth cathode|electrolyte interface achieved in the former (VOPO₄|i-ZIP-20|Zn). For further clarity, the volume-rendered 3D CT-image of a pristine electrode is shown where the current collector, as well as the coating of VOPO₄ active materials, are distinguishable from one another (**Figure 5.12**). The GCD plots representing the change in specific capacity of VOPO₄|i-ZIP-20|Zn, VOPO₄|ZIP-20|Zn, and VOPO₄|liquid|Zn cells at 1st and 50th cycles are also presented in **Figure 5.13a-c**.

AC-based electrodes with a mass-loading of 2 mg cm^{-2} are used for *in situ* fabrication of ZMPS. The cyclic voltammetry and GCD profiles of the *in situ* fabricated AC|i-ZIP-20|Zn polymeric hybrid supercapacitors are summarized in **Figure 5.14a** and **b**, respectively. ZMPS displays a specific capacity of 60 mAh g^{-1} at 0.05 Ag^{-1} and retains $\approx 87\%$ of the initial capacity over 600 cycles at a high current density of 0.5 Ag^{-1} (**Figure 5.14c**). The high cycling stability of ZMPS compared to ZMPB is due to the difference in the type of electrochemistry occurring at the active cathode materials. In the former case, the simple adsorption-desorption process facilitates high-cyclic stability similar to a conventional supercapacitor, whereas the redox reactions in the latter result in faster degradation of the electrode materials, leading to reduced cycling stability as in the case of the pseudocapacitors/batteries.⁵⁰ Also, the effectiveness of the cathode|electrolyte interface in the *in situ* processed ZMPS is proved by employing CT-imaging. **Figure 5.14d** represents the volume-rendered 3D CT-image of the pristine AC electrode where the AC-layer and the current collectors are visible. When an AC-based i-electrode is considered (**Figure 5.14e**), an intimate electrode|electrolyte interface similar to the VOPO_4 -based i-electrode can be achieved. At higher magnification, the extension of i-ZIP-20 into the bulk-regimes of the AC can be discerned (marked in green). These results further indicate the robustness of the *in situ* process in improving the interfacial contact between the electrode and electrolyte, and active material utilization, which results in facilitating a better overall electrochemical performance.

5.4 Conclusion

In conclusion, this work represents the easy and scalable preparation of crosslinked polymer electrolytes that can be used for the fabrication of nonaqueous zinc-metal cells (batteries and hybrid supercapacitors). The synthesis of ZIPs is achieved in a single step using UV-light-induced photo-polymerization. This is the first report, which uses free-radical polymerization for the preparation of the zinc-ion conducting polymer electrolytes. The optimized ZIP possesses a high room temperature ionic conductivity in the order of $\approx 10^{-3} \text{ S cm}^{-1}$ with excellent plating/stripping profiles for hundreds of cycles. The salt content in ZIPs is found to have an impact on the dendrite induced cell failure. Hence, the sample with 20 wt.% of the salt content displayed a comparatively stable and dendrite-free plating/stripping profile. Finally, the practicality of the ZIPs for the fabrication of ZMPB and ZMPS is demonstrated by utilizing the *in situ* process. This stands out as another novel aspect of the current work, where ZIPs are generated directly on the electrode surface in line with the device fabrication. Using

techniques such as EIS and CT analyses, it is proved that the *in situ* process improves the cathode|electrolyte interface in the zinc-metal cells. Ultimately, this study provides the scope for further improving the prospects of the zinc-based nonaqueous electrochemistry with the judicial tuning of the polymer electrolyte and tailor-made electrode materials.

5.5 References

- [1] Placke, T.; Kloepsch, R.; Dühnen, S.; Winter, M., Lithium ion, lithium metal, and alternative rechargeable battery technologies: the odyssey for high energy density. *Journal of Solid State Electrochemistry* **2017**, *21* (7), 1939-1964.
- [2] Winter, M.; Barnett, B.; Xu, K., Before Li Ion Batteries. *Chemical Reviews* **2018**, *118* (23), 11433-11456.
- [3] Fang, G.; Zhou, J.; Pan, A.; Liang, S., Recent Advances in Aqueous Zinc-Ion Batteries. *ACS Energy Letters* **2018**, *3* (10), 2480-2501.
- [4] Xu, W.; Wang, Y., Recent Progress on Zinc-Ion Rechargeable Batteries. *Nano-Micro Letters* **2019**, *11* (1), 90.
- [5] Tang, B.; Shan, L.; Liang, S.; Zhou, J., Issues and opportunities facing aqueous zinc-ion batteries. *Energy & Environmental Science* **2019**, *12* (11), 3288-3304.
- [6] Ghosh, M.; Vijayakumar, V.; Kurungot, S., Dendrite Growth Suppression by Zn²⁺-Integrated Nafion Ionomer Membranes: Beyond Porous Separators toward Aqueous Zn/V₂O₅ Batteries with Extended Cycle Life. *Energy Technology* **2019**, *7* (9), 1900442.
- [7] Khayum M, A.; Ghosh, M.; Vijayakumar, V.; Halder, A.; Nurhuda, M.; Kumar, S.; Addicoat, M.; Kurungot, S.; Banerjee, R., Zinc ion interactions in a two-dimensional covalent organic framework based aqueous zinc ion battery. *Chemical Science* **2019**, *10* (38), 8889-8894.
- [8] Dong, L.; Ma, X.; Li, Y.; Zhao, L.; Liu, W.; Cheng, J.; Xu, C.; Li, B.; Yang, Q.-H.; Kang, F., Extremely safe, high-rate and ultralong-life zinc-ion hybrid supercapacitors. *Energy Storage Materials* **2018**, *13*, 96-102.
- [9] Sun, G.; Yang, H.; Zhang, G.; Gao, J.; Jin, X.; Zhao, Y.; Jiang, L.; Qu, L., A capacity recoverable zinc-ion micro-supercapacitor. *Energy & Environmental Science* **2018**, *11* (12), 3367-3374.
- [10] Park, M. J.; Yaghoobnejad Asl, H.; Therese, S.; Manthiram, A., Structural impact of Zn-insertion into monoclinic V₂(PO₄)₃: implications for Zn-ion batteries. *Journal of Materials Chemistry A* **2019**, *7* (12), 7159-7167.

- [11] Wu, S.; Chen, Y.; Jiao, T.; Zhou, J.; Cheng, J.; Liu, B.; Yang, S.; Zhang, K.; Zhang, W., An Aqueous Zn-Ion Hybrid Supercapacitor with High Energy Density and Ultrastability up to 80 000 Cycles. *Advanced Energy Materials* **2019**, *9* (47), 1902915.
- [12] Huang, S.; Zhu, J.; Tian, J.; Niu, Z., Recent Progress in the Electrolytes of Aqueous Zinc-Ion Batteries. *Chemistry – A European Journal* **2019**, *25* (64), 14480-14494.
- [13] Hou, Z.; Zhang, X.; Li, X.; Zhu, Y.; Liang, J.; Qian, Y., Surfactant widens the electrochemical window of an aqueous electrolyte for better rechargeable aqueous sodium/zinc battery. *Journal of Materials Chemistry A* **2017**, *5* (2), 730-738.
- [14] Li, C.; Zhang, X.; He, W.; Xu, G.; Sun, R., Cathode materials for rechargeable zinc-ion batteries: From synthesis to mechanism and applications. *Journal of Power Sources* **2020**, *449*, 227596.
- [15] Wan, F.; Zhang, Y.; Zhang, L.; Liu, D.; Wang, C.; Song, L.; Niu, Z.; Chen, J., Reversible Oxygen Redox Chemistry in Aqueous Zinc-Ion Batteries. *Angewandte Chemie International Edition* **2019**, *58* (21), 7062-7067.
- [16] Zhang, L.; Rodríguez-Pérez, I. A.; Jiang, H.; Zhang, C.; Leonard, D. P.; Guo, Q.; Wang, W.; Han, S.; Wang, L.; Ji, X., ZnCl₂ “Water-in-Salt” Electrolyte Transforms the Performance of Vanadium Oxide as a Zn Battery Cathode. *Advanced Functional Materials* **2019**, *29* (30), 1902653.
- [17] Zhang, C.; Holoubek, J.; Wu, X.; Daniyar, A.; Zhu, L.; Chen, C.; Leonard, D. P.; Rodríguez-Pérez, I. A.; Jiang, J.-X.; Fang, C.; Ji, X., A ZnCl₂ water-in-salt electrolyte for a reversible Zn metal anode. *Chemical Communications* **2018**, *54* (100), 14097-14099.
- [18] Zhang, L.; Chen, L.; Zhou, X.; Liu, Z., Towards High-Voltage Aqueous Metal-Ion Batteries Beyond 1.5 V: The Zinc/Zinc Hexacyanoferrate System. *Advanced Energy Materials* **2015**, *5* (2), 1400930.
- [19] Liu, Z.; Huang, Y.; Huang, Y.; Yang, Q.; Li, X.; Huang, Z.; Zhi, C., Voltage issue of aqueous rechargeable metal-ion batteries. *Chemical Society Reviews* **2020**, *49* (1), 180-232.
- [20] Kasnatscheew, J.; Streipert, B.; Röser, S.; Wagner, R.; Laskovic, I. C.; Winter, M., Determining oxidative stability of battery electrolytes: validity of common electrochemical stability window (ESW) data and alternative strategies. *Physical Chemistry Chemical Physics* **2017**, *19* (24), 16078-16086.

- [21] Cekic-Laskovic, I.; von Aspern, N.; Imholt, L.; Kaymaksiz, S.; Oldiges, K.; Rad, B. R.; Winter, M., Synergistic effect of blended components in nonaqueous electrolytes for lithium ion batteries. In *Electrochemical Energy Storage*, Springer: 2019; pp 1-64.
- [22] Han, S.-D.; Rajput, N. N.; Qu, X.; Pan, B.; He, M.; Ferrandon, M. S.; Liao, C.; Persson, K. A.; Burrell, A. K., Origin of Electrochemical, Structural, and Transport Properties in Nonaqueous Zinc Electrolytes. *ACS Applied Materials & Interfaces* **2016**, *8* (5), 3021-3031.
- [23] Pan, C.; Zhang, R.; Nuzzo, R. G.; Gewirth, A. A., ZnNixMnxCo2–2xO4 Spinel as a High-Voltage and High-Capacity Cathode Material for Nonaqueous Zn-Ion Batteries. *Advanced Energy Materials* **2018**, *8* (22), 1800589.
- [24] Chae, M. S.; Heo, J. W.; Kwak, H. H.; Lee, H.; Hong, S.-T., Organic electrolyte-based rechargeable zinc-ion batteries using potassium nickel hexacyanoferrate as a cathode material. *Journal of Power Sources* **2017**, *337*, 204-211.
- [25] Han, S.-D.; Kim, S.; Li, D.; Petkov, V.; Yoo, H. D.; Phillips, P. J.; Wang, H.; Kim, J. J.; More, K. L.; Key, B.; Klie, R. F.; Cabana, J.; Stamenkovic, V. R.; Fister, T. T.; Markovic, N. M.; Burrell, A. K.; Tepavcevic, S.; Vaughey, J. T., Mechanism of Zn Insertion into Nanostructured δ -MnO₂: A Nonaqueous Rechargeable Zn Metal Battery. *Chemistry of Materials* **2017**, *29* (11), 4874-4884.
- [26] Long, L.; Wang, S.; Xiao, M.; Meng, Y., Polymer electrolytes for lithium polymer batteries. *Journal of Materials Chemistry A* **2016**, *4* (26), 10038-10069.
- [27] Nair, J. R.; Imholt, L.; Brunklaus, G.; Winter, M., Lithium Metal Polymer Electrolyte Batteries: Opportunities and Challenges. *The Electrochemical Society Interface* **2019**, *28* (2), 55-61.
- [28] Wang, Y.; Song, S.; Xu, C.; Hu, N.; Molenda, J.; Lu, L., Development of solid-state electrolytes for sodium-ion battery—A short review. *Nano Materials Science* **2019**, *1* (2), 91-100.
- [29] Vijayakumar, V.; Anothumakkool, B.; Torris A. T, A.; Nair, S. B.; Badiger, M. V.; Kurungot, S., An all-solid-state-supercapacitor possessing a non-aqueous gel polymer electrolyte prepared using a UV-assisted in situ polymerization strategy. *Journal of Materials Chemistry A* **2017**, *5* (18), 8461-8476.
- [30] Porcarelli, L.; Shaplov, A. S.; Bella, F.; Nair, J. R.; Mecerreyes, D.; Gerbaldi, C., Single-Ion Conducting Polymer Electrolytes for Lithium Metal Polymer Batteries that Operate at Ambient Temperature. *ACS Energy Letters* **2016**, *1* (4), 678-682.

- [31] Wei, Z.; Chen, S.; Wang, J.; Wang, Z.; Zhang, Z.; Yao, X.; Deng, Y.; Xu, X., A large-size, bipolar-stacked and high-safety solid-state lithium battery with integrated electrolyte and cathode. *Journal of Power Sources* **2018**, *394*, 57-66.
- [32] Ye, H.; Xu, J. J., Zinc ion conducting polymer electrolytes based on oligomeric polyether/PVDF-HFP blends. *Journal of Power Sources* **2007**, *165* (2), 500-508.
- [33] Zhao, Q.; Liu, X.; Stalin, S.; Khan, K.; Archer, L. A., Solid-state polymer electrolytes with in-built fast interfacial transport for secondary lithium batteries. *Nature Energy* **2019**, *4* (5), 365-373.
- [34] Anothumakkool, B.; Torris A. T, A.; Veeliyath, S.; Vijayakumar, V.; Badiger, M. V.; Kurungot, S., High-Performance Flexible Solid-State Supercapacitor with an Extended Nanoregime Interface through in Situ Polymer Electrolyte Generation. *ACS Applied Materials & Interfaces* **2016**, *8* (2), 1233-1241.
- [35] Porcarelli, L.; Gerbaldi, C.; Bella, F.; Nair, J. R., Super Soft All-Ethylene Oxide Polymer Electrolyte for Safe All-Solid Lithium Batteries. *Scientific Reports* **2016**, *6* (1), 19892.
- [36] Verma, V.; Kumar, S.; Manalastas, W.; Zhao, J.; Chua, R.; Meng, S.; Kidkhunthod, P.; Srinivasan, M., Layered VOPO₄ as a Cathode Material for Rechargeable Zinc-Ion Battery: Effect of Polypyrrole Intercalation in the Host and Water Concentration in the Electrolyte. *ACS Applied Energy Materials* **2019**, *2* (12), 8667-8674.
- [37] Sun, Y.; Wu, C.; Xie, Y., Sonochemical synthesis of nanostructured VOPO₄ · 2H₂O/carbon nanotube composites with improved lithium ion battery performance. *Journal of Nanoparticle Research* **2010**, *12* (2), 417-427.
- [38] Shi, H.-Y.; Song, Y.; Qin, Z.; Li, C.; Guo, D.; Liu, X.-X.; Sun, X., Inhibiting VOPO₄·x H₂O Decomposition and Dissolution in Rechargeable Aqueous Zinc Batteries to Promote Voltage and Capacity Stabilities. *Angewandte Chemie International Edition* **2019**, *58* (45), 16057-16061.
- [39] Azmi, B. M.; Ishihara, T.; Nishiguchi, H.; Takita, Y., Vanadyl phosphates of VOPO₄ as a cathode of Li-ion rechargeable batteries. *Journal of Power Sources* **2003**, *119-121*, 273-277.
- [40] Mei, P.; Kaneti, Y. V.; Pramanik, M.; Takei, T.; Dag, Ö.; Sugahara, Y.; Yamauchi, Y., Two-dimensional mesoporous vanadium phosphate nanosheets through liquid crystal templating method toward supercapacitor application. *Nano Energy* **2018**, *52*, 336-344.

- [41] Igarashi, H.; Tsuji, K.; Okuhara, T.; Misono, M., Effects of consecutive oxidation on the production of maleic anhydride in butane oxidation over four kinds of well-characterized vanadyl pyrophosphates. *The Journal of Physical Chemistry* **1993**, *97* (27), 7065-7071.
- [42] Falco, M.; Simari, C.; Ferrara, C.; Nair, J. R.; Meligrana, G.; Bella, F.; Nicotera, I.; Mustarelli, P.; Winter, M.; Gerbaldi, C., Understanding the Effect of UV-Induced Crosslinking on the Physicochemical Properties of Highly Performing PEO/LiTFSI-Based Polymer Electrolytes. *Langmuir* **2019**, *35* (25), 8210-8219.
- [43] Chaurasia, S. K.; Singh, R. K.; Chandra, S., Ion–polymer and ion–ion interaction in PEO-based polymer electrolytes having complexing salt LiClO₄ and/or ionic liquid, [BMIM][PF₆]. *Journal of Raman Spectroscopy* **2011**, *42* (12), 2168-2172.
- [44] Vijayakumar, V.; Diddens, D.; Heuer, A.; Kurungot, S.; Winter, M.; Nair, J. R., Dioxolanone-Anchored Poly(allyl ether)-Based Crosslinked Dual-Salt Polymer Electrolytes for High-Voltage Lithium Metal Batteries. *ACS Applied Materials & Interfaces* **2020**, *12* (1), 567-579.
- [45] Kundu, D.; Hosseini Vajargah, S.; Wan, L.; Adams, B.; Prendergast, D.; Nazar, L. F., Aqueous vs. nonaqueous Zn-ion batteries: consequences of the desolvation penalty at the interface. *Energy & Environmental Science* **2018**, *11* (4), 881-892.
- [46] Senguttuvan, P.; Han, S.-D.; Kim, S.; Lipson, A. L.; Tepavcevic, S.; Fister, T. T.; Bloom, I. D.; Burrell, A. K.; Johnson, C. S., A High Power Rechargeable Nonaqueous Multivalent Zn/V₂O₅ Battery. *Advanced Energy Materials* **2016**, *6* (24), 1600826.
- [47] Liu, F.; Chen, Z.; Fang, G.; Wang, Z.; Cai, Y.; Tang, B.; Zhou, J.; Liang, S., V₂O₅ Nanospheres with Mixed Vanadium Valences as High Electrochemically Active Aqueous Zinc-Ion Battery Cathode. *Nano-Micro Letters* **2019**, *11* (1), 25.
- [48] Li, X.; Qian, K.; He, Y.-B.; Liu, C.; An, D.; Li, Y.; Zhou, D.; Lin, Z.; Li, B.; Yang, Q.-H.; Kang, F., A dual-functional gel-polymer electrolyte for lithium ion batteries with superior rate and safety performances. *Journal of Materials Chemistry A* **2017**, *5* (35), 18888-18895.
- [49] Winter, M., The solid electrolyte interphase—the most important and the least understood solid electrolyte in rechargeable Li batteries. *Zeitschrift für physikalische Chemie* **2009**, *223* (10-11), 1395-1406.
- [50] Winter, M.; Brodd, R. J., What Are Batteries, Fuel Cells, and Supercapacitors? *Chemical Reviews* **2004**, *104* (10), 4245-4270.

Chapter 6

Summary & Future Perspectives

6.1 Summary

The events reflected in this dissertation are presented in the four working chapters aligned with the core theme of designing polymer electrolytes for electrochemical energy storage devices (EEDs). Considering the contemporary importance and interest, two of the most important EEDs, *viz.*, rechargeable batteries, and supercapacitors, are selected for the investigation. In the introductory chapter of this thesis (**Chapter 1**), the fundamental differences between the batteries and supercapacitors are stated with special emphasis on lithium-ion batteries (LIBs), lithium metal batteries (LMBs), zinc metal batteries (ZMBs), electric double layer capacitors (EDLCs) and pseudocapacitors. Considering the safety concerns associated with the conventional liquid electrolytes used in these devices, the inevitability of the imminent transition to solid-state electrolytes (SSEs) is thoroughly discussed. Among the SSEs, the discussion is confined to gel polymer electrolytes (GPEs) owing to their advantages related to the possibility of achieving a variety of ion conduction ranging from monovalent (Li^+ , Na^+ , etc.) and multivalent (Zn^{2+} , Mg^{2+} , etc.) cations or even proton (H^+) and hydroxide ion (OH^-). Compared to the all-solid-state-electrolytes (ASSEs) such as solid polymer electrolytes (SPEs) and inorganic solid electrolytes (ISEs), GPEs possess high ionic conductivity due to the presence of a certain amount of liquid phase present in them. In all the chapters, a simple and scalable method of direct conversion of a mixture of polymerizable monomers and liquid electrolytes to GPEs by ultraviolet (UV)-light induced photopolymerization is employed. The first chapter also discusses the restrictions imposed by SSEs (ISE pellets, SPE, and GPE films) in compromising the electrode|electrolyte interface in EEDs. To emulate the liquid electrolyte-like electrode|electrolyte interface in the GPE-based supercapacitors and batteries, the thesis introduces the novel concept of the *in situ* process for the EED fabrication. In this method, the polymer electrolyte and electrode|electrolyte interface formation takes place in a single step in line with the EED fabrication with the assistance of UV-curing. The significant achievements of this thesis as they appear in different working chapters are listed as follows:

Water-in-acid Gel Polymer Electrolyte Realized through a Phosphoric Acid-Enriched Polyelectrolyte Matrix toward Solid-State Supercapacitors (Chapter 2)

A proton conducting free-standing GPE membrane as an alternative to the conventional GPE solutions based on PVA is proposed in this work. It also introduced the concept of *water-in-acid* GPEs in which conc. H_3PO_4 is entrapped in a polymer host exhibiting polyelectrolyte

character. The GPE was easily processed as a mechanically stable film and later used for polyaniline (PANI)-based supercapacitor fabrication. The UV-polymerized GPE was found to help in improving the cycling stability of the supercapacitor retaining 100% of the initial capacitance over 9000 continuous charge-discharge cycles. In the case of conventional PVA-H₃PO₄ electrolyte (termed as *acid-in-water* due to a large amount of water used for dilution), the cycling stability of the supercapacitor device was far inferior to the *water-in-acid* counterparts. The flexible aspects of the GPE-based supercapacitor device and the enhanced shelf-life were also demonstrated. Ultimately, this work lays the foundation for this thesis inspiring further investigations on the UV-polymerized GPE towards better supercapacitor and battery devices. However, the GPE presented in this work was constrained by its low voltage window of < 1.23 V due to the presence of water/H⁺ ions demanding alternatives to be used with high-voltage supercapacitors.

A High-Voltage Supercapacitor Possessing Nonaqueous Gel Polymer Electrolyte Prepared Using the *In Situ* Polymerization Process (Chapter 3)

To overcome the limitations associated with the low voltage window of the proton conducting GPE introduced in **Chapter 2**, **Chapter 3** conceived a nonaqueous GPE. The nonaqueous GPE could be operated beyond 2 V so that high-voltage EDLCs could be developed. The Li⁺-ion conducting GPE is prepared by UV-curing of an acrylate monomer 2-hydroxy-3-phenoxypropyl acrylate (HPA) in the presence of a liquid electrolyte (propylene carbonate (PC)/LiClO₄). The detailed investigation provided insights into the non-covalent cross-linking interactions contributing to the mechanical stability of the GPE. During the EDLC fabrication, this work successfully mimicked the electrode|electrolyte interface similar to that of a liquid electrolyte with a GPE, which is often difficult with the conventional SSEs. For this purpose, the direct generation of GPE over the porous carbon electrode is adopted by UV-curing. In this process, the electrolyte formation and the electrode|electrolyte interface generation taken place in a single step facilitating the maximum utilization of the electrode material. Therefore, the term *in situ* process is coined to represent this technique. Using the electrochemical and electron microscopy analyses, it was proven that the electrode|electrolyte interface offered by the *in situ* process is more or less similar to that of the liquid electrolyte and superior to the conventional GPE solutions based on PMMA/LiClO₄ and other GPE films. The demonstration of the excellent electrochemical performance with high mass-loaded electrodes as well as the fabrication of flexible supercapacitor devices was also achieved by using the *in situ* process.

Dioxolanone Anchored Poly (Allyl Ether)-Based Cross-Linked Dual-Salt Polymer Electrolytes for High-Voltage Lithium Metal Batteries (Chapter 4)

This chapter extrapolated the strategy of UV-light induced polymerization for the preparation of high-voltage Li^+ -ion conducting cross-linked GPEs (XPEs) for the LMB fabrication. Unlike the acrylate monomers used in **Chapters 2 and 3**, in this work, allyl ether monomers were employed for the XPE preparation. The structure of the polymer host consisted of dioxalanone tethered polyethylene chains crosslinked by poly (allyl ether) units. The novel XPE prepared using the above-mentioned novel polymer host exhibited varying electrochemical properties as a function of the amount and type of the Li-salt present in them. For instance, the high LiTFSI content helped in improving the oxidation stability of the XPE. The LiTFSI-based XPE (S-XPE, where ‘S’ refers to single-salt) exhibited stable cycling over 120 cycles in LFP||Li full-cells (4 V at 60°C). However, to make them suitable to be used with high-voltage NCA cathode, a small amount of another salt (LiFSI) was introduced to the XPE. These XPEs were termed as (D-XPE, where ‘D’ refers to dual-salt). The D-XPE exhibited high oxidation stability of ≈ 4.3 V vs. Li|Li⁺ so that high-voltage LMBs (NCA||Li, 4.3 V) that are operable for over 1000 cycles could be developed. The excellent interfacial stability of the D-XPE with Li-metal could be also proven by using Li-plating/stripping experiments. It is worth mentioning that most of the reported works on polymer electrolyte-based LMBs use low-voltage cathodes (such as LFP) that are free from Ni and Co, whereas, the potential of the XPE to be used along with both low and high-voltage cathodes is demonstrated in this work.

An *In Situ* Cross-linked Nonaqueous Polymer Electrolyte for Zinc-Metal Polymer Batteries and Hybrid Supercapacitors (Chapter 5)

The final working chapter of this thesis explored the scope of realizing a nonaqueous zinc-ion conducting polymer electrolyte (ZIP) using the UV-polymerization method for application in ZMBs. Considering the rarely explored chemistry of the nonaqueous ZMBs even in liquid electrolytes, the mentioned work is a solid leap towards the development of futuristic ZMBs. The room temperature ionic conductivity of the ZIP was in the order of 10^{-3} S/cm. The ZIP displayed high oxidation stability beyond 2.5 V vs. Zn|Zn²⁺ along with high mechanical stability. In this chapter also, the *in situ* process is adopted to fabricate the ZMB full-cells to tune the electrode|electrolyte interface. The superior electrochemical performance of the *in situ* processed cell was proven by comparing it with the ZIP-film and liquid electrolyte-based cells. Also, this work employed the sophisticated technique of computed tomography (CT)-analysis to visualize the electrode|electrolyte, which could be extended to other EEDS in the future.

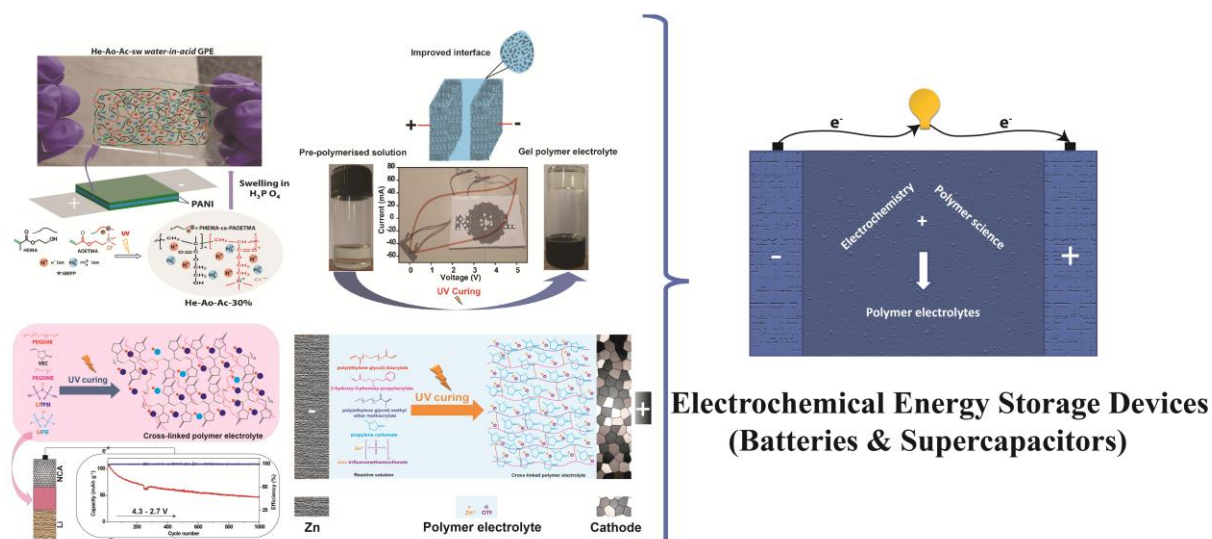
Apart from the ZMB (VOPO₄||Zn), a hybrid supercapacitor device fabrication using the activated carbon as the electrode material is also shown (AC||Zn).

6.2 Future perspectives

The current thesis is an attempt to put forward the potential of the GPEs as a universal electrolyte that can be employed for various types of EEDs. The simple strategy of UV-light induced polymerization as it appears in the four working chapters of this thesis is expected to receive broad attention in the field of electrochemical energy storage and conversion devices. Although only three types of ion conduction involving H⁺, Li⁺, and Zn²⁺ are explored in the context of this thesis, the prospect of using the UV-light induced polymerization can be elaborated for developing GPEs or SPEs exhibiting other types of ion conduction as well. For example, apart from ZMBs, other post-lithium battery technologies (sodium-ion/metal batteries, magnesium-ion/metal batteries (MIBs), etc.,) also require polymer electrolytes exhibiting the desired type of ionic conductivity. The concepts developed during this thesis can be directly applied to the aforementioned devices as well. In the case of supercapacitors, the nonaqueous GPE demonstrated in **Chapter 3** can be employed for the fabrication of high-voltage asymmetric supercapacitors. The UV-polymerizable proton conducting membranes as explained in **Chapter 2** can be employed for proton exchange membrane fuel cells (PEMFCs) as well. Few developments in this direction have already been reported from our lab. For example, recent work from our lab successfully adopted the concept of employing the *in situ* process as a tool to tune the electrode|electrolyte interface in fuel cells. The fabrication of asymmetric supercapacitors using nonaqueous GPEs is also demonstrated. The application of the UV-polymerization strategy for the development of alkaline-ion (OH⁻) conducting polymer electrolytes is also being explored. Such membranes could be handy in developing devices such as air-batteries or anion exchange fuel cells.

Adopting the UV-polymerization method to design organic/inorganic composite polymer electrolytes can also be envisioned as another promising aspect. In this method, the inorganic nanoparticles or even the ISEs can be dispersed in the polymerizable monomers in the presence of a conducting salt (and solvent/plasticizer if any) to result in the all-solid-state or gel-based composite polymer electrolytes followed by UV-curing. These composite polymer electrolytes could be handy to be employed in LMBs and other related EEDs. Another interesting investigation would be exploring the processes occurring at the electrode|electrolyte interface through *in situ* and operando characterization methods. For example, in the case of LMBs/LIBs, the solid electrolyte interphase (SEI)/cathode electrolyte interphase (CEI) formed at the electrode|electrolyte interface can provide insights on the chemical compatibility of the

polymer electrolytes and electrode. These pieces of information related to the nature of the chemical species formed at the electrode|electrolyte interface can be handy in developing better polymer electrolytes that can ensure improved safety, cycling stability, and shelf-life to EDD. In **Chapter 4**, insights related to the CEI in LMB cells have been retrieved through certain quantum chemical studies. Such insights are still absent in the field of ZMBs. Since the polymers are high molecular weight macromolecules, expensive quantum chemical approaches are to be employed for the calculation. However, bridging the gap between experimental and theoretical electrochemistry related to polymer electrolytes should be helpful for further advancements in the field. Overall, the synergy between polymer chemistry and electrochemistry is an interesting interdisciplinary research area that can heavily contribute to achieving energy sustainability.



ACHIEVEMENTS

JOURNAL ARTICLES

1. Dioxolanone-Anchored Poly (allyl ether)-Based Cross-Linked Dual-Salt Polymer Electrolytes for High-Voltage Lithium Metal Batteries, **V Vijayakumar**, D Diddens, A Heuer, S Kurungot, M Winter, JR Nair, ACS Appl. Mater. Interfaces 2020, 12, 1, 567-579.
2. An all-solid-state-supercapacitor possessing a non-aqueous gel polymer electrolyte prepared using a UV-assisted *in situ* polymerization strategy, **V Vijayakumar**, B Anothumakkool, SB Nair, MV Badiger, S Kurungot, J. Mater. Chem. A, 2017, 5, 8461-8476.
3. *Water-in-acid* gel polymer electrolyte realized through a phosphoric acid enriched polyelectrolyte matrix toward solid-state supercapacitors, **V Vijayakumar**, M Ghosh, A Torris AT, SB Nair, MV Badiger, S Kurungot, ACS Sustainable Chem. Eng. 2018, 6, 10, 12630-12640.
4. An *In Situ* Cross-linked Nonaqueous Polymer Electrolyte for Zinc-Metal Polymer Batteries and Hybrid Supercapacitors, **V Vijayakumar**, M Ghosh, M Kurian, S Dilwale, A Torris, MV Badiger, M Winter, JR Nair, S Kurungot, Small, 2020, vol. 16, no 35, p. 2002528.
5. Zinc ion interactions in a two-dimensional covalent organic framework based aqueous zinc ion battery, A Khayum, M Ghosh, **V Vijayakumar**, A Halder, M Nurhuda, S Kumar, M Addicoat, S Kurungot, R Banerjee, Chem. Sci., 2019, 10, 8889-8894.
6. Convergent covalent organic framework thin sheets as flexible supercapacitor electrodes, A Khayum M, **V Vijayakumar**, S Karak, S Kandambeth, M Bhadra, K Suresh, N Acharambath, S Kurungot, R Banerjee, ACS Appl. Mater. Interfaces 2018, 10, 33, 28139-28146.
7. A rationally designed self-standing V₂O₅ electrode for high voltage non-aqueous all-solid-state symmetric (2.0 V) and asymmetric (2.8 V) supercapacitors, M Ghosh, **V Vijayakumar**, R Soni, S Kurungot, Nanoscale, 2018,10, 8741-8751.
8. Dendrite Growth Suppression by Zn²⁺-Integrated Nafion Ionomer Membranes: Beyond Porous Separators toward Aqueous Zn/V₂O₅ Batteries with Extended Cycle Life, M Ghosh, **V Vijayakumar**, S Kurungot, Energy Technology 7 (9), 1900442.

9. Synthesis of Carbon Nanosheets and Nitrogen-Doped Carbon Nanosheets from Perylene Derivatives for Supercapacitor Application, R Soni, **V Vijayakumar**, S Kurungot, ACS Appl. Nano Mater. 2018, 1, 9, 4576-4586.
10. Nafion Ionomer-Based Single Component Electrolytes for Aqueous Zn/MnO₂ Batteries with Long Cycle Life, M Ghosh, **V Vijayakumar**, B Anothumakkool, S Kurungot, ACS Sustainable Chemistry & Engineering 8 (13), 5040-5049.
11. Weak Intermolecular Interactions in Covalent Organic Framework-Carbon Nanofiber Based Crystalline yet Flexible Devices, AK Mohammed, **V Vijayakumar**, A Halder, M Ghosh, M Addicoat, U Bansode, S Kurungot, R Banerjee, ACS Appl. Mater. Interfaces 2019, 11, 34, 30828-30837.
12. Unravelling the mechanism of electrochemical degradation of PANI in supercapacitors: achieving a feasible solution, P Sekar, B Anothumakkool, **V Vijayakumar**, A Lohgaonkar, S Kurungot, ChemElectroChem 3 (6), 933-942.
13. High-performance flexible solid-state supercapacitor with an extended nanoregime interface through *in situ* polymer electrolyte generation, B Anothumakkool, A Torris AT, S Veeliyath, **V Vijayakumar**, MV Badiger, S Kurungot, ACS applied materials & interfaces 8 (2), 1233-1241.
14. Hierarchical Nano Polyaniline Bridged Structures for Enhanced Supercapactiance Retention, VA Mooss, **V Vijayakumar**, S Kurungot, AA Athawale, Polymer , 2020, p. 123169.
15. The *In Situ* Preparation of Ionomer as a Tool for Triple Phase Boundary Enhancement in 3D Graphene Supported Pt Catalyst, PK Gangadharan, **V Vijayakumar**, SA Nediyrakkal, RT Fernandez, AV Siddharthan, S Kurungot, Advanced Sustainable Systems, 2020, p. 2000125.
16. Scalable synthesis of manganese-doped hydrated vanadium oxide as the cathode material for rechargeable zinc-metal battery, M Ghosh, **V Vijayakumar**, S Kurungot, ACS Appl. Mater. Interfaces 2020, 12, 43, 48542–48552.

PATENTS FILED

1. An Electrolyte Composition and a Process for the Preparation Thereof, S Kurungot, MV Badiger, B Anothumakkool, A Torris, **V Vijayakumar** (Indian patent granted, Patent No: IN 346319).
2. A Metal-Ion Battery having Ionomer Membrane Separator and Free-Standing Electrode, M Ghosh, **V Vijayakumar**, S Kurungot, (Application No. 201911004481, Patent under process).

REVIEW ARTICLES

1. In Situ Polymerization Process: An Essential Design Tool for Lithium Polymer Batteries, **V Vijayakumar**, B Anothumakkool, S Kurungot, M Winter, JR Nair, (Review article under revision from *Energy & Environmental Science*).

CHAPTERS IN BOOKS

1. Electrolytes for Microsupercapacitors, **V Vijayakumar**, M Ghosh, R Soni, B Anothumakkool, S Kurungot, M Winter, JR Nair, (under editorial revision, *Elsevier Publications*).
2. 2D Nanomaterials as Polymer Composite Electrolytes for Lithium-Based batteries, **V Vijayakumar**, M Ghosh, PK Samantaray, S Kurungot, M Winter, JR Nair, (submitted in inorganic materials books series published by the *RSC*).

CONFERENCE/SEMINAR PRESENTATIONS

1. Presented a poster entitled **An in situ generated allyl ether based gel polymer electrolyte for high voltage lithium metal battery** at the international conference of *Advanced Automotive Battery Conference Europe 2019 (AABC Europe 2019)* held at Strasbourg, France, in January 2019.
2. Presented a poster entitled **Poly (vinyl ethylene carbonate) cross-linked by PEO units as gel polymer electrolytes for high voltage lithium metal batteries** in CSIR-Inter Institutional Student Conference on “Sustainable Chemistry for Health, Environment and Materials (SuCHEM YUVA July 2019) at ICT, Hyderabad, India.
3. ECS-PRiME 2020, Virtual Conference, October 2020, digital poster presenter titled **Zinc-Ion Conducting Nonaqueous Polymer Electrolyte for Zinc-Metal Batteries through UV-Light Induced Cross-Linking Polymerization**.

AWARDS & RECOGNITIONS

1. Recipient of K.M. Abraham travel grant award from The Electrochemical Society for attending the ECS PRiME Virtual Conference, October 2020.
2. Best poster award in SuCHEM YUVA July 2019, a CSIR-Inter Institutional Student Conference at ICT, Hyderabad, India (2019 January).
3. CSIR-UGC NET and Junior Research Fellowship (JRF) with an all India rank of 83 (June, 2014).

Erratum